Heliospheric Cataloguing, Analysis and Techniques Service

EU Project #: 606692

FP7-SPACE-2013-1

HELCATS Final Report

Version: 2.0

Title:	**HELCATS Final Report**
Document Number:	**HELCATS_STFC_D1_8_1**
Project Deliverable:	**D1.8**
Release/Date	**Version: 2.0 2017-06-01**
Editor:	**Richard Harrison & Jackie Davies**
Contributors:	**HELCATS Consortium**
Reviewed By:	**HELCATS Steering Committee**
Distribution:	**EU & PROJECT**

Document Information:

REVISION HISTORY

Issue	Date	Lead Author	Comments
1.0	2017-01-05	Richard Harrison and Jackie Davies, STFC	Initial release
1.1	2017-18-04	Richard Harrison and Jackie Davies, STFC	Updated after comments from Reviewer and HELCATS team
2.0	2017-06-01	Richard Harrison and Jackie Davies, STFC	Submited version after comments from Reviewer and discussion at final HELCATS meetings in Vienna

ACRONYM LIST

AMDA	Automated Multi-Dataset Analysis (software tool)
CIR	Co-rotating Interaction Region
CME	Coronal Mass Ejection
CNRS	Centre National de la Recherche Scientifique
EUV	Extreme UltraViolet
GCS	Graduated Cylindrical Shell model
GMU	George Mason University
HELCATS	Heliospheric Cataloguing, Analysis and Techniques Service
HI	Heliospheric Imager/Imaging
ICME	Interplanetary CME
IMPERIAL	Imperial College of Science, Technology and Medicine, London
IPR	Intellectual property rights
IPS	Interplanetary Scintillation
MGT	Management
MHD	Magnetohydrodynamics
ROB	Koninklijke Sterrenwacht van Belgie
RTD	Research and Technology Development
RAL	Rutherford Appleton Laboratory
OTH	Other
SIR	Stream Interaction Regions
STEREO	Solar Terrestrial Relations Observatory (mission)
STFC	Science and Technology Facilities Council
TCD	The Provost, Fellows, Foundation Scholars & the other members of Board of the College of the Holy and Undivided Trinity of Queen Elizabeth near Dublin
UGOE	Georg-August-Universitaet Goettingen Stiftung Oeffentlichen Rechts
UH	Helsingin Yliopisto
UNIGRAZ	Universitaet Graz
UPS	Universite Paul Sabatier Toulouse III
WP	Work Package

TABLE OF CONTENTS

1 HELCATS PROJECT OVERVIEW

HELCATS – Providing a unique, global analysis of solar-generated transients in the heliosphere, exploiting European space-based instrumentation, through the first comprehensive cataloguing of the transient events whilst assessing key modelling methods and validating their performance through the association of solar source regions and event arrivals at Earth.

The advent of wide-angle imaging of the inner heliosphere has revolutionised the study of the solar wind and, in particular, transient solar wind structures such as Coronal Mass Ejections (CMEs) and Co-rotating Interaction Regions (CIRs). CMEs comprise enormous plasma and magnetic field structures that are ejected from the Sun and propagate at what can be immense speeds through interplanetary space, whilst CIRs are characterised by extensive swathes of compressed plasma/magnetic field that form along flow discontinuities of solar origin that permeate the inner heliosphere. With Heliospheric Imaging (HI) came the unique ability to track the evolution of these features as they propagate through the inner heliosphere. Prior to the development of wide-angle imaging of the inner heliosphere, signatures of such solar wind transients could only be observed within a few solar radii of the Sun, and in the vicinity of a few near-Earth and interplanetary in-situ probes. HI has, for the first time, filled that vast and crucial observational gap. Recognising that a number of lines of research have addressed the deceleration and deflection of CMEs and interaction between CMEs and between CMEs and CIRs, and that considerable evolution of a CME can be witnessed in the HI images during its passage through the heliosphere, exploiting the HI images in studying the propagation of CMEs through the heliosphere must become an essential element of future space weather application; it is not acceptable to simply rely on knowledge of the passage of a CME through the corona and await its arrival at 1 AU.

The HELCATS project provides an unprecedented focus for world-leading European expertise in the novel and revolutionary, European-led field of HI, in terms of instrumentation, data analysis, modelling and science. HELCATS is a strategic project that empowers the wider scientific community, in Europe and beyond, by providing access to advanced catalogues - validated and augmented through the use of techniques and models - for the analysis of solar wind transients, based on observations from European-led space instrumentation. All of the beneficiaries are at the forefront of heliospheric research and bring distinct, yet highly complementary, skills to the project. HELCATS adds significant value to the exploitation of existing European space instrumentation, providing a strong foundation for enhanced exploitation and advancement of European heliospheric research.

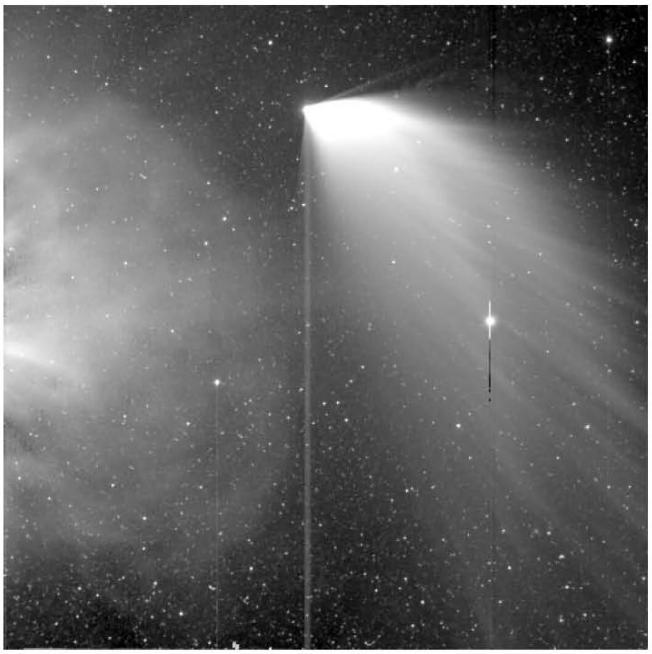

Figure 1.1 - STEREO/HI 20^ox20^o image (HI-1B camera). The Sun is 4^o off the left hand side. The Earth is the bright star, middle right. Comet PanSTARRS is passing through the inner Solar System and a CME can be seen in the left hand side of the frame. (Credit STEREO/HI team)

HELCATS recognises the synergy between solar and heliospheric physics research (both of which are European strengths) and their applied space weather aspect, currently a topic of vigorous debate in many political and scientific arenas. With the current development of a European space weather capability, within ESA's Space Situational Awareness programme, HELCATS has real, practical relevance. Certainly the HI concept is high on the priority lists for the payloads of missions that are being defined at this time, and the exploitation of those instruments, for the detection and analysis of

potentially Earth-impacting events, will be significantly enhanced by the outcome of the HELCATS project studies, in defining methods and models for adoption.

The HELCATS consortium is led by STFC's Rutherford Appleton Laboratory. The Coordinator is Professor Richard A Harrison, the Scientific Manager is Dr Jackie A Davies, and the Technical Manager is Dr Chris Perry. The fundamental aim of the HELCATS project is to start with heliospheric imaging observations and, from that, build up facilities, methods and assessment studies in a logical programme of activities. The work is managed by STFC, involving a total of eight European research groups, or beneficiaries. The activities of the beneficiaries are tailored to their scientific and technical strengths, maximizing the potential scientific return for the project.

The list of beneficiaries and the principal contacts for them is given in Table 1.1. Key to the success of HELCATS has been the combination of space-hardware, observations, data, theory, modelling, across a critical range of solar and heliospheric disciplines, that the beneficiary group provides. In addition, the HELCATS project includes two third parties, not shown in Table 1.1. This includes George Mason University (USA), to enable close modelling ties between UPS and the developer of the Enlil model that is used extensively in some aspects of the project. The second is CNRS, which is the employer of the key staff at UPS; CNRS is included as a formal third party for managerial reasons rather than direct input to the project.

Table 1.1: HELCATS Beneficiaries

No	FORMAL NAME	LEAD CONTACT	SHORT NAME	COUNTRY
1	SCIENCE AND TECHNOLOGY FACILITIES COUNCIL	Prof Richard Harrison	STFC	United Kingdom
2	UNIVERSITAET GRAZ	Dr Christian Möstl	UNIGRAZ	Austria
3	UNIVERSITE PAUL SABATIER TOULOUSE	Dr Alexis Rouillard	UPS	France
4	GEORG-AUGUST-UNIVERSITAET GOETTINGEN STIFTUNG OEFFENTLICHEN RECHTS	Dr Volker Bothmer	UGOE	Germany
5	KONINKLIJKE STERRENWACHT VAN BELGIE	Dr Luciano Rodriguez	ROB	Belgium
6	IMPERIAL COLLEGE OF SCIENCE, TECHNOLOGY AND MEDICINE	Dr Jonathan Eastwood	IMPERIAL	United Kingdom
7	HELSINGIN YLIOPISTO	Dr Emilia Kilpua	UH	Finland
8	THE PROVOST, FELLOWS, FOUNDATION SCHOLARS & THE OTHER MEMBERS OF BOARD OF THE COLLEGE OF THE HOLY & UNDIVIDED TRINITY OF QUEEN ELIZABETH NEAR DUBLIN	Prof Peter Gallager	TCD	Ireland

The HELCATS workpackage (WP) structure is given in Table 1.2; the involvement of each beneficiary is outlined in the WP sections, later. Each WP activity is defined as Management (MGT), Research, Technology and Development (RTD) or OTHER, as defined by the Commission, to identify the category of the work, in particular to define the funding model. This annual report is broken down into reports from each WP. Thus, to aid the reading of these WP reports, we repeat the WP strategy and structure details here, and refer the reader to the WP structure diagram of Figure 1.2.

Table 1.2: The HELCATS WP structure

WP No	WP ACTIVITY TYPE	WP TITLE	WP LEAD
1	MGT	MANAGEMENT	STFC
2	RTD	PRODUCING A DEFINITIVE CATALOGUE OF CMES IMAGED BY STEREO/HI	STFC
3	RTD	DERIVING/CATALOGUING THE KINETIC PROPERTIES OF STEREO/HI CMES BASED ON GEOMETRICAL AND FORWARD MODELLING	UGOE
4	RTD	VERIFYING THE KINEMATIC PROPERTIES OF STEREO/ HI CMES AGAINST IN-SITU CME OBSERVATIONS AND CORONAL SOURCES	UNIGRAZ
5	RTD	PRODUCING A DEFINITIVE CATALOGUE OF CIRS IMAGED BY STEREO/HI THAT INCLUDES VERIFIED MODEL- DERIVED KINEMATIC PROPERTIES	UPS
6	RTD	INITIALISING ADVANCED NUMERICAL MODELS BASED ON THE KINETIC PROPERTIES OF STEREO/HI CMES AND CIRS	UPS
7	RTD	ASSESSING THE COMPLEMENTARY NATURE OF RADIO MEASUREMENTS OF SOLAR WIND TRANSIENTS	IMPERIAL
8	OTHER	DISSEMINATION	STFC

WP1: Management - The HELCATS consortium includes 8 European groups from 7 EU countries and two third parties. The project coordinates work involving observations, cataloguing, modelling, and studies in validation and assessment. WP1 covers the formal management roles of the HELCATS project. This includes administrative tasks, maintaining project infrastructure, coordinating inputs and reporting as required and handling a range of project issues. WP1 oversees the website production and management.

WP2: Producing a definitive catalogue of CMEs imaged by STEREO/HI - This WP provides the foundation for this project (including scientific coordination), namely the production of a catalogue of CMEs in the heliosphere. The catalogue is produced from manual inspection of STEREO/HI data but use of automated techniques has been investigated, allowing the manual and automated methods to be compared. Comparisons with coronal (coronagraph) CME catalogues have also been made, to compare the detection and analysis of CMEs in the corona with those detected in the solar wind.

WP3: Deriving/cataloguing the kinematic properties of STEREO/HI CMEs based on geometrical and forward modelling - Here we apply recently established geometrical, forward and (prototype) inverse modelling methods to derive CME parameters, which are added to the catalogue (including back- and forward-projections to 'predict' CME launch and arrivals at various Solar System locations). Comparisons have been made between the parameters yielded by the different models.

WP4: Verifying the kinematic properties of STEREO/HI CMEs against in-situ CME observations and coronal sources - This WP catalogues in-situ CME information (at Earth and elsewhere) for comparison to the

projected data from WP3 in order to assess the performance of the aforementioned models. Similarly, comparisons are made with solar 'surface' phenomena. These allow a thorough validation of the models.

WP5: Producing a definitive catalogue of CIRs imaged by STEREO/HI that includes verified model-derived kinematic properties - In parallel with the CME cataloguing, modelling and model assessment in WP2-4, this WP performs an analogous activity for CIRs, again with cataloguing, geometrical modelling and the validation of results through comparisons to in-situ/solar data.

WP6: Initialising advanced numerical models based on the kinematic properties of STEREO/HI CMEs and CIRs - This WP recognises the potential for using HI data as input to numerical MHD models of the heliosphere (in terms of both CME and CIR phenomena) by considering the use of HI images for initialisation/driving of the ENLIL model. The results are compared to traditional methods for running such models, based on coronal and photospheric inputs, to assess their potential.

WP7: Assessing the complementary nature of radio measurements of solar wind transients - WP7 explores the value of incorporating radio observations, to augment the HI data. It assesses the value of using interplanetary scintillation (IPS) observations and Type II radio burst data in conjunction with HI data, both of which can provide additional information.

WP8: Dissemination - WP8 brings the results to the community through (1) the publication of results in the open, refereed literature, (2) the running of annual open meetings, (3) the installation of all relevant documentation, catalogues and reports on the website and (4) the dissemination of information to the public and policy makers. This includes ingestion of the products into the AMDA data-mining tool the IRAP (UPS) propagation tool, and integration with projects such as HELIO. This WP coordinates the exploitation of the project outputs, such that they feed into numerous research activities and future space weather applications.

Overall, the HELCATS strategy is to coordinate a range of observational and modelling studies of heliospheric phenomena to provide a foundation for enhancing the scientific discipline and the exploitation of European investment in the hardware involved. It is also a benchmark in the provision of facilities to understand the nature and development of solar transients in the heliosphere.

Full details of the HELCATS project can be seen in the description of work documents (606692_DOW_PART_A.pdf and 606692_DOW_PARTB.pdf) agreed with the European Commission in early 2014. Those documents also outline the resources per beneficiary, and by WP, in terms of finance and staff time. These are reproduced in Tables 1.3 and 1.4.

In the following sections we address each WP in turn, providing detailed descriptions of the WP activities and outcomes. HELCATS was a three-year project with a clearly defined schedule of activities, milestones and deliverables and this report demonstrates that the project ran pretty much to schedule. The WP summaries have been produced from material provided by the WP leaders; this does mean that the WP sub-sections vary slightly in their style and format. However, the aim is to produce a thorough statement on the outcome of the project and the future legacy, and this, we believe has been done effectively.

In terms of the productivity of HELCATS we do stress that the project was designed to provide a unique, timely facility for the research community, to drive a significantly better understanding of solar-generated transients and their passage through the heliosphere, as well as their sources and impacts. Thus, in keeping with the spirit of many EU projects, the aim is to provide the legacy of a thorough, global catalogue of heliospheric transients, that has previously not been available, and, in doing so, assess and validate a range of available models. The project is not a portal allowing use of a number of space-related data-bases; it is built on a specific instrumental and observational strength in heliospheric imaging, with the analysis and modelling activities that provide a global view of solar transients in the heliosphere that has not existed before. The project has added significant value to existing facilities and is clearly of direct interest to space weather applications in the near future. However, in providing the facilities (catalogues) and the assessment and exploitation of different models and methods, the project clearly provides a facility that is valuable to the wider research community and is not *per se*, a research project in itself. The basic aim was to deliver a legacy that can enable major scientific steps. Nevertheless, many of the results are published in the scientific literature and these are noted in the text and included in the publication list.

Table 1.3: The distribution of work between beneficiaries and WP (person-months)

Beneficiary	WP1	WP2	WP3	WP7	WP4	WP5	WP6	WP8	Total per Beneficiary
1 – STFC	8.50	25.00	9.00	19.50	0.00	0.00	0.00	11.50	73.50
2 - UNIGRAZ	0.00	0.00	6.00	0.00	30.00	0.00	0.00	0.00	36.00
3 – UPS	0.00	0.00	0.00	0.00	2.00	25.00	24.00	10.00	61.00
CNRS	0.00	0.00	0.00	0.00	2.00	8.00	3.00	0.00	13.00
4 – UGOE	0.00	6.00	21.00	0.00	12.00	0.00	0.00	0.00	39.00
5 – ROB	0.00	20.50	0.00	3.00	6.00	0.00	0.00	0.00	29.50
6 - IMPERIAL	0.00	0.00	0.00	17.00	3.00	0.00	0.00	0.00	20.00
7 – UH	0.00	0.00	0.00	0.00	13.00	9.00	0.00	0.00	22.00
8 – TCD	0.00	0.00	15.00	0.00	0.00	0.00	0.00	0.00	15.00
Total	8.50	51.50	51.00	39.50	68.00	42.00	27.00	21.50	309.00

Table 1.4: The distribution of estimated eligible costs at the start of the project (€) (note: there were no sub-contracting costs)

Beneficiary	Personnel costs	Other direct costs	Indirect costs	Total	Requested EU contribution
1 – STFC	413,539	84,082	434,216	931,837	781,718
2 - UNIGRAZ	201,000	22,375	134,025	357,400	270,000
3 – UPS	295,342	36,625	199,180	531,147	427,547
CNRS	56,000	0	33,600	89,600	67,200
4 – UGOE	195,000	34,200	137,520	366,720	277,200
5 – ROB	147,500	19,875	100,425	267,800	202,200
6 - IMPERIAL	129,196	16,089	87,171	232,456	176,862
7 – UH	127,234	18,875	87,665	233,774	176,680
8 – TCD	80,354	18,500	59,312	158,166	120,424
Total	1,645,165	250,621	1,273,115	3,168,901	2,499,833

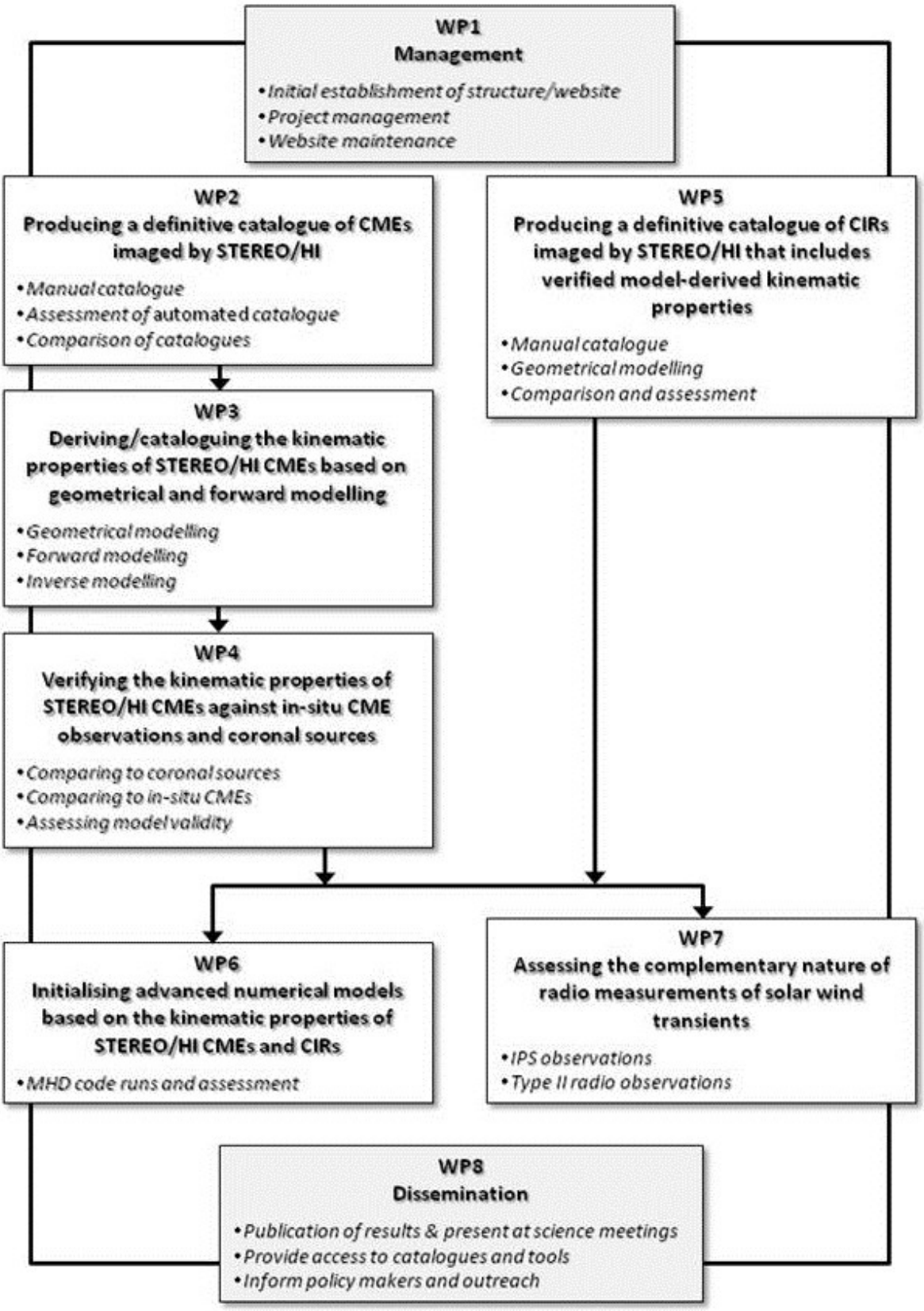

Figure 1.2 - The HELCATS WP structure and study logic

2 OVERVIEW OF THE CATALOGUES

One of the international benchmarks for CME research is the CDAW (Coordinated Data Analysis Workshops) catalogue of events identified in the SOHO/LASCO coronagraph data (see https://cdaw.gsfc.nasa.gov/CME_list/). This facility has provided the gold standard in event identification and in enabling a wide range of investigations that have advanced the field of CME research considerably over the past 20 years. It does not replace the research; it enables the research by providing access to the event listings and the data, as well as basic analysis of the kinematics. The CDAW/LASCO event list is referenced directly in a large number of research papers. All of this relates to the passage of solar ejecta through the corona.

With the advent of the STEREO/HI instruments (Eyles et al., 2009), following on from the Coriolis/SMEI instrument, we are now observing CMEs in the heliosphere on a regular basis, well beyond the limits of LASCO's field of view, and through interplanetary space to beyond 1 AU. The STEREO/HI instruments are led by RAL Space (STFC). Whilst recognising the value of heliospheric CME investigations to fundamental research, we also note the requirements of the space weather community, and these both stress the need for a similar benchmark facility for heliospheric CMEs. Hence, the concept behind HELCATS was born.

In many ways, the HI instrumentation and the HELCATS project work focus on the fact that prior to the advent of heliospheric imaging, CMEs could be observed in the corona but were then not detected until and unless they passed over spacecraft with in-situ instrumentation. As mentioned above, we recognise a 200 Rs 'gap' in observational capability that has now been closed. Tracking CMEs and studying their structure and evolution in the inner heliosphere enables studies of a wide range of issues such as CME onset and Earth arrival studies, CME-CME interaction, CME deceleration and deflection, the shock-CME relationship, and studies of other transients such as SIRs/CIRs. The value of such work for space weather impacts is clear, as is the opening of this vast new region for fundamental research into heliospheric physics. Thus, the value of HI observations is clearly of great importance for heliophysics research as well as space weather interests.

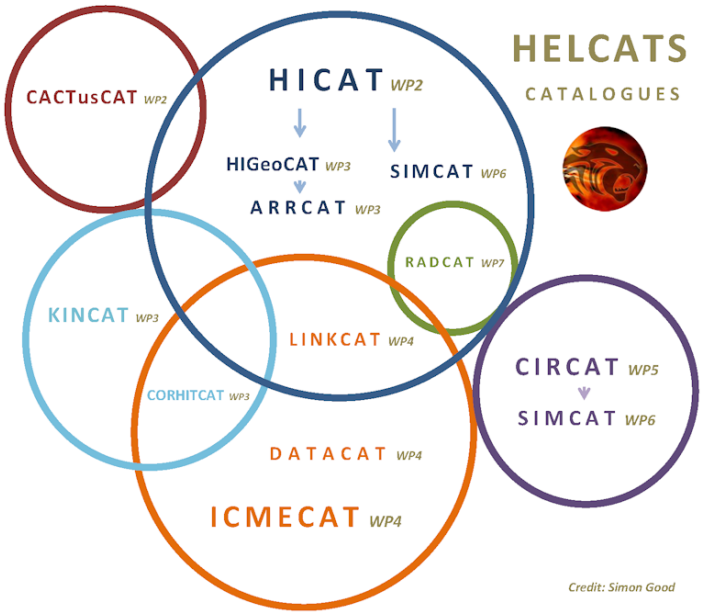

Figure 2.1 – A schematic outline of the relationship between the different catalogues of the HELCATS project

The HELCATS project work-plan outlined a set of clear elements and results, defined very much through the unique set of catalogues that have been subsequently developed, as detailed in the bullets, below. All of the catalogues mentioned are accessible through the HELCATS website, using the PRODUCTS tab. We group the catalogues for clarity:

Heliospheric Imaging of CMEs (HICAT, HIGeoCAT and CACTusCAT)

- HICAT – The first definitive catalogue of CMEs in the heliosphere from outside the Sun-Earth line (WP2). The foundation of the project is the manual inspection and analysis of the STEREO/HI data to identify and catalogue all CMEs in the heliosphere from April 2007 to February 2017 (Version 4, released 2017-04-06). This is the HICAT catalogue, currently with 1,601 entries. Once identified, events are labelled with a unique ID, and the date, time, spacecraft, CME position angles and event quality are listed. HICAT has become the official and definitive event list of the STEREO/HI instruments and, as such, the lists will be maintained and updated by the STEREO project after the completion of the HELCATS project. Events will continue to be included as the STEREO mission continues, and inclusion of HICAT as the official event list through the STEREO project ensures wide community use of the catalogue. Clicking on a listed event opens up an event data page for the selected CME. (Catalogue doi 10.6084/m9.figshare.1492351).

- HIJoinCAT – Identifying CMEs in HICAT detected by STEREO-A and STEREO-B (WP2). HIJoinCAT comes from manual inspection of the STEREO-A and STEREO-B events in the HICAT database, and through the comparison of locations and timing, identifies events that are seen from both spacecraft. This identifies CMEs that can be analysed by stereoscopic means, i.e. from widely separated platforms. Version 1 was released o n 2017-04-20 and it contains 546 entries.

- HIGeoCAT - Extends the HICAT catalogue through the addition of kinematic parameters from geometrical modelling (WP3). HIGeoCAT takes all of the HICAT CMEs for which geomagnetic modelling can be employed, to derive and list kinematic parameters, such as speed and 3D direction, and projected onset times. Later work, using the in-situ observations of CME arrivals at Earth, is used to validate the models. The HIGeoCAT catalogue is also in version 4, released on 2017-04-06, and it contains 1,414 CMEs. Clicking on a listed event opens up an event data page for the selected CME. The production of the HIGeoCAT catalogue provides for the heliospheric community what the CDAW catalogue has provided for the coronal community; this is a resource that will be used extensively and is endorsed by the STEREO team. (Catalogue doi applied for).

- CACTusCAT – Provides a list of automated CME detections for comparison with the manual HICAT and HIGeoCAT catalogues (WP2). Exploiting and developing the CACTus method that has long been employed on the SOHO/LASCO coronal CME data for automated CME detection, HELCATS has demonstrated a capability for automated CME detection in HI data and favourable comparisons made with the manual methods. The current release runs from January 2007 to August 2014. A real-time version of CACTusCAT is being run by ROB at www.sidc.be/cactus/hi/.

Solar coronal and 'surface' events: CMEs in the corona and solaractivity (KINCAT, LOWCAT)

- KINCAT – Catalogue of coronagraph observations using the GCS model (WP3). This catalogue aims to allow a comparison of the HI-derived CME parameters of the HICAT and HIGeoCAT catalogues with an associated catalogue of coronal CME parameters. Events are identified using the STEREO/COR2 observations (1071 events in all) and the CME parameters (speed, direction, mass) derived from the application of a Graduated Cylindrical Shell model (that assumes a flux-rope topology). Some 122 events are catalogued May 2007 to December 2011 for which the GCS model could be employed. This event-set is used to make a thorough assessment of the relationship between events seen in the corona and in the heliosphere. (Catalogue doi applied for).

- LOWCAT – Catalogue of low coronal events (WP3). LOWCAT identifies events in the low corona that are associated in space and time with the projected onsets of the HI CMEs. This includes COR2 (STEREO) CMEs, along with flare, active region and filament listings. This includes entries for 1673 events.

In-situ predictions and observations of CMEs (ARRCAT, ICMECAT)

- ARRCAT – A catalogue of CME predicted arrivals (WP4). This catalogue uses the Self Similar Expansion model (see WP3 and 4 sections of the report) on the HIGeoCAT events to list the predicted arrival times of CMEs at Earth/L1, STEREO-A, STEREO-B, Venus, MESSENGER, Mars, Saturn, Ulysses, Mars Science Laboratory (MSL), MAVEN and Rosetta. ARRCAT lists some 1995 possible impacts on

these targets. It is these impacts and their timings that are used later to compare with and validate the heliospheric CME models. The current version (version 1) covers the perios January 2007 to December 2015, and was released 2017-02-28. (Catalogue doi 10.6084/m9.figshare.4588324.v1).

- ICMECAT – A catalogue of in-situ CME observations (WP4). Following on from the HIGeoCAT and subsequent ARRCAT catalogues, the actual in-situ identification of CMEs at Earth/L1, STEREO-A, STEREO-B, Venus, MESSENGER, Mars, Saturn, Ulysses, Mars Science Laboratory (MSL), MAVEN and Rosetta is given in the ICMECAT catalogue. ICMECAT includes 668 events (note that many CMEs observed with HI will not impact any of the spacecraft), and was released on 2017-02-28. Parameters such as the mean magnetic field and minimum Bz component have been derived, to aid comparisons to the predicted CME arrivals. (Catalogue doi 10.6084/m9.figshare.4588315.v1).

- CORHITCAT – Catalogue of STEREO COR2 coronal CMEs with predicted arrival times at spacecraft (WP4). Complementary to the HI-related data, CORHITCAT takes the STEREO COR2 coronagraph observations to produce predictions of arrivals at different spacecraft, and compares to the in-situ events identified. This allows a comiparison of both HI and coronagraph analyses. (Catalogue doi 10.6084/m9.figshare.4903241.v1).

Linking coronal, heliospheric and in-situ catalogues (LINKCAT)

- LINKCAT – Linking the solar, heliospheric and in-situ events (WP4). LINKCAT is the glue between the coronal, heliospheric and in-situ catalogues, connecting the events that are spatially and temporally consistent. LINKCAT v1 (released 2016-07-11) includes some 143 entries, identifying the potential solar source associated activity and the parameters of the potentially associated event arrivals with each HIGeoCAT event for which such associations could be found (remembering that many of the HIGeoCAT events do not impact the spacecraft being used (near-Earth or at Mars, Venus or elsewhere). With LINKCAT, we have the first catalogue of CMEs linking from in-situ observations, through the heliosphere, the corona, and to the solar source regions. Again, linking these datasets allows a thorough test of the modelling employed in the analyses, projected to 1 AU and back-projected to the Sun. (Catalogue doi 10.6084/m9.figshare.4588330.v2).

Co-rotating/Stream interaction regions (CIR/SIR) catalogue (CIRCAT)

- CIRCAT – Catalogue of co-rotating/stream interaction regions (WP5). CIRs/SIRs can be detected in the HI data through the passage of blob-like structures entrained in the interface regions. Given the experience with the CME observations within the HELCATS project, it was logical to perform a parallel study of CIR/SIRs. CIRCAT (version 2, released in 2017-03-27) provides a catalogue of the parameters of 212 events from April 2007 to August 2014. This is the first such analysis and catalogue of its kind and, as with the HI CME catalogue (HICAT/HIGeoCAT) is providing the first benchmark for studies of the phenomenon. (Catalogue doi applied for).

Solar wind background simulation database (SIMCAT)

- SIMCAT – Simulating the background solar wind (WP6). Recognising the extensive use of background solar wind simulations for space weather application, especially through the Enlil-WSA model, the HELCATS project, through WP6, attempts to simulate the background solar wind structure for advanced numerical modelling based on the kinetic properties of the CMEs and CIRs/SIRs observed and analysed through the use of HI data, rather than projected from solar magnetogram data using the so-called WSA empirical model. The simulated maps appear in the SIMCAT catalogue and it is through that catalogue that their value is assessed in comparison to the established methods.

Radio catalogues (RADCAT, IPSCAT)

- RADCAT – Cataloguing radio Type II signatures associated with CMEs (WP7). The RADCAT listing, provides a set of Type II radio events in the period March 2008 to August 2014 (March 2008 was the first event recorded; the analysis extended to earlier dates). These are Type II data recorded by the S/WAVES instrument on STEREO, in the frequency range 100 to 2000 kHz, which means that they are both coronal and heliospheric in nature and could, thus be readily associated with the HI CMEs (ground based Type II observatories cannot extend to such wavelengths and are generally only able

to detect CMEs in the outer corona). RADCAT v3 (released 2016-10-19) lists parameters for 156 entries. (Catalogue doi applied for).

- IPSCAT – Catalogue of IPS events (WP7). This catalogue exploits the interplanetary scintillation (IPS) radio observations of the European EISCAT and LOFAR facilities in the detection of signatures of CMEs. It is a speculative pilot study aimed at identifying potential IPS events and comparing these to the HICAT/HIGeoCAT events to assess how well IPS techniques might work. Version 1 of the IPSCAT was released on 2017-04026. (Catalogue doi applied for).

It is the catalogue structure given here that describes the backbone of the HELCATS project; it provides facilities for future research by the community, as a clear legacy, and the published results from the project itself will spearhead the exploitation of these. The work also provides many pointers for future development, the radio studies being a good example.

Details of the work relating to the development of the catalogues and the modelling activities pertaining to each are given in the following sections, which describe the Work Packages in turn.

3 WORK PACKAGE SUMMARIES AND REPORTS

WORK PACKAGE 1 (WP1): MANAGEMENT

WP1 ACTIVITY TYPE: MGT

WP1 DURATION: MONTHS 1 – 36

WP1 LEAD BENEFITIARY: STFC (1)

WP1 LEADER: Professor Richard A Harrison

WP1 CONTRIBUTORS: n/a

WP1 OVERVIEW: WP1 provided the overall management of the HELCATS project, with the WP led by the Project Co-ordinator. The main tasks of WP1 were the initial establishment of the management structure for the HELCATS project, and its support and communication tools, the general operation of this structure, and its termination at the end of the project together with the delivery of the regular and final reports. The HELCATS consortium consists of 8 European groups (involving 7 EU counties), plus two third-party groups from the USA and France. The project is a complex coordination of activities involving observations and cataloguing, the development of models and their application, and exercises in validation and assessment. The objective of WP1 was to provide the necessary management structure to implement the HELCATS project effectively, overseeing all administrative matters, assembling and submitting formal reports, overseeing finance auditing, and arranging meetings as appropriate. Thus, the work package consisted of two major, specified tasks, namely, the HELCATS Project Management and the HELCATS website maintenance.

WP1 TASK 1.1: HELCATS PROJECT MANAGEMENT (TASK LEAD: STFC)

Task 1 covered the formal management roles of the project. This included administrative tasks, maintaining project infrastructure, coordinating inputs and reporting as required and handling a range of project issues.

At the onset of the project, in May 2014, the Executive Board established the formal communication with the Steering Committee, setting up monthly teleconferences and the kick off meeting. The first draft of the HELCATS website was released. The kick off meeting was held on 14-15 May 2014, hosted at the STFC Rutherford Appleton Laboratory. It was attended by all of the beneficiaries and the EU Project Officer, Dr Sabri Mekaoui. All WPs were discussed in detail. The meeting schedule and locations, for the Bi-Annual Project Meetings/Workshops and the Annual open Workshops were decided for the entire period of the project, ensuring that most beneficiaries hosted at least one meeting. The website was also discussed in detail and formally released (**https://www.helcats-fp7.eu/**) after the kick-off meeting. Minutes of the meeting and of all subsequent Steering Committee teleconferences are placed on the website (teleconference minutes are held within the project wiki, in the project private area on the website). The Steering Committee consisted of the STFC management team (Project Co-ordinator, Scientific and Technical Managers, and the WP and beneficiary leads).

Steering Committee telecons were held regularly, starting on July 15, 2014 (see Wiki for minutes). Particular focus at the telecons was given to the impending deliverables, to the arrangements of upcoming meetings and the discussion of any issues that attendees wish to raise. The activities related to the telecons and the bi-annual meetings were managed through a live action list, which was maintained within the minutes posted in the Wiki.

The schedule agreed for the six-monthly project team meetings and the Annual Open Workshops, as decided at the kick off meeting is given in Table 3.1.1, with the actual dates and locations of the meetings also given. Note that the final meetings of the HELCATS project were held in association with the 2017 European

Geosciences Union (EGU) assembly in Vienna (24-28 April 2017), with the final Annual Open meeting being a formal session of the EGU meeting on April 24, the final bi-annual Steering Committee closed meeting being held on April 25. Also, on April 28, also at the EGU Assembly, the final HELCATS Project Review took place with the Steering Committee, the Project Officer (now Andrej Rozkov) and the reviewer (Professor Brigitte Schmieder). Again, minutes for all of the listed meetings are posted in the HELCATS website Wiki.

Table 3.1.1: Schedule and locations of the planned and actual principal meetings of the HELCATS project

Planned Month	Meeting/Review	Planned Location	Actual Location (date)
1 (May 2014)	Kick off meeting	RAL (STFC) [UK]	RAL (STFC), Harwell, UK (May 14-15, 2014)
6 (Nov 2014)	First bi-annual project team meeting	ROB [Belgium]	ROB, Brussels, Belgium (Nov 5-6, 2014)
12 (May 2015)	Second bi-annual project team meeting and first Annual Open Workshop	RGOE [Germany]	RGOE, Göttingen, Germany (May 18-22, 2015)
18 (Nov 2015)	Third bi-annual project team meeting	UH [Finland]	UH, Helsinki, Finland (November 3-4, 2015)
24 (May 2016)	Fourth bi-annual project team meeting and second Annual Open Workshop	UPS (Toulouse)	Albena, Bulgaria (June 7-8, 2016) **Hosted by UPS. Held in association with SCOSTEP, VarSITI meeting to increase exposure of project to community*
30 (Nov 2016)	Fifth bi-annual project team meeting	TCD [Ireland]	TCD, Dublin, Ireland
36 (May 2017)	Sixth bi-annual project team meeting and final Annual Open Workshop	IMPERIAL [UK]	Vienna, Austria (April 24-25, 2017) ** Hosted by IMPERIAL. Held in association with 2017 EGU Assembly, to maximise exposure to scientific community*
36 (Apr 2017)	HELCATS Final Review	STFC [UK]	Vienna, Austria (April 28, 2017)

On total, six bi-annual project team meetings were planned, and held, throughout the project, and three Annual Open Workshops were planned and completed. The bi-annual project team meetings reviewed all actions, deliverables and progress, and covered any technical and managerial issues as required. These were closed meetings for the Steering Committee (the Project Reviewer attended the second, third, fourth and sixth bi-annual meetings). The Annual Open Workshops were open to anyone; good attendance of groups beyond the HELCATS team was evident at the first Workshop, in Göttingen, but to increase the exposure of the project to the wider community, the second Workshop was incorporated within the VarSITI meeting in Bulgaria. This succeeded in delivering a number of major HELCATS talks to a large community. The same approach was agreed by the Steering Committee for the final Workshop, which, as noted, was held in association with the EGU assembly in Vienna. This strategy has given HELCATS excellent exposure, especially

to younger scientists and to the space weather community.

Through this WP, the project has maintained contact with the EU through the Project Officer and has dealt with any formal project communication as required. Minutes and reports have been produced as required (summarised below). Overall, the basic structure of the project and the progress of the WPs have been established and delivered as planned.

Finance reporting of the project has been somewhat independent of the scientific and technical aspects of the project, mainly because the latter are performed within the monthly reporting cycles of the telecons. The formal financial reporting is linked to the two payment milestones at 18 months and the end of the project. Thus, we have formally reported on the status of the finance at 18 months and do the same after completion of the project. However, in conjunction with the telecons, the STFC group have requested occasional financial information from the beneficiaries to maintain an overview of the financial position of the project.

WP1 TASK 2.1: HELCATS WEBSITE MAINTENANCE (TASK LEAD: STFC)

The HELCATS website (**https://www.helcats-fp7.eu**) was launched at the start of the project. The basic aim of the site is to facilitate communication within the project, including the lodging of minutes and actions (within the private Wiki area), plus the dissemination of information, including the catalogues to anyone.

*Figure 3.1.1 – The HELCATS website – **https://www.helcats-fp7.eu***

The site includes news items and information on meetings. However, in terms of outputs of the study, one of the principal tabs of interest is the 'products' tab, which provides access to the catalogues that are described in section 2, and in detail in the subsections of section 4. The aim at the end of the project has been to set up the web facility as a permanent window to the archives and to maintain a number of aspects beyond the formal completion of the project (e.g. the STEREO/HI event lists). The website will provide the window to the legacy of the HELCATS project for the wider community into the future. In addition to the products such as the archives, the website holds a list of project-related publications and reports, and outreach material, including a gallery. At the time of writing (May 2017), the website is still a working website for a live project; over the coming months it will be set up in a 'legacy mode', i.e. the team will ensure that all required information and facilities are set up and available.

WP1 DELIVERABLES:

WP1 has nine associated deliverables, which are defined and their status outlined, in Table 3.1.2. At the time of writing, the first seven of the deliverables had been submitted and five had been approved. The project team await the approval of D1.6 and D1.7. All of the deliverables, except for one (D1.1), were in the form of a report which can be uplinked to the ECAS website. The dissemination levels indicate, in this case, whether the deliverable is publically available (PU) or available only to the project, the project Officer and reviewer (PP).

Table 3.1.2: The HELCATS deliverables for WP1

No.	Title	Lead Beneficiary	Nature	Dissemination Level	Delivery Date (m)	Status/Comment
D1.1	HELCATS website launch	STFC	Other	PU	3	**Submitted/approved**
D1.2	Minutes of kick-off meeting	STFC	Report	PP	2	**Submitted/approved**
D1.3	Progress report to the Commission (6 months)	STFC	Report	PP	7	**Submitted/approved**
D1.4	Annual progress report and cost statement – Year 1	STFC	Report	PP	13	**Submitted/approved**
D1.5	Progress report to the Commission (18 months)	STFC	Report	PP	19	**Submitted/approved**
D1.6	Annual progress report and cost statement – Year 2	STFC	Report	PP	25	Submitted*/awaiting approval
D1.7	Progress report to the Commission (30 months)	STFC	Report	PP	31	Submitted/awaiting approval
D1.8	Final HELCATS report and cost statement	STFC	Report	PP	36	**Pending**
D1.9	Final public report	STFC	Report	PP	36	**Pending**

The deliverable date is given as the month, from 0 to 36. With reports typically appearing one month after the related meeting or workshop. Deliverable D1.5 became more substantial than anticipated because it

coincided with the 18 month cost statement and the related stage payment. Thus, it was agreed with the Project Officer that the subsequent Annual report (action D1.6) could be upgraded to a definitive publication describing the HELCATS project but also providing links to the catalogues and other project facilities, to be published in the professional literature. This was agreed, and a statement to that effect was uplinked as the formal D1.6 deliverable (hence the asterisk). Thus, the HELCATS definitive paper is in production; the plan was to deliver this on completion of the work to ensure that the catalogues were complete and links and references up to date. Thus, the submission was to be after April 2017 and it anticipated in May/June 2017.

Deliverable D1.8 is, in fact, the current report, whch we listed as a formal deliverable of the project. Deliverable D1.9 is a final report for public consumption which is drafted and will be released along with this report.

WP1 CONCLUSIONS:

The activities of WP1 have been implemented according to the original proposal very much as planned, and this has given the project a clear working structure that has allowed the required cataloguing, modelling and assessment activities to perform, also as planned, without too much administrative activity. Completion of the proposed regular meetings and telecons, and of most deliverables, means that the team is now placing the emphasis on the legacy of the project and the exploitation of the results. This will be enhanced by the publication of the definitive HELCATS paper, the final public report (D1.9) and the consolidation of the website at the end of the project. We note also that many of the activities, such as the cataloguing of STEREO/HI transients in the heliosphere will continue, on the HELCATS website, under the auspices of the STEREO/HI Post Launch Support project, led by the STFC group.

WORK PACKAGE 2 (WP2):

PRODUCING A DEFINITIVE CATALOGUE OF CMES IMAGED BY STEREO/HI

WP2 ACTIVITY TYPE: RTD

WP2 DURATION: MONTHS 1 – 36

WP2 LEAD BENEFITIARY: STFC (1)

WP2 LEADER: Dr Jackie Davies

WP2 CONTRIBUTORS: UGOE (4); ROB (5)

WP2 OVERVIEW: WP2 involved the production of a catalogue of CMEs in the heliosphere through visual inspection of white-light imagery from the STFC-led HI Instruments (Principal Investigator Richard Harrison, Project Scientist Jackie Davies) on NASA's twin-spacecraft STEREO mission. In addition, autonomous cataloguing of STEREO/HI CMEs, based on use of the long-established CACTus software package, was also investigated within this WP. The latter was demonstrated to be viable and the two catalogues inter-compared, as well as being compared with other, pre-existing, coronal CME catalogues. WP2 included four tasks. Whilst tasks 2.1 and 2.2 comprised the manual and automated CME catalogue production, led by STFC and ROB, respectively, task 2.2 (led by UGOE) covered the comparison of the resultant CME catalogues with each other and with pre-existing coronal CME catalogues. Task 2.4 (led by STFC), was incorporated within WP2, but was rather different, covering the HELCATS scientific management**.** A summary of the work in each of these tasks is given below.

[Relevant catalogues: HICAT, CACTusCAT]

WP2 TASK 2.1: MANUAL CATALOGUING OF STEREO/HI CMES (TASK LEAD: STFC)

WP2 provides a comprehensive catalogue of the observational properties of CMEs observed using the STEREO/HI instruments since the beginning of the science phase of the mission (April 2007). This catalogue was produced as part of task 2.1 and it is upon this CME list that much of the subsequent HELCATS work is based. A full description of the work summarized here is given by Harrison *et al.* (2017), Davies *et al.* (2017) and Barnes *et al*. (2017), to be published on completion of the project. The WP2 catalogue contains the most basic observational properties of each CME, which includes the following six fields;

1. A unique CME identifier
2. The time of the first observation of the CME in the HI field of view (UTC)
3. The observing spacecraft (A or B)
4. The northernmost position angle extent of the CME (degrees)
5. The southernmost position angle extent of the CME (degrees)
6. A quality flag indicating whether the CME is considered poor, fair or good

The unique identifier is a string of the form HCME_*C*__*YYYYMMDD_NN*, where *C* is a letter denoting the observing spacecraft, *YYYYMMDD* an eight letter string containing the date of first observation and *NN* a two digit number, beginning at 01, to differentiate between multiple CMEs that occur on the same day. Fields 4 and 5 represent the position angle of the northernmost and southernmost extent of the CME in position angle. This is typically found to be within about 20° of the solar equator during solar minimum and about 40° during solar maximum. In the case that a CME exceeds the field of view of HI1, a greater- or less-than symbol is included in fields 4 and 5, respectively. The quality flag has been introduced to account for the fact that some degree of ambiguity is introduced by identifying CMEs by manual inspection. A good event is one where there is no doubt that a CME is observed. A fair event resembles a CME, however some observers may disagree. A poor event is an object spanning at least 20° in position angle but which poorly resembles a CME. CMEs, or any objects, less than 20° are excluded entirely from the catalogue.

The catalogue has been completed from the beginning of April 2007 up to September 2014 for STEREO-B data, at which point contact was lost with the spacecraft. Contact was partially restored, however efforts to fully restore the spacecraft are ongoing and therefore no new data are available presently. For STEREO-A the catalogue has been completed for the same duration, plus the period from October 2015 up to January 2017, after STEREO-A emerged successfully from superior conjunction with the Sun. The STEREO-A and –B catalogues contain 1081 CMEs and 936 CMEs respectively.

Further to the work undertaken in task 2.1, we give here a brief description of the augmented CME catalogues developed as part of WP3 task 1 and WP2 task 3. These tasks are not officially listed as deliverables but are both a development of the basic catalogue produced in WP2 task 1. In WP3 task 1 the CMEs identified in the initial catalogue are tracked using time/elongation plots, to which geometric models are applied in order to estimate the CME speeds, directions and launch times. Task 2.3 identifies those CMEs from the initial catalogue that are observed simultaneously by instruments on both STEREO spacecraft. To these CMEs stereoscopic versions of the geometric models are applied using time/elongation data from both spacecraft, as a further part of task 3.1.

The deliverable D2.1 is listed in the HELCATS description of work as 'A catalogue of observational parameters of HI-1 manually identified CMEs'. The additional work described in the previous paragraph, but not listed officially in terms of deliverables, includes (i) a catalogue of geometrically-modelled CMEs, including CME kinematic properties, (ii) a list of CMEs from the initial catalogue that are observable by both STEREO-A and –B, and (iii) the kinematic properties of these STEREO-A and –B CMEs based on stereoscopic modelling.

This manual CME catalogue contains the six basic observational properties of HI CMEs, as listed above. Figure 3.2.1 shows one such CME in three HI-1A images, each spaced six hours apart. The CME ID and north/south position angle extent is over-plotted. This is an example of a CME considered to be good.

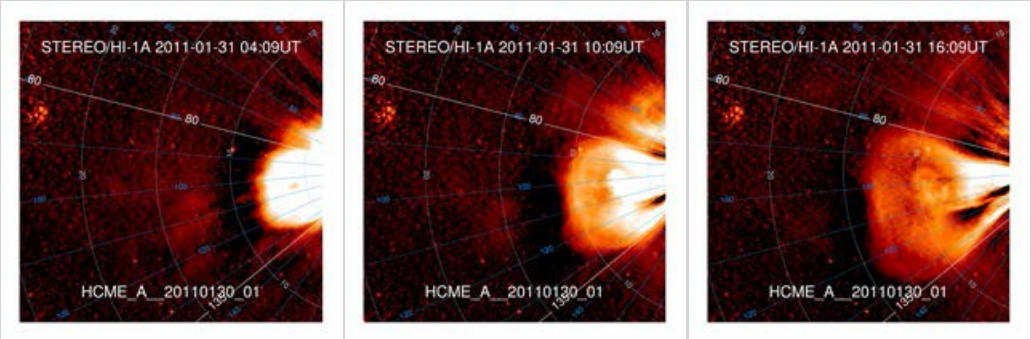

Figure 3.2.1 – Three STEREO/HI-1A images of a heliospheric CME over a 12 hour period.

These observational properties were recorded for every event observed in the HI data and were compiled into a catalogue available on the HELCATS website (https://www.helcats-fp7.eu/catalogues/wp2_cat.html). Figure 3.2.2 shows an example of this information as it appears on the website. Users may filter the CME list online, by date or PA range, or alternatively the complete dataset is available for download in ASCII, VoTable and JSON formats. The website also contains a description of each of the fields contained in the catalogue.

The catalogue forms the heart of the HELCATS study and is known as the HICAT (HI Catalogue).

Figure 3.2.3 shows histograms representing the monthly CME rates from each of the STEREO-A and –B catalogues. Additionally data from the LASCO CDAW catalogue are shown, as is the monthly sunspot number for the same period. All four data sets show behaviour consistent with the solar cycle, however the there are differences in the total number of CMEs observed in the HI and CDAW catalogues. These are due to the different instruments used to observe them and the different selection criteria, e.g. HICAT lists only ejecta that are >20° in angular position angle extent to avoid listing numerous blob-like features in the solar wind.

As part of task 3.1 (of WP3), CMEs in the HICAT lists are tracked through successive images using time/elongation plots (figure 3.2.4). Again, this is achieved via manual inspection. The CMEs are tracked at a single position angle, corresponding approximately to the centre of their angular extent. Figure 3.2.4 shows an example of a CME observed by both STEREO spacecraft; however the results of the geometric models shown in the figure are based on single-spacecraft observations.

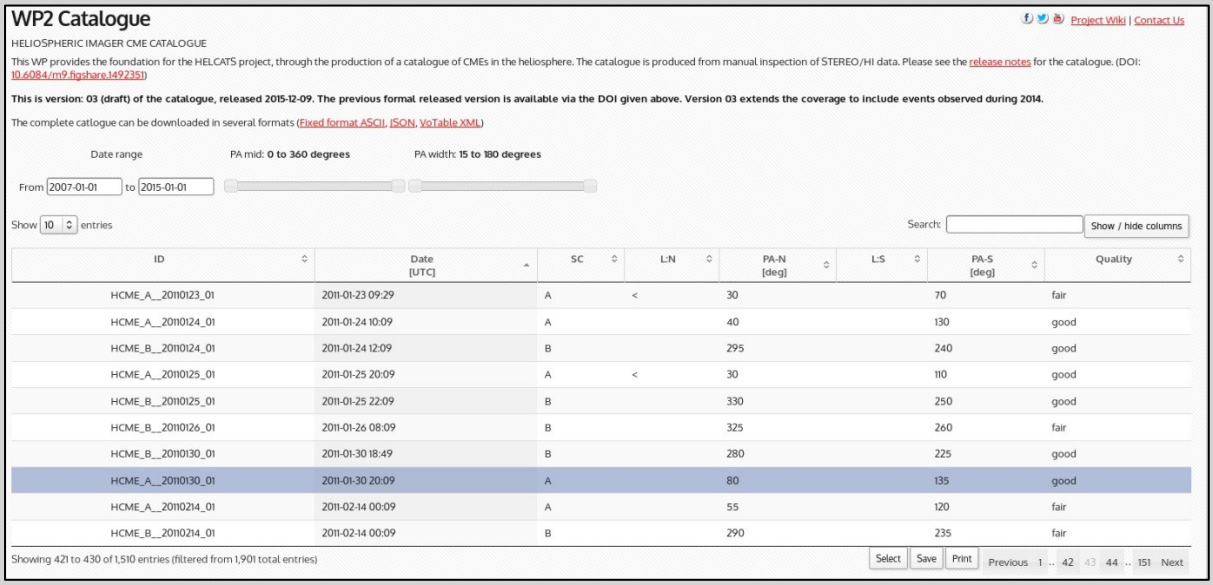

WP2 Catalogue

Project Wiki | Contact Us

HELIOSPHERIC IMAGER CME CATALOGUE

This WP provides the foundation for the HELCATS project, through the production of a catalogue of CMEs in the heliosphere. The catalogue is produced from manual inspection of STEREO/HI data. Please see the release notes for the catalogue. (DOI: 10.6084/m9.figshare.1492351)

This is version: 03 (draft) of the catalogue, released 2015-12-09. The previous formal released version is available via the DOI given above. Version 03 extends the coverage to include events observed during 2014.

The complete catalogue can be downloaded in several formats (Fixed format ASCII, JSON, VoTable XML)

Date range PA mid: **0 to 360 degrees** PA width: **15 to 180 degrees**

From 2007-01-01 to 2015-01-01

Show 10 entries Search: Show / hide columns

ID	Date [UTC]	SC	L:N	PA-N [deg]	L:S	PA-S [deg]	Quality
HCME_A__20110123_01	2011-01-23 09:29	A	<	30		70	fair
HCME_A__20110124_01	2011-01-24 10:09	A		40		130	good
HCME_B__20110124_01	2011-01-24 12:09	B		295		240	good
HCME_A__20110125_01	2011-01-25 20:09	A	<	30		110	good
HCME_B__20110125_01	2011-01-25 22:09	B		330		250	good
HCME_B__20110126_01	2011-01-26 08:09	B		325		260	fair
HCME_B__20110130_01	2011-01-30 18:49	B		280		225	good
HCME_A__20110130_01	2011-01-30 20:09	A		80		135	good
HCME_A__20110214_01	2011-02-14 00:09	A		55		120	fair
HCME_B__20110214_01	2011-02-14 00:09	B		290		235	fair

Showing 421 to 430 of 1,510 entries (filtered from 1,901 total entries) Select Save Print Previous 1 .. 42 43 44 .. 151 Next

Figure 3.2.2 – The HI CME catalogue as it appears on the HELCATS website.

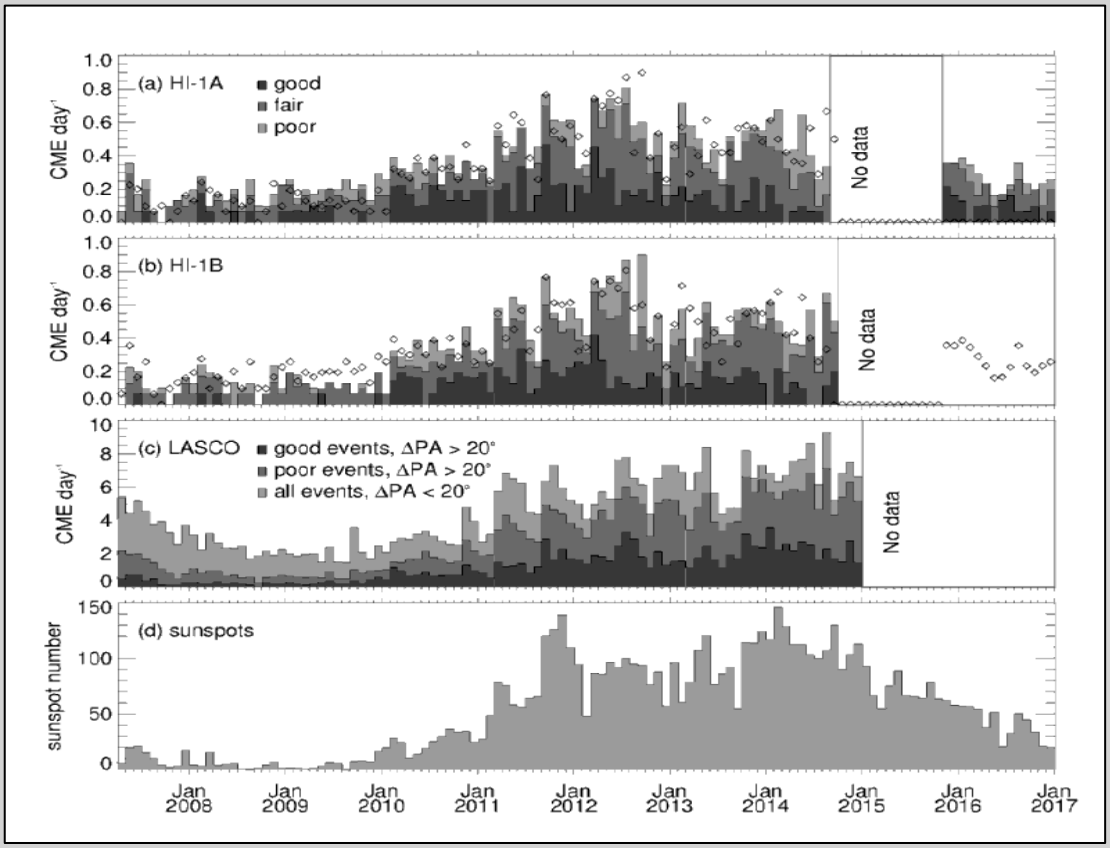

Figure 3.2.3 - Histograms showing the monthly rate of CMEs per day from (a) the STEREO-A and (b) the STEREO-B catalogues of HICAT. (c) shows the corresponding rate from the LASCO CDAW catalogue and (d) shows the monthly sunspot number.

Once tracked, the geometric model of Davies *et al.* (2012) (Figure 3.2.5) is applied to the time/elongation data in order to

determine the CME speed, direction and launch time. This is achieved by assuming that the CME propagates at a constant speed and in a constant direction, both of which are, for many CMEs, reasonable assumptions at the distance from the Sun observed in HI. The equation used to constrain the data is

$$v(t-t0) = r0\ \sin\varepsilon(t)(1+\sin\lambda) / \sin(\varepsilon(t)+\phi)+\sin(\lambda),$$

where v is the CME speed t0 the launch time and ϕ the propagation direction. The values of t and ε from the time/elongation tracks are used to constrain the solution and λ, the angular half-width, is a parameter that may be varied to alter the assumed CME morphology. The final catalogue contains results using three values of λ: 0°, 30° and 90°. These are referred to respectively as the fixed-phi (FP), self-similar expansion (SSE) and harmonic mean (HM) models.

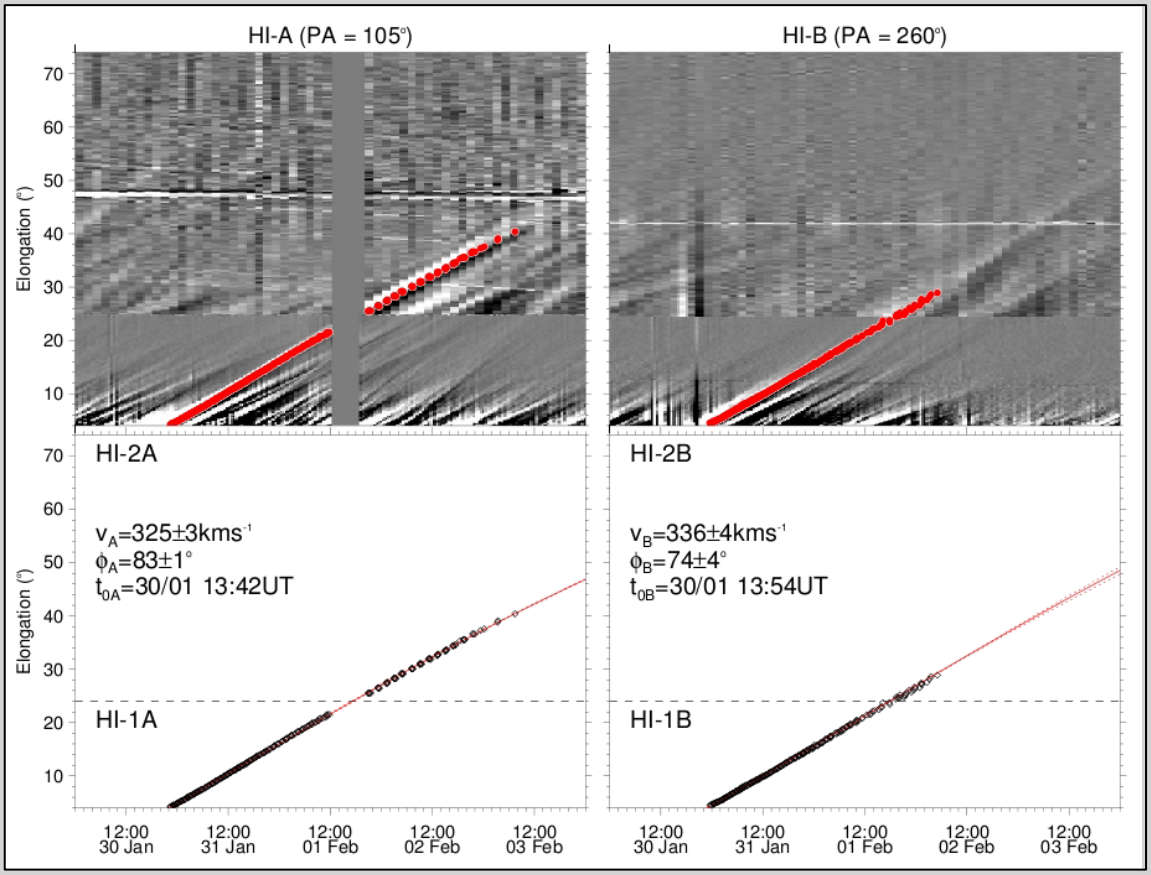

Figure 3.2.4 - (top) Time/elongation plot of a CME observed separately by STEREO-A and –B during 2011. The CME is manually tracked (red dots), which is used to constrain a model to provide CME launch time, speed and direction (bottom).

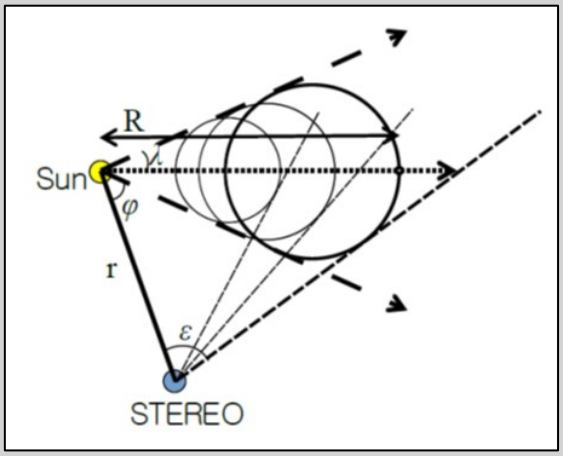

Figure 3.2.5 - Geometric model applied to time/elongation data (Davies et al., 2012).

Due to the difficulty in tracking the smaller CMEs in this way, the poor events were not included in this modelling and the final catalogue of CME kinematic properties contains 776 CMEs for STEREO-A and 654 for STEREO-B. Figure 3.2.6 shows an example of the catalogue as it is available on the HELCATS website at **https://www.helcats-fp7.eu/catalogues/wp3_cat.html** (alternatively use the PRODUCTS tab and select the WP2 or WP3 catalogues). Again, the user can filter CMEs based on the properties contained in the catalogue, or download the full data-set in a variety of formats. The original time/elongation data are also available for download, should users wish to apply their own models. Additionally, each CME in this catalogue possesses its own event page, a web page that is accessed by clicking the any row in the table shown in Figure 3.2.6. This page contains images, videos and diagrams relating to the CME, as well as a listing of the observational and kinematic properties.

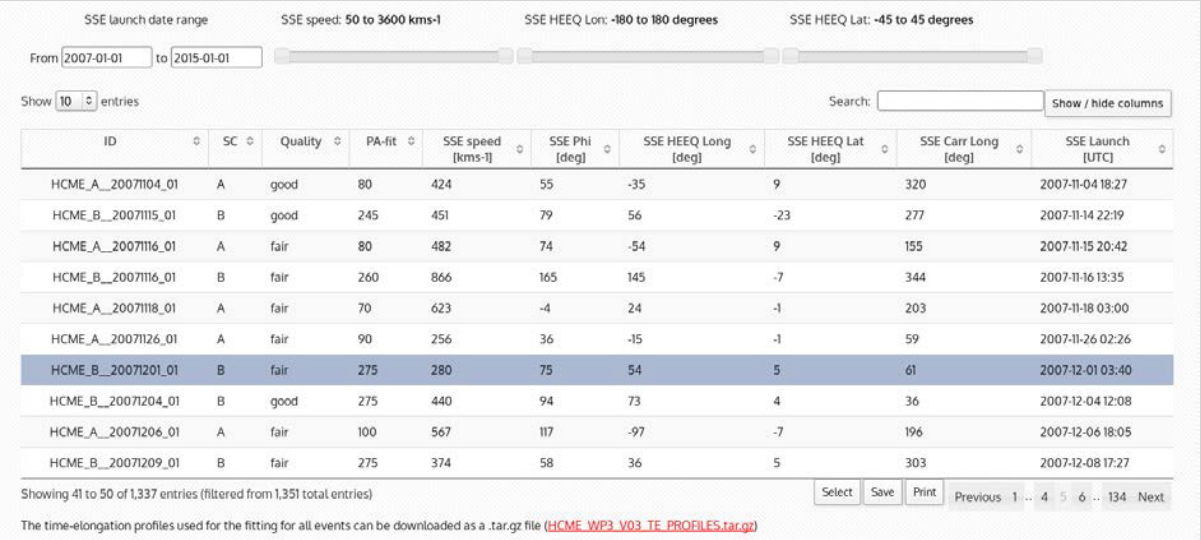

SSE launch date range | SSE speed: **50 to 3600 kms-1** | SSE HEEQ Lon: **-180 to 180 degrees** | SSE HEEQ Lat: **-45 to 45 degrees**

From 2007-01-01 to 2015-01-01

Show 10 entries | Search: | Show / hide columns

ID	SC	Quality	PA-fit	SSE speed [kms-1]	SSE Phi [deg]	SSE HEEQ Long [deg]	SSE HEEQ Lat [deg]	SSE Carr Long [deg]	SSE Launch [UTC]
HCME_A__20071104_01	A	good	80	424	55	-35	9	320	2007-11-04 18:27
HCME_B__20071115_01	B	good	245	451	79	56	-23	277	2007-11-14 22:19
HCME_A__20071116_01	A	fair	80	482	74	-54	9	155	2007-11-15 20:42
HCME_B__20071116_01	B	fair	260	866	165	145	-7	344	2007-11-16 13:35
HCME_A__20071118_01	A	fair	70	623	-4	24	-1	203	2007-11-18 03:00
HCME_A__20071126_01	A	fair	90	256	36	-15	-1	59	2007-11-26 02:26
HCME_B__20071201_01	B	fair	275	280	75	54	5	61	2007-12-01 03:40
HCME_B__20071204_01	B	good	275	440	94	73	4	36	2007-12-04 12:08
HCME_A__20071206_01	A	fair	100	567	117	-97	-7	196	2007-12-06 18:05
HCME_B__20071209_01	B	fair	275	374	58	36	5	303	2007-12-08 17:27

Showing 41 to 50 of 1,337 entries (filtered from 1,351 total entries) | Select | Save | Print | Previous 1 .. 4 5 6 .. 134 Next

The time-elongation profiles used for the fitting for all events can be downloaded as a .tar.gz file (HCME_WP3_V03_TE_PROFILES.tar.gz)

Figure 3.2.6 - HELCATS catalogue of CME kinematic properties based on geometric modelling.

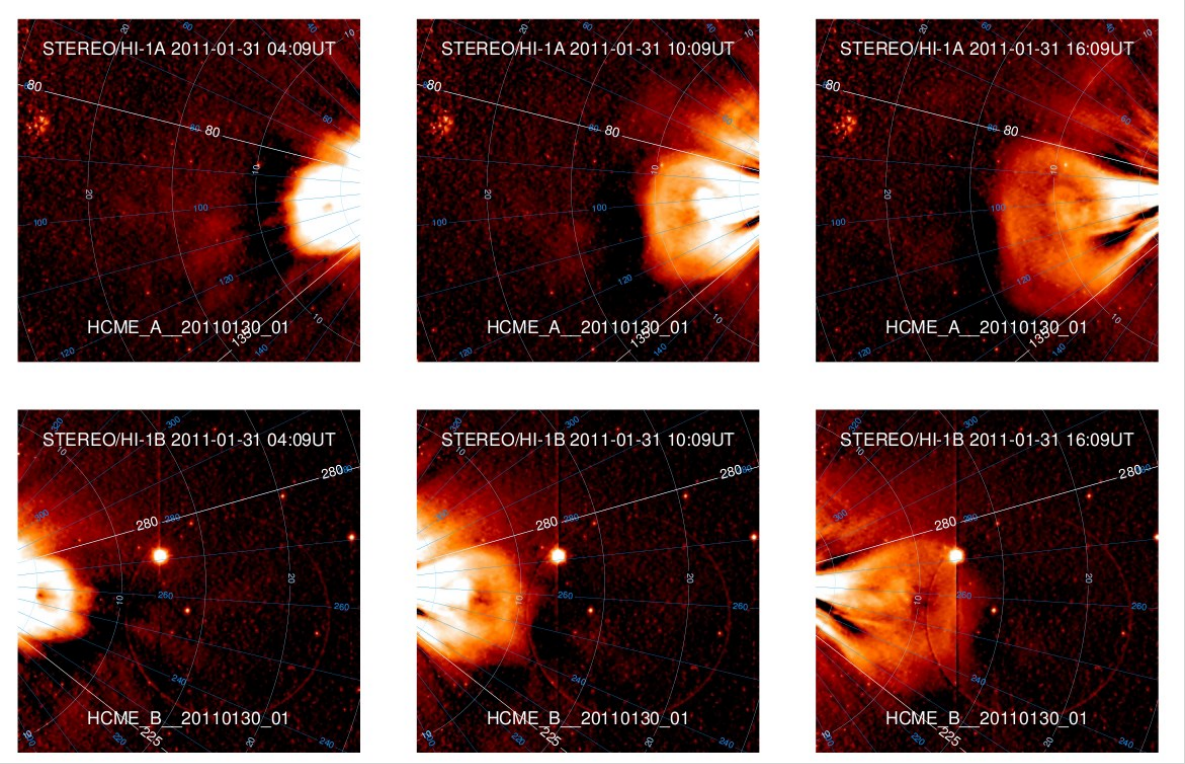

Figure 3.2.7 - CME observed by both STEREO-A and -B.

As part of task 2.3, CMEs were identified that are observable by both STEREO spacecraft, as shown in Figure 3.2.7. Here the top row displays HI-1A data and the bottom row HI-1B data for the same times, which clearly corresponds to the same CME. A list of these CMEs was compiled from the entire HI data-set, which contains 273 events. The distribution of these CMEs throughout the mission is shown in Figure 3.2.8.

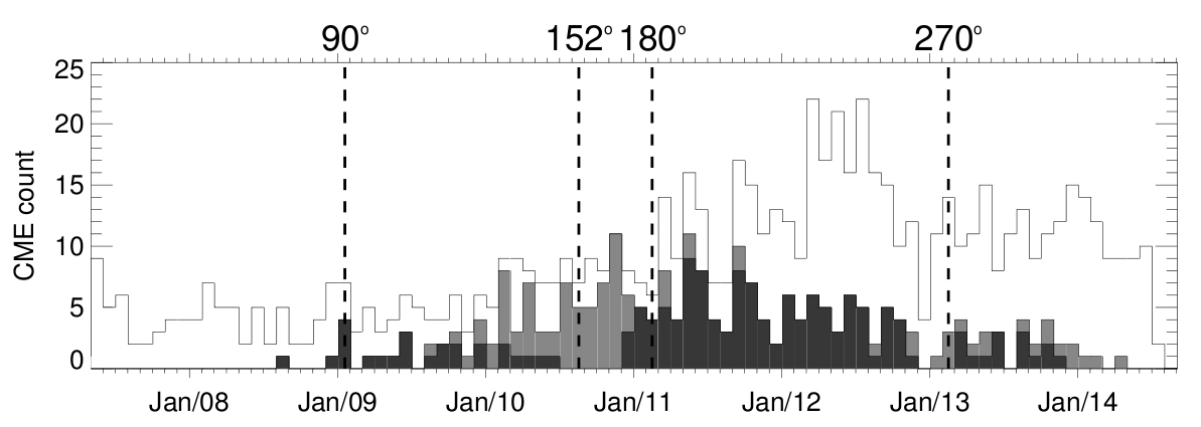

Figure 3.2.8 - The unshaded region shows the total CME rate from the observational catalogue. The darker regions show the number of CMEs determined to be observable by both spacecraft. The lighter shaded region shows CMEs that were excluded from the stereoscopic mode.

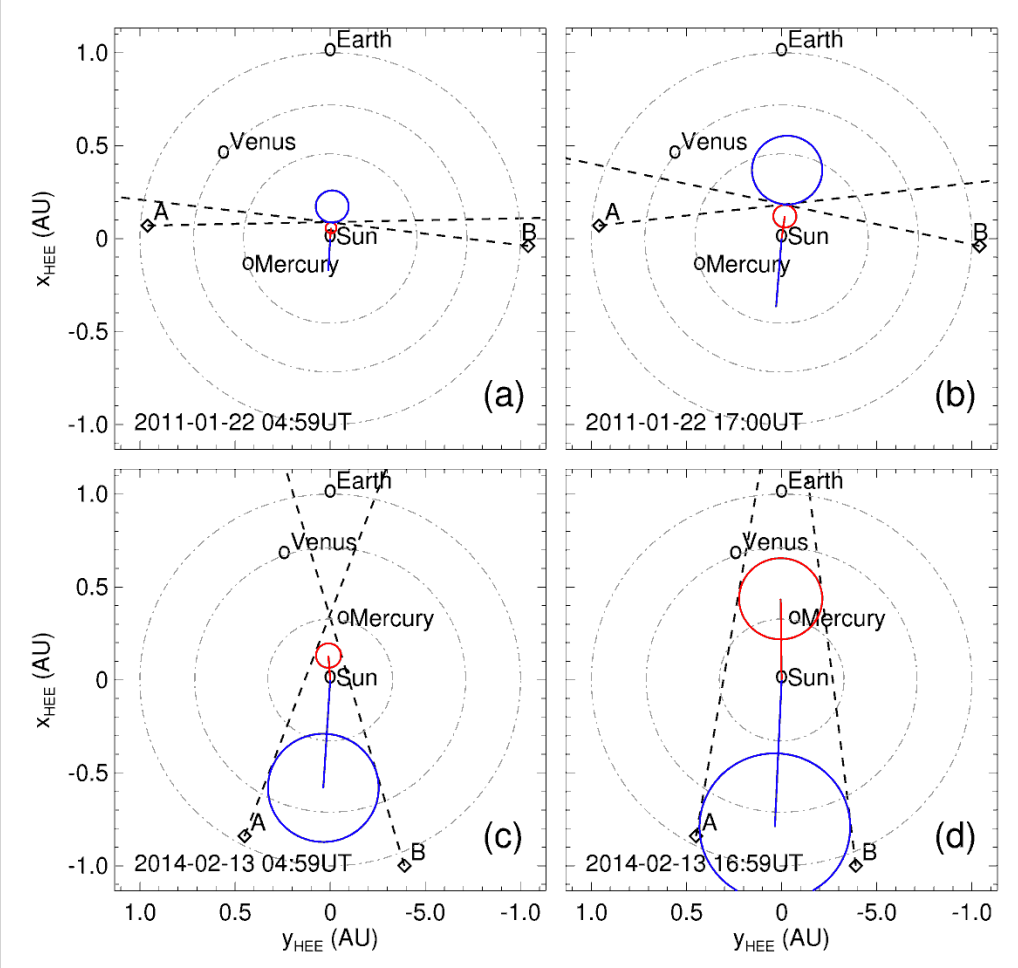

Figure 3.2.9 - Method of determining CME position using stereoscopic modelling. In each case there are two solutions, one of which is usually unphysical (blue circle in (a) and (b)).

Linking CMEs observed by each spacecraft allows stereoscopic modelling (Davies et al., 2013) to be used to determine CME kinematic properties (WP3 task 1). Unlike the single-spacecraft modelling, described above, the constant speed and constant direction assumptions may be dropped. The time/elongation data from each spacecraft are combined to locate CMEs, based on the assumed morphology shown in Figure 3.2.5. This is demonstrated in Figure 3.2.9, where the dashed lines from each spacecraft show the CME elongation angle, at a given time. This may be used to constrain the location of the CME for a given half-width. The solution is found to have two mathematical solutions, shown as red and blue circles, one of which is discarded.

WP2 TASK 2.2: AUTOMATIC CATALOGUING OF STEREO/HI CMES (TASK LEAD: ROB)

CMEs are intrinsically difficult to identify and trace in heliospheric imager data. The challenge of task 2.2 is to identify CMEs during the STEREO mission automatically, without human intervention. As will be reported, this is the first time that this has been achieved successfully. This task used ROB's extensive experience in autonomous detection of CMEs in coronagraph images from the SOHO/LASCO instrument and, more recently, from STEREO/COR2 (Robbrecht *et al.,* 2009).

The HI instruments consist of two cameras, HI-1 and HI-2, which have 20° and 70° fields of view (FOV) and are off-pointed from Sun-centre by 14.0° and 53.7°, respectively. This arrangement provides coverage over solar elongation angles from 4.0° to 88.7°, on the ecliptic plane (Eyles et al., 2009). This very wide FOV represents the main difference with a coronagraph (such as STEREO-SECCHI-COR or SOHO-LASCO) which images the area close to the Sun (up to 30 Rs, whereas HI covers up to 330 Rs, in the plane of the sky).

The technique used for the automatic detection of CMEs consists of an adaptation of CACTus (**http://sidc.oma.be/cactus/**, see also Robbrecht and Berghmans, 2004) to HI data. This is a method that uses advanced image processing techniques in order to extract the CME from the images and measure its properties (speed, angular width, etc.), without human intervention.

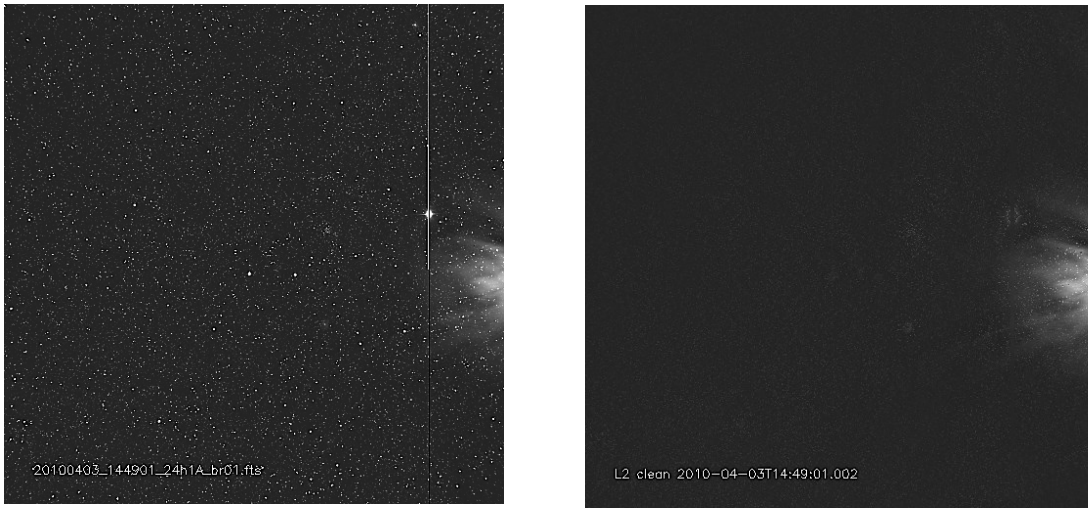

Figure 3.2.10 - Example of a Level-2 image before (left panel) and after (right panel) cleaning.

The procedure is started with HI-1 level-2 images. A daily background is removed from the images (see **http://www.ukssdc.ac.uk/solar/stereo/documentation/HI_processing.html** and **http://www.ukssdc.ac.uk/solar/stereo/documentation/HI_processing_L2_data.html#HI_L2** for more information on how level-2 images are obtained). In those images artificial vertical strips arise from an attempt to get rid of the artefacts of blooming on the CCD from the presence of sources in the FOV such as planets (Mercury in the left image in Figure 3.10). Stars and remnant brightness around planets are removed by using a sigma filter. This filter works by computing the mean and standard deviation of pixels in a box of 51 pixels width, centred at each pixel of the image, but excluding the centre pixel. If the centre pixel exceeds 4 sigma from the mean, it is replaced by the mean in the box. Then the black strips are replaced by a smoothed version of the neighbouring pixels. The original and resulting images are show in in Figure 3.2.10. A CME that erupted on April 3, 2010 can be seen as the bright feature observed in the images, this same event will be used for the

following figures. Note that this is the CME that eventually caused the failure of the Galaxy 15 satellite.

A conversion to polar coordinates is needed in order to be able to apply the Hough transform (Jähne 1997) to the images. This transform is the kernel of CACTus, as it is used to detect features moving outwards (CMEs) in the FOV. HI images are originally in HPC (Helioprojective-Cartesian) coordinates; in this system the position of any point in the images is given by its latitude and longitude. The first step consists of converting them into HPR (Helioprojective-Radial) coordinates, which provide position angle and elongation, these quantities are needed in order to apply our technique. This conversion is done with the Solarsoft routine *wcs_conv_hpc_hpr*. In these coordinate systems, observations are projected against the celestial sphere. Therefore, physical distances are represented by angles. Finally, a conversion of the elongation angle into projected distance is carried out. A detailed explanation of the coordinate systems is given in Thomson (2006).

In a polar image, the X-axis represents the angle from solar north (2° binned to a single pixel, binning is done by averaging the original pixels) and the Y-axis shows the projected distance from the Sun (10000 km/pixel), as shown in Figure 3.2.11.

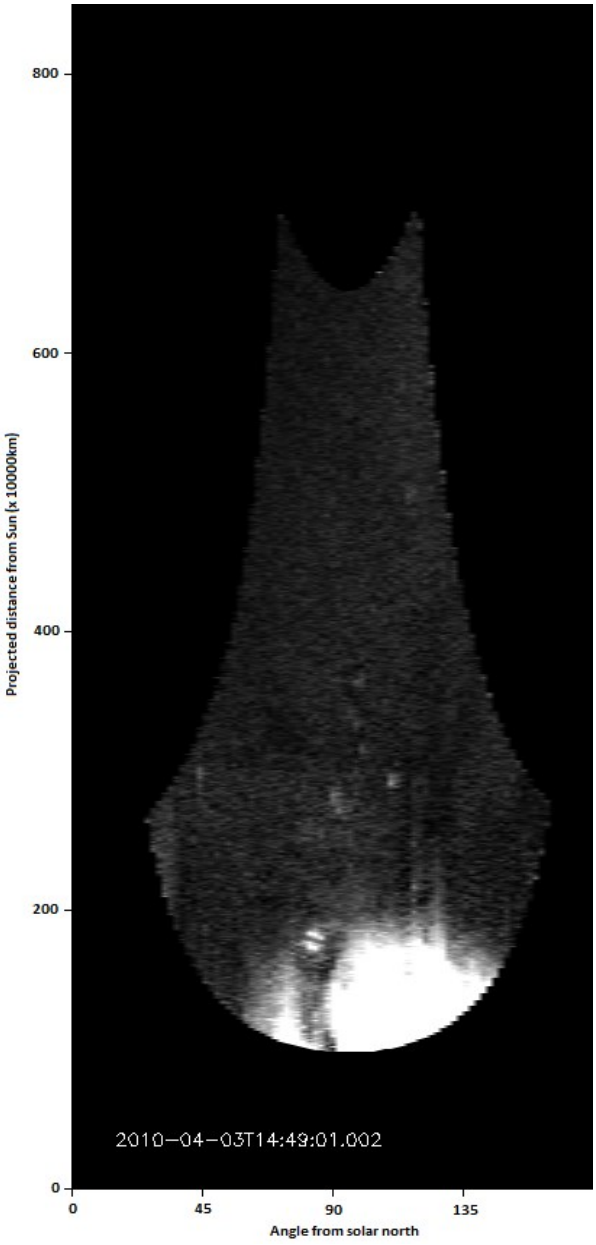

Figure 3.2.11 - Example of an image converted to polar coordinates.

All of the polar images (ordered in time) are then stacked in a datacube, which consists of a set of images with the angle from solar north as X-axis and distance from the Sun as Y-axis (such as the one shown in Figure 3.2.11). Noise is removed from the images by applying a median filtering over 3 sequential images in time in the datacube. Next, running difference (based again on sequential images) is applied to the data, as illustrated in Figure 3.2.12.

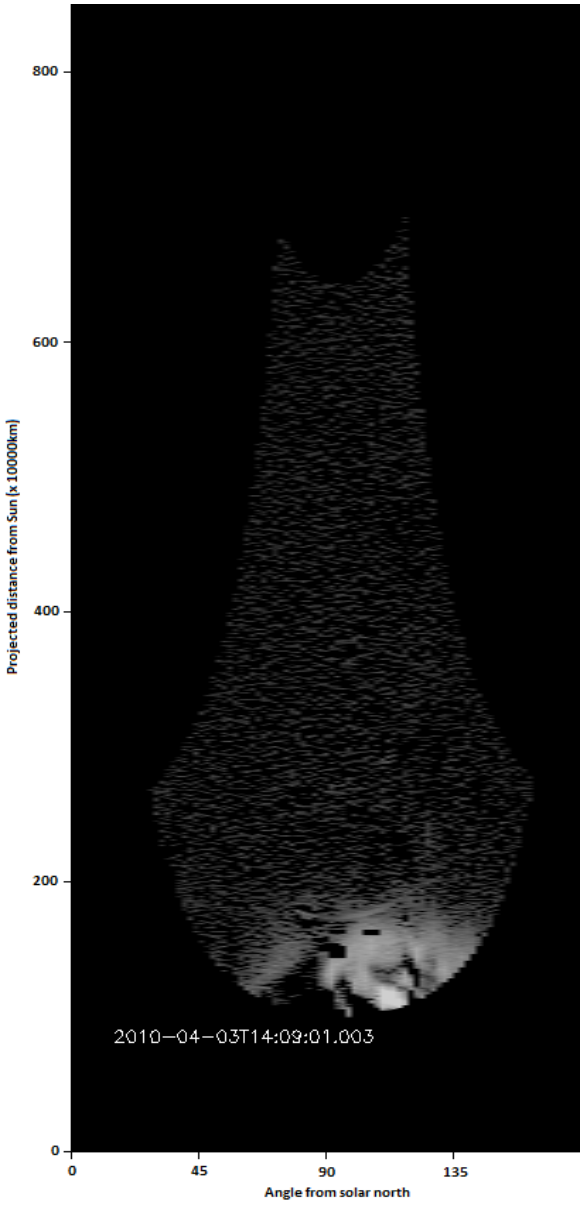

Figure 3.2.12 - Example of a running difference polar image.

Prior to the application of the Hough transform, the images are converted into distance – time (r – t) slices for each angle (see Figure 3.2.13). The slices are 2 degrees wide, because while converting to polar coordinates 2 degrees were binned in a single pixel.

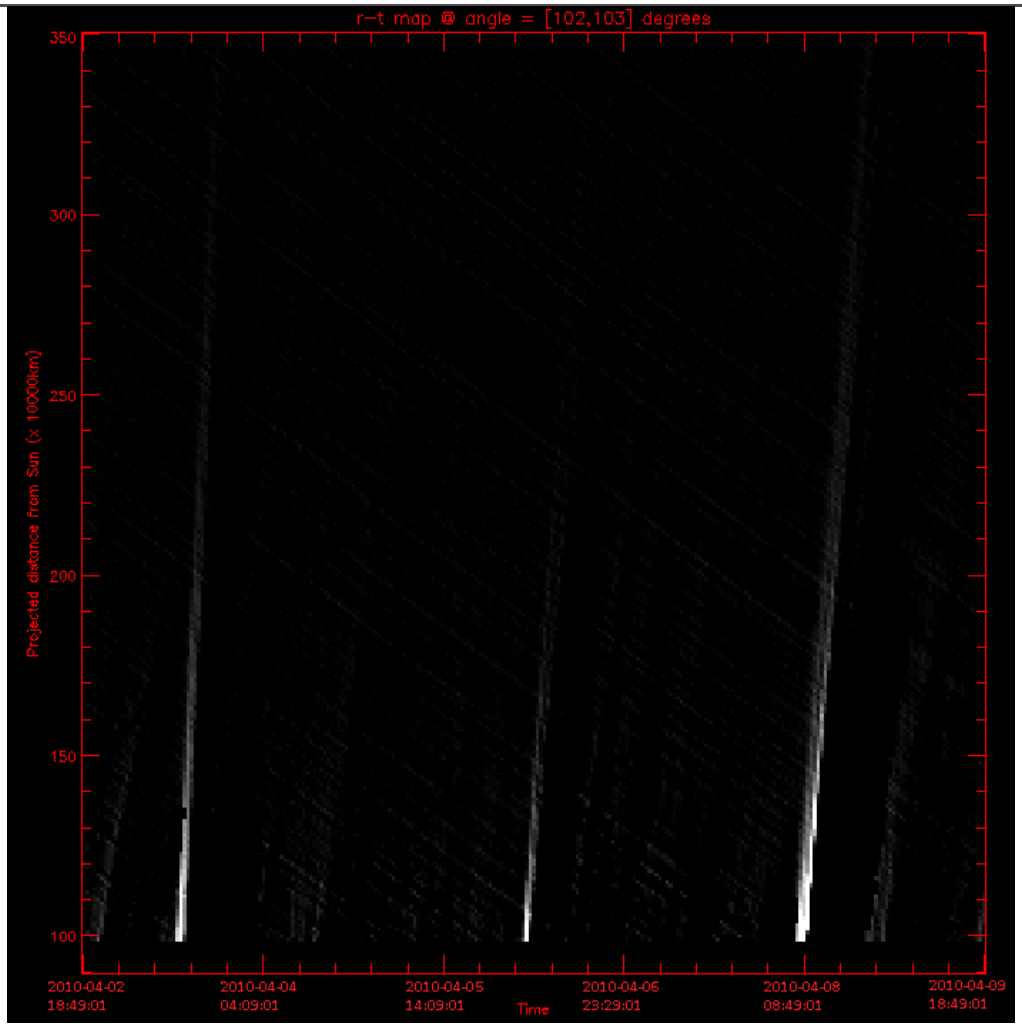

Figure 3.2.13 - Example of a distance - time (r – t) image.

In these distance-time maps, CMEs can be seen as inclined bright ridges, with the inclination corresponding to the propagation speed. The Hough transform is a technique used to identify and extract linear features in an image. It is applied to the r – t maps at all angles. Speeds between 100 kms^{-1} and 2100 kms^{-1} are considered. This then yields a time-speed (t – v) map which is summed along the speed dimension to provide a time-angle (t – a) image, which contains all information about the CMEs. An example is shown graphically in Figure 3.2.14, with the details in Table 3.2.2.

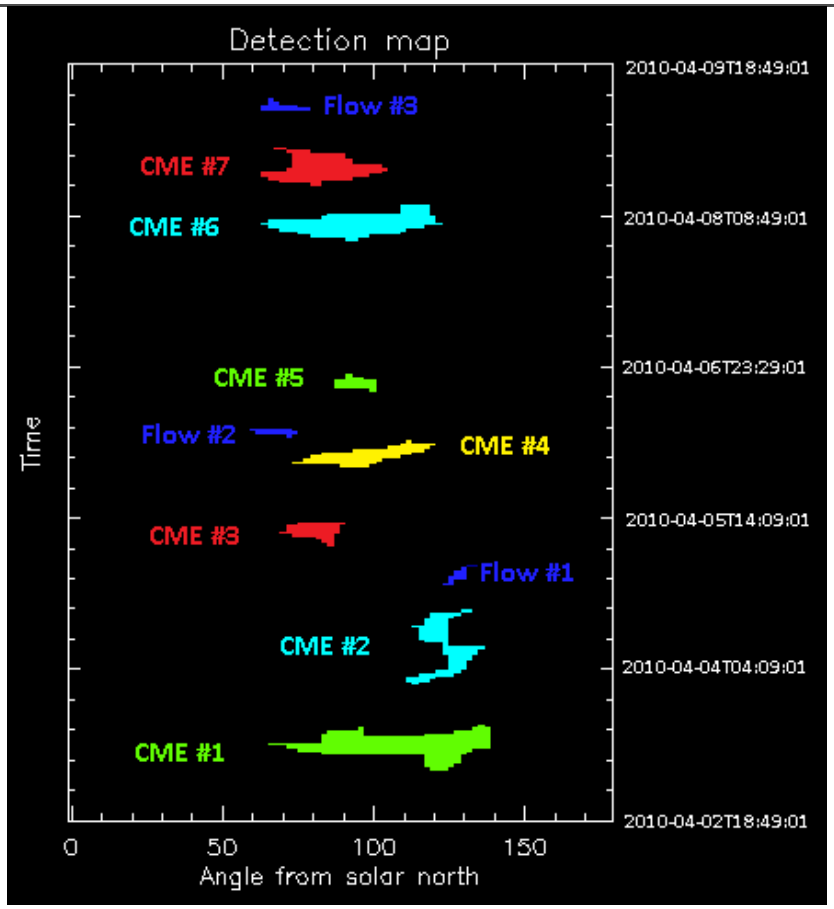

Figure 3.2.14 - Example of a time - angle (t – a) map. Where each color represents a different event. Dark blue events are considered as very suspicious detections, and termed flows to differentiate them from the clearer CMEs.

Table 3.2.2: Computed parameters for the detected events; where t0 is the time of 1st appearance in HI-1 FOV, pa is the principal angle counterclockwise from solar north, da is the angular width, NoPA is the northernmost propagation angle, SuPa is the southernmost propagation angle, v is the median projected velocity in km/s, dv is the standard deviation of the velocities over the width of the CME, minv and mav are the lowest and highest detected velocities within the CME.

#CME	t0	pa	da	NoPA	SuPA	v	dv	minv	maxv
0007	2010/04/08 18:09	0084	040	0064	0104	0249	0060	0196	0402
0006	2010/04/08 06:49	0093	058	0064	0122	0544	0053	0454	0668
0005	2010/04/06 20:49	0094	012	0088	0100	0283	0119	0268	0520
0004	2010/04/06 04:09	0097	046	0074	0120	0582	0278	0416	1264
0003	2010/04/05 12:09	0080	020	0070	0090	0268	0009	0256	0285
0002	2010/04/04 04:09	0124	024	0112	0136	0397	0084	0357	0562
0001	2010/04/03 12:09	0102	072	0066	0138	0823	0110	0571	1041

#Flow	t0	pa	da	NoPA	SuPA	v	dv	minv	maxv
0003	2010/04/09 08:49	0071	014	0064	0078	0188	0083	0178	0357
0002	2010/04/06 08:09	0067	014	0060	0074	0301	0011	0287	0319
0001	2010/04/04 23:29	0129	010	0124	0134	0319	0023	0285	0357

In the detection map, for each t – a pair (each point of each coloured zone) a speed is associated. This speed corresponds to the ridge which contains the highest signal in the r - t slice. Each CME (coloured zone) is associated with the median of the velocities placed in it. This results in velocity vs. angle (v – a) plots, as shown in Figure 3.2.15. This is the final output of CACTus, in this way speed and angular width are computed for each

CME.

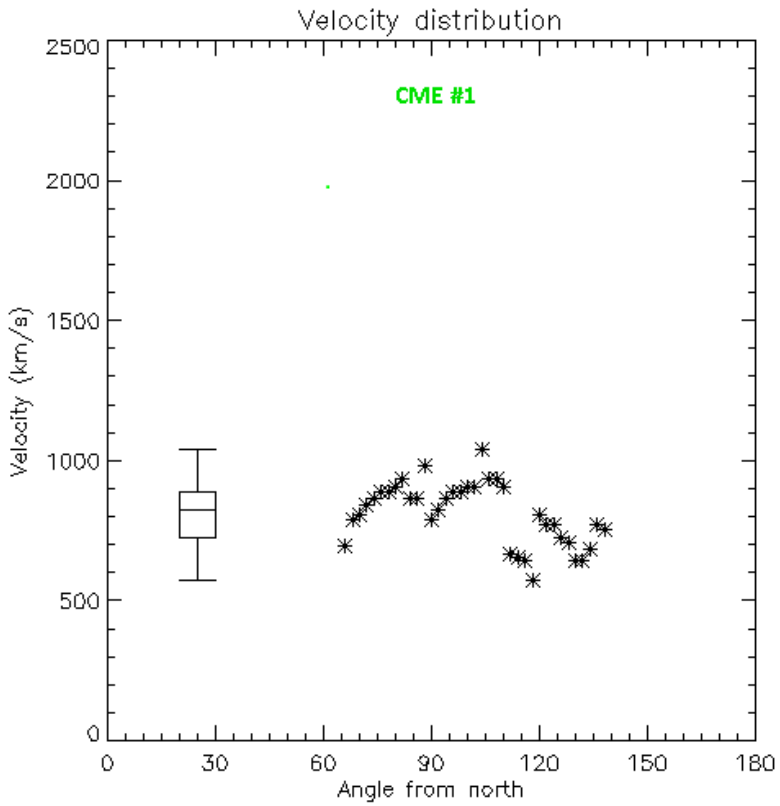

Figure 3.2.15 - Example of a velocity vs. angle (v – a) map for a CME.

The procedure described in the previous section is applied to all the STEREO data, both from STEREO-A and STEREO-B for the duration of the mission (2008 – 2014). An extract of the catalogue is shown in Figure 3.2.16. The quality of the results is lower for STEREO-B, due to the data being corrupted by occasional, small, but significant jitter of the HI-1B focal plane assembly due to resonances with the spacecraft reaction wheels.

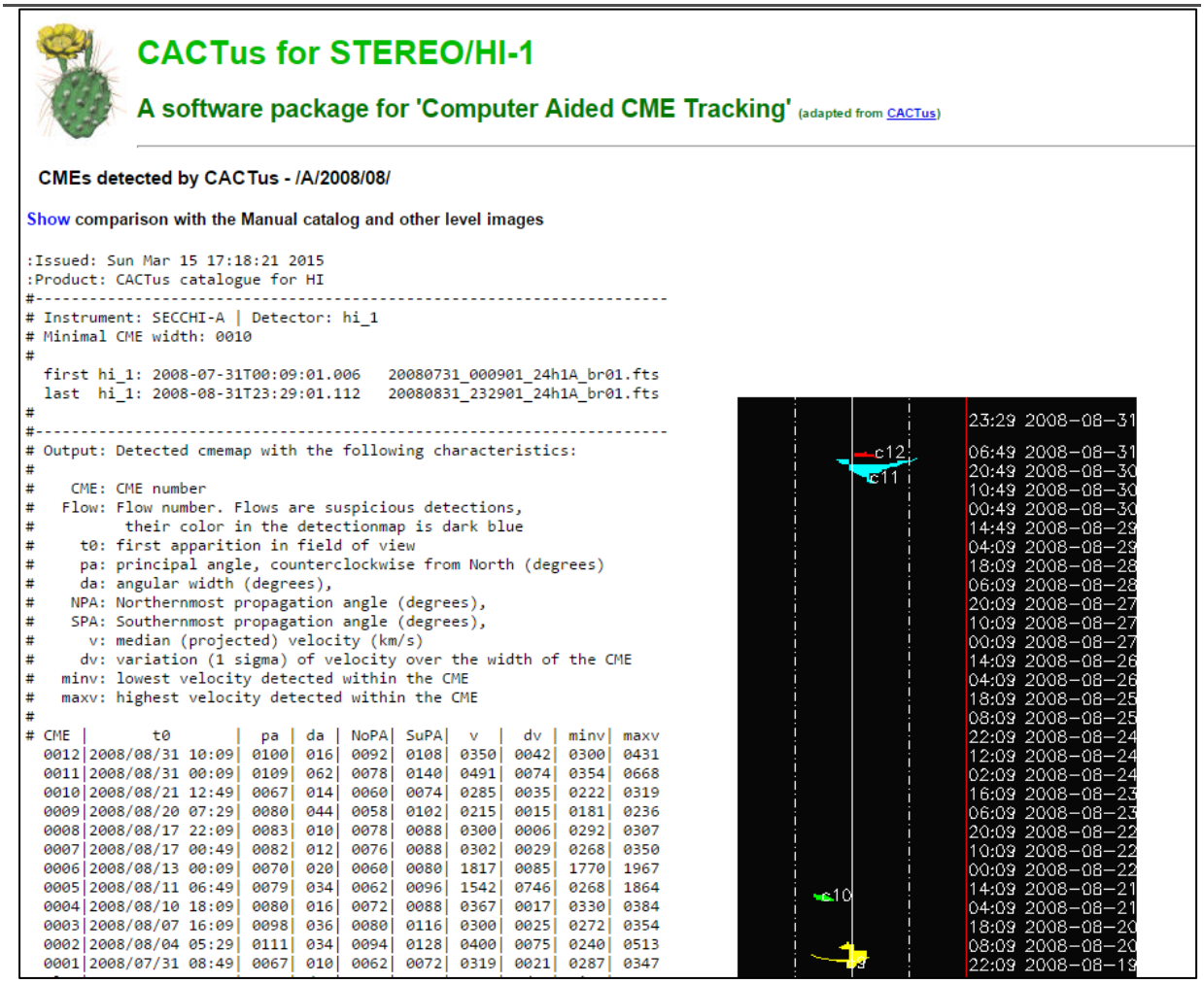

CACTus for STEREO/HI-1

A software package for 'Computer Aided CME Tracking' (adapted from CACTus)

CMEs detected by CACTus - /A/2008/08/

Show comparison with the Manual catalog and other level images

```
:Issued: Sun Mar 15 17:18:21 2015
:Product: CACTus catalogue for HI
#-------------------------------------------------------------------------
# Instrument: SECCHI-A | Detector: hi_1
# Minimal CME width: 0010
#
  first hi_1: 2008-07-31T00:09:01.006   20080731_000901_24h1A_br01.fts
  last  hi_1: 2008-08-31T23:29:01.112   20080831_232901_24h1A_br01.fts
#
#-------------------------------------------------------------------------
# Output: Detected cmemap with the following characteristics:
#
#    CME: CME number
#   Flow: Flow number. Flows are suspicious detections,
#         their color in the detectionmap is dark blue
#     t0: first apparition in field of view
#     pa: principal angle, counterclockwise from North (degrees)
#     da: angular width (degrees),
#    NPA: Northernmost propagation angle (degrees),
#    SPA: Southernmost propagation angle (degrees),
#      v: median (projected) velocity (km/s)
#     dv: variation (1 sigma) of velocity over the width of the CME
#   minv: lowest velocity detected within the CME
#   maxv: highest velocity detected within the CME
#
# CME |       t0       |  pa | da | NoPA| SuPA|  v   |  dv | minv| maxv
  0012|2008/08/31 10:09| 0100| 016| 0092| 0108| 0350| 0042| 0300| 0431
  0011|2008/08/31 00:09| 0109| 062| 0078| 0140| 0491| 0074| 0354| 0668
  0010|2008/08/21 12:49| 0067| 014| 0060| 0074| 0285| 0035| 0222| 0319
  0009|2008/08/20 07:29| 0080| 044| 0058| 0102| 0215| 0015| 0181| 0236
  0008|2008/08/17 22:09| 0083| 010| 0078| 0088| 0300| 0006| 0292| 0307
  0007|2008/08/17 00:49| 0082| 012| 0076| 0088| 0302| 0029| 0268| 0350
  0006|2008/08/13 00:09| 0070| 020| 0060| 0080| 1817| 0085| 1770| 1967
  0005|2008/08/11 06:49| 0079| 034| 0062| 0096| 1542| 0746| 0268| 1864
  0004|2008/08/10 18:09| 0080| 016| 0072| 0088| 0367| 0017| 0330| 0384
  0003|2008/08/07 16:09| 0098| 036| 0080| 0116| 0300| 0025| 0272| 0354
  0002|2008/08/04 05:29| 0111| 034| 0094| 0128| 0400| 0075| 0240| 0513
  0001|2008/07/31 08:49| 0067| 010| 0062| 0072| 0319| 0021| 0287| 0347
```


Figure 3.2.16 - The automated CME catalogue constructed for STEREO-HI.

The catalogue is available online, and is obtainable through the PRODUCTS tab on the HELCATS website. Clicking on any particular CME entry will reveal associated plots and movies. In the future, we plan a fine-tuning of the code in order to remove narrow detections and only consider events with a width larger than 20°. Furthermore, false detections will be removed based on their speed profile.

In conclusion, this task, and the associated deliverable, have shown how the automatic identification of CMEs in HI data was made possible by an adaptation of the CACTus technique, and a catalogue containing all the CMEs detected during the STEREO mission was built and is available to the wider community. This work has now been published by Pant *et al.* (2016).

We note that a real time version of CASCTusCAT is being run by ROB and can be accessed at **http://www.sidc.be/cactus/hi/**.

WP2 TASK 2.3: COMPARISON OF CME CATALOGUES (TASK LEAD: UGOE, CONTRIBUTORS: STFC, ROB)

This task involves the comparison of CME catalogues. In the first element, a comparison between the manual and automated catalogues of CMEs in the heliosphere, from tasks 2.1 and 2.2, is performed. A second element, comparisons are made between the heliospheric CME catalogues of tasks 2.1 and 2.2 with coronal CME coronagraph catalogues.

Comparison of the manual and automated HI CME catalogues

In Table 3.2.3 the number of heliospheric CME events identified and listed in both the manual and automatic

catalogues of tasks 2.1 and 2.2 are displayed. The manual catalogue contains a comparable number of events for both STEREO spacecraft, whereas the automatic one contains approximately 20% more events detected by STEREO-B. We believe that this increase in events detected in HI-B is not real; the HI-B data are corrupted by occasional, small but significant jitter (as mentioned above) that triggers the automatic detection erroneously. Therefore we will focus our comparison to the events detected by HI-A.

Table 3.2.3: Comparison of number of CMEs detected manually and automatically

	Manual A	**Manual B**	**Automatic A**	**Automatic B**
Date	17.04.2007 - 29.12.2013	15.04.2007 - 31.12.2013	13.01.2007 - 18.08.2014	20.01.2007 - 28.08.2014
Total events	**856**	**817**	**1501**	**1794**
Date	15.04.2007 - 31.12.2013	15.04.2007 - 31.12.2013	15.04.2007 - 31.12.2013	15.04.2007 - 31.12.2013
Total events	**856**	**817**	**1308**	**1556**

Table 2. Events between 15.04.2007 and 31.12.2013. Common events (starttime differs by le 2 hours, overlap ge 60% of the minimum width).

	Manual A	**Manual B**	**Automatic A**	**Automatic B**
Total number	856	817	1308	1556
width >= 20 (width < 20)	855 (1)	813 (4)	884 (424)	1290 (266)
Poor events	144	179	-	-
Events out fov	361	317	-	-
Poor and out fov events	490	458	-	-
Common events	499	404	499	404
with speed estimations	425	328	(425)*	(328)*

*CACTus gives a speed estimation for all its detections but obviously for speed comparisons we only consider the events for which we have an estimation in the manual catalogue.

We restrict the comparison to the period where both catalogues overlap in time (15.04.2007 – 13.12.2013). The total number of events detected by the automatic method is much higher than in the manual case (1308 vs. 856). This difference is sorted out if we set the automatic algorithm to detect only events with an angular width larger than 20°, as it is the case in the manual catalogue. By doing so, the total number of events in the automatic catalogue reduces to 884 and becomes comparable with the manual number. This means that an important portion (one third) of the CMEs captured by the automatic algorithm have a narrow angular width (<20°). It should be noted that the manual CME catalogue only identifies CMEs of angular width greater than 20^{o} to avoid confusion with the numerous blob-like transient features that are detected in the inner heliosphere.

In order to compare the CME parameters present in both catalogues, the common events in the manual and automatic catalogue have to be found. For this purpose, we have applied two methods. The first one consists of the use of an algorithm to compare the events and select those which fulfil pre-defined criteria: A CME listed in both catalogues with a difference in starting time lower than 2 hours and with at least 60% overlap in angular extent will be considered to be the same event. The second approach is to do a visual inspection of all the CMEs, one by one, and creating a link between the two catalogues when it corresponds.

By applying the first (automatic) method, 499 common events were found, they are the subject of the following paragraphs. The visual inspection of the events (the second method) is being applied at present and its results will be presented in the future.

As stated in the previous section, there are 499 CMEs which are common to both the automatic and the manual catalogues. In this section we will compare several features of these events.

Figure 3.2.17 shows a comparison of CME position angle. The left hand panel displays a histogram whilst the right hand one shows a scatter plot. In both it can be seen that the values in the two catalogues correlate well, position angle is a parameter which is well recovered by CACTus.

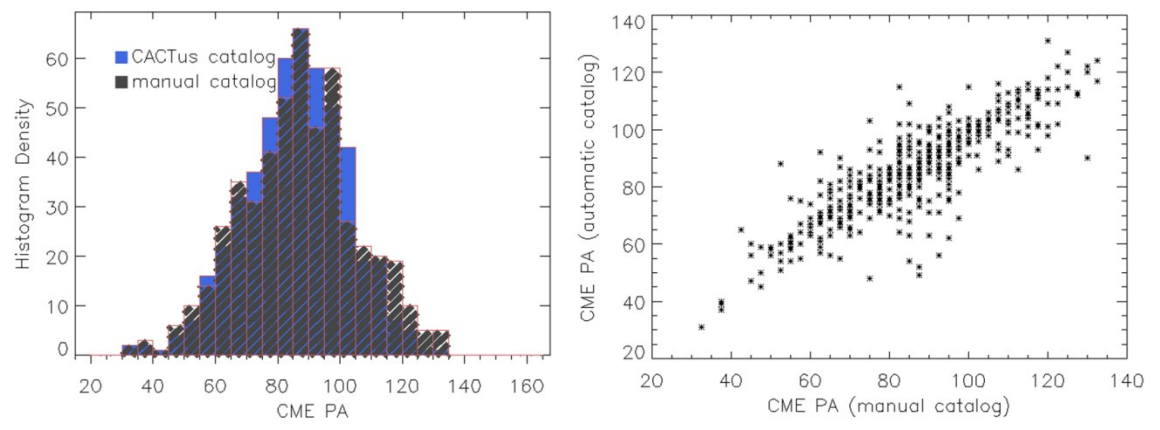

Figure 3.2.17 - Comparison of CME position angle (PA) between the manual and automatic catalogues. As a histogram (left) and scatter plot (right).

Figure 3.2.18 shows the angular widths of CMEs in both catalogues, in a similar format as Figure 3.2.17. In this case, we can see a lack of wide events (> 125°) in the automatic catalogue, and also it contains many more small events (< 50°) than the manual one. This occurs because the automatic detection algorithm is dividing large events into several smaller ones. This is a known problem with CACTus, there is a trade-off between this effect and the number of false alerts (i.e. reducing this effect increases the false alert rate of the method).

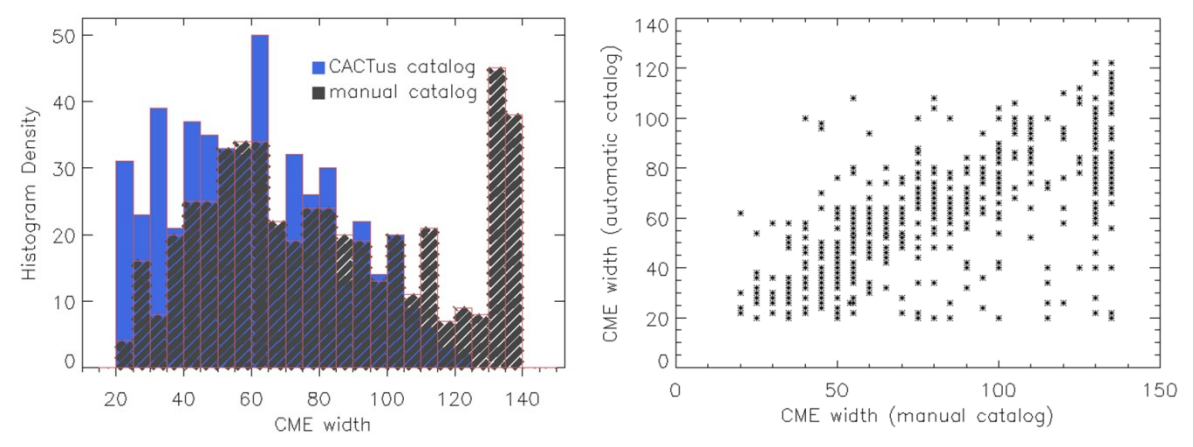

Figure 3.2.18 - Comparison of CME angular widths between the manual and automatic catalogues. As a histogram (top) and scatter plot (bottom).

In Figure 3.2.19, we compare the speeds of the CMEs derived from the CACTusCAT catalogues and the speeds derived for the HICAT events as discussed in WP3 (the HIGeoCAT catalogue). In the manual catalogue, speeds are calculated using three different methods, we have chosen to show the speeds calculated using the Self Similar Expansion (SSE) method described in Davies et al., 2012 (the results when using the other methods do not differ significantly). The results agree for low speeds (less than 1000 km/s). For larger speed values, the correlation is poor. This is a consequence of the fact that higher speed CMEs means fewer images in which the CME is present, increasing the errors in the measurements of both the manual and the automatic methods.

In summary, a comparison of the manual and automatic CME catalogues was carried out. If one takes the manual catalogue as the “ground truth” against which the automatic catalogue is compared then the following conclusions can be extracted:

- The automatic method performs well in terms of position angle of CMEs.
- The angular width of CMEs is well detected, except for large events which are divided into smaller ones.
- The speeds are well detected for slow events, for fast ones the measurements become more difficult as there are fewer images available (this is affecting both the manual and automatic catalogues).

In future work, the results of the visual inspection of both catalogues can be extended into more detailed comparison of different parameters.

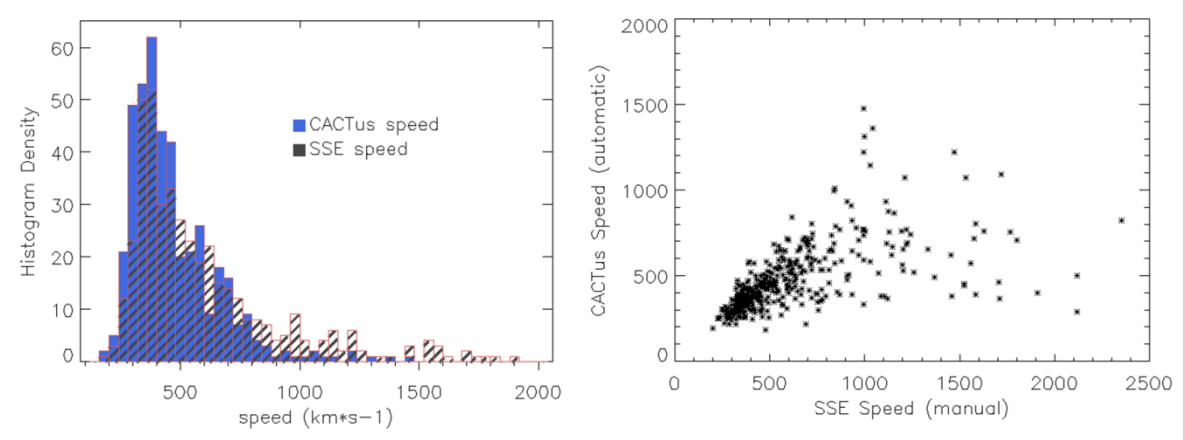

Figure 3.2.19 - Comparison of CME speeds, using the Self Similar Expansion method (SSE), between the manual and automatic catalogues. As a histogram (left) and scatter plot (right).

Comparison of the (manual and automated) HI CME catalogues with coronagraph catalogues

The HICAT and CACTusCAT catalogues established in tasks 2.1 and 2.2 of WP2 have been compared with the UGOE STEREO/SECCHI/COR2 CME-Database. The basic aim is to compare the CMEs detected in the heliosphere (STEREO/HI) with co-incident coronal observations of CMEs. The UGOE database, which is available at **http://www.affects-fp7.eu/cme-database/database.php**, was established under the framework of the DLR project STEREO/Corona, the EU FP7 project SOTERIA and the EU FP7 project AFFECTS, and was extended until the end of 2011 within the HELCATS project. It includes a total of 1071 CME events between 2007 and the end of 2011.

In order to identify corresponding events in the HICAT catalogue with those in the COR2 database, all events within a time window of 24 hours before the first observation time of a CME in the field of view (FOV) of the HI-1 instrument and within an angular range of +/- 90 degree in the position angle (PA) were investigated. In the next step the definite event associations were made through manual inspection of the COR2 and HI datasets that allowed backtracking of the HI-1 features. In the time range from 2007 until the end of 2011, 260 unique matches were found in the FOV of HI-1A and 278 in the FOV of HI-1B. These CME events were observed under separation angles between both spacecraft ranging from a few up to 180^{o}.

A comparison of these two sets of events with the Graduated Cylindrical Shell (GCS; see Bosman *et al.*, 2012) modelled "COR2-Best-of-list", available at **http://www.affects-fp7.eu/cme-database/database.php**, resulted in a final "HISCORCAT" (HI synchronized with COR) list comprising 91 events.

The HEEQ (Heliocentric Earth Equatorial) coordinate longitudes and latitudes of these events derived from GCS-modelling in the COR2 FOV and from the three different geometrical models the Fixed-Phi Fit (FPF), Self-Similar Expansion Fit (SSEF) and Harmonic Mean Fit (HMF) (see task 2.1) applied to the HI-1 FOV, are compared in Figure 3.2.20. The velocity distributions derived from CAT modelling of the "COR2-Best-of-list" and derived from the different HI modelling techniques are shown in bins of 100 kms^{-1} in Figure 3.2.21. The direct comparison for of the velocities is shown in Figure 3.2.22.

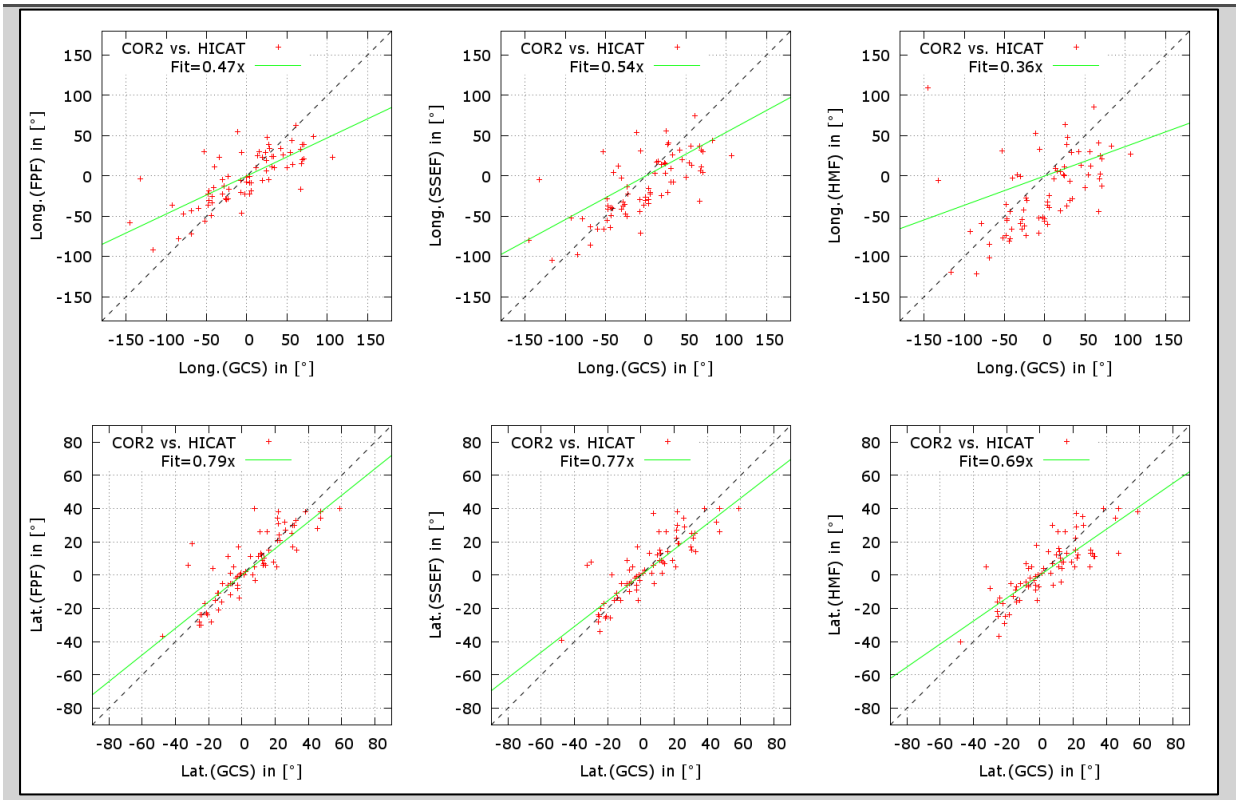

Figure 3.2.20 - Comparison of HEEQ longitudes(top) and latitudes (bottom) derived from GCS-modelling in the COR2 FOV (x-axes) and from the three different geometrical models FPF, SSEF and HMF (left to right) applied to the HI 1 FOV (y-axis) for the "HISCOR" list. The dashed lines denotes 1:1 agreements, the green line is a linear fit to the data.

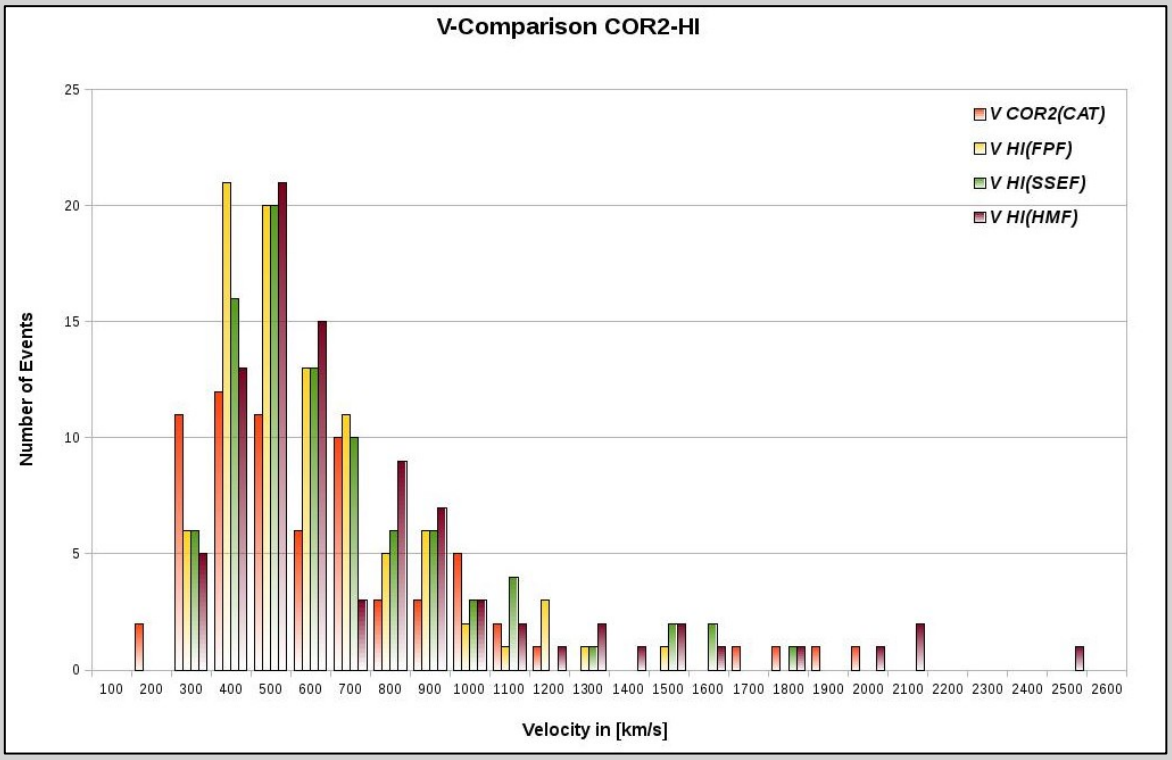

Figure 3.2.21 - The velocity distributions derived from CAT modelling of the "COR2-Best-of-list" and derived from the different HI modelling techniques are shown in bins of 100 kms^{-1}.

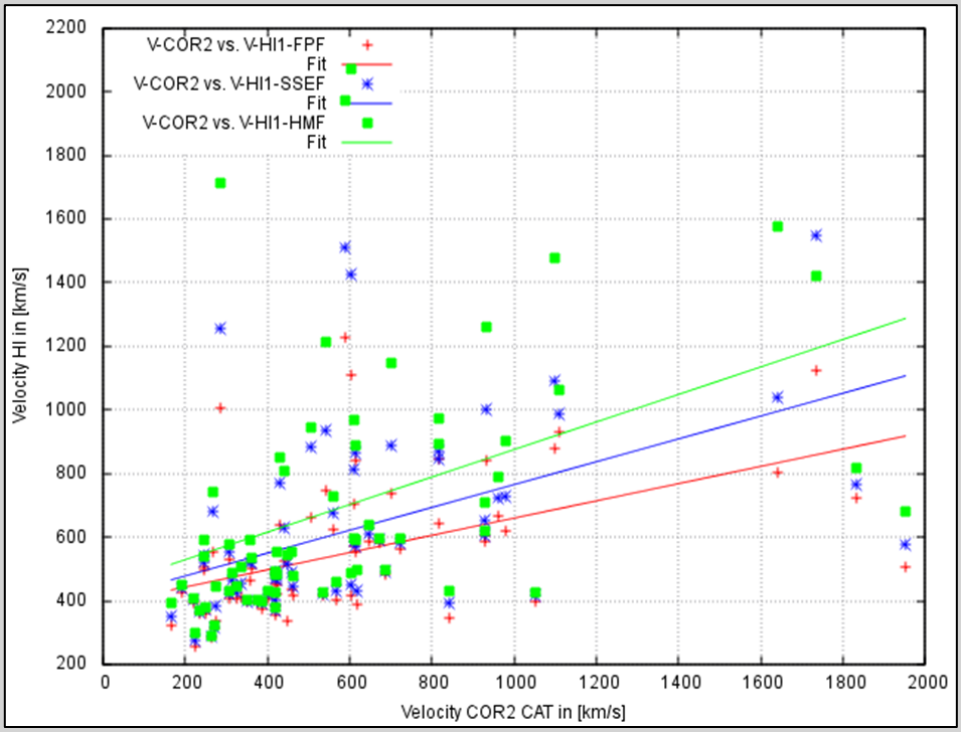

Figure 3.2.22 - *Direct comparison of the CME velocities derived from CAT modelling of the "COR2-Best-of-list" and derived from the different HI modelling techniques.*

As sample case for the comparisons being made, the results for the December 16th 2009 CME are shown in Figure 3.2.23 for the FOV of HI-1A and in Figure 3.2.24 for COR2. The GCS, FPF, SSEF, and HMF model results for this event are summarised in Table 3.2.4.

Table 3.2.4: Comparison of modelled results for the GCS number of CMEs detected manually and automatically

	COR 2 (GCS/CAT)	HI1 FPF	HI1 SSEF	HI1 HMF
Velocity [kms^{-1}]	464	479	513	552
Long. Carrington [deg]	238	209	195	179
Latitude [deg]	7	10	11	12

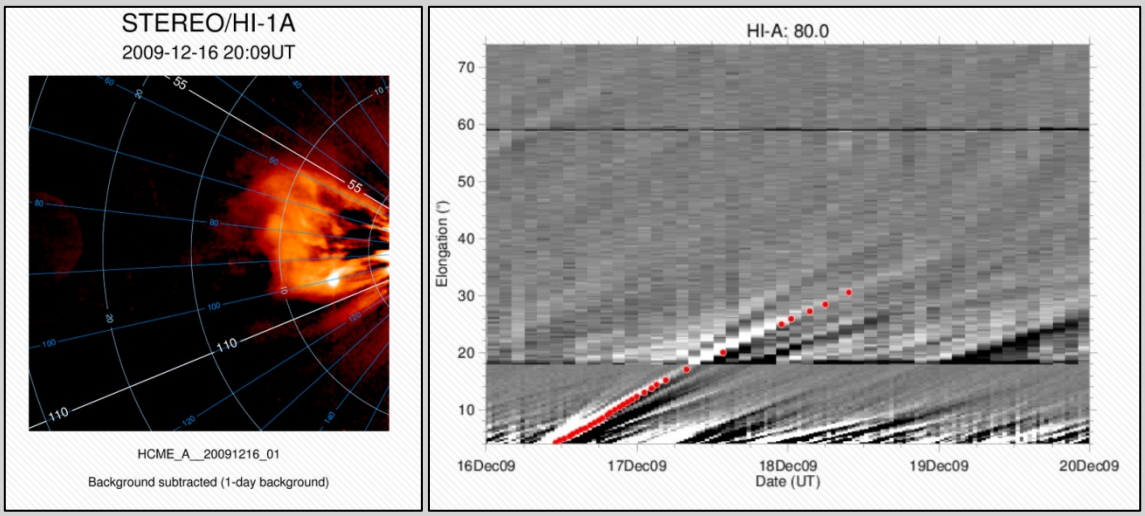

Figure 3.2.23 - Left: Background subtracted HI-1A observation of the CME observed on December 16, 2009 with position angle grid. Right: J-map of the CME derived from HI-1A and HI-2A observations.

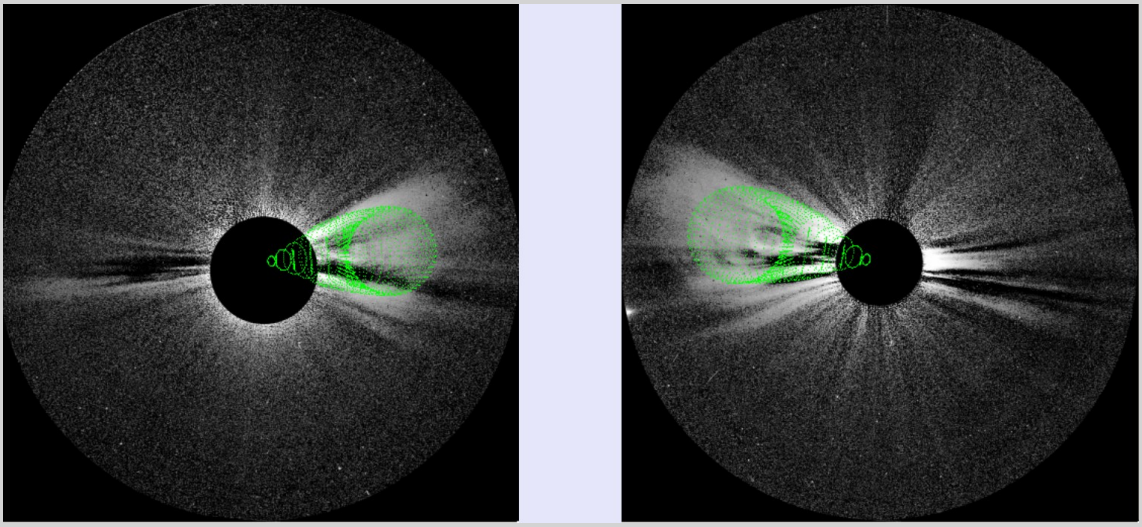

Figure 3.2.24 - White-light coronagraph images of the CME observed on December 16, 2009 with modelled GCS wireframe in green. Left: COR2 B. Right: COR2 A. STEREO A and B were separated by 130° in longitude.

WP2 TASK 2.4: SCIENTIFIC MANAGEMENT (TASK LEAD: STFC)

Whereas WP1 covers the administrative management of the HELCATS project, WP2, through task 2.4 included an element for the scientific and technical management. Thus, whereas WP1 included aspects such as the oversight of the meeting and teleconference structure, the WP2 effort coordinated the scientific and technical discussion between the WP leaders and the wider team. Throughout the project activities this focused on the teleconference discussions, the kick-off and six monthly meetings and the technical details of the report writing; it also covered the regular technical communication with the WP teams on a range of issues as the project progresses. Thus, this WP ran in parallel with the logistical management of the project and continued throughout the HELCATS project. It was coordinated by the Scientific and Technical Managers, Dr Jackie Davies and Dr Chris Perry, respectively. The activities relating to this coordination are noted in the minutes of the monthly minutes and the bi-annual and annual meetings, and these are lodged in the project private Wiki area of the project website.

WP2 CONCLUSIONS:

The activities of WP2 were to construct the basic catalogues of heliospheric CMEs from both manual (HICAT catalogue) and automated (CACTusCAT catalogue) procedures from the STEREO/HI data, to then assess and compare these two catalogues and, to compare them to coronal CME catalogue data. An additional element was the scientific and technical management of the HELCATS project. All of the activities and goals that were set out for this WP were achieved. The catalogues are on line and available to the public, and prepared in such a way as to be a valuable resource for the future of heliospheric research. The manual and automated catalogues were shown to be largely consistent, underlining the success in applying the CACTus approach to HI data. The comparisons to coronagraph data (KINCAT) demonstrated a clear capability to exploit the HELCATS facilities to make detailed comparisons of CMEs in the heliosphere and in the corona. The distributions of relevant paramaters were basically consistent, especially when taking into account observational and geometrical considerations.

WP2 HIGHLIGHTS:

- Creation of the first (manual) definintive HI interplanetary CME catalogue, HICAT, containing over 1600 entries for the period from 2007 to 2017.
- Successful assessment of automated detection of CMEs in the HI data exploiting the CACTus method, leading to the production of the CACTusCAT catalogue of events identified automatically.
- Comparison of the manual and automated interplanetary CME catalogues (HICAT and CACTusCAT) shows good correlation of the numbers of events identified, and, also, of their basic parameters (widths, speeds).
- The capability for detailed comparisons of the interplanetary CME (HICAT, HIGeoCAT (see WP3) and CACTusCAT) and coronagraph (KINCAT) is demonstrated, showing a tendency for similar parameter distributions with differences that can be addressed through a consideration of the observational geometries.

WORK PACKAGE 3 (WP3):

Deriving/cataloguing the kinematic properties of STEREO/HI CMEs based on geometrical and forward modelling

WP3 ACTIVITY TYPE: RTD

WP3 DURATION: MONTHS 1 – 36

WP3 LEAD BENEFITIARY: UGOE (4)

WP3 LEADER: Dr. Volker Bothmer

WP3 CONTRIBUTORS: UGOE (4); TCD (9); STFC (1); UNIGRAZ (2)

WP3 OVERVIEW: The key objectives of WP3 are deriving and cataloguing the kinematic properties of the STEREO/HI CMEs identified and catalogued in WP2 as HICAT, based on geometrical and forward modelling in KINCAT. For these purposes the recently established geometrical, forward (and prototype) inverse CME-modelling methods are applied. The derived CME parameters were included in the established HICAT, KINCAT, LOWCAT and HIGeoCAT catalogues, including back- and forward-projections to 'predict' CME launch and arrivals at various solar system locations. Comparisons are made between the parameters yielded by the different models and finally compared to the photospheric and low coronal source regions for dedicated events.

[Relevant catalogues: KINCAT, LOWCAT]

WP3 TASK 3.1: Geometrical modelling of STEREO/HI CMEs (TASK LEAD: STFC, CONTRIBUTORS: UNIGRAZ, UGOE)

The STFC contribution to WP3 is principally through task 3.1, the geometrical modelling of STEREO/HI CMEs. This task involves the derivation of the kinematic properties of those CMEs visually identified in WP2.1. This is achieved by selecting the track made by each CME in a time-elongation map (J-map) and applying the assumptions about its geometry and dynamics summarized in Davies et al. (2012). This makes use of three established geometrical approaches, assuming that the CME can be modelled (i) as a point-like feature propagating outwards (known as the Fixed Phi method), (ii) as an expanding circle whose diameter is defined by the CME apex and Sun-centre (known as the Harmonic Mean method), and (iii) as a self similarly expanding circle propagating outward between two fixed position angles (known as the Self Similar Expansion method).

The CMEs are assumed to travel at a constant speed in a fixed direction. The three different fitting methods are applied to each CME (see Davies et al., for details). For a given CME, the path of its (apparent) leading edge through a J-map is manually tracked at a position angle close to its apex and each of the three fitting procedures is applied to estimate its 3D speed and propagation direction. These values are, in turn, used to derive launch times for each event, which are then applicable to WP4.1, and to generate arrival times at various locations in the heliosphere for comparison with in-situ measurements (WP4.2).

Many details of this work are covered in the description of WP2.1 because the activities are intimately linked. The reader is referred to that section. However, specific to this task is the analysis of the J-maps and the specific deliverable, beyond that of the population of the catalogue, was the provision of the J-maps themselves. Thus, we expand on that work here.

Thus, the formal deliverable is realised through the main WP3 catalogue area on the HELCATS website, **https://www.helcats-fp7.eu/catalogues/wp3_cat.html**. The deliverable item (D3.1) consists of several parts and in particular

- The geometrical fitting catalogue
- Time elongation maps

Although not explicitly stated as part of the deliverable the implementation also provides

- Time elongation profiles for the manually identified events
- HI movies, images, plots of spacecraft location etc. that help to put the observation in context.

Where possible, time elongation tracks are extracted for each CME along a defined position angle corresponding approximately to the apex of the CME. Single spacecraft geometric fitting techniques (see Davies et al., 2012) are used to determine the kinematic properties (direction, speed and launch time) for three different simple assumptions of the CME morphology (Fixed Point, Self-Similar Expansion and Harmonic Mean). The result is a super-set of the WP2 catalogue containing both the observed parameters and the derived kinematics. Please read the release notes for the catalogue for further information and caveats related to this catalogue.

As noted in the description of WP2, the catalogue is accessible via the HELCATS web site at **https://www.helcats-fp7.eu/catalogues/wp3_cat.html** (see Figure 3.3.1). The complete set of fields contained within the catalogue are summarised in Table 3.3.1.

Options are provided on the web page to filter the contents based on:

- SSE launch date
- SSE Speed
- SSE Longitude (HEEQ)
- SSE Latitude (HEEQ)
- Event ID (via a free text search)

The filtered catalogue can be saved as a CSV format file or the complete catalogue can be downloaded in its original fixed format, JSON format or as a standard VoTable XML file.

The ID used within the catalogue is unique and tied to specific events such that it can be used to cross reference with catalogues developed within the other work packages.

Clicking on a specific row within the catalogue brings up a separate detailed information page (Figure 3.3.2) for that event which includes the time elongation maps and other contextual information as described in the section about task 2.1.

Below the main catalogue table is a link to the time-elongation profiles used as input to the geometric fitting algorithms, the contents of which is described below.

The provision of time elongation maps and other contextual information is implemented through the CME event page which is accessed from the main WP3 catalogue by clicking on an event row or can be called directly if the required event ID is known using a URL of the form shown below where the ID follows the standard HELCATS CME naming convention of HCME_[A|B]__yyyymmdd_nn (nn is the number within the day): e.g. **https://www.helcats-fp7.eu/catalogues/event_page.html?id=HCME_A__20070509_01.**

The event pages have been developed in order to link information created as part of all the HELCATS work packages, in particular this includes the linkage between events that are seen by both STEREO-A and STEREO-B, and "ground truth" in-situ detections and characterisations of CMEs based on observations at L1 and other heliospheric locations.

Table 3.3.1: Fields of the WP3 CME kinematics catalogue

Column	Description
ID	The unique identifier for the observed CME.
Date [UTC]	The date and time of the first observation of the CME in HI1 camera.
SC	The observing STEREO spacecraft, (A=Ahead or B=Behind).
L-N	Indicator that CME extends beyond the northern edge of the field-of-view (< for sc A, > sc B, blank if edge within FOV).
PA-N [deg]	The most northern position angle of the CME span.

L-S	Indicator that CME extends beyond the southern edge of the feld-of-view (> for sc A, < for sc B, blank if edge within FOV).
PA-S [deg]	The most southern position angle of the CME span.
Quality	A measure of "good", "fair" or "poor", that indicates the quality of the CME observation and confidence that the eruption is by definition a CME. It is recommended that Poor events are not used for CME based studies.
PA-fit [deg]	The position angle used in the time-elongation fitting
FP Speed [kms-1]	CME speed using on Fixed-Phi fitting
FP Speed Err [kms-1]	Uncertainty in Speed using Fixed-Phi fitting
FP Phi [deg]	Spacecraft-Sun-CME angle phi in degrees using Fixed-Phi fitting
FP Phi Err [deg]	Uncertainty in phi using Fixed-Phi fitting
FP HEEQ Long [deg]	CME HEEQ Longitude using on Fixed-Phi fitting
FP HEEQ Lat [deg]	CME HEEQ Latitude using on Fixed-Phi fitting
FP Carr Long [deg]	CME Carrington Longitude using Fixed-Phi fitting
FP Launch [UTC]	CME Launch time (r=0) using Fixed-Phi fitting
SSE Speed [kms-1]	CME speed using on Self-Similar Expansion fitting
SSE Speed Err [kms-1]	Uncertainty in speed using Self-Similar Expansion fitting
SSE Phi [deg]	Spacecraft-Sun-CME angle phi in degrees using Self-Similar Expansion fitting
SSE Phi Err [deg]	Uncertainty in phi using Self-Similar Expansion fitting
SSE HEEQ Long [deg]	CME HEEQ Longitude using on Self-Similar Expansion fitting
SSE HEEQ Lat [deg]	CME HEEQ Latitude using on Self-Similar Expansion fitting
SSE Carr Long [deg]	CME Carrington Longitude using Self-Similar Expansion fitting
SSE Launch [UTC]	CME Launch time (r=0) using Self-Similar Expansion fitting
HM Speed [kms-1]	CME speed using on Harmonic-Mean fitting
HM Speed Err [kms-1]	Uncertainty in speed using Harmonic-Mean fitting
HM Phi [deg]	Spacecraft-Sun-CME angle phi in degrees using Harmonic-Mean fitting
HM Phi Err [deg]	Uncertainty in phi using Harmonic-Mean fitting
HM HEEQ Long [deg]	CME HEEQ Longitude using on Harmonic-Mean fitting
HM Carr Long [deg]	CME Carrington Longitude using Harmonic-Mean fitting
HM HEEQ Lat [deg]	CME HEEQ Latitude using on Harmonic-Mean fitting
FP Launch [UTC]	CME Launch time (r=0) using Harmonic-Mean fitting

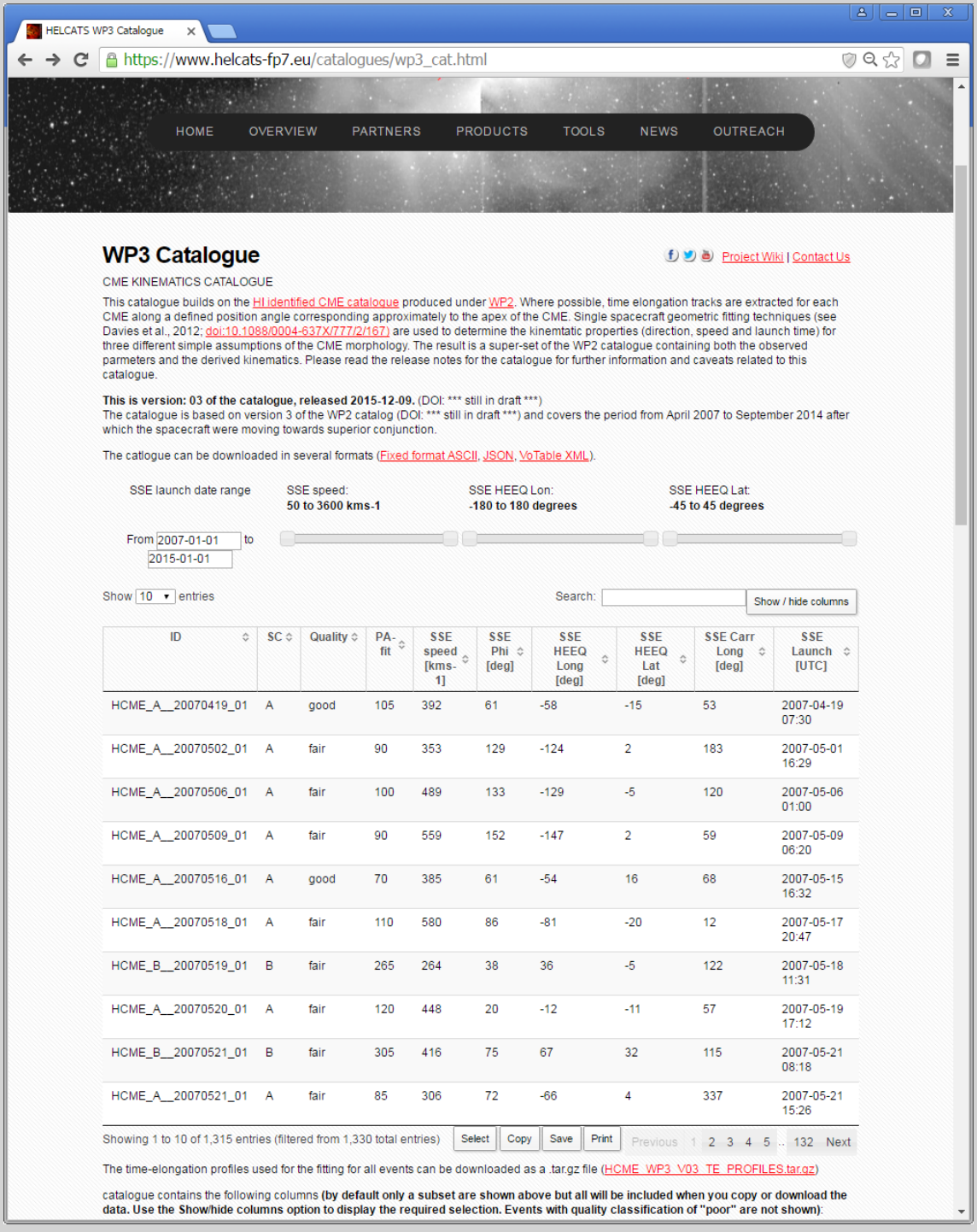

Figure 3.3.1 - The HELCATS kinematic properties catalogue generated as part of the WP3 activities. Clicking on an individual row will bring up the corresponding even information page for that event.

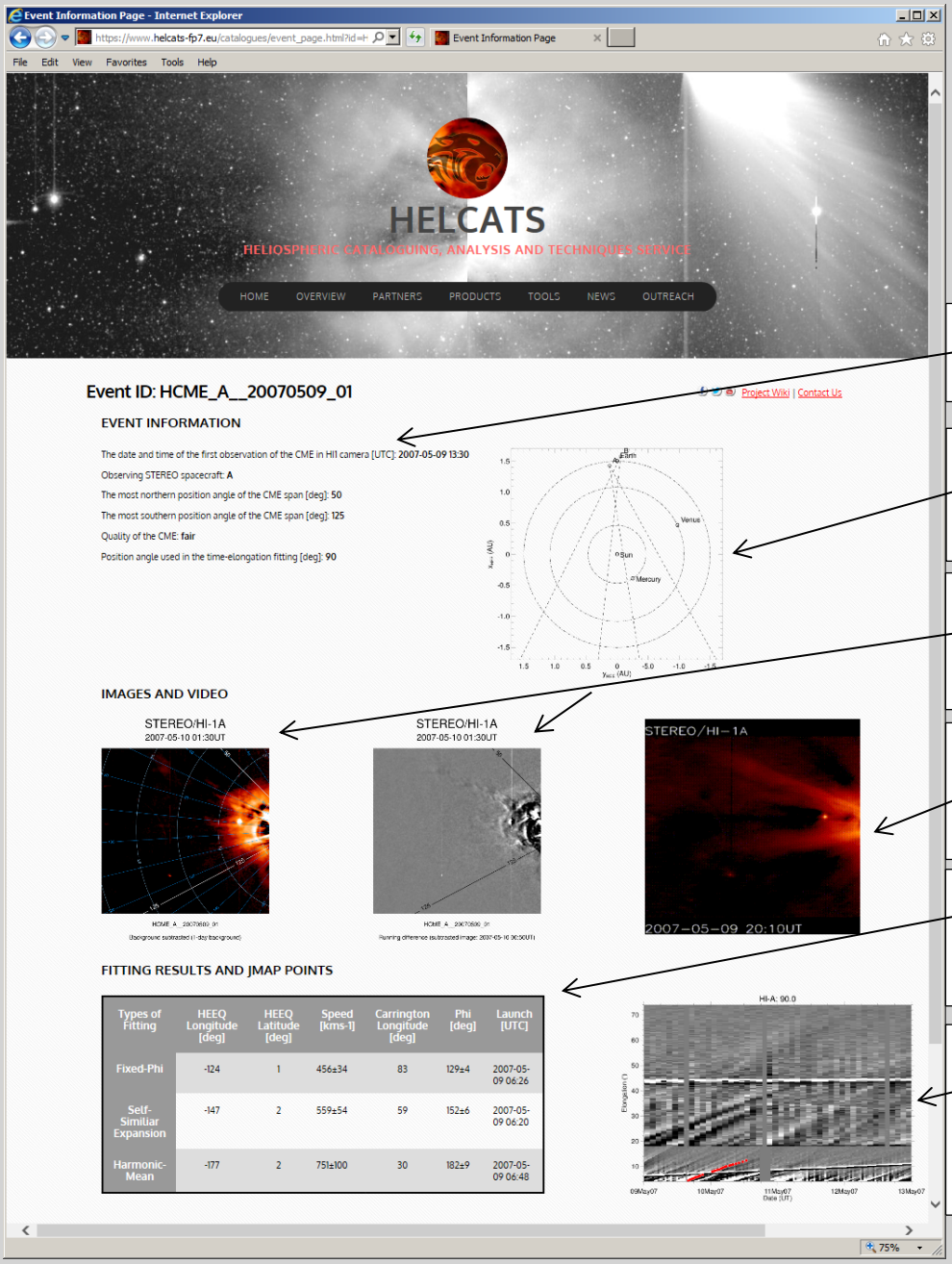

Manually identified CME properties

STEREO A/B location at the time of observation

Background subtracted and difference images from the HI instrument

Background subtracted movie from the HI instrument

CME kinematics based on geometric fitting of the time elongation profile

Time elongation maps from HI (J-maps) for the identified position angle and including SSE fit profile

Figure 3.3.2 - HELCATS CME Event information page.

The time-elongation profiles are the manually selected points from the J-maps that were used as input to the geometric fitting and determination of the CME kinematic properties.

The profiles for all currently identified events are contained in separate files that have then been collected in a single compressed tar archive (.tar.gz file). This can be downloaded from the WP3 catalogue page or directly at https://www.helcats-fp7.eu/catalogues/data/tracks/HCME_WP3_V03_TE_PROFILES.tar.gz

Each event is named according to the event ID and the position angle used for the fitting (HCME_[A|B]__yyyymmdd_nn_PAxxx.dat where nn is the event number within the day and xxx is the position angle in degrees with leading zeros where necessary).

0	2007-04-19T13:48:00.000	4.19141	105.00	A
0	2007-04-19T17:06:00.000	4.82031	105.00	A
0	2007-04-19T17:52:17.143	5.14844	105.00	A
0	2007-04-19T21:48:51.429	7.85547	105.00	A
0	2007-04-19T22:27:25.714	8.18359	105.00	A
0	2007-04-19T23:11:08.571	8.56641	105.00	A
0	2007-04-19T23:44:34.286	8.92188	105.00	A
0	2007-04-20T00:33:25.714	9.30469	105.00	A
0	2007-04-20T01:45:25.714	9.82422	105.00	A
0	2007-04-20T02:26:34.286	10.31641	105.00	A
0	2007-04-20T03:05:08.571	10.69922	105.00	A
0	2007-04-20T03:51:25.714	11.13672	105.00	A
0	2007-04-20T04:24:51.429	11.49219	105.00	A
0	2007-04-20T05:11:08.571	11.92969	105.00	A
0	2007-04-20T05:47:08.571	12.42188	105.00	A
0	2007-04-20T06:28:17.143	12.91406	105.00	A

Figure 3.3.3 - An example time-elongation profile.

Each file contains a set of five independently identified profiles although the points are combined when the geometric fitting is undertaken to improve the accuracy of the fit. A fixed ASCII format is used as shown in Figure 3.3.3.

The columns in the file correspond to:

1. The individual fit number that the data correspond to (0 to 4)
2. The date/time of the point on J-map time elongation profile
3. The elongation of the point on the J-map time elongation profile
4. The position angle along which the time-elongation profile is taken, usually corresponding to the apex or some other clearly defined feature in the CME images.
5. The STEREO spacecraft for which the profile was taken (A or B)

Finally, we note that the combination of WP2 task 2.1 and WP3 task 3.1 completes the HICAT catalogue, which is an unprecedented catalogue of CME activity in the heliosphere. It is freely available through the PRODUCTS tab on the main web page of the HELCATS website as a unique resource for future heliospheric research, in particular related to solar mass ejection and space environment physics and also space weather. By making this catalogue available, we have satisfied the core deliverable of the HELCATS project to the community. The key publications related to this work, that are to be submitted to the professional literature at the completion of the project (Harrison et al., 2017, Davies et al.., 2017, and Barnes et al.., 2017) have been referred to in WP2.

WP3 TASK 3.2: Forward modelling of STEREO/HI CMEs (TASK LEAD: UGOE)

From investigation of the STEREO/SECCHI/COR2 synoptic movies (available at https://secchi.nrl.navy.mil) from start of the science mission in January 2007, after launch of the STEREO mission in October 2006, until the end of 2011, 1071 CME events have been identified and catalogued in the framework of the DLR Stereo/Corona and the EU FP7 SOTERIA, AFFECTS projects. The selected time interval thus spans an angular separation angle up to 180°, reached in February 2011. The field of view of COR2 covers the range 2.5-15 RS.

From this so-called COR2 CME list available at http://www.affects-fp7.eu/cme-database/database.php, bright and clear appearing white-light events were extracted in the framework of the AFFECTS project for analysis with the Graduated-Cylindrical-Shell (GCS) model introduced by Thernisien, Howard and Vourlidas (2006) based on the 3-D concept for CMEs proposed by Cremades & Bothmer (2004). The COR2 “Best-of-list”, available at http://www.affects-fp7.eu/cme-database/database.php includes modelling results for 241 events.

For the GCS-fits the image with the CME appearing most developed and most complete in shape was selected. The "Best-of" event list was compared in the frame of the HELCATS project with the STEREO/HI event list established in WP2. This yielded a set of 109 events which were newly modelled dynamically to derive height-time profiles and 3-D de-projected CME speeds. If more than 6 data points could be determined in the COR2 FOV, higher order fits were calculated. A sample event observed in December 2008 is shown in Figure 3.3.4. The GCS-fits were established based on assumption that the CME expands self-similar within the COR2 FOV. This means that distortions due to interactions with the ambient solar wind or coronal structures can be identified from deviations from the GCS-structure in individual images. The non-linear development of the CME speed is shown in the bottom diagram of Figure 3.3.4. For better comparison of individual events, the CME speed provided in the event catalogue was standardized to a distance of 12 RS.

The programs developed for calculation of the masses of the CMEs are based on the method 'First Determination of the True Mass of Coronal Mass Ejections: A Novel Approach to Using the Two STEREO Viewpoints' described by Colanino and Vourlidas (2009) and in 'Comprehensive analysis of coronal mass ejection mass and energy properties over a full solar cycle' by Vourlidas et al. (2010). The mass calculation method was applied to the GCS-fits (in collaboration with A. Vourlidas, R.A. Howard, A. Thernisien and N. Savani at the STEREO/SECCHI PI institution at the Naval Research Laboratory, Washington, DC, USA) in the following way:

- Define pre-event image for background subtraction and determine brightness image (Figure 3.3.5)
- Use GCS-fit of brightness image to determine longitudinal offset ϕ between POS and CME
- Use "Billings equation" (1966) for Thomson scattered light to obtain mass per pixel image: m = Bobs/Be(theta) x 1.97 x 10-24 g, under assumption of CME mass distribution of 90% H, 10% He (Hildner et al., 1975)
- Determine time series of CME masses through COR2 FOV through integration over GCS-shape

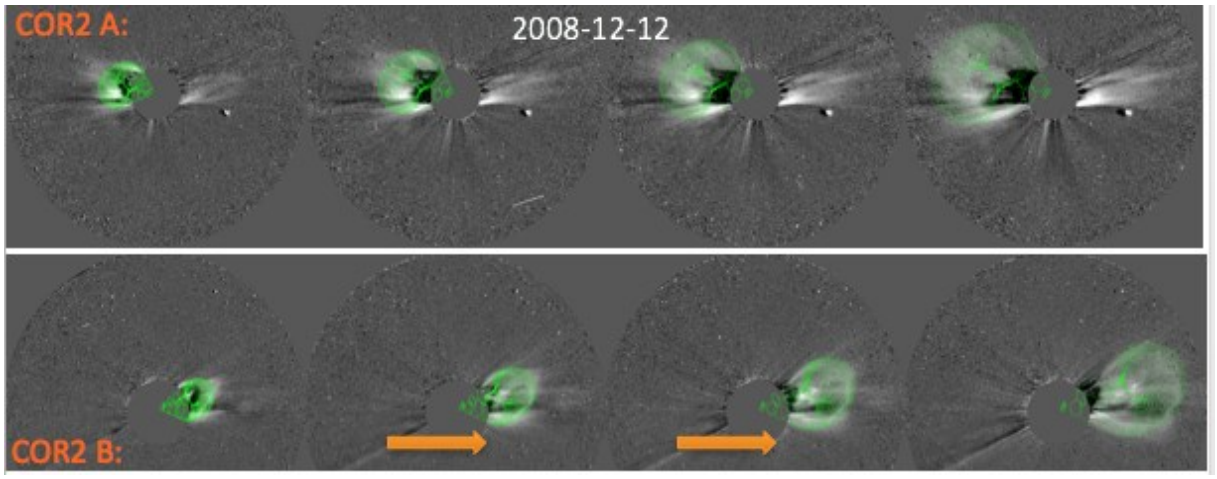

Figure. 3.3.4 - Sample of kinematic CME modelling in the STEREO/SECCHI/COR2 FOV for the December 12, 2008 event. Top COR2 A, bottom COR2 B. The arrow points towards increasing time, i.e. CME development.

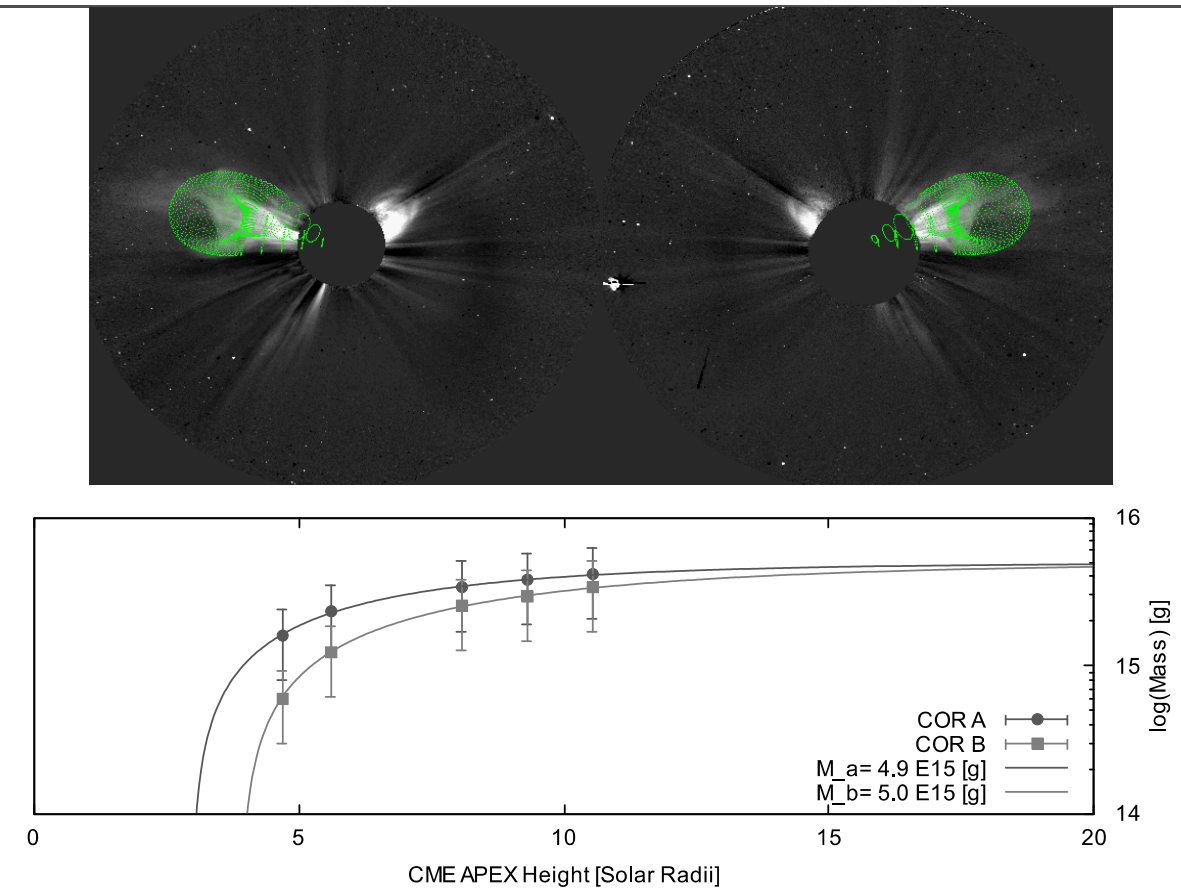

***Figure. 3.3.5** - Sample mass determination for a CME observed on 4 April 2011. **Top:** CME-fits, **Bottom:** mass calculations through the COR2 A and B FOVs.*

The increase of mass through the COR2 FOVs and a convergence at the end of the FOV near 15 RS is typically found from the calculations and is attributed to CME evolution and obscured area by the occulter in the early phase of the event (Colanino and Vourlidas, 2009).

Figure 3.3.6 shows the derived mass distribution for the COR2 FOVs and the mass-speed distribution.

The full set of GCS-modelling and mass determination results has been integrated in the HELCATS main database and has also been published online as "KINematic CATalogue" (KINCAT) available at http://www.affects-fp7.eu/helcats-database/database.php (Figure 3.3.7). Information on the positions of the two STEREO spacecraft, COR2 synoptic movies and movies of the GCS-fits have been added.

Since an important subject of the HELCATS project is dedicated on clarification of the CME-ICME relationships including solar wind measurements at Earth, the KINCAT event list has been updated with 13 events derived from comparison with the LINKCAT event database established in WP4 for on-disk events as viewed from Earth. For these events the GCS-modelling has been extended through SOHO/LASCO observations as shown in Figure 3.2.8.

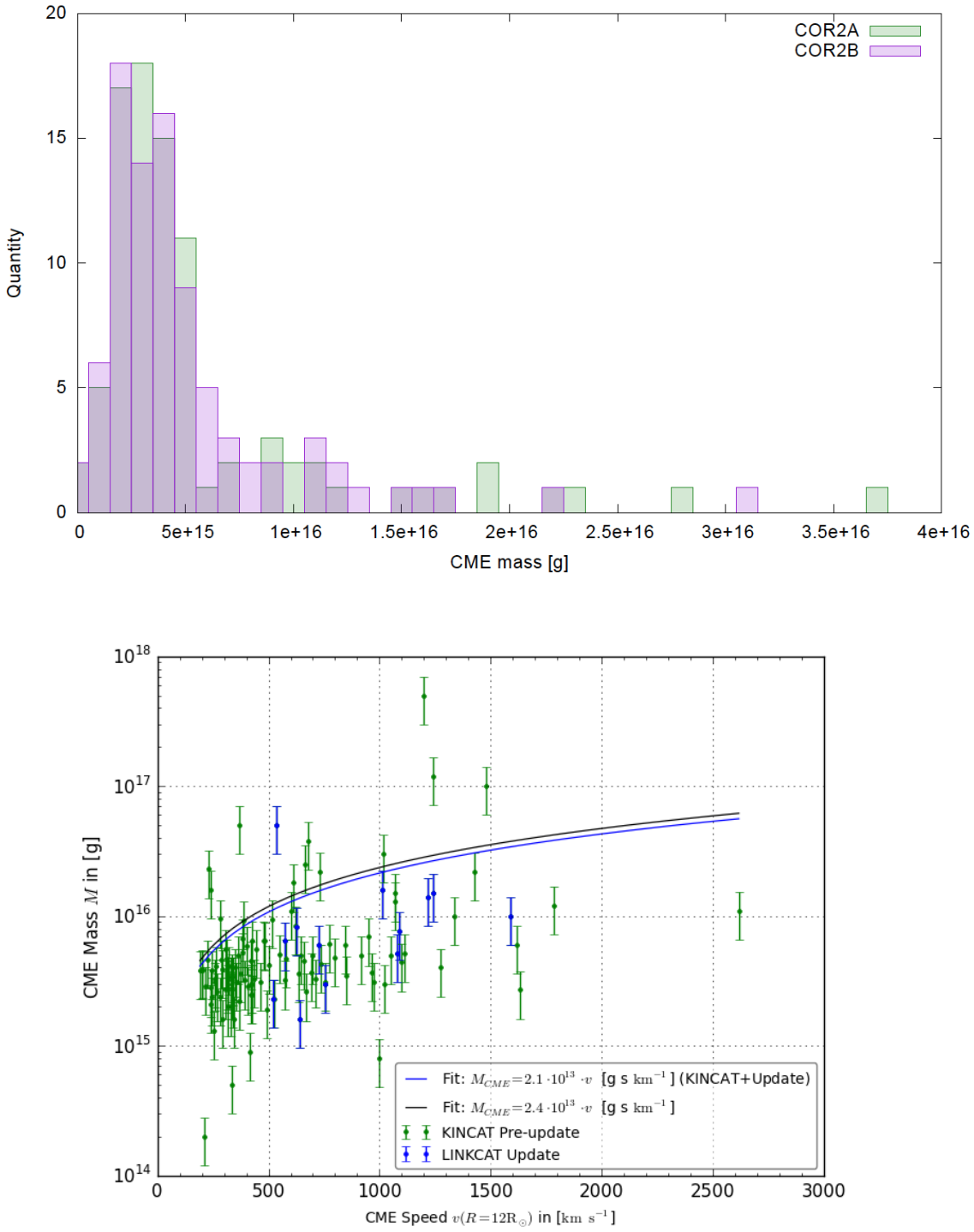

Fig. 3.3.6 - Top: Derived COR2 CME mass distribution in bins of 1015 g. Bottom: CME mass vs. speed distribution.

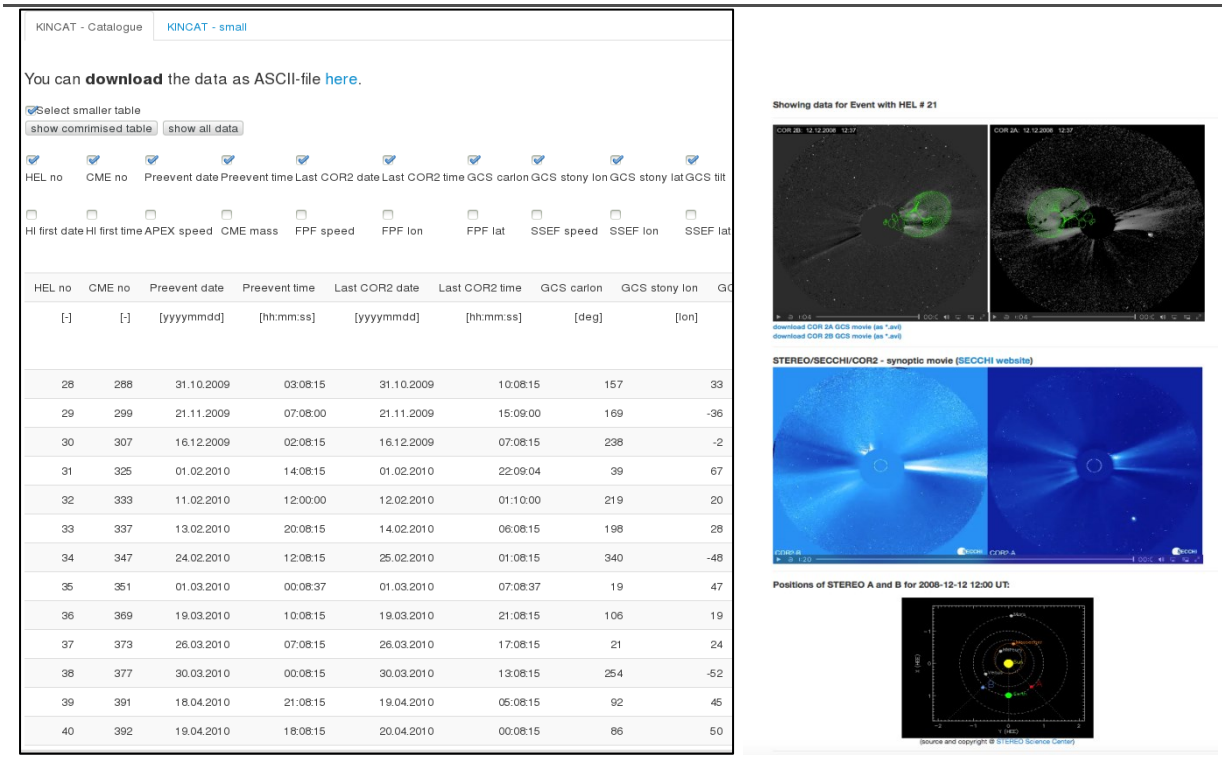

Figure 3.3.7 - The KINCAT database at http://www.affects-fp7.eu/helcats-database/database.php providing information on dynamical modelling results, GCS-movie, COR2 synoptic movies and position of the STEREO spacecraft at times of the CME events.

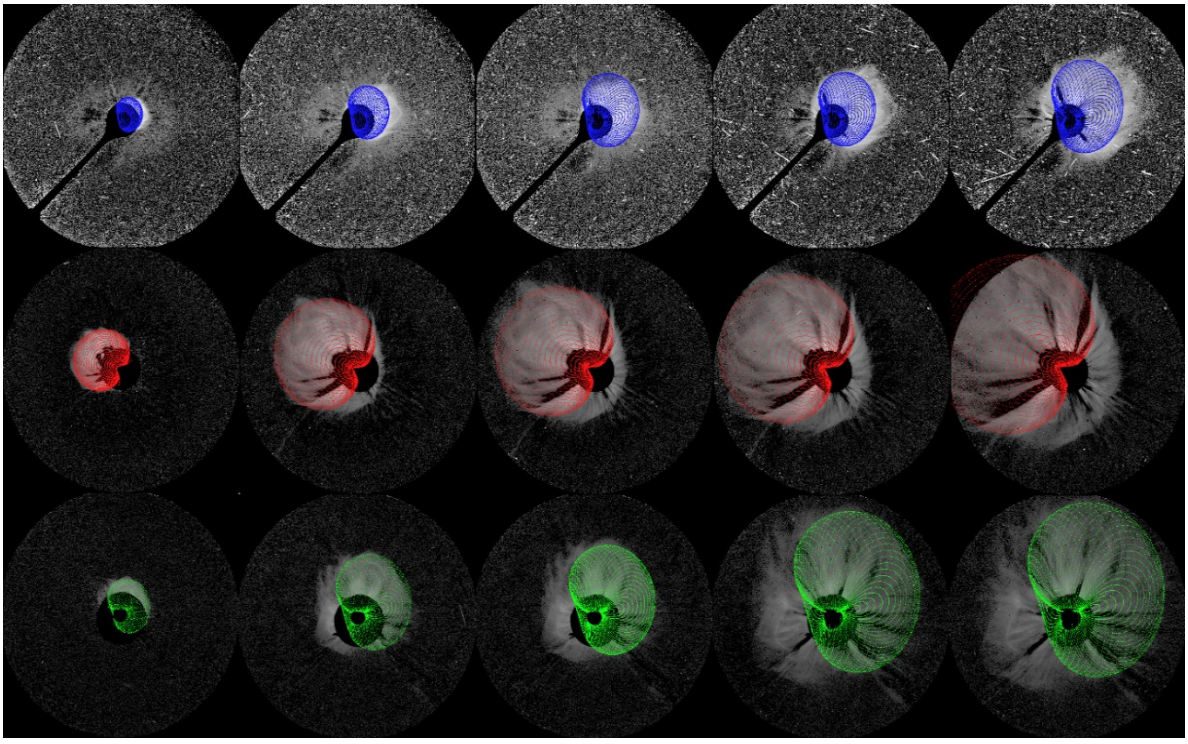

Figure 3.3.8 - GCS modelling with SOHO/LASCO C3 (blue) and STEREO COR 2 A (red) & COR 2 B (green) for the 13 March 2012 CME event.

WP3 TASK 3.3: Inverse modelling of STEREO/HI CMEs (TASK LEAD: UGOE, CONTRIBUTOR: TCD)

In order to compare CME properties, such as speeds, masses, angular widths, derived from GCS-modelling or from in-situ analysis in WP4, the photospheric SR of the individual events must be identified and analysed. The following sections describe how the SRs have been determined and how the LOWCAT database has been established. In the next step the KINCAT events of HICAT were identified. Finally, those events were analysed with the SMART code.

The LOWCAT catalogue

In parallel with the comparisons of white-light imaging and in-situ observations, work has been undertaken to examine the solar surface activity associated with coronal mass ejection (CME) launch. Studying the source of solar eruptions is key to improving space weather forecasting efforts, an area that is currently limited (Zheng et al, 2013). To that end, an automatic algorithm has been developed that uses back-propagation to identify flare events and active regions sources correlated with the CME event list created in WP2.

Assuming constant radial velocity and constant CME width, a simple ballistic propagation model is used to search for candidates. First the algorithm identifies a time window during which a STEREO/HI (Eyles et al, 2009) observed CME might have been observed by COR2. Here the initial distance can be taken as 12 RS final distance 2 RS and a typical range of CME speeds as defined by Yurchyshyn et al (2005) is used to constrain the search. The CACTUS database (Robbrecht et al, 2004), which contains events identified by an automated method developed at ROB, is searched for CME events occurring during this time window. The algorithm selects a COR2-observed CME with the closest angular width to the HI-observed CME, constrained by the north and south position angles.

Ballistic propagation is again used to define a time window of possible associated flares, using the identified COR2 CME event speeds where available. Here, the initial distance is taken as 2 RS and final distance can be set as high as 0.5 RS to take into account the non-constant speed of the initial CME phase. The algorithm searches for flare events in the SolarSoft Latest Events Archive1, the NOAA/SWPC Edited Solar Event Lists2, and the RHESSI flare list3. The results are constrained by solar hemispheric location, and if multiple flares are found within the search window the closest flare to the time window start is selected. The algorithm also limits the output to flares of GOES B-class magnitude and above, and for the RHESSI event list it allows only confirmed flare detections with a high-quality level defined in the flare list flags4.

Finally, the algorithm associates any identified flare events with corresponding SWPC-numbered active regions. The flare peak location is used to search for nearby active regions on the solar disk if no number has been listed in the flare database. Properties of the active regions are obtained from the SWPC Solar Region Summaries, including the Modified Mount Wilson (Kunzel, 1965) and McIntosh (McIntosh, 1990) classifications. The Solar Monitor Active Region Tracker algorithm (SMART; Higgins et al, 2011) is also run on regions using SOHO/MDI (Scherrer et al, 1995) and SDO/HMI (Scherrer et al, 2012) line-of-sight magnetograms depending on the date of the observations (HMI data being available from mid 2010). SMART calculates more complex magnetic properties related to the polarity inversion line (PIL), including PIL length, bipole separation, R value (amount of total flux near a PIL; Schrijver, 2007) and WLSG (the sum of the gradient along a PIL; Falconer et al, 2008). A full list of active region information outputted by the algorithm is listed in Table 3.3.2.

The algorithm has been run for version 4 of the HELCATS WP 2 HICAT catalogue, which contains over 2,000 events from 2007 to 2017. It is worth noting that much of the data available in the catalogue was from a period of deep solar minimum during which there were considerably less active regions, and the algorithm also flags limb events since magnetic field analysis of these regions would not be as accurate. However, the algorithm still identifies ~35% of the CME events in the WP2 HI list to be associated with flare events, and ~85% of those flare events are then associated with active region properties. Figure 3.3.9 shows an example of the results, specifically for the HCME_B__20120305_01 event , which has been previously studied by Magdelenic (2014). The algorithm identified a CME from the CACTUS database at starting at 2016-03-05 02:54 UT (see Figure 3.3.9b), which matches well with the expected launch times from the fixed-phi (02:06 UT), self-

[1] http://www.lmsal.com/solarsoft/latest_events_archive.html
[2] ftp://ftp.swpc.noaa.gov/pub/warehouse
[3] http://hesperia.gsfc.nasa.gov/hessidata/dbase/hessi_flare_list.txt
[4] http://sprg.ssl.berkeley.edu/~jimm/hessi/hsi_flare_list.html

Table 3.3.2: Magnetic source active region properties obtained from the SWPC Solar Region Summary and SMART algorithm outputs.

Source	Property	Unit	Description
SWPC	srs_no	-	SWPC-determined active region number of candidate region
SWPC	srs_mcintosh	-	SWPC-determined Zurich classification of the group
SWPC	srs_hale	-	SWPC-determined Hale classification
SWPC	srs_area	Millionths of a solar hemisphere	SWPC-determined active region total corrected area
SWPC	srs_ll	Heliographic degrees	SWPC-determined longitudinal extent
SWPC	srs_nn	-	SWPC-determined total number of visible sunspots in the group
SMART	smart_totflx	Maxwell	Total magnetic flux of SMART region
SMART	smart_posflx	Maxwell	Total magnetic flux in positive polarity part of SMART region
SMART	smart_negflx	Maxwell	Total magnetic flux in negative polarity part of SMART region
SMART	smart_frcflx	-	Flux fraction of SMART region, i.e., (POSFLUX – NEGFLX) / TOTFLX
SMART	smart_totarea	Millionths of a solar hemisphere	Total magnetic area of SMART region
SMART	smart_posarea	Millionths of a solar hemisphere	Total magnetic area of positive polarity part of SMART region
SMART	smart_negarea	Millionths of a solar hemisphere	Total magnetic area of negative polarity part of SMART region
SMART	smart_bmin	Gauss	Total negative magnetic field strength of SMART region
SMART	smart_bmax	Gauss	Total positive magnetic field strength of SMART region
SMART	smart_bmean	Gauss	Mean magnetic field strength of SMART region
SMART	smart_psllen	Megameters	Polarity separation line length of SMART region
SMART	smart_rvalue	Maxwell	R value of SMART region
	smart_wlsg	Gauss per Megameter	WLSG value of SMART region
SMART	smart_bipolesep	Megameters	Bipolar separation of SMART region

similar expansion (02:18 UT), and harmonic mean models (02:25 UT). The algorithm associated this COR2 event with a GOES X1.1 flare from the Latest Events Archive (Figure 3.3.9c) starting at 2012-03-05 02:30UT, from NOAA Region 11429 (SMART identified Region 5 in Figure 3.3.9d).

The resulting 'LOWCAT' catalogue is freely available online at figshare.com (doi: 10.6084/m9.figshare.4970222.v1; see Figure 3.3.10), which is also linked from the HELCATS website. The algorithm has also been run for the Framework Package 7 AFFECTS project KINCAT catalogue, which contains a more limited number of manually identified events. The algorithm will be described in detail in an upcoming paper by Murray et al (manuscript in preparation, 2017).

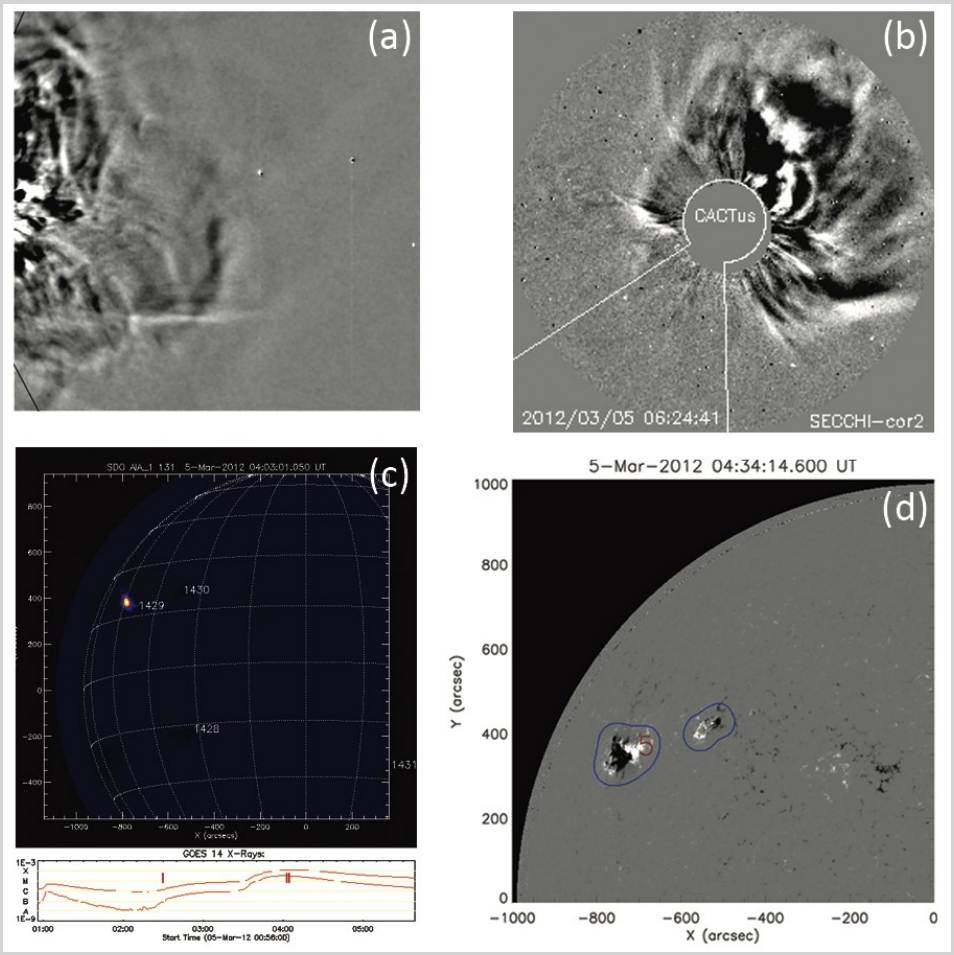

Figure 3.3.9 - Example of results obtained by the automatic back-propagation method for the HCME_B__20120305_01 event: (a) STEREO/SECCHI HI-1B running difference image of CME at 2012-03-05 17:29 UT (subtracted image: 2012-03-05 16:49 UT), (b) STEREO/SECCHI COR2-B difference image at 2012-03-05 06:24 UT taken from the CACTUS database, (c) Flare locator image at 2012-03-05 04:03 UT taken from the Latest Events Archive, (d) Image showing SMART detections on HMI magnetogram at 2012-03-05 04:34 UT.

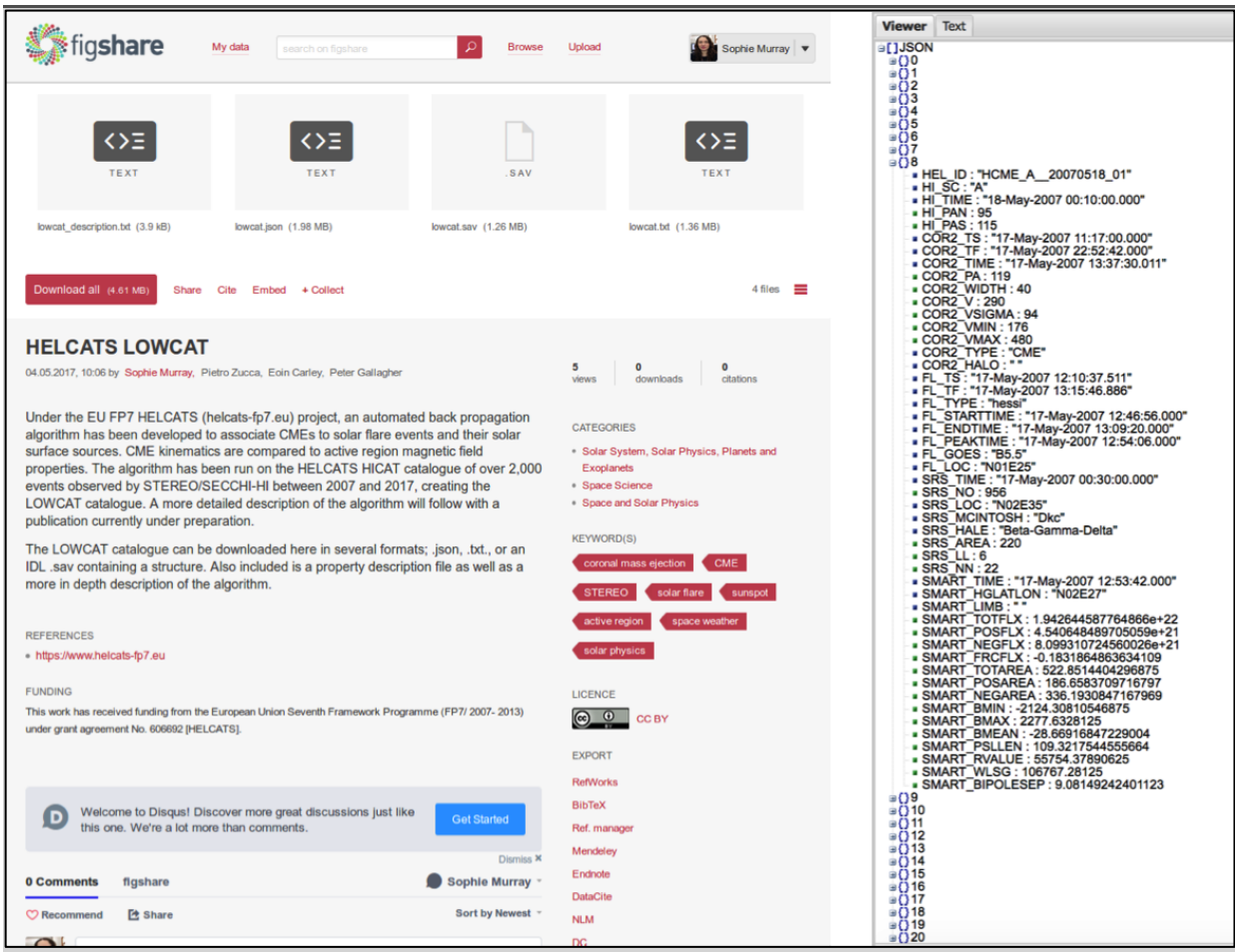

Figure 3.3.10 - Left: Screenshot of figshare.com page containing LOWCAT catalogue data in .json, .txt, and .sav formats. Right: Example of JSON object containing CME, flare, and active region information in the LOWCAT catalogue.

Determining the solar source regions for the KINCAT events of HICAT

In order to identify the corresponding source regions (SR) for the KINCAT CME events, available at http://www.affects-fp7.eu/helcats-database/database.php and https://www.helcats-fp7.eu/catalogues/wp3_kincat.html, we determined CME launch times from height-time profiles. As the next step, bright CME features identified in the COR2 and also COR1 FOVs close to the calculated launch time were tracked back to the solar “surface”.

Comparing the derived launch times and locations with those provided in the SOHO LASCO Catalogue by the CDAW Data Center, see e.g. Figure 3.3.11 for KINCAT event no. 49, and through the HEC databases (http://hec.helio-vo.eu/hec/hec_gui.php), we identified associated X-flare regions on the visible solar disk, as seen from Earth, for 54 out of 122 events.

As briefly mentioned previously, SMART is an automated system for detecting, tracking, and cataloguing active regions throughout their evolution. The algorithm relies on consecutive image differencing to remove both quiet-Sun and transient magnetic features, and region-growing techniques to group flux concentrations into classifiable features. It also uses persistence to associate developed active regions with emerging flux regions in previous measurements, and to track regions beyond the limb through multiple solar rotations. See Higgins et al (2011) for more details about how the algorithm works. Figure 3.3.12 shows an example of a SMART detection on 2011 June 21. The dark blue lines in the Figure indicate the boundaries of the SMART active region detections, within which various magnetic field properties are calculated.

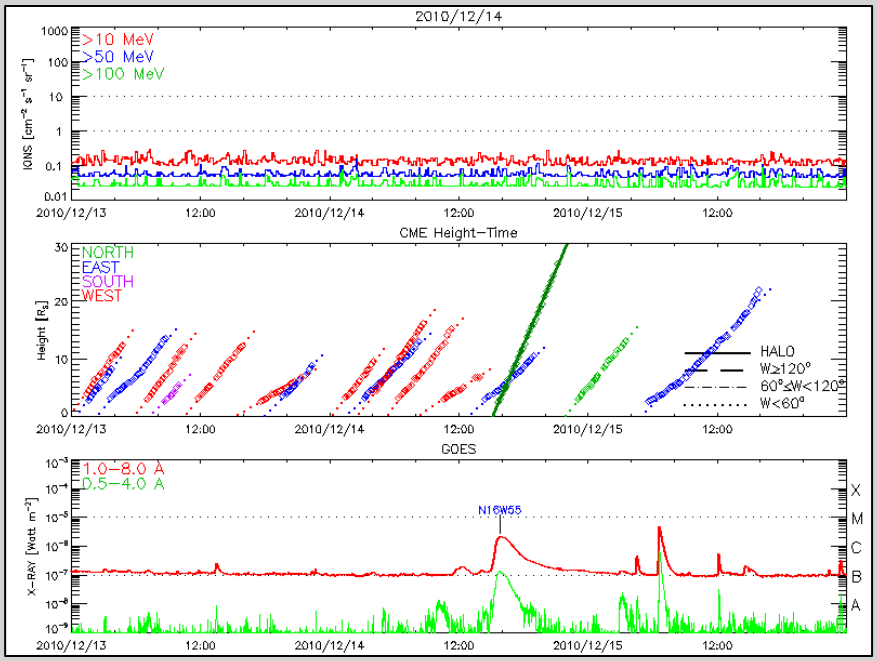

Figure 3.3.11 - Top panel: GOES proton channels >10, >50 and >100 MeV. Middle panel: CME height time profiles observed with SOHO LASCO for KINCAT event no. 49 (dark green line at 4 pm on 14th December 2010). Bottom panel: GOES soft X-ray measurements, with the corresponding C2.3 flare labelled. Source: *https://cdaw.gsfc.nasa.gov/CME_list/*

Analysis of solar photospheric CME source regions with SMART

For 44 out of the 54 KINCAT events (not all events were available to analyse due to limb position or lack of active region association), the source region magnetic properties were obtained by TCD using the SMART algorithm.

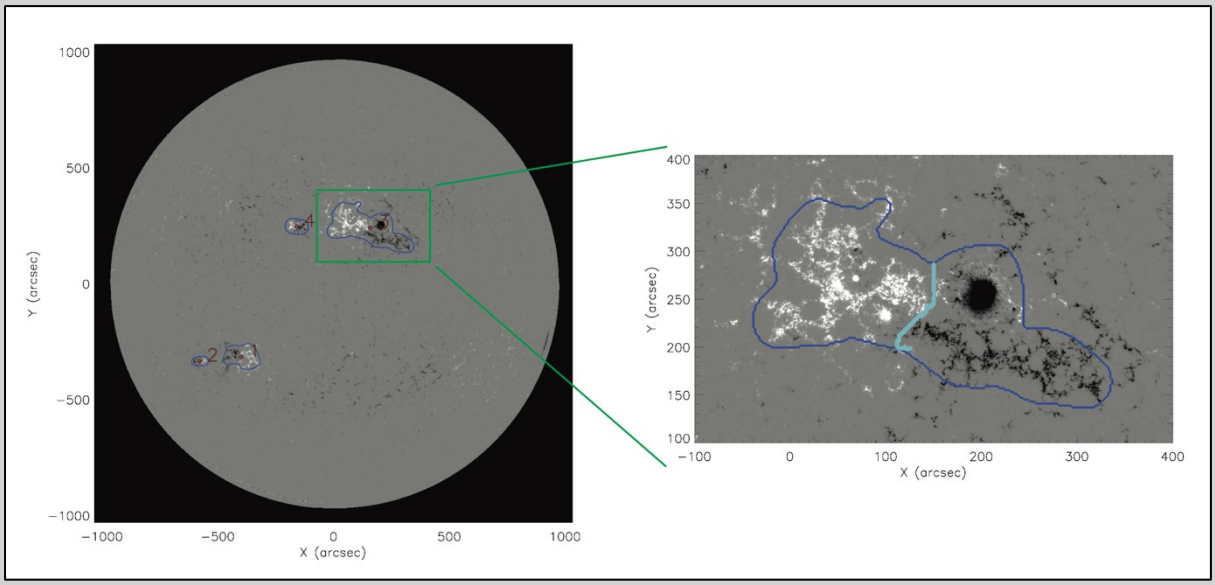

Figure 3.3.12 - SMART detections for a HMI line-of-sight magnetogram on 2011 June 21 04:10 UTC (left). The zoomed-in region (right; green box on left) shows detection number 3, which corresponds to NOAA/SWPC active region number 11236, and was the source of a C-class flare on 2011 June 21 as listed in the KINCAT database. The dark blue line indicates the detection boundary, and light blue line the PIL.

For the case of the KINCAT database, SMART was used to analyse the solar surface magnetic field of the source regions associated with the flare events.

Only one magnetogram was chosen for each flare event, at the closest available time to the flare peak. As per the LOWCAT catalogue, SDO/HMI line-of-sight magnetograms were run with SMART for events from 2010 May 1 onwards (when the data became available), and SOHO/MDI magnetograms were used for any events before this date. The flare peak location was used to identify which SMART-detected region corresponds to the flare, if any. The flare peak location was also used to identify any corresponding NOAA/SWPC-numbered active regions in the Solar Region Summary produced the day of the flare peak. Note this is a human-determined space weather forecast product rather than an automated method. A variety of magnetic properties were obtained from the SWPC and SMART source regions, with the SMART algorithm providing more complex parameters related to the magnetic PIL within the identified region (as already outlined in Table 3.3.2). An extra parameter was also calculated by TCD for further analysis by UGOE, namely the tilt angle of the magnetic PIL in degrees clockwise from solar North.

Summary

An automatic back propagation algorithm has been developed to identify source regions associated with CME events. The algorithm traces HI-identified events back to COR-identified events, associates flares with these COR-identified events, and then associates the flares with their active region sources. The SMART algorithm is then run to obtain complex photospheric magnetic field properties of these identified active regions. This method has been run for both the HELCATS project HICAT catalogue, producing the LOWCAT catalogue, and the AFFECTS project KINCAT catalogue, the results of which have been absorbed into KINCAT. The algorithm has been written such that other catalogues could also easily be run with it in the future.

A detailed study of CME vs source region KINCAT properties has been undertaken as part of WP3, the results of which are now available in the report for Deliverable 3.3. The LOWCAT CME vs flare vs active region properties are currently under further analysis as part of the exploration WP of the EU Horizon 2020 FLARECAST project (www.flarecast.eu), which provides an extensive database of vector magnetic field properties rather than the line-of-sight information obtained by SMART. The catalogues are freely available online, and thus use by the wider scientific community for research purposes is also activity encouraged.

WP3 TASK 3.4: Comparison of modelling results (TASK LEAD: UGOE, CONTRIBUTORS: STFC, TCD)

This section reports on the inter-comparison between the results of the geometrical, forward and inverse modelling undertaken as part of WP3 (see deliverable D3.3). The report is divided into sections that consider (i) an inter-comparison between geometrical modelling results, (ii) a comparison between forward and geometrical modelling results, and (iii) a comparison between forward and inverse modelling results.

As part of task 2.1 (see deliverable D2.1) a comprehensive catalogue of all CMEs visually identified in STEREO/HI imagery was compiled (HICAT). This spans April 2007 – August 2014 and October 2015 – present for observations from STEREO-A, and April 2007 – September 2014 for those from STEREO-B. The gap in the STEREO-A CME catalogue between August 2014 and October 2015 was due to the spacecraft being in superior conjunction; the termination of the STEREO-B CME catalogue in September 2014 was due to the loss of contact with the spacecraft at this time. HELCATS task 3.1 was concerned with tracking the path of these CMEs through the HI field-of-view and applying single-spacecraft geometric models (Davies et al., 2012) to them (see also deliverable D2.1) in order to determine their kinematic properties: speeds, directions and launch times (HIGeoCAT). In task 2.3, CMEs that were observed simultaneously by STEREO-A and -B are identified (HIJoinCAT), to which stereoscopic geometric models (Davies et al., 2013) are also applied (again in Task 3.1) in order to determine similar kinematic properties. Unlike the single-spacecraft technique, the stereoscopic technique does not rely on the assumptions that each CME is moving at a constant speed and in a constant direction. This allows further information, such as CME accelerations and deflections to be inferred. For a discussion of the stereoscopic models the reader is again directed to deliverable D2.1. Sections 2.1 and 2.2 of this document respectively, inter-compare the results of the different single-spacecraft models and as a comparison between the results of the single-spacecraft and stereoscopic models.

A further objective of HELCATS was to derive and catalogue the characteristics of CMEs observed with the STEREO/COR2 & HI imagers based on forward modelling (Task 3.2). In this deliverable, we also present the results of the analysis of a subset of the 122 CME events that have been dynamically modelled with the GCS-method in the COR2 field of view and which are compiled in the KINCAT database at http://www.affects-fp7.eu/helcats-database/database.php. We address the comparison between the forward and geometrical modelling results. In a later sub-section, the CME properties, such as speeds, masses, angular widths, as derived from GCS forward modelling are compared with magnetic field properties of the corresponding solar source active region, such as magnetic flux, area, and polarity inversion line characteristics as derived from source region (SR) analysis with the SMART code described in D3.4 (this so-called inverse-modelling work was undertaken in Task 3.3). The results indicate which photospheric SR parameters have implications for the properties of CMEs at distances around 12 solar radii. The results have further implications for space weather forecasts.

Inter-comparison between single-spacecraft models

The deliverable items with regards to the inter-comparison of geometric models are:

- An inter-comparison of single-spacecraft fitted CME kinematic properties (HIGeoCAT) from STEREO-A and STEREO-B;
- A comparison between single-spacecraft (HIGeoCAT) and dual-spacecraft (HIJoinGeoCAT) kinematic properties**.**

Further to this, a comparison between the forward (KINCAT) and geometrical/inverse models is presented:

- A comparison between forward and geometrical modelling by means of a comparison of the KINCAT and HIGeoCAT modelling results;
- A comparison between forward (KINCAT) and inverse modelling (LOWCAT) results.

For each of the CMEs tracked in HIGeoCAT (see section 2.2 of deliverable D2.1), we apply three models that each assume a different CME half-width (see Davies et al., 2012). The fixed-phi (FP) model uses 0°, the self-similar expansion (SSE) model uses 30° and the harmonic mean model (HM) uses 90°. For each CME we therefore determine three estimates of speed; vFP, vSSE and vHM, and three estimates of propagation direction; ϕFP, ϕSEE and ϕHM, where ϕ is the spacecraft-Sun-apex angle. Figure 1 shows a comparison between each combination of pairs of velocities (left-hand plots) and each combination of pairs of directions (right-hand plots). The top row shows a comparison between the most extreme cases; FP and HM. If we look at the top-left plot, the majority of points lie close to the identity line, which appears more evident for CMEs tracked far into the HI FOV. However this is likely to a superficial effect because they are far fewer in number than the shorter tracks, but have been plotted on top for emphasis. Another clear trend is that VFP < VHM, with just one exception, which is a CME with a particularly short track. The top-right plot shows a more systematic relationship between ϕFP and ϕHM, where the data are very clustered. The range of ϕHM values is broader than that of ϕHM, due to the restriction placed on the solving algorithm that the CME must lie within 0-180°, whilst the permissible range of ϕHM is within ±180°. For propagation angles exceeding 45°, ϕHM is generally greater than ϕFP , whilst the opposite applies to angles less than 45°. The colour scheme reveals a grouping of points by maximum elongation; for a given value of ϕFP, ϕHM lies further from the observing spacecraft when the CME is tracked further into the FOV. Similar behaviour is seen in each row of Figure 3.3.13, however the FP vs HM case is the most extreme.

Comparison of single- and dual-spacecraft models

A subset of 546 CMEs from HIGeoCAT (273 observed by STEREO-A and 273 by STEREO-B) are identified that are determined to be the same CME observed by each spacecraft (HIjoinCAT). A further subset of 302 (151 from each spacecraft) is selected, to which stereoscopic geometric modelling is applied. Figure 3.3.14 shows the distribution of CMEs observed throughout the period April 2007 to September 2014, with emphasis on those observed by both STEREO-A and STEREO-B (shaded regions). The darkest region shows those CMEs to which stereoscopic geometric modelling is applied. The reason that many CMEs are omitted in and around 2010 (lighter grey regions) is because the HI-1A and HI-1B instruments are pointed directly at one another,

which introduces difficulties in the stereoscopic fitting method. This occurs when the spacecraft are separated by 152°.

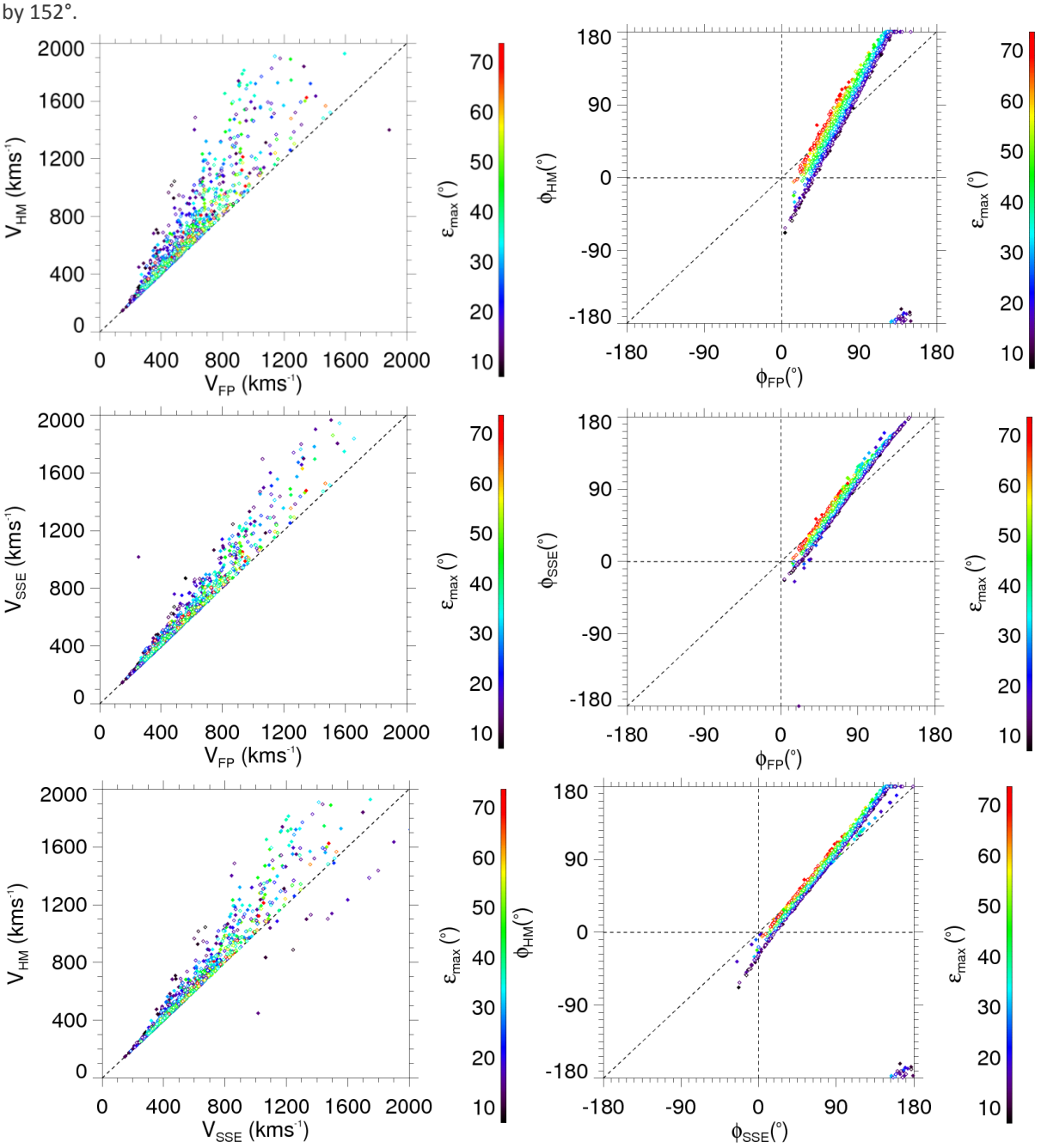

Figure 3.3.13 - A comparison between the results from each of the three fitting methods; the top row shows FP vs HM, the middle row FP vs SSE and the bottom row SSE vs HM. The left hand figures are a comparison between velocities and the right hand column a comparison between propagation angles. The colour bar represents the maximum elongation to which the CME was tracked. The filled diamonds are HI-A CMEs and the open diamonds HI-B CMEs.

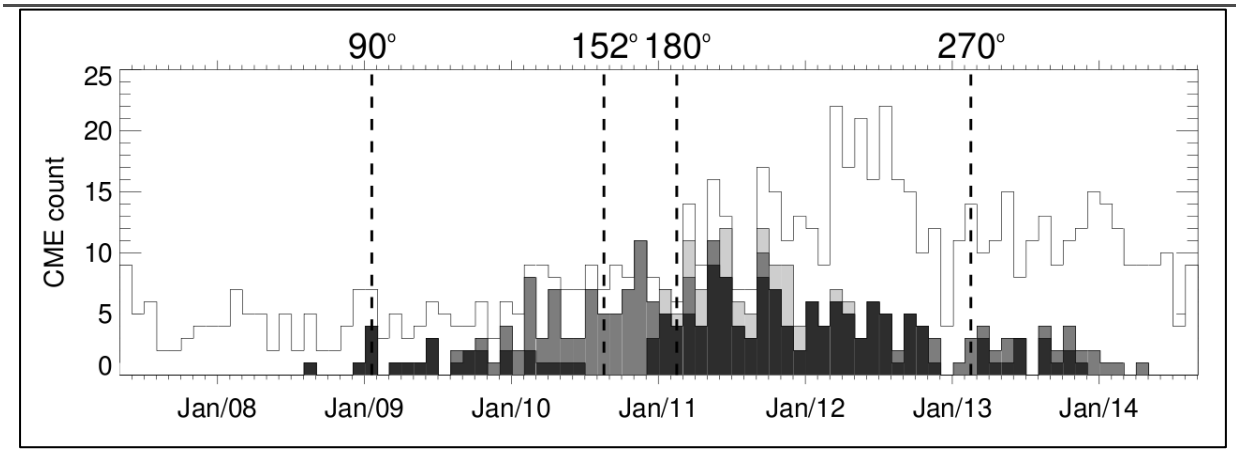

Figure 3.3.14 - Monthly CME count throughout the period April '07 to September '14, when both STEREO-A and –B. The total bin height shows the highest number of CMEs detected by either HI-A or HI-B. The shaded regions represent the monthly number of CMEs that were identified to be observable by both spacecraft. The darkest region shows the number of CMEs to which the stereoscopic modelling has been applied. Milestones in the separation angle between STEREO-A and –B are indicated by the vertical dashed lines.

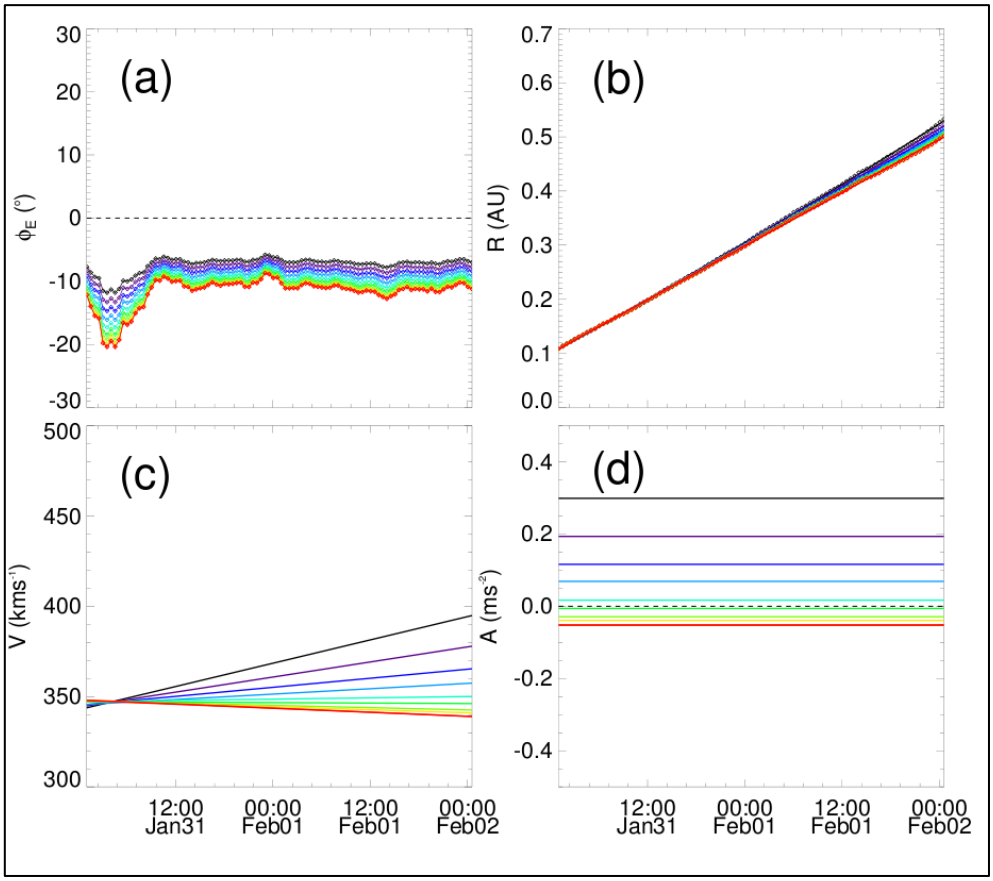

Figure 3.3.15 - An example of SSSE derived kinematics for HCME_A__20110122_01. The fitting procedure is applied using ten different half-widths, ranging from 0° (black) to 90° (red) in 10° increments. (a) shows the CME apex longitude in the ecliptic relative to Earth. (b) shows the CME apex distance as a function of time. (c) and (d) show CME velocity and acceleration, respectively, which are calculated by fitting a second or polynomial to (b) and taking the first and second derivatives.

A description of how the stereoscopic triangulation of CME positions is performed can be found in Davies et al. (2013). By tracking CMEs over periods of hours or days, the evolution of position may be determined, as is shown in Figure 3.3.15. A second order polynomial is fitted to the CME apex distance (b) , as a function of time.

The first and second derivative of this gives, respectively, CME velocity (c) and acceleration (d).

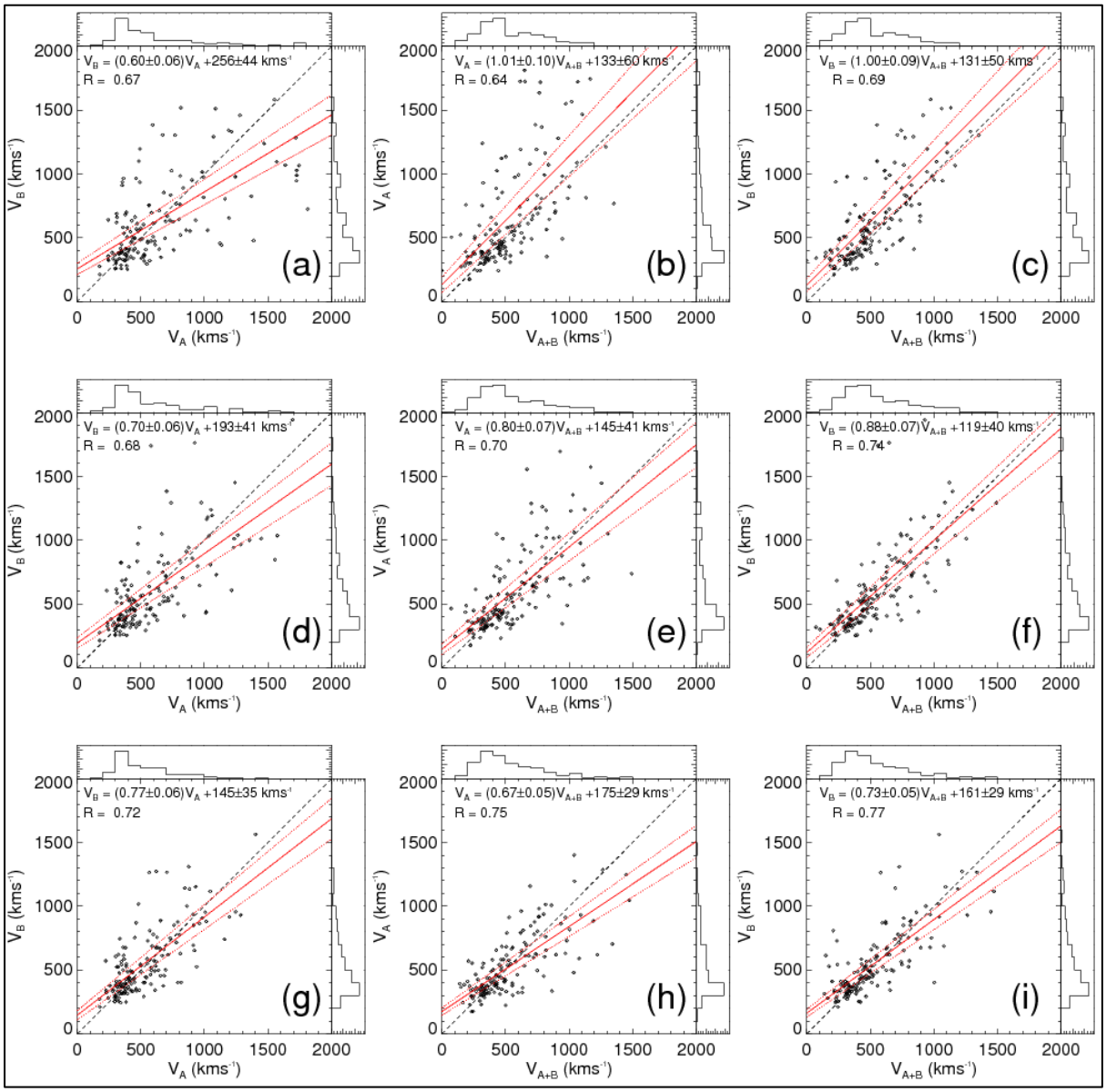

Figure 3.3.16 - Scatter-plots showing a comparison between speeds derived from each of the single-spacecraft (V_A, V_B) and the stereoscopic fitting methods (V_{A+B}). The top row shows velocities determined using the FP model, the middle row using an 30° SSE model and the bottom row the HM model.

Figure 3.3.16 shows a comparison between the velocities determined from each of the single-spacecraft (V_A, V_B) and the stereoscopic fitting methods (V_{A+B}). (a), (b) and (c) represent the FP model, (d), (e) and (f) the SSE model and (g), (h) and (i) the HM model. In the worst case, (b), the correlation coefficient is 0.64 and in the best case (i) it is 0.77. The agreement in CME speeds between each of the single-spacecraft and the stereoscopic models is therefore consistently good, and this is particularly so as the CME-half-width is increased.

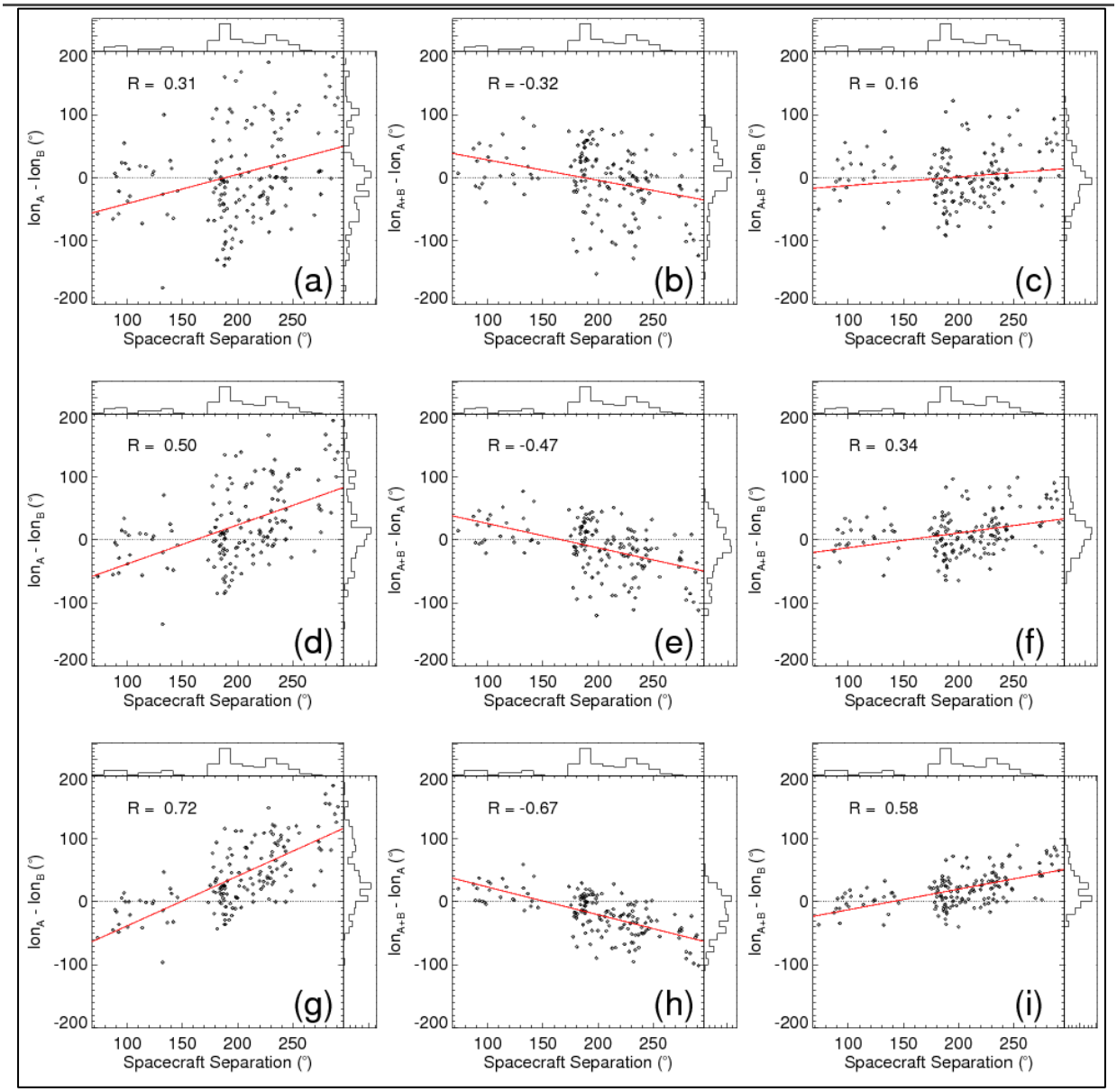

Figure 3.3.17 -: Scatter-plots showing a comparison between the difference in CME propagation direction from each of the fitting methods. lon_A, lon_B and lon_{A+B} represent the HEEQ longitude from the single spacecraft STEREO-A and –B fitting and the stereoscopic fitting methods, respectively. The difference is plotted against the spacecraft separation angle at the time that the CME was observed. The top row shows velocities determined using the FP model, the middle row using an 30° SSE model and the bottom row the HM model.

Figure 3.3.17 shows a comparison between the difference in CME propagation direction from each combination of pairs of fitting methods. This is plotted as a function of spacecraft separation angle to highlight the correlation between the two. Were the models to agree on CME propagation direction, we would expect all the points to lie near zero on the y-axis, which is shown by the dashed line. The fact that this is not the case suggests that the models we apply are perhaps incorrect in there assumptions. The dependence of the difference on spacecraft separation angle is an interesting feature. This is seen most strongly with the HM model, (g), (h) and (i), and also when comparing lon_A and lon_B, (d) and (e).

Comparison of KINCAT and HICAT modelling results

The latitudinal and longitudinal positions in HEEQ-coordinates derived from GCS-modelling in the COR2 FOV and through application of the FPF-, SSEF- and HMF- single-spacecraft methods in the HI FOV derived from j-maps, are compared in Figure 3.3.18 for the individual KINCAT and HIGeoCAT events.

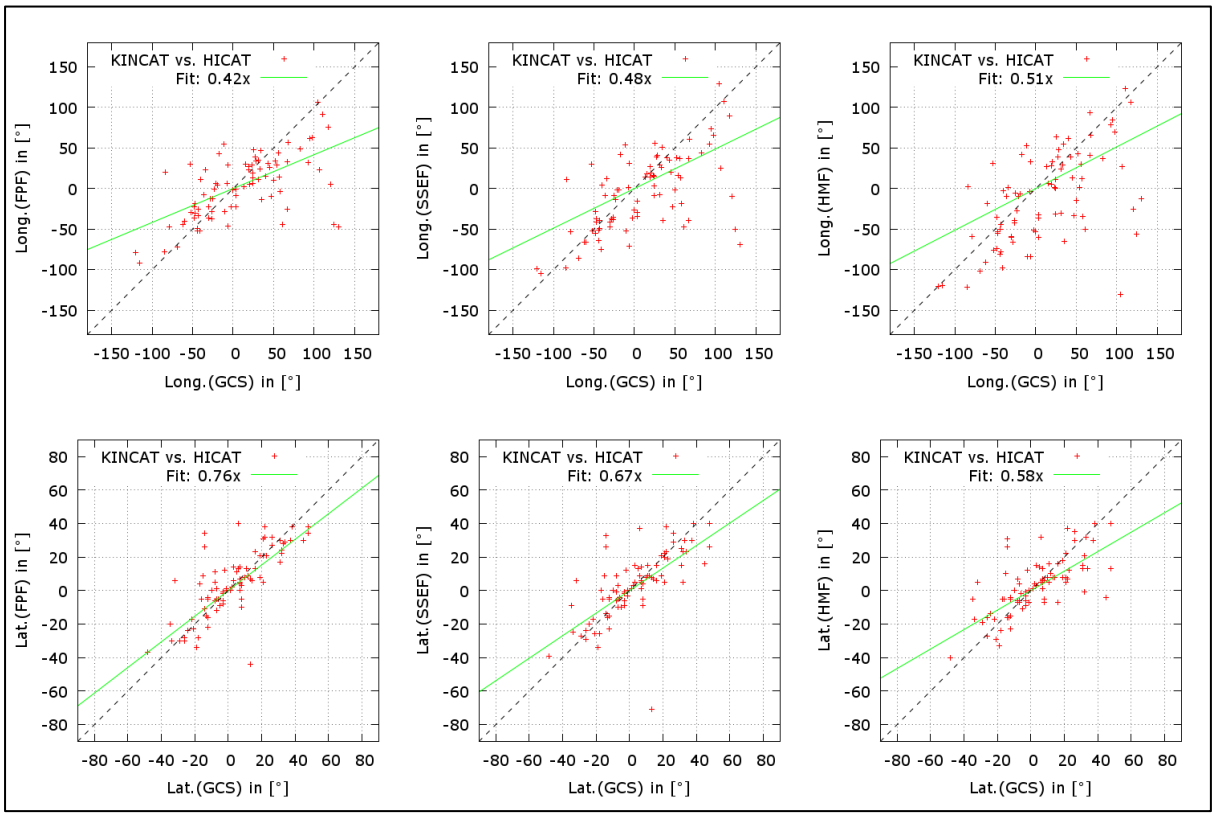

Figure 3.3.18 - Comparison of the longitudinal (top) and latitudinal (bottom) positions in HEEQ-coordinates derived from GCS-modelling in the COR2 FOV and through application of the FPF-, SSEF- and HMF-methods (left to right) in the HI FOV derived from j-maps for the individual KINCAT and HICAT events (red data points). The linear fits are shown through the green solid lines, the 1:1 correlation by the dashed black lines. The slopes of the fits are provided in the legends.

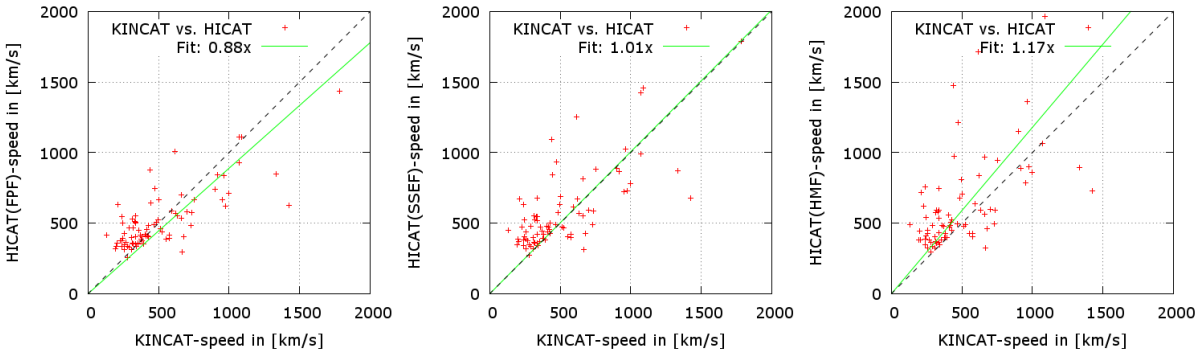

Figure 3.3.19 - Comparison of the CME apex speeds derived from GCS-modelling in the COR2 FOV and through application of the FPF-, SSEF- and HMF-methods (left to right) in the HI FOV derived from j-maps for the individual KINCAT and HICAT events (red data points). The linear fits are shown through the green solid lines, the 1:1 correlation by the dashed black lines. The slopes of the fits are provided in the legends.

In general, we find a good correspondence in the determined HEEQ-latitudes for all comparisons, with the best one derived for the FPF-method. For some events, we find considerable deviations in the longitudinal directions, with no clear preference for one method. The agreement in latitude is not surprising because one can assume that the CME-apexes propagate outwards with almost constant direction angle, i.e. only small latitudinal deflections occur at distances beyond about 15 R_S. Further on the latitudinal positions of the CME apexes can be determined relatively precise already with in-ecliptic single point observations. For the longitudinal positions, the POS ambiguities can be quite large depending on the spacecraft positions with respect to the CME 3D propagations in the different events.

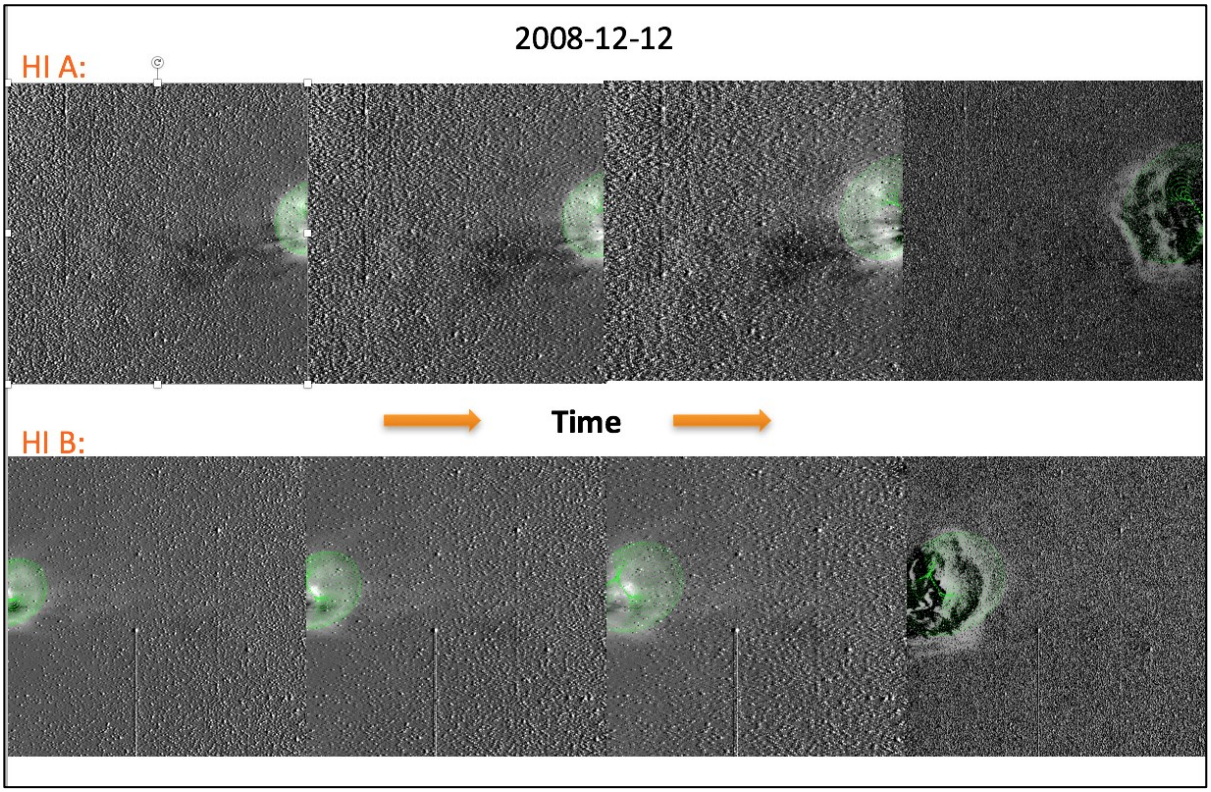

Figure 3.3.20 - GCS-fitting expanded to the HI FOV for the CME observed in December 2008. STEREO A and B were separated by about 90° in ecliptic longitude.

Figure 3.3.19 shows the comparisons of the derived CME speeds for the different model-applications. The best agreements are found in the comparison with the FPF-method. For slow CMEs, the speeds derived in the HI FOV are generally higher than in the coronagraph FOV; for faster CMEs, the speeds in the HI FOV are generally lower than those in the coronagraph FOV. This is in agreement with the common assumption of slow CME acceleration and fast CME deceleration with increasing distance from the Sun (e.g., Sachdeva et al., 2015).

The h-t diagram for the CME event fitted from COR2 into the HI FOV (Figure 3.3.20) is shown in Figures 3.3.21. A drag-based model has been applied to the fitting method (Sachdeva et al., 2015). The deceleration of the CME in the FOV is obvious in this case from the different speeds derived in the COR2 and HI FOVs.

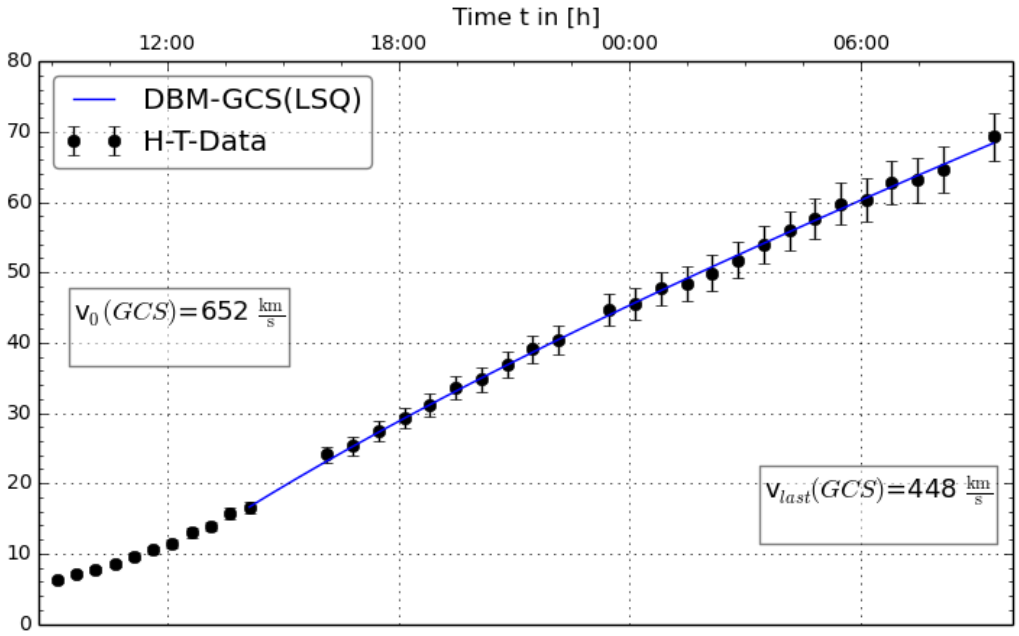

Figure 3.3.21 - Height-time diagram for the CME observed in December 2008 combining COR2 and HI observations and using a drag-based model (Sachdeva et al., 2015). The initial and final speeds in the FOV are provided in the legend. STEREO A and B were separated by about 90° in ecliptic longitude.

Comparisn of source region parameters with COR2 modelling results

The resulting values for the magnetic field area and flux derived by application of the SMART code in D3.4 (LOWCAT) have been compared with the geometric parameters of the CMEs derived from GCS-modelling (KINCAT) in the COR2 FOV.

A comparison of the determined KINCAT and HIGeoCAT SR locations with the SR locations for the 44 X-flare regions (D3.4) is shown in Figure 3.3.22. The SR locations are generally in good agreement with each other. A shift of the SR latitudes to the ecliptic plane between the SRs derived from CME modelling in the COR2 and HI FOV is obvious, indicating the deflection of CMEs to lower latitudes in agreement with previous results reported in the literature (e.g., Cremades and Bothmer, 2004). Figure 3.3.23 shows the distributions of the maximum and minimum magnetic field values of the SRs. Most SRs show absolute maximum magnetic flux values of 1500-2000 G. The distribution of the magnetic area shown in Figure 3.3.24 reveals that most CMEs were launched from SRs with an area of 500-1000 solar hemispheres divided by 10^6.

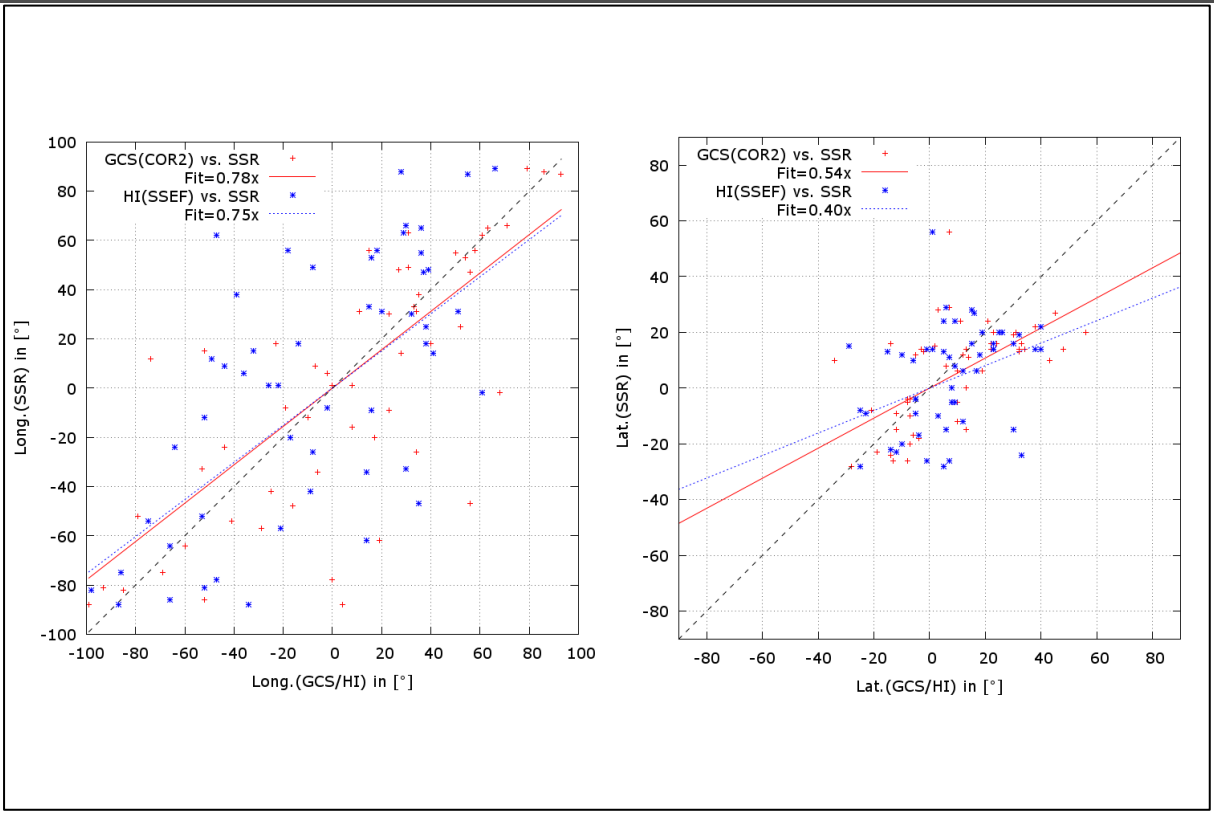

Figure 3.3.22 - Comparison of KINCAT (red) and HICAT (blue) SR locations with the associated X-ray flare positions (y-axes). Left diagram x-axes: HEEQ longitudes, right diagram: HEEQ latitudes. GCS-values are labelled in red, HI-values are labelled in blue. The dashed straight line represents 1:1 correspondences, the red and blue lines fits to the data.

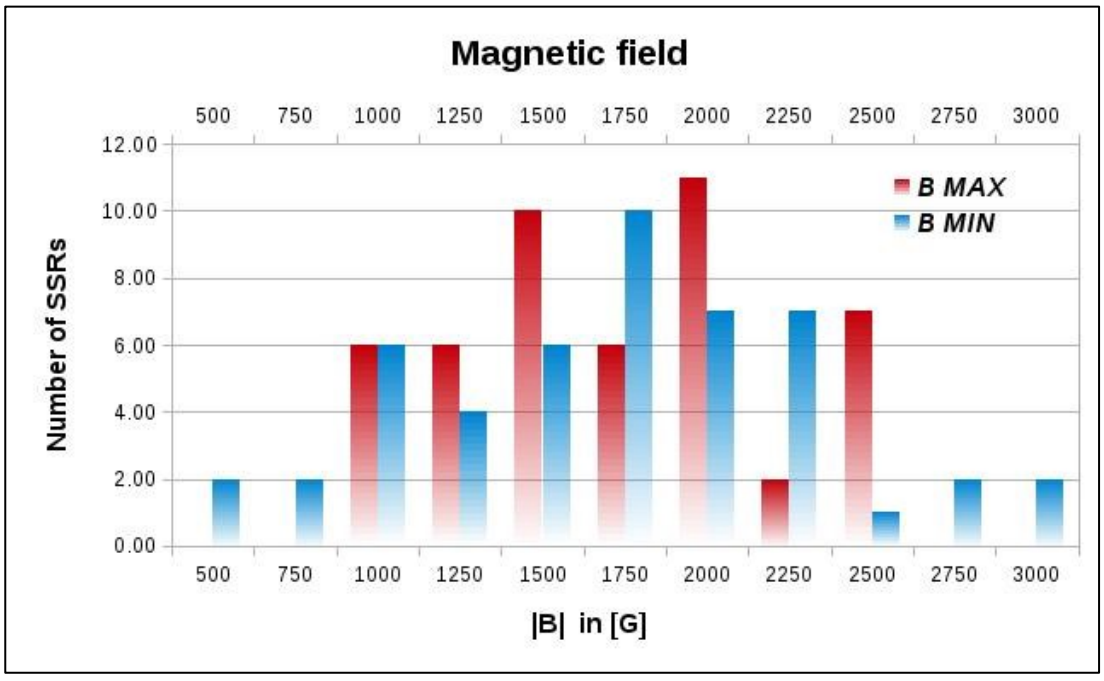

Figure 3.3.23 - Distribution of the maximum (red bars) and minimum (blue bars) magnetic field values of the KINCAT CME SRs.

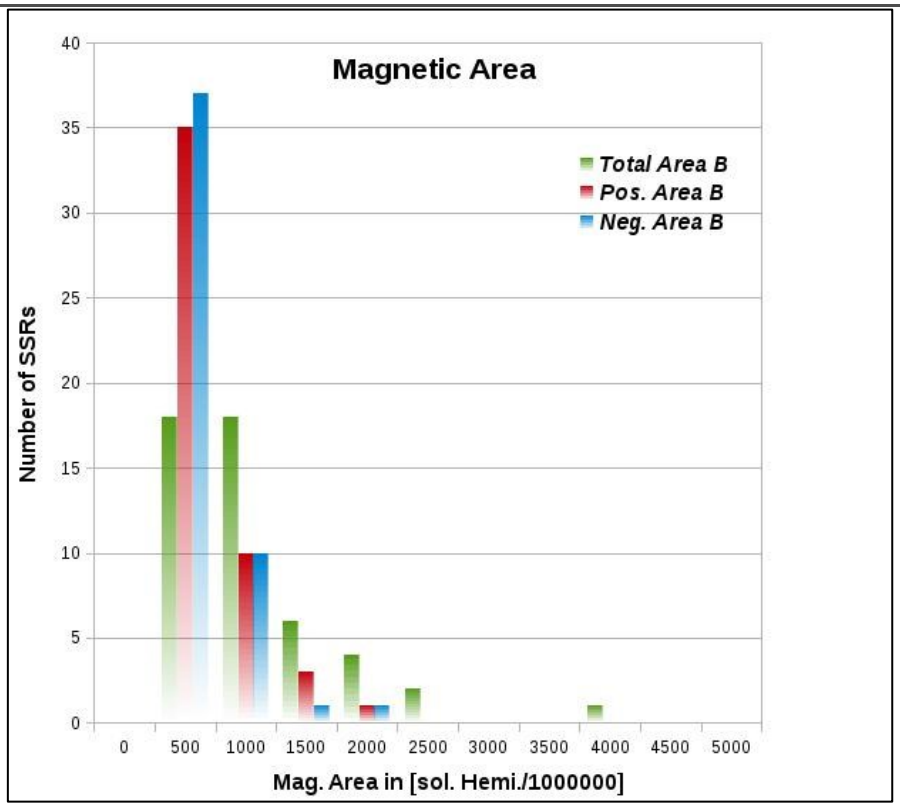

Figure 3.3.24 - Distribution of the magnetic area of the SRs. The green bars represent the total magnetic areas, the red bars the positive magnetic areas and the blue bars the negative magnetic areas.

The comparisons of the CME masses determined through GCS fitting with the SR parameters total flux, magnetic area, PSL length, bipolar separation, maximum and minimum magnetic field and Schrijver's R value are shown in Figure 3.3.25. All SR parameters are results of the SMART code. No clear dependences of these SR parameters with the CME masses derived from GCS-modelling are found. The total unsigned flux R is within ~15 Mm of strong-field, high-gradient polarity-separation lines, which are a characteristic appearance of magnetic fibrils carrying electrical currents as they emerge through the photosphere. No clear dependences of these SR parameters with the CME masses derived from GCS-modelling are found. Comparison of the CME speeds derived from dynamic GCS-fitting at 12 RS with the same SR parameters is shown in Figure 3.3.26. As in Figure 3.3.25, no clear dependencies between the speed and the SR parameters are found.

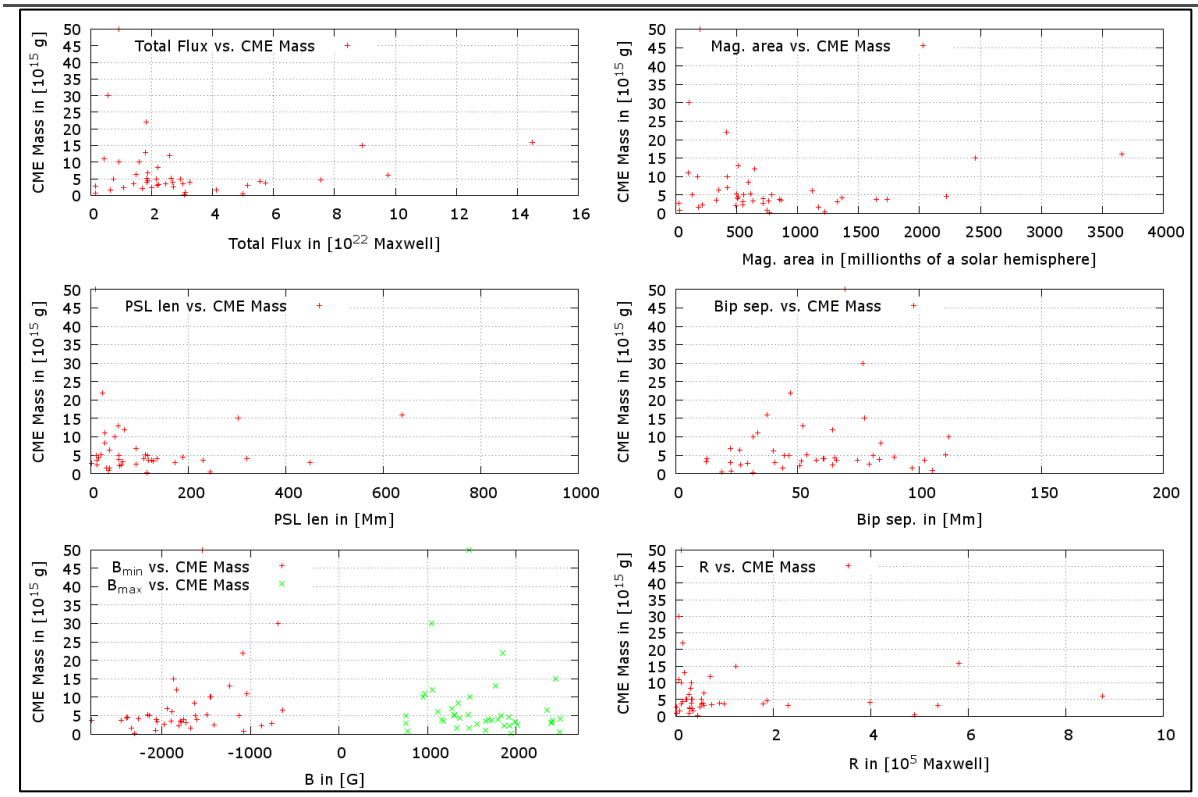

Figure 3.3.25 - Comparison of the CME masses determined through GCS fitting with the SR parameters: Total Flux, magnetic area, PSL length, Bipolar separation, maximum and minimum mag. field and Schrijver's R value. All SR parameters are results of the SMART code.

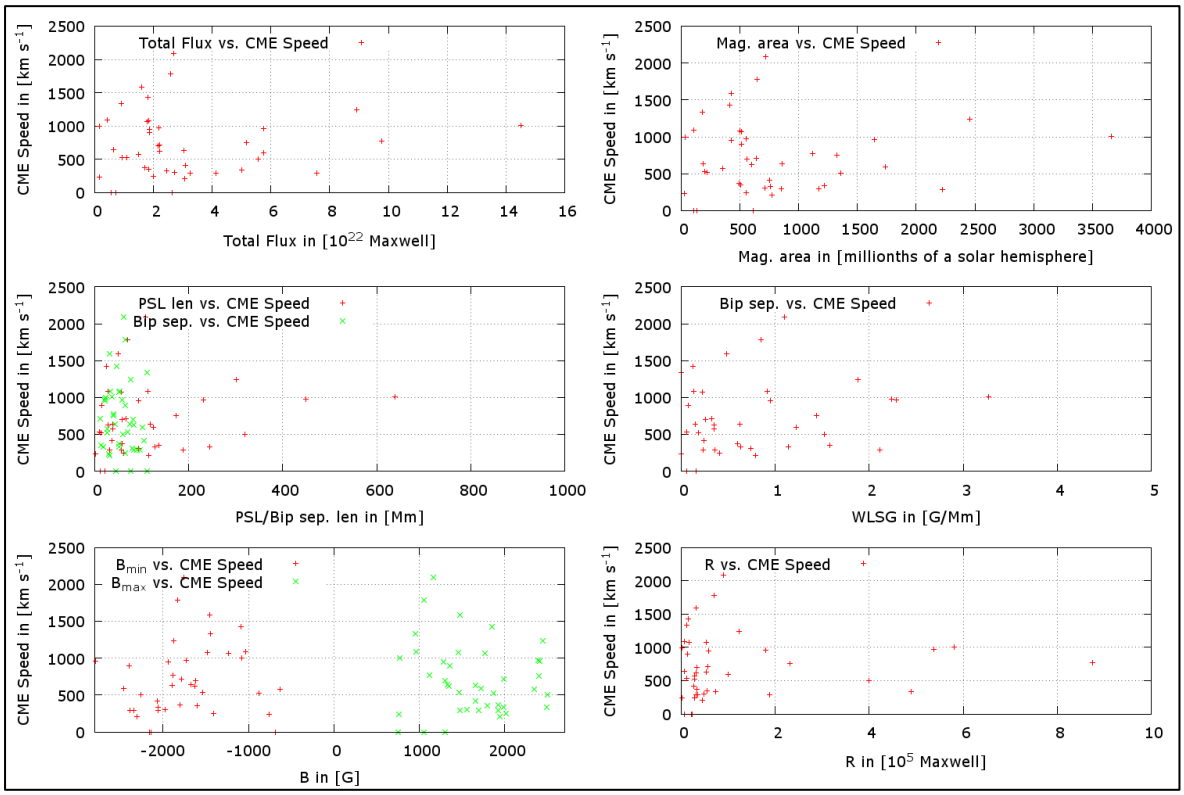

Figure 3.3.26 - Comparison of the CME speeds determined through GCS fitting at 12 R_S, with the SR parameters: Total Flux, mag. area, PSL length, Bip. seperation, maximum and minimum mag. field and Schrijver's R value. All SR parameters are results of the SMART code.

Comparison of the CME speeds derived from dynamic GCS-fitting at 12 R_S with the same SR parameters are shown in Figure 3.3.26. As in Figure 3.3.25, no clear dependencies between the speed and the SR parameters are found.

Finally, Figure 3.3.27 shows the comparison of the SMART PSL tilt angles and those derived from GCS-modelling. There are only a few high inclined CME flux ropes seen at 12 R_S whereas the PSL title angles of the SRs show a lack of low inclined, i.e. being in the range of -20°, i.e. S, to +20°, i.e. N, of the solar equator. This result is indicating that the flux ropes assumed to overly the photospheric SR may already be flattened in their inclinations and that further smoothing occurs until they had expanded to distances of about 10-15 R_S, the distance typical for fitting the full CME FR body in the COR2 FOV.

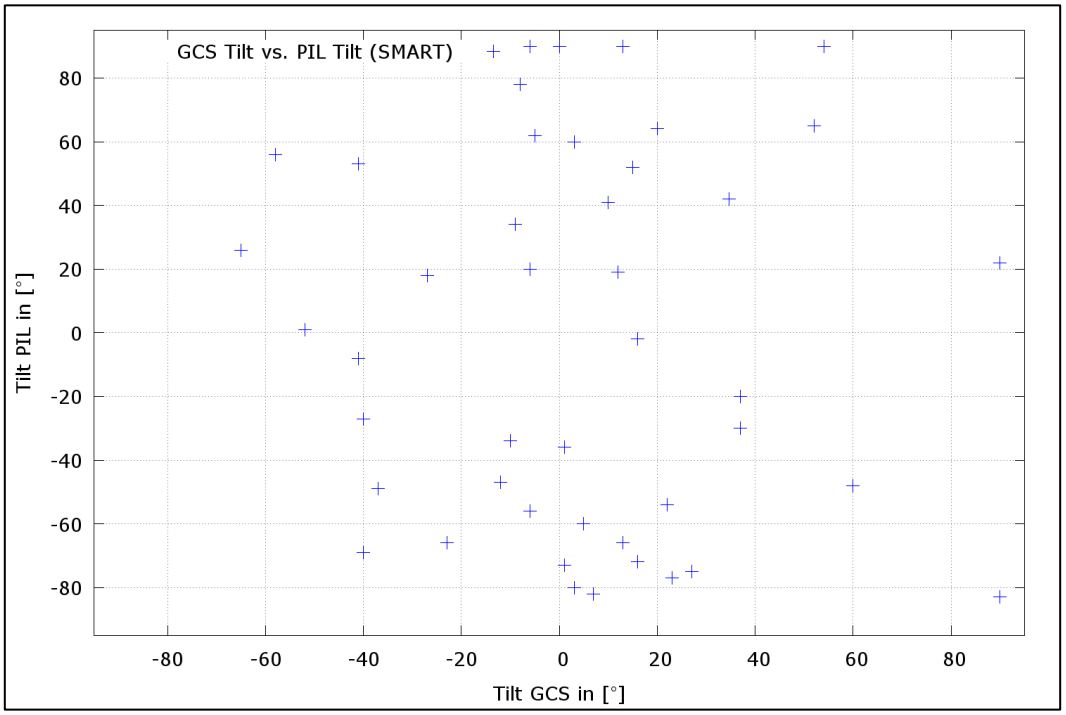

Figure 3.3.27 - Comparison of tilt angles determined with GCS fitting and SR tilt angles of the PSL (PIL) determined with SMART.

After comparing the SR parameters derived with the SMART code with CME speeds and masses derived from GCS-modelling in Figures 3.3.25 and 3.3.26, Figure 3.3.28 shows a comparison of these parameters with the GOES X-ray flare classes observed in the different events. A dependence of increasing CME mass, speed and thus of kinetic energy with the X-ray flare class is obvious.

The CME apex latitude as derived from GCS-modelling is projected onto the photospheric magnetic field diagram (Hathaway, https://solarscience.msfc.nasa.gov/images/magbfly.jpg) in Figure 3.3.28. CME occurrences show a close connection to the overall evolution of the photospheric emerging and decaying flux, as reported by Bosman et al. (2012).

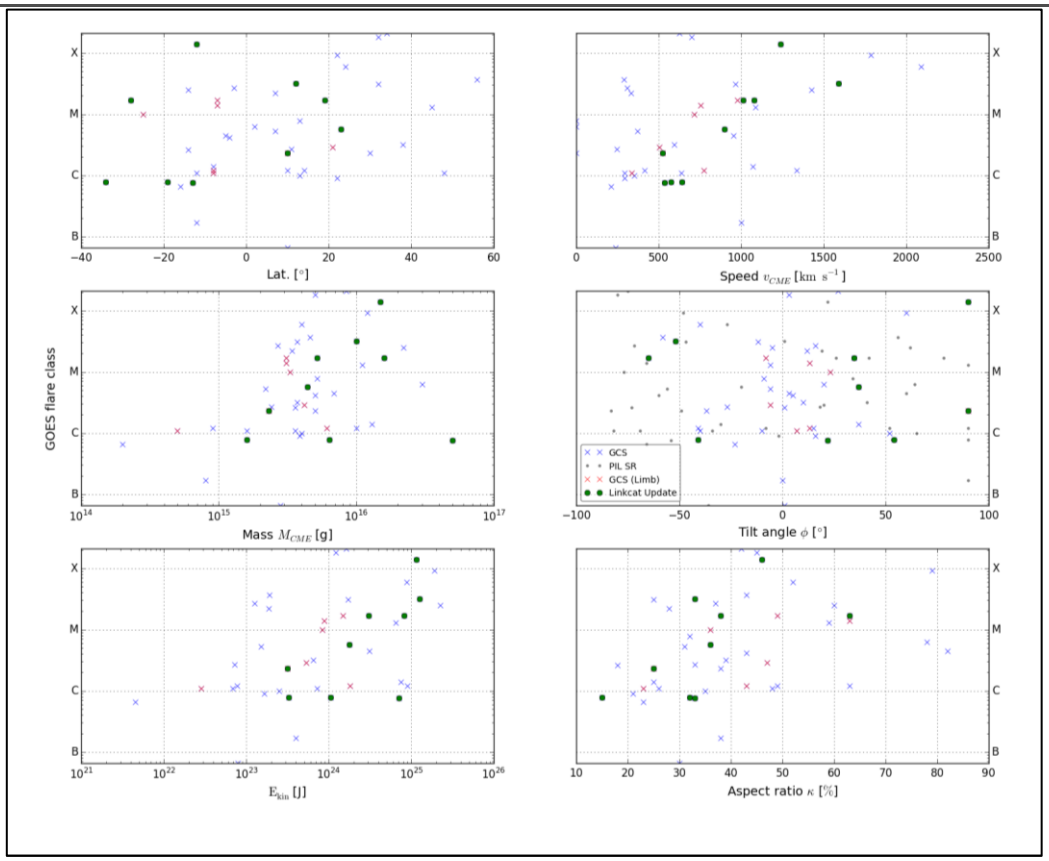

Figure 3.3.28 - Comparison of GOES flare-class and GCS model parameters.

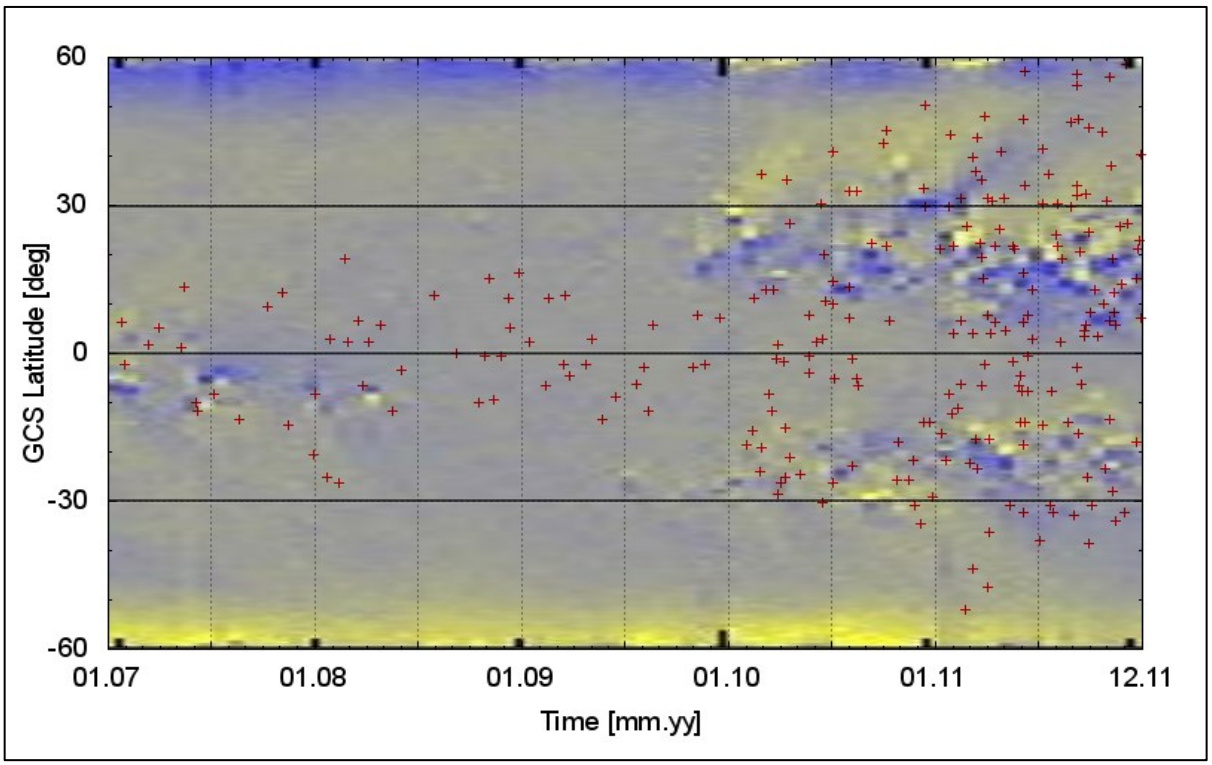

Figure 3.3.29 - The CME's apex latitude plotted vs. time with an overlay of a synoptic magnetogram from Hathaway/NASA /MSFC. Blue and yellow indicate the photo-spheric magnetic polarities. The intensity ranges from -10 G (blue) to +10 G (yellow). The events comprise the COR2 "Best-of-list".

WP3 CONCLUSIONS:

All of the activities and goals that were set out for this WP were achieved. The catalogues are on line and available to the public, and prepared in such a way as to be a valuable resource for the future of heliospheric research.

From the comparisons of the CME apex longitudinal and latitudinal positions in HEEQ coordinates and the speeds derived from CME modelling in the COR2 and HI FOVs, and from comparisons of the SR magnetic parameters derived by applying the SMART code to the joint HIGeoCAT, KINCAT events, the following conclusions can be drawn:

- We find a good correspondence between the speeds derived from geometrical modelling using both single-spacecraft models and stereoscopic techniques. This is true for the FP, SSE and HM models, however the correlation increases with half-width.
- We find that CME directions from each of the single-spacecraft and stereoscopic models agree less well. The discrepancy between each appears to have some dependence on spacecraft separation angle in some cases. This would suggest that the assumptions of CME geometry used by the models may be inaccurate.
- In general, we find a good correspondence in the determined HEEQ-latitudes for all comparisons, with the best one derived for the FPF-method. The agreement in latitude is not surprising because one can assume that the CME-apexes propagate outwards with almost constant direction angle, i.e. only small latitudinal deflections occur at distances beyond about 15 RS. Further on the latitudinal positions of the CME apexes can be determined relatively precise already with in-ecliptic single point observations.
- For some events, we find considerable deviations in the longitudinal directions, with no clear preference for one method. For the longitudinal positions, the POS ambiguities can be quite large depending on the spacecraft positions with respect to the CME 3D propagations in the different events.
- The best agreements for the COR2 and HI FOV speed comparisons are found for the FPF-method. The speeds derived in the HI FOV are slower for faster CMEs, which is in agreement with the common assumption of CME deceleration with increasing distance from the Sun, as can be explained by drag forces due to CME interactions with the ambient solar wind.
- All CMEs detected by STEREO/SECCHI/COR2 originated from photospheric regions with enhanced magnetic flux, including emerging and decaying ones.
- CMEs closely follow the photospheric magnetic flux evolution of the solar cycle.
- The typical peak magnetic field fluxes of the source regions were in the range 1.000-2.500 G, with areas of $5\text{-}10 \cdot 10^{-4}$ hemispheres.
- The statistical comparisons of source region magnetic fluxes with CME-parameters derived from GCS-modelling, such as mass, speed and angular width, did so far not show clear correlations.
- The flux ropes assumed to overlie the photospheric SR may already be flattened in their inclinations and that further smoothing occurs until they had expanded to distances of about 10-15 R_S, the distance typical for fitting the full CME FR body. in the COR2 FOV.
- Comparison of the CME speeds, masses and kinetic energies show a correlation with the X-ray flare class, i.e. increasing flaring implies the lift-off of faster and more massive CMEs.

Further studies are needed to clarify the connection between photospheric, low coronal and heliospheric processes.

WP3 HIGHLIGHTS:

- Augmentation of the STEREO/HI CME catalogue with the model results in KINCAT and HICAT, and supply those results as input for comparisons with coronal source regions and in-situ observations in the validation of WP4 in LOWCAT and LINKCAT.
- Update of the STEREO/COR2 CME COR2 database, initiated under the SOTERIA FP7 project, until the end of 2011 (including the application of forward modelling to the appropriate CMEs).
- Dynamic GCS-modelling of COR2 CMEs in KINCAT.
- Update of KINCAT based on comparisons with LINKCAT until end of 2013.
- Comparison of the results from the geometrical and forward modelling of HI CMEs with the modelling results for COR2
- Prototype of the use of inverse modelling to derive typical HI CME parameters (speed, size, mass), for photospheric and low coronal source regions typically associated with CMEs

WORK PACKAGE 4 (WP4):

Verifying the kinematic properties of STEREO/HI CMEs against in-situ CME observations and coronal sources

WP4 ACTIVITY TYPE: RTD

WP4 DURATION: MONTHS 10 – 36

WP4 LEAD BENEFITIARY: UNIGRAZ (2)

WP4 LEADER: Dr Christian Möstl

WP4 CONTRIBUTORS: UNIGRAZ (2), UPS (3), UGOE (4), ROB (5), IMPERIAL (6), UH (7)

WP4 OVERVIEW: The primary goal of WP4 was to provide researchers with a catalogue that links CMEs observed remotely in the heliosphere (HICAT and HIGeoCAT) and in the corona (KINCAT) with their in-situ counterpart observations. To this end, individual lists of CMEs and their solar, coronal and heliospheric parameters and in-situ data have been established, covering the timeframe from April 2007 to December 2016. **[Relevant catalogues: LINKCAT, ICMECAT, CORHITCAT]**

The in situ observing spacecraft used in this activity were MESSENGER, Venus Express (VEX), STEREO-Ahead and Behind and Wind, which were all operating almost continously as STEREO/HI was observing prior to solar conjunction in September 2014. To cover all 4 terrestrial planets, interplanetary CMEs observed by MAVEN at Mars have also been catalogued, but MAVEN started to orbit Mars just as STEREO went into solar conjunction so there is no overlap with STEREO/HI data for Mars.

WP4 included two main activities. First, we wanted to establish a list of CME events that can be traced back from in situ data to the corona in order to provide a basis for better understanding how CME in situ parameters, and in particular their magnetic field configurations, are produced during solar eruptions. This is the LINKCAT catalogue and this work was covered in tasks 4.1 and 4.2, and is summarized in deliverable 4.1. The results on magnetic field configurations (Palmerio *et al.* 2017) are presented in deliverable 4.2. We want to emphasize that this involves tracing a CME backward in time from the in situ spacecraft to their solar origins. Second, we wanted to assess how well the predictions with STEREO/HI work for the arrival time and speed of CMEs at the aforementioned in situ spacecraft. To this end, the ARRCAT from WP3 is compared to the WP4 ICMECAT. This is described in deliverable 4.2. Thus, in this case we follow CMEs forward in time, from their launch on the Sun to their planetary impacts, which is published in Möstl et al. (2017).

In a slightly different form to the preceding WPs, here, the initial deliverable (D4.1) was the establishment of an on-line catalogue of potentially associated solar source and in-situ phenomena. Since this task encompasses both task 4.1 and 4.2, we describe the work here. The heart of this work is LINKCAT, the catalogue that links the associated events of the coronal, heliospheric and in-situ catalogues; it is available through the HELCATS website under the PRODUCTS tab and WP4. Details about what it contains, how it was established and how it may be used are summarized here.

LINKCAT provides a baseline dataset for many possible investigations on the CME evolution from the Sun to the heliosphere. Why are we interested in a establishing the LINKCAT? In-situ and remote sensing observations have both their advantages and disadvantages. The biggest potential for new scientific discoveries and breakthroughs in understanding CME initiation and evolution for improving space weather forecasting emerges when remote-sensing and in-situ observations are combined. LINKCAT provides a unique database of CME observations from the low corona all the way to the in-situ detection. The global view of a CME in remote-sensing images is insufficient to understand its geomagnetic effects: the CME magnetic field cannot be measured with any current remote-sensing techniques, and therefore, we do not have knowledge of the CME

flux rope structure before it is sampled directly. In situ CME detections have the great advantage of showing us the local CME magnetic field, which is often a structure that is physically understood as a magnetic flux rope (MFR). However, this observation is affected by the trajectory of the spacecraft through the MFR, and in many cases clear MFR signatures are not identified. Single spacecraft in-situ observations lack the global context and to get information on where the CME is propagating and which part of it is observed by the spacecraft one has to use different MFR modeling techniques. CME MFRs may lead to prolonged and strong southward magnetic field (Bz < 0) intervals at Earth and they drive the strongest geomagnetic storms (e.g. Zhang et al. 2007), thus understanding the origin and evolution of CME MFRs is one of the central unsolved problems in space weather forecasting.

The linkage between remote and in situ observations that we provide in LINKCAT can be used for better understanding (1) how CMEs evolve in the heliosphere, depending on their interaction with the ambient wind structure which can be revealed by multipoint measurements (e.g. Rollett *et al.* 2014), and (2) how to predict the orientation of CME flux ropes based on solar images and modeling of the solar global magnetic field (e.g. Bothmer and Schwenn, 1998; Isavnin *et al.* 2014; Marubashi *et al*. 2015). (3) Our list may provide a deeper knowledge of the physical nature of CME flux ropes, e.g. how their field lines are twisted, based on observations and modeling of twist in MFRs in-situ and in comparison to twist signatures in their solar sources (e.g. Hu *et al.* 2014). (4) LINKCAT could also be used to shed light on the way that the orientation of a CME flux rope might change between the Sun and the Earth, as there is some evidence for ongoing rotations in the interplanetary medium (e.g. Isavnin *et al.* 2014; Good *et al*. 2015). However, possible applications are certainly not limited to the aforementioned points.

It needs to be emphasized that the LINKCAT list provides potential associations between solar and heliospheric observations. This is the first effort in establishing such a list by a systematic and rigorous search for these linkages using heliospheric imaging. The list is produced both automatically (for the in-situ–HI connection) and manually (for the HI-solar source connection). It is based on assumptions for time and space windows that we define for a fair association of the imaged CMEs with the in situ observations. We have largely ruled out interacting CME-CME events, but we need to explicitly state that LINKCAT limited by the assumptions of the SSEF30 technique, which are (1) constant speed, (2) constant direction and (3) constant CME angular width. In particular (1) and (3) are certainly only rough approximations of the nature of CMEs. Thus our LINKCAT may be challenged with future updates of SSEF30 (e.g. ElEvoHI, Rollett *et al.* 2016), as using a different model for HI could change the entries in the LINKCAT list. SSEF30 is the Self Similar Expansion Fit, with 30 degree angular half-width (see Davies *et al.,* 2012). LINKCAT should thus be understood as a first take on the problem of how to link solar and in-situ observations of CMEs with heliospheric imaging. However, the methodology we have developed will definitely aid in establishing connections for combinations of data from future missions such as Solar Orbiter, Solar Probe Plus, BepiColombo, DSCOVR and STEREO in the next decade.

Concerning in-situ observations, we also want to make clear that we have taken the ICME (by definition the full length of the disturbed solar wind interval) and magnetic obstacle (MO) start and end times from various published catalogues (e.g. Winslow et al. 2015, Good & Forsyth 2016), and not evaluated them ourselves. The term ICME is used here to denote the detection of a CME in interplanetary space using in-situ observations. It is a well-known issue in the field that the definition of ICME boundary times is often ambiguous and they may vary from one catalogue to another. Using the boundary times given in the cataloguess we have derived basic ICME parameters, like the mean total field and minimum Bz component, from the respective in-situ data (in 1-minute time resolution) that the catalogs were based upon. Different definitions on how ICME solar wind intervals were selected can be found in the studies containing the individual ICME lists, but are not considered further here for simplicity of the analysis.

The LINKCAT list contains 39 parameters on the solar source, HI CME parameters (speeds, direction), predicted arrival times and speeds, in-situ magnetic field values, and flux rope orientations (with MVA and GSR, if possible).

The LINKCAT files include the following:

- HELCATS_LINKCAT_v10.txt (catalogue as ASCII)
- HELCATS_LINKCAT_v10.sav (catalogue as IDL .sav file)

- HELCATS_LINKCAT_v10_header.txt (header file, with definition of the parameters)

It is available through the HELCATS webpage (-> Products -> WP4) and on figshare: **https://doi.org/10.6084/m9.figshare.4588330**. The doi: 10.6084/m9.figshare.4588330 can be cited in peer reviewed papers.

In python, .sav files can be read with the scipy package, e.g.
cat=scipy.io.readsav('HELCATS_LINKCAT_v10.sav', verbose='true').

In IDL, using the .sav file and to see the list of variables, open any IDL terminal, make sure that the .sav file is in the current directory and write:

IDL >> restore, 'HELCATS_LINKCAT_v10.sav', /verbose

To access the catalogue:

IDL>> help, linkcat, /st

To see the description of each parameter:

IDL>> print, comments

The first step in the procedure to establish LINKCAT was to create the individual catalogue of CMEs observed in HI including the SSEF30 modeling results (in WP3, called HIGeoCat), then estimate the spacecraft and planetary impacts from this list (arrival catalogue or ARRCAT), and match this list to in situ CME detections (ICMECAT). For ICMECAT, the ICME events are taken from individual spacecraft-specific catalogues and the ICME parameters (e.g. mean total magnetic field strength) were derived by from the in-situ magnetic field and plasma data. Note that for VEX and MESSENGER the ICME detection is based solely on magnetic field data. The ARRCAT and ICMECAT have been matched by a procedure detailed below resulting in the LINKCAT list. We have essentially traced the observation of the CME in situ back in time to HI and to the identified solar source region.

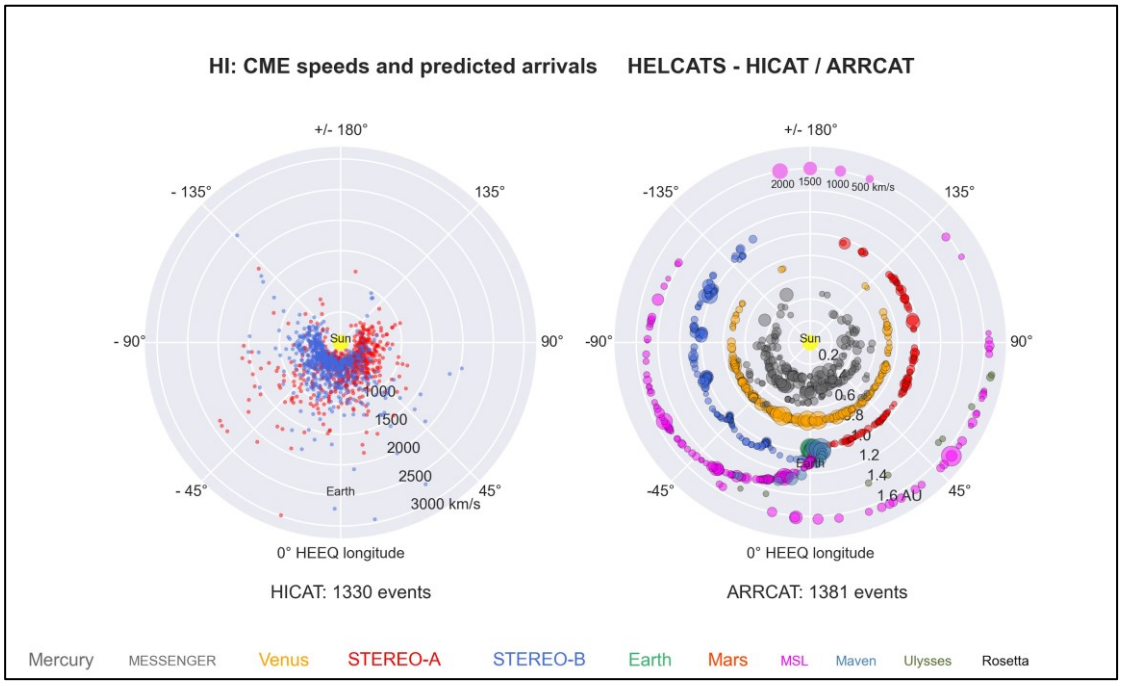

Fig. 3.4.1 - Left: Overview of HIGeoCATv3 CME speeds and directions (HEEQ longitude). Right: In the arrival catalogue (ARRCAT v5), all these CMEs are checked for their arrivals at various planets and spacecraft as indicated by the color code at the bottom, based on the shape model of a self-similar expanding circle with 30° half-width (SSEF30). Each dot marks a predicted arrival at MESSENGER, VEX, STEREO-A/B, Earth_L1, MAVEN, MSL and Ulysses. For MSL and MAVEN, impacts during the cruise to Mars are nicely highlighted. The size of the dot indicates the predicted impact speed, which is overestimated due to the constant speed assumption of the SSEF30 method.

Concerning the link from HI to in situ observations, a CME is selected for an entry into LINKCAT if there is a correlation between a predicted arrival with HI with the SSEF30 technique at an in-situ spacecraft, and a reported in-situ observation at that spacecraft, based on magnetic field (all in-situ spacecraft) and additional plasma data (available for STEREO-A/B and Wind). We have used SSEF30 because it contains a clearly limited shape of the CME in the solar equatorial plane of 60° total width. An assessment of the CME arrival time and speed for the FPF (point-like shape) or HMF techniques (180° total width) is not possible without introducing further additional assumptions which result in non-self-consistent calculations (see section 2.2 in Möstl et al. 2011).

We start with the in-situ list of ICME events (ICMECAT). Each entry in ICMECAT is checked for a possible predicted arrival of a CME observed with HI that was modeled with SSEF30 (see arrival catalogue or ARRCAT below). This means that the space window for this association is defined by the 60° full width of the CME modeled with SSEF30 - a hit along that 60° wide circular front is considered a possible impact, and if that SSEF30 circle does not hit, the event is not considered further (constraint 1). Please see Figure 3.4.1 for an illustration. We also consider longitude only for this selection, and not latitude, as most CMEs that could be traced with HI have a part close to the solar equatorial plane (along PAs of 90° and 270°).

Figure 3.4.2 also shows the constraints with using time windows: if an in situ CME has a HI-predicted impact in the time window of +/- 24 hours around the start time of the ICME (defined by the shock arrival or density enhancement), it is further considered for LINKCAT (constraint 2). However, to make the HI to in-situ association unique, there must be only 1 predicted CME within that +/- 24 hour time window (constraint 3).

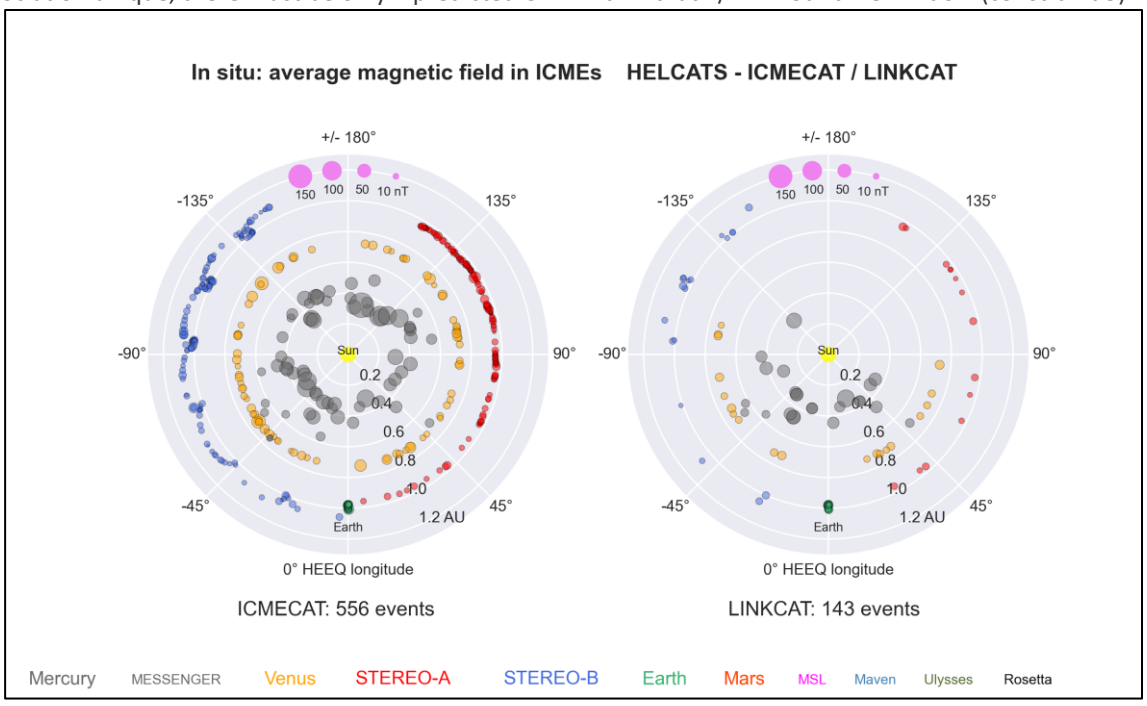

Fig. 3.4.2 - Left: Overview of in-situ ICME detections, showing the longitude and radial distance when detected, as catalogued in ICMECAT (Apr 2007 - Dec 2013). The size of the circle indicates the mean magnetic field strength during the magnetic obstacle of the in situ CME detection. Right: Shows the position of the events in HEEQ that make up the linked catalogue or LINKCAT, which is a correlation of ARRCAT with ICMECAT for events that can be connected concerning the predicted CME impacts and the actual in situ detections. LINKCAT contains events at MESSENGER, VEX, STEREO-A, STEREO-B, Wind.

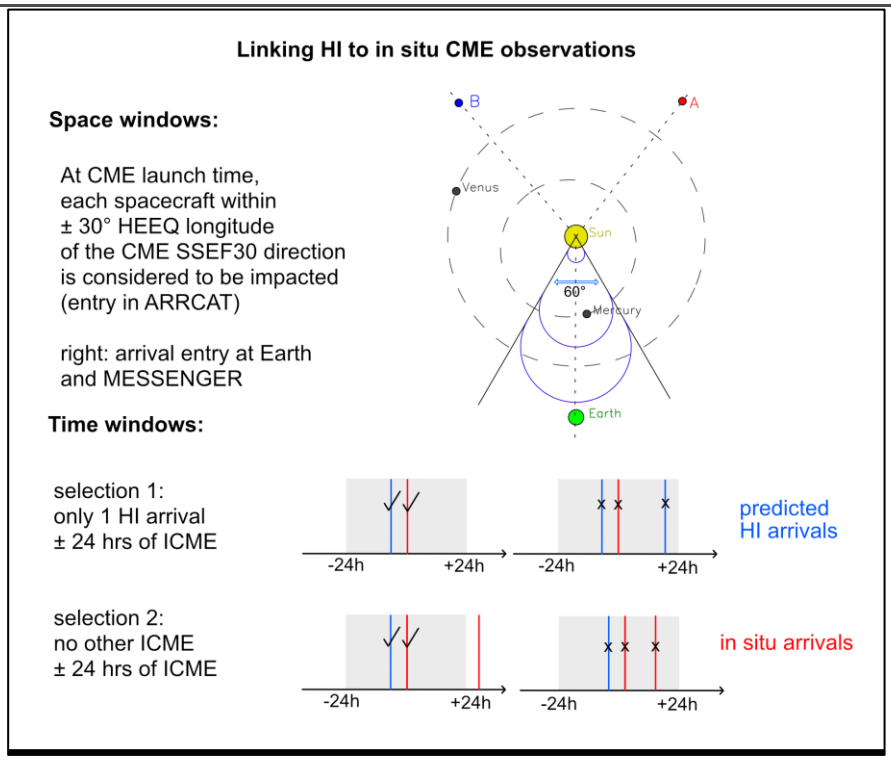

Fig. 3.4.3 - An illustration of the algorithm to establish the connection from HI to in situ data. The SSEF30 circle must impact a spacecraft, and there must not be another predicted CME arrival time nor a different ICME_START_TIME within +/-24 hours of the in situ CME under question.

Further, the association must be unique the other way around, so that one HI CME cannot be connected to 2 in situ ICMEs (constraint 4). The latter happens when 2 ICMEs are detected and catalogued within +/- 24 hours of the given ICME_START_TIME under question.

Only if all 4 constraints are fulfilled, an entry into LINKCAT is produced. However, we cannot rule out some possible misidentifications. It may happen that another CME is just outside the +/- 24 hour window, or that the edge of another CME passes the spacecraft a few degrees further east or west. Thus it must be kept in mind that our algorithm for linking HI modeling results (HICAT) to the in situ ICME detections (ICMECAT) may be improved in future versions of the catalogue for more stringent space and time windows. The current process results in 143 connections, with 118 unique CMEs. The in situ locations of those events can be seen in Figure 3.4.4 (right panel). There are 8 multipoint in situ events, and 17 possible stereoscopic events.

Then, for the 118 CME events in LINKCAT the coronal sources are searched for and established (by UGOE). For those 118 events, the GS reconstruction results were added, if possible, for STEREO and Wind (by UH), because plasma and magnetic field observations are needed for this technique.

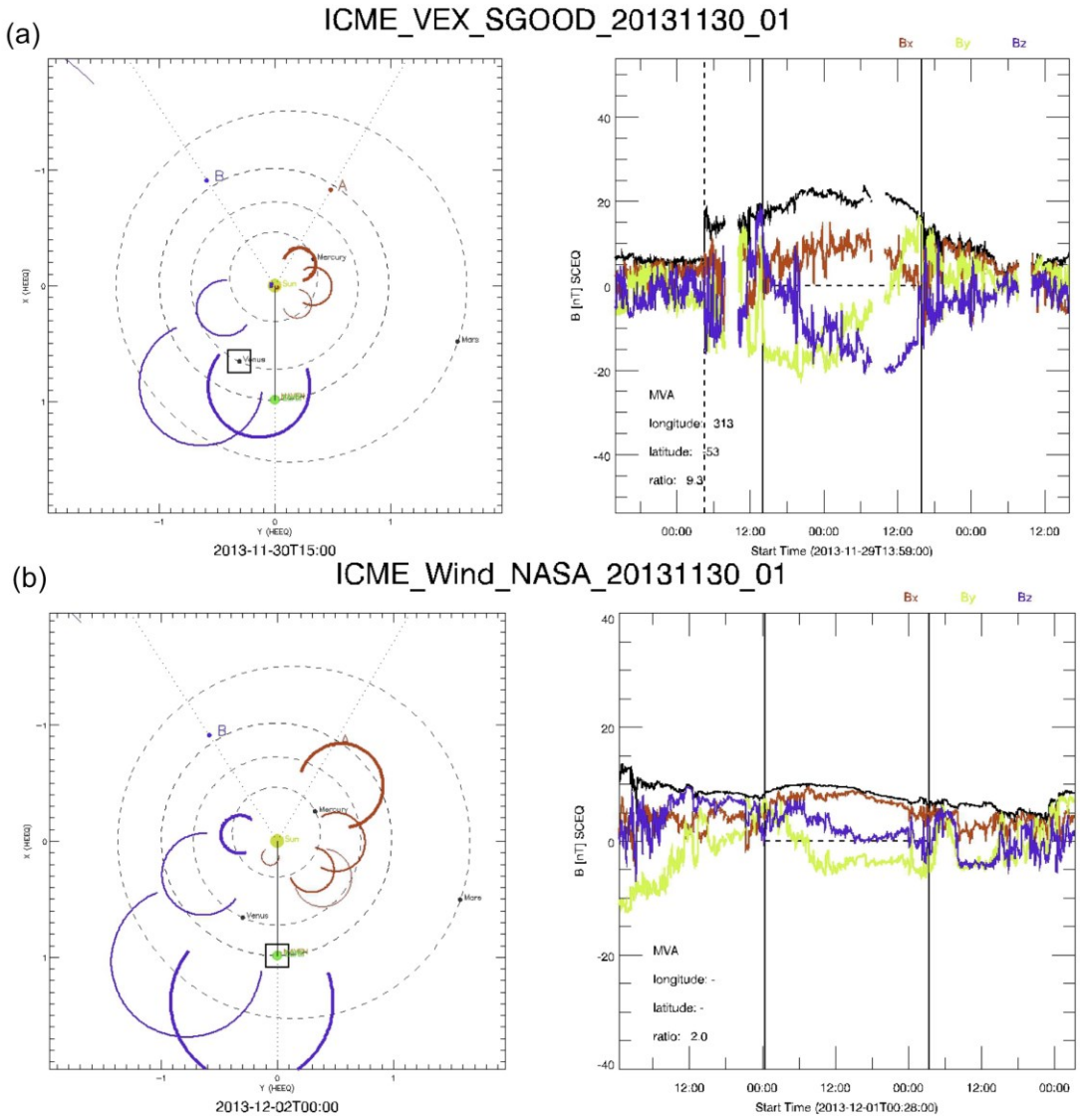

Fig. 3.4.4 - Sample of the available in situ data plots, showing a multipoint in situ CME detection contained in LINKCAT. (a) Left panel: the solar system in the solar equatorial plane (HEEQ coordinates, Earth at fixed position). The in situ observing spacecraft is marked with a square. Right: Magnetic field components and total field at VEX, with vertical lines delimiting the magnetic obstacle (MO_START_TIME to MO_END_TIME), and the dashed line showing the shock arrival. (b) Similar for Wind, which likely observed the same ICME at 1 AU. The event id in ICMECAT is given on top of each panel.

WP4 TASK 4.1: Comparing to coronal sources (TASK LEAD: UGOE)

In order to identify the corresponding solar source regions (SSRs) of the 143 ICME events of the LINKCAT ICME catalogue, white-light and EUV observations from the LASCO and EIT instruments on SOHO, the SECCHI/EUVI and COR2 instruments on STEREO, the AIA and HMI instruments on SDO, and the SWAP instrument from PROBA-2 were investigated. The SSRs of the backtracked events were commonly associated with flares and filament eruptions. The start-, peak- and end-times of the flares, their locations and classes were taken from the “GOES Soft X-ray Flare List”. For detailed study of the physical properties of the investigated CME source regions, information about the underlying photospheric fields derived from solar magnetograms are needed. This requirement reduced the number of SSR events to 83 cases for which the SSR and associated activity parameters (e.g., position, flare time and class) have been included for further analyses in WP3 and WP4.

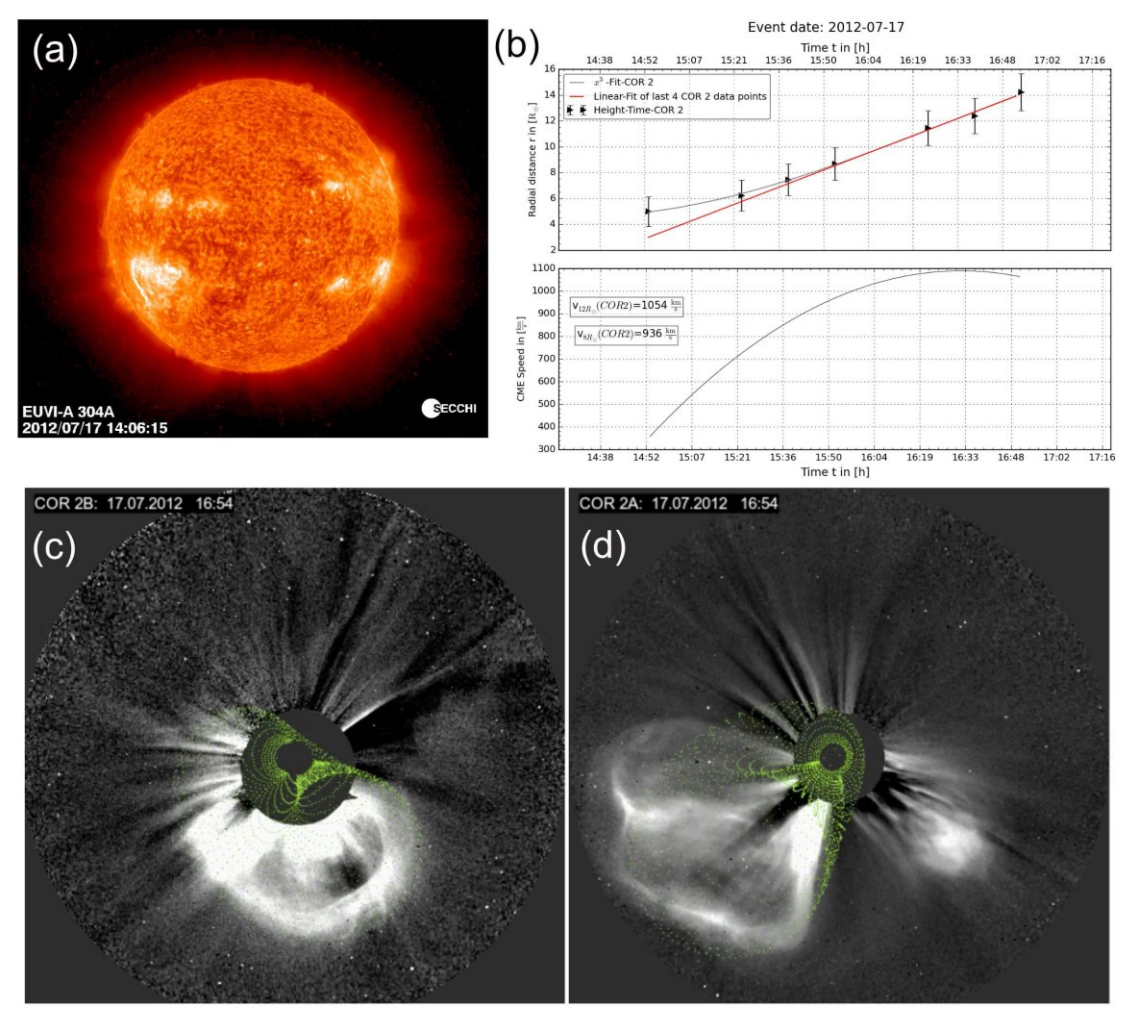

Fig. 3.4.5 - Solar source example. (a) STEREO/SECCHI/EUVI/A 30.4 nm image showing the flaring region in the Sun's southeast-hemisphere on 2012 July 17 1406 UT. (b) Height-time profile of the CME-apex observed by the two STEREO-A/B SECCHI/COR2 telescopes on 2012 July 17 based on GCS modelling. Note that, different from the KINCAT database, here a higher order fit is shown together with the CME's speed evolution shown in the lower panel. The linear fit shown in red in the upper panel yields a later CME onset time in agreement with HI SSEF30 back extrapolations. (c) CME observed by the STEREO-Behind COR2 telescope on 2012 July 17 16:54 UT. The green grid represents the GCS-modelled flux rope as provided through the KINCAT database at http://www.affectsfp7.eu/helcats-database/database.php as event 112. (d) Same for STEREO-Ahead/COR2.

Solar onset times were derived from back-tracking CMEs in SOHO LASCO C2/C3 and STEREO/COR2 images using the STEREO synoptic movies at http://secchi.nrl.navy.mil/sccmovies/ and the SOHO CME CDAW catalogue at http://cdaw.gsfc.nasa.gov/CME_list/. Identifications of low coronal activity features (e.g., filaments, post-eruptive arcades) were established using EUV observations from STEREO/SECCHI/EUVI, SOHO/EIT, SDO/AIA and PROBA-2/SWAP. X-ray flares were identified from the NOAA-SWPC GOES satellite data and by using the HEC database: http://hec.heliovo.eu/hec/hec_gui.php . A sample CME event traced back to the solar source region is shown in Figure 3.4.5.

Details of the catalogue activity are described above and, to keep a logical structure to the reporting of the relevant analyses, much of the discussion is covered under task 4.3, below.

WP4 TASK 4.2: Comparing to in-situ measurements (TASK LEAD: UH, CONTRIBUTORS: UNIGRAZ, UPS, UGOE, IMPERIAL)

Again, much of the discussion of the cataloguing process, relevant to the in-situ measurements is described

above, and, to aid the flow of the discussion, much of the relevant analyses performed under the auspices of task 4.2 are covered under the description in task 4.3, below. However, beyond the in-situ measurement discussion reported above, we note that a Grad-Shafranov (GS) reconstruction was conducted for all events from the LINKCAT list measured at 1 AU, i.e., from Wind and STEREO A/B spacecraft, for 88 events in total. The GS approach and the procedure carried out is described by Isavnin *et al.* (2011). For each event the following parameters were obtained: start and end time for the unperturbed part of a flux rope, local orientation of the invariant axis of the flux rope in HEEQ and SCEQ coordinate systems, and reconstructed magnetic field map (see example in Figure 3.4.6) of the cross-section of the flux rope. The plots of the magnetic field maps, residual maps and transverse pressure profiles are also provided. Some of the analyzed events were found to contain multiple flux ropes. Due to the nature of GS reconstruction its successful application depends on properties of each particular event and geometry of spacecraft-ICME encounter. Thus, for the 88 analyzed events GS reconstruction was applied successfully to 63, i.e., a 71.5% success rate. All the parameters of reconstructions and relevant plots are included in the LINKCAT database.

We have ensured the quality of the published parameters and linkages by performing independent checks of our derived ICME parameters against published catalogues and single event studies, and checked the consistency of the ARRCAT, ICMECAT and LINKCAT lists with independent calculations of the planetary CME arrivals. Also the animations we have produced (see below) have shown to be very useful for double checking the correctness of the planetary arrivals, the validity of the in situ data and ICME detection times.

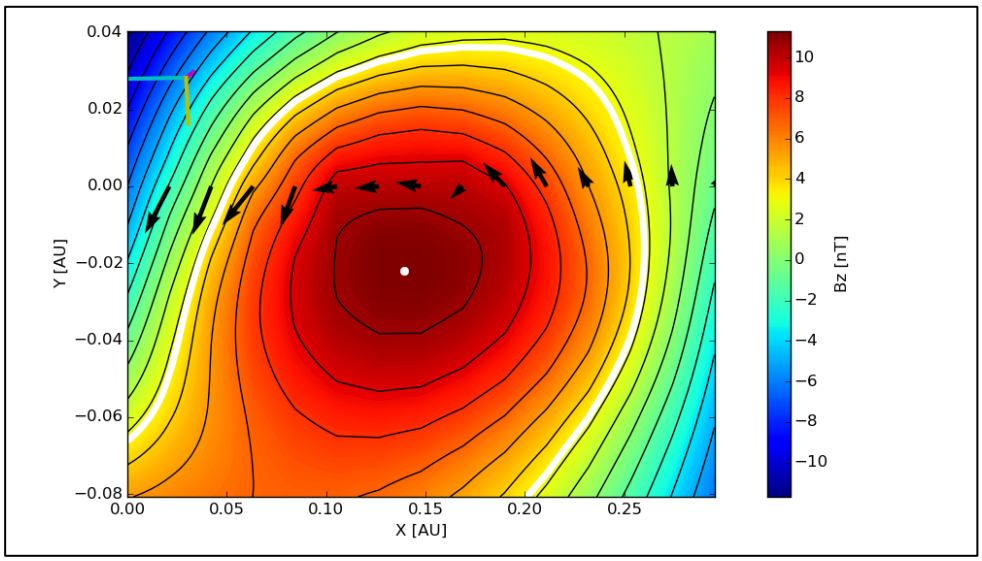

Fig. 3.4.6 - Magnetic field map reconstructed using the GS technique for ICME from the LINKCAT catalogue registered by the STEREO-B spacecraft on December 23, 2013. Solid contours show equipotential levels, magnetic field is color-coded. The invariant axis of the flux rope is denoted with white dot, while the boundary of the unperturbed part of the flux rope is shown in white. The projected trajectory of STEREO-B spacecraft through the ICME goes from left to right and projected measurements of the magnetic field are depicted with black arrows. In the top left corner of the image the projection of RTN coordinates are shown (R-cyan, T-magenta, N-yellow).

Description of Catalogues Used

HICAT (RAL, UNIGRAZ): Located on the HELCATS website at the PRODUCTS tab under WP3, the kinematic HI catalogue, forms the basis of the WP4 investigation. Figure 3.4.1 (above) shows a polar plot of the speeds and directions (heliospheric longitude) of the CMEs in HICAT, in the HEEQ system where Earth is always at a fixed position. For quality control and visualization, UNIGRAZ (C. Möstl, P. Boakes) has made a visualization of HICAT (see https://www.youtube.com/watch?v=MBYQ3wjHZQQ&t=569s).

A screenshot is shown as Figure 3.4.7, below. The animation shows the SSEF30 circles propagating away from the Sun, for the inner heliosphere up to Mars orbit, for all CMEs observed by HI. For each CME, kinematics have been established by calculating $R(t) = V_{sse}\ t$, with R(t) the distance to Sun-center, V_{sse} the speed from SSEF30 and t the time, starting with the SSE launch time. These kinematics are then interpolated to the movie frames

times, at 00, 06, 12, 18 UT for each day. All apex positions for each CME are then sorted by time. When plotting the movie, for each movie frame, it is checked how many CMEs are currently active at that particular moment in time in the spatial domain covering approximately 0 to 2.1 AU. The SSE circle is then plotted for +/- 110 degrees around the apex position, resulting in a circular arc-like CME front. This is repeated for each currently active CME. The movie has a 6 hour resolution, a size of 250 MB, and covers 2007-2017. The animation is also on the HELCATS gallery webpage (under the OUTREACH tab).

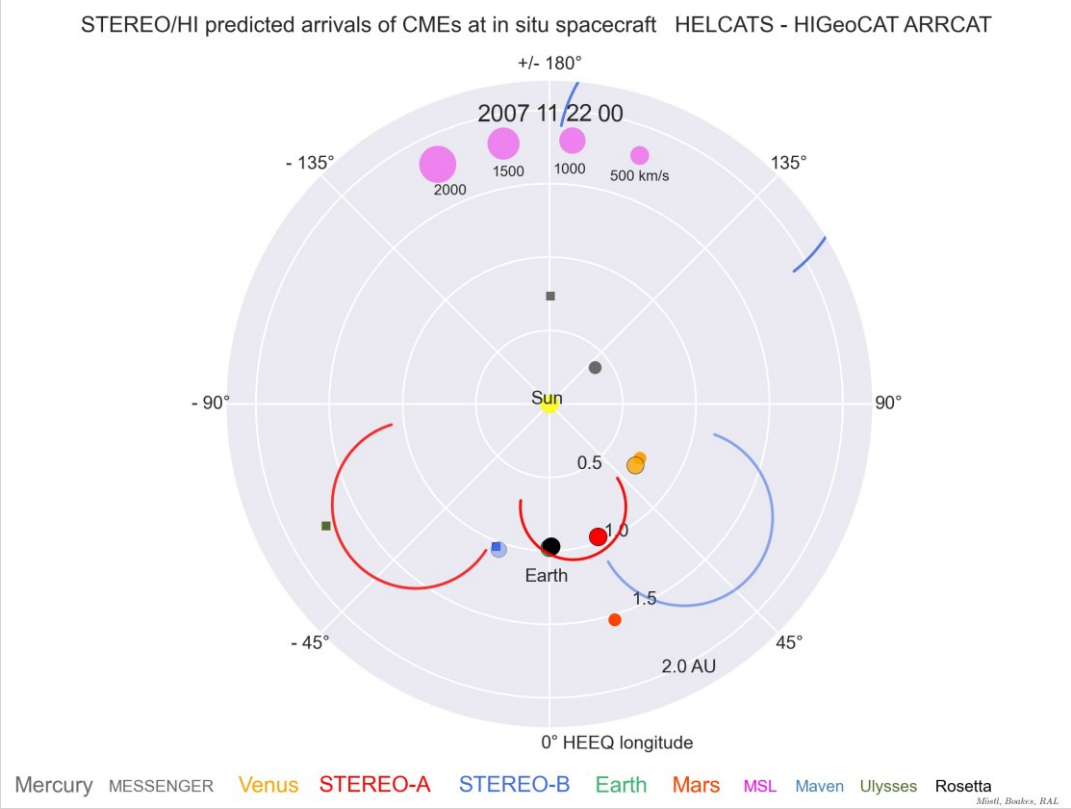

Fig. 3.4.7 - Screenshot of animation 1 visualization movie of the HICAT and ARRCAT catalogues, covering 2007-2017, at a 6 hour time resolution. It shows planets (filled circles) and spacecraft (filled squares) projected in the solar equatorial plane, in colours as indicated at the bottom. Large red (blue) circles are CMEs modeled with SSEF30 and moving at constant propagation speed, with constant direction and constant angular width of 60° HEEQ longitude, modeled after HI observations by STEREO-Ahead (STEREO-Behind). At an ARRCAT impact time, a circle with the color of the spacecraft and size related to the impact speed at the target according to the legend on the upper part of the figure is produced. This circle fades with time so an impact is better visible.

We include, below, some more detailed information about Animation 1:

1. The CME latitude in HEEQ varies from event to event. This is because in the HI images every event is measured at a certain position angle at which the CME can be tracked well. For this reason darker lines for plotting the CME front are used where the central position angle of a given CME (average between north and south extension in PA) is close to the solar equator, and lighter lines where it is further away (up to 40° in PA). Also, each CME that sweeps over a planet or spacecraft position produces a hit, regardless of its central latitude.

2. Every circle in the movie has a full width of 60°, which was chosen to be consistent with the average CME width in SOHO coronagraph observations (Yashiro et al. 2004).

3. The HI prediction with the SSEF30 model has the problem of assuming constant speed, so the predicted speeds are definitely too high, because CMEs largely decelerate in reality.

4. We know from previous studies (e.g. Möstl et al. 2014) that the CME direction from SSEF30 should also not be taken too literally - sometimes one can see two circles (one red and one blue) which are obviously the same

CME seen from STEREO A and B, but the directions differ easily on the order of 30°, although they describe the same CME.

5. The position where the CME impacts a planet or spacecraft is shown as a small circle which fades with time. The size of this circle depends on the predicted arrival speed. At Mars, Venus and Mercury, this position is a few degrees away from the planet position at the time of the hit. For STEREO and Earth, this problem does not occur because in HEEQ, their position moves very little (STEREO) or not at all (Earth) in this coordinate system. The reason is that the position of the planet and spacecraft for assessing the impact time, speed and hit or miss is taken at the SSE launch time. This is a problem inherent to the current method of arrival time calculation, and may be fixed in future updates.

ARRCAT (UNIGRAZ): This is the ARRival CATalogue for all CMEs contained in HICAT. For the LINKCAT, we have used the internal version ARRCAT. We have applied the method from Möstl & Davies (2013) for calculating speeds and arrival times of the CMEs modelled with SSEF30 to all CMEs in HICAT. If the SSEF30 circle hits a spacecraft or planet, an entry in ARRCAT is produced. ARRCAT contains impacts at Earth/L1, STEREO-A, STEREO-B, Venus, MESSENGER, Mars, Saturn, Ulysses, Mars Science Laboratory (MSL), MAVEN, and Rosetta. The position of Venus Express is assumed equal to the location of Venus. Arrivals at Ulysses are calculated only around its last ecliptic pass in August 2007. For Rosetta, no arrivals are calculated during its deep space hibernation from 2011 June 8 to 2014 January 20. For MESSENGER, MSL and MAVEN ARRCAT covers both the cruise and orbit phases of those missions. ARRCAT contains a time range similar to HICATv3. For the 1330 CME events in HICAT, we find 1959 possible impacts at the aforementioned targets. In Figure 3.4.1 (right panel), we have omitted Mars, Rosetta and Saturn, showing 1381 ARRCAT events at the other targets, thus demonstrating an almost 360° coverage of heliospheric CME arrivals with respect to Earth. We made sure that the calculations are correct by assessing the arrivals in the ARRCAT list with the Animation 1.

DATACAT (UH, UNIGRAZ): This is the catalogue of all the in situ magnetic field and plasma data, downloaded from various online sources at the respective sites of the missions. Animation 2 at https://www.youtube.com/watch?v=Jr4XRzGCaaQ&t=346s (Figure 3.4.8 – see also HELCATS outreach gallery) provides a convenient overview of the magnetic field components and total field for the full duration of the data we study in HELCATS, with an almost complete coverage of the data from the missions that we study.

We have produced IDL .sav and python pickle .p files for STEREO-A/B (plasma and magnetic field), Wind (plasma/magnetic field), VEX (magnetic field only) and MESSENGER (magnetic field only). For LINKCAT v1, the data from Apr 2007 to Dec 2015 were used. Each data file contains a single structure covering the full time range. The files are available in HEEQ and SCEQ coordinates. The SCEQ (SpaceCraft Equatorial Coordinates) system is defined by: Z is the solar rotation axis, X points from the Sun to the spacecraft, at the intersection of the solar equator and solar central meridian as seen from the spacecraft, and Y completes the right handed triad and points to solar west. Compared to HEEQ, this system is centered on the respective in situ spacecraft, with an orientation that is close to RTN coordinates. The solar equatorial plane as the reference plane is similar for all spacecraft. For the position of Earth and the Sun-Earth L1 point, HEEQ and SCEQ are identical.

ICMECAT (UH, UNIGRAZ, IMPERIAL): We have gathered lists of in situ CME observations from various authors, in the timeframe January 2007-December 2015, which overlaps fully with the HICAT catalogue v3. This results in 556 ICME events. Figure 3.4.2 (left panel) gives an overview of the positions where those ICMEs have been detected with respect to Earth, demonstrating the 360° heliospheric coverage of ICMEs provided by HELCATS. Table 3.4.1 details the sources of the individual ICME catalogues.

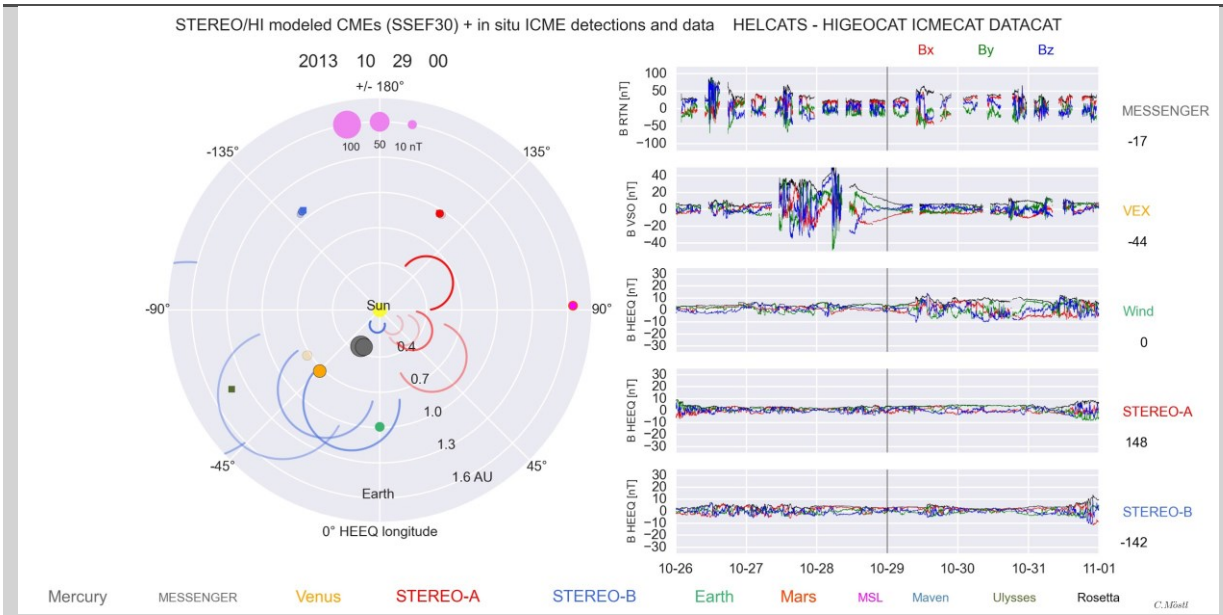

Fig. 3.4.8 - Screenshot of animation 2, showing the solar system in the solar equatorial plane, in similar format to Animation 1. The time range is April 2007 to December 2015. Here, circles that light up (when the time is inside the magnetic obstacle MO_START_TIME and MO_END_time) and fade are actual ICME detections, contained in ICMECAT. The size of the circle that lights up is related to the mean magnetic field in the ICME as given in ICMECAT, with the legend on the upper part of the figure. On the right hand side, the in situ magnetic field components in colors (Bx red, By green, Bz blue) and the total field (black) are shown for the 5 spacecraft MESSENGER, VEX, Wind, STEREO-A, and STEREO-B. The number below each spacecraft label on the far right is the HEEQ longitude of the spacecraft. This animation is particularly useful for identifying lineup CME observations of planets and spacecraft and cross-checking the results of LINKCAT. For the movie go to: ***https://www.youtube.com/watch?v=Jr4XRzGCaaQ&t=346s***

Table 3.4.1: In-situ CME observations

Spacecraft	Provider	Number of ICMEs
Wind	T. Nieves-Chinchilla http://wind.nasa.gov/index_WI_ICME_list.htm	133
STEREO-A/B	L. Jian http://www-ssc.igpp.ucla.edu/forms/stereo/stereo_level_3.html	141/133
VEX	Good & Forsyth (2016)	81
MESSENGER	Good & Forsyth (2016), Winslow et al. (2015)	68

In summary, 407 ICMEs were observed close to 1 AU (Wind, STEREO-A, STEREO-B), plus 149 events in the inner heliosphere by VEX and MESSENGER. In case of overlaps of the MESSENGER list by Winslow et al. (2015) and Good we have taken the times from R. Winslow because they include both the ICME start time and the magnetic obstacle times, whereas in the S. Good list only the magnetic obstacle times were available.

For VEX, IMPERIAL (V. Krupar, J. Eastwood) has added shock times to the list by Good & Forsyth (2016) for those events were a clear shock preceded the magnetic obstacle.

For all ICMEs, various parameters (e.g. mean magnetic field, minimum Bz component) have been derived from the data again by us in a homogeneous way, thus eliminating the need to compile different parameters from the catalogs which might differ in their definitions from one catalog to another.

Minimum Variance Analysis (MVA, done by UNIGRAZ) results are given for all in situ spacecraft, for the magnetic obstacle (MO) intervals. Criteria: the intermediate-to-minimum eigenvalue ratio must be > 2. For all MO intervals at least 75% of the data points must be present (i.e. not NaN), otherwise MVA is not performed. For MO intervals where between 75% and 100% of all data points are present, the missing ones are linearly interpolated. Figure 3.4.4 shows an example of the data plots that are available for each event in ICMECAT and LINKCAT.

WP4 TASK 4.3 Assessing the validity of the HI modelling (TASK LEAD: UNIGRAZ, CONTRIBUTORS: UPS, UGOE, ROB, UH)

Comparison with in-situ measurements

A major goal of the HELCATS project is to check on the validity of using HI for space weather forecasting, in particular for the CME arrival time and arrival speed. These are essential results for a possible future space weather mission to the L5 point, which could continuously monitor the Sun and the space between the Sun and Earth. An HI instrument will also be onboard Solar Orbiter, and STEREO-Ahead/HI continued to observe the solar wind between the Sun and Earth in November 2015. This work has been submitted as a peer-reviewed publication to the journal *Space Weather* (Möstl et al., 2017).

It has been shown previously (e.g. Colannino *et al.* 2013, Möstl *et al.* 2014, Tucker-Hood *et al.* 2015) that STEREO/HI showed a great potential to enhance the warning times and the accuracy of CME predictions, even in real time (Tucker-Hood *et al.* 2015). However, the conclusion by these works was that there is still room for improvement and the statistics have been unclear as the maximum number of events that were ratified with in situ observations was only around 20 (e.g. Möstl *et al.* 2014, Tucker-Hood *et al.* 2015). There was also a mixture of real-time (Tucker-Hood *et al.* 2015) and hindsight predictions (Möstl *et al*. 2014, Rollett *et al.* 2016). In our work, all "predictions" were in fact made in hindsight. Testing CME forecasts with HI against a large event-sample of CMEs observed in situ in the solar wind is clearly needed, for a variety of reasons. For predicting space weather at all the terrestrial planets it is necessary to test the HI techniques for distances other than 1 AU. Studies so far have focused on in situ data near 1 AU (Möstl *et al*. 2014, Rollett *et al*. 2016) or those taken in the near-Earth solar wind (Tucker-Hood *et al*. 2015). The aim of HELCATS WP4 was thus twofold: to drastically increase the number of CME events available for the analyses of prediction performance to obtain better statistics, and to test the forecasts based on HI data for heliocentric distances other than 1 AU. This is of relevance for planetary space weather and even a human Mars mission. Our deliverable demonstrates that we have achieved these two goals.

This is the first work to test a large scale sample, of 1337 CMEs observed with both STEREO/HI instruments, against 668 interplanetary coronal mass ejection events observed in-situ, obtained between January 2007 and December 2015 and ranging in heliocentric distances from 0.3 to 1.5 AU. We have established 2 catalogues: the catalogue of predicted arrivals is called the ARRCAT (version 6 used here), and the catalogue of the in situ ICME observations the ICMECAT (version 10). It contains data from the solar wind observatories Wind, STEREO-A, STEREO-B, VEX, MESSENGER, and ULYSSES. We use all spacecraft for a comparison to HI except ULYSSES. Both catalogues have been described above.

Figure 3.4.9a shows an overview of the predicted arrivals with HI in the inner heliosphere as collected in ARRCAT, and Figure 3.4.9b gives the locations and the mean magnetic field strength of all ICMEs in ICMECAT. ICMECAT is available on figshare at: **https://doi.org/10.6084/m9.figshare.4588315**. ARRCAT is available on figshare at: **https://doi.org/10.6084/m9.figshare.4588324**.

Both figures nicely show the 360° coverage of the heliosphere with respect to Earth. STEREO moved from its launch in 2006 to solar conjunction in 2014/2015. Figure 3.4.10 illustrates the decline of the ICME magnetic obstacle total and average magnetic fields with heliocentric distance by plotting all events in ICMECAT. This serves to demonstrate the distribution of magnetic field strengths. For better orientation, the shaded areas give the distances of the planets Mars, Earth, Venus, Mercury, from right to left. The distances of the planned close approaches of Solar Probe Plus are shown as a pink shaded area. The exponent of the power law for the maximum magnetic field strength is -1.77, which is quite consistent with previous studies (e.g. Leitner et al. 2007, Winslow et al. 2015), though the sample size here is considerably larger. In the right panel we added a data point at 10 solar radii based on the work of Patsourakos & Georgoulis (2016) at 0.03 G or 3000 nT. The exponent for the <B> fit is -1.73, including the solar data point it is -1.75, which means that the power law could

be valid too for the smallest heliocentric distances that will be observed by Solar Probe Plus.

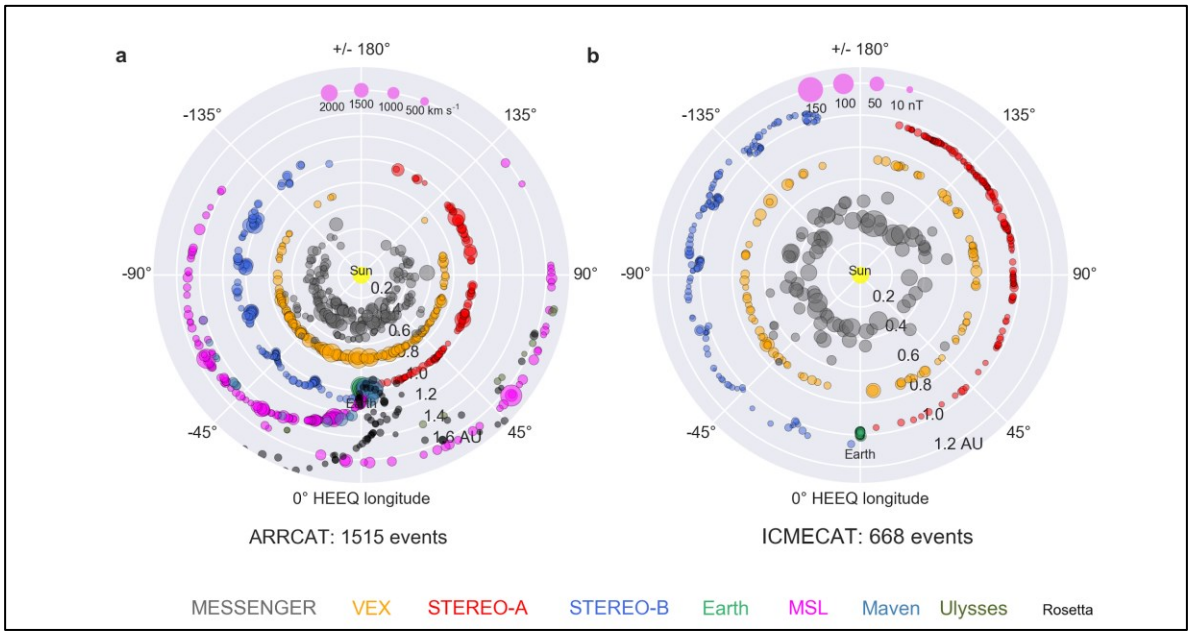

Fig. 3.4.9 - Overview of ARRCAT and ICMECAT. Both panels show the solar equatorial plane. (a) All CMEs in HIGeoCAT were checked if they potentially arrive at various planets and spacecraft as indicated by the colour code at the bottom, based on the shape model of a self-similar expanding circle with 30° half-width (SSEF30). Each dot marks a predicted arrival at MESSENGER, VEX, STEREO-A/B, Earth L1, MSL, MAVEN and Ulysses and Rosetta. For MSL and MAVEN, impacts during the cruise to Mars are nicely highlighted. The size of the dot indicates the predicted impact speed, which is an overestimate due to the constant speed assumption of SSEF30. (b) Overview of in situ detections of ICMEs, showing the longitude and radial distance at which the detection happened, as collected in ICMECAT. The size of the circle indicates the mean magnetic field strength during the magnetic obstacle of the in situ CME detection.

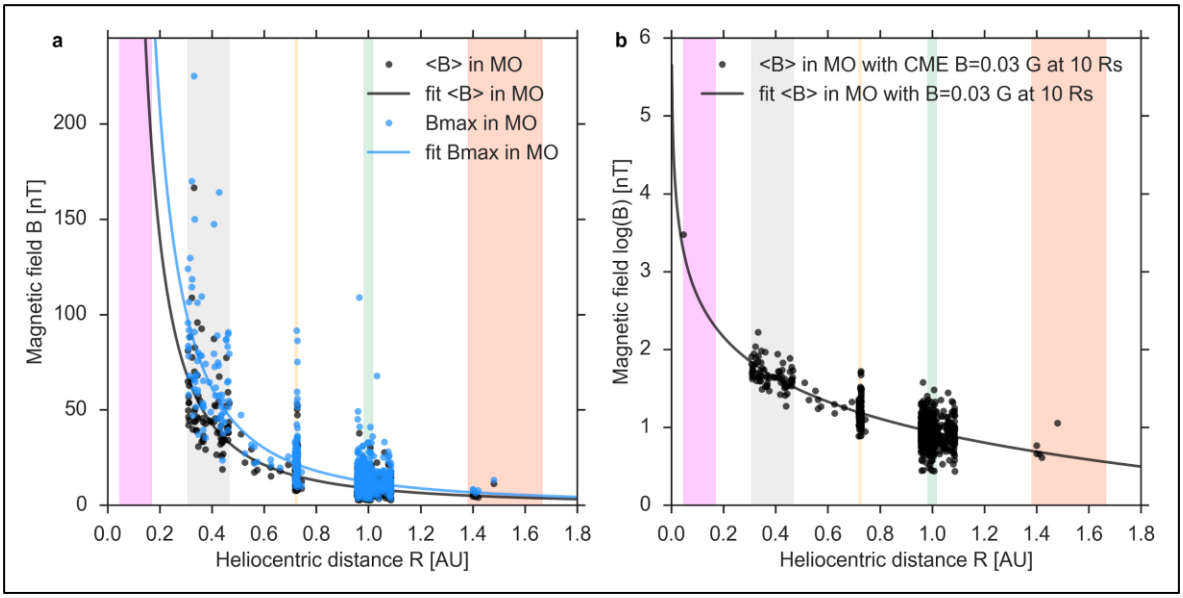

Fig. 3.4.10 - ICME magnetic fields as function of heliocentric distance. (a) The decline of the ICME magnetic obstacle (MO) total and average magnetic fields with heliocentric distance in ICMECAT. (b) It shows the average MO magnetic field as a logarithmic plot and includes a data point from solar magnetic field observations.

To test the predictive capabilities of STEREO/HI, we have essentially verified the ARRCAT with respect to the ICMECAT. We will further describe here some fundamental results from this analysis, regarding three main

issues as stated in the HELCATS WP4 work plan.

(1) comparing HI-derived CME direction with spacecraft position (hit or miss predictions)

Figure 3.4.11 (upper panel) demonstrates the number of predicted impacts per year in ARRCAT derived from HI SSEF30 modeling. Shown are the sums for HIA and HIB, and the color code indicates the spacecraft for which the arrivals are predicted. By far the most hits are predicted for Earth/L1 because it was always in the HI field of views (FoVs) as compared to the other spacecraft, which were situated in the solar wind and at Mercury and Venus, thereby entering and leaving the FoVs continuously. The total number of predicted arrivals for the five spacecraft were 620 (HIA) and 569 (HIB).

The lower panel of Figure 3.4.11 demonstrates the number of ICMECAT events per year for each spacecraft. Clearly, there is a rise from solar minimum (2008, 2009) to maximum (2012, 2013), and the decrease of ICME numbers in the declining phase in 2014 is already seen too. The relative drop in 2011-2014 for MESSENGER and VEX compared to spacecraft near 1 AU might be explained by the more difficult identification of ICMEs because from these spacecraft only magnetometer data were used. It can be seen clearly that the number of ICMEs is far less than the number predicted arrivals for Earth L1, VEX and MESSENGER but not for STEREO. The number of ICMEs rises in solar maximum to around 30 events per year, which averages to slightly above 2 events per month.

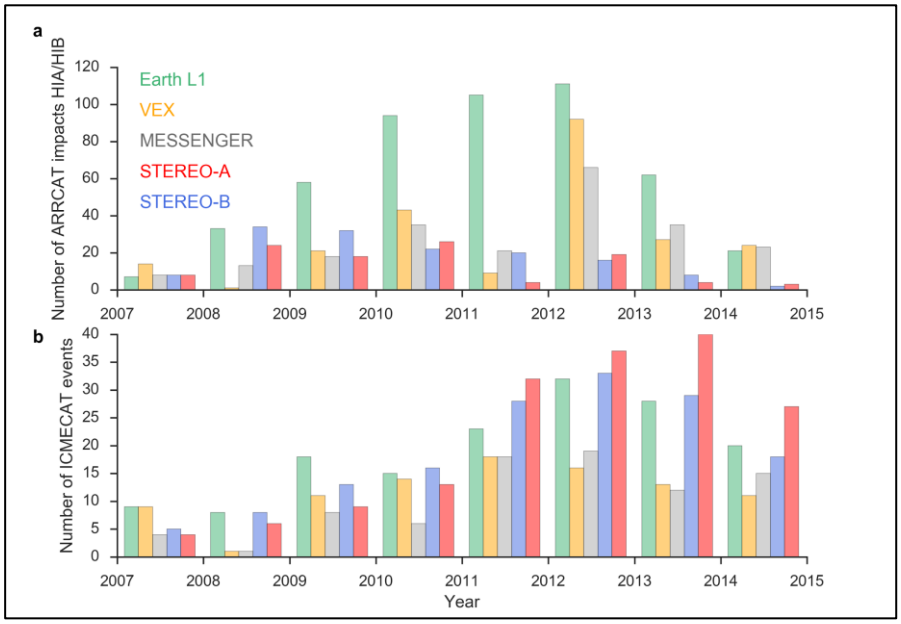

Fig. 3.4.11 – Impact statistics. (a) Number of predicted impacts per year derived from HI SSEF30 modelling as given in the ARRCAT catalogue. Bars are sums of the numbers for HIA and HIB. (b) Number of ICMECAT events per year for each spacecraft.

In Figure 3.4.12 we assess hit and miss predictions: The upper panel shows the number of predicted CME hits, only from HI-A, for each year as shaded bars. The lower panel shows the same based on HI-B observations. The solid bars represent the number of impacts that are accompanied by an actual ICME in situ detection at the respective planet or spacecraft indicated by the color code. To this end, a time window of +/- 1.5 days was used. Table 1 shows the numbers for each spacecraft and for HIA/HIB separately. The average for MESSENGER and VEX at distances < 1 AU is 22 %, for the other spacecraft close to 1 AU it is 25 % without self-predictions. With self-predictions we denote CMEs that were observed by a STEREO spacecraft with HI and in situ. The accuracy percentage of the self-predictions are significantly higher with 38%, when averaging the numbers from both spacecraft. This underpins the idea that heliospheric imaging might work well also from L1 or Earth orbit (DeForest *et al*. 2016, DeForest & Howard, 2015).

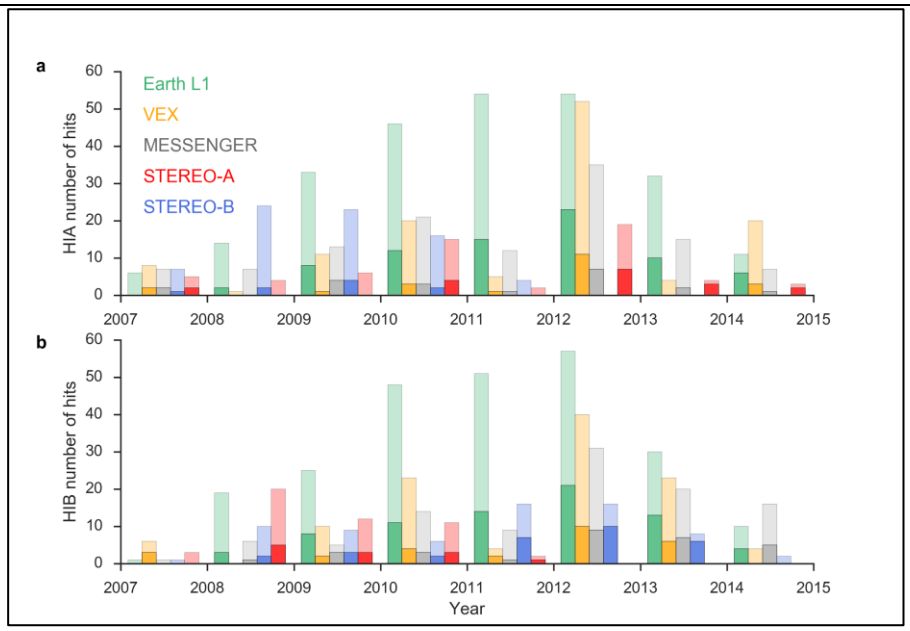

Fig. 3.4.12 - Comparison of correct predictions and false alarms. (a) The number of predicted CME hits with SSEF30 based on HIGeoCAT for each year (only HIA) is shown as bars as a function of time. The solid parts of the bars are the number of impacts that are accompanied by an actual ICME in situ detection at the respective planet or spacecraft indicated by the color code. The shaded part of the bars indicates the number of false alarms. (b) Same based on HIB observations.

Overall, the prediction accuracy is 26%, so 1 out of 4 predicted impacts actually caused a clear ICME observed in the solar wind. This compares well to Tucker-Hood *et al*. (2015) who found that 20 predicted arrivals out of 60 in total lead to an ICME at Earth/L1, though their time window was larger. If we choose a different time window than 1.5 days, a window of 1.0 days leads for Earth to a percentage of 24%, a window of 0.5 days to 15%, and a window of 2.0 days to 37 %, so the true positives range between 1 out of 3 and 1 out of 6, depending which time window is deemed appropriate.

For a time window of 1.5 days, this means that for every correct prediction (solid bars in Figure 3.4.4) there are about 3 false alarms (shaded bars). The average for HIB (31 %) is higher than for HIA (21%), which might imply that the "view" from L5 works better compared to L4, but it is hard to tell if this difference is significant without further analysis. The statistics are solid, though: for Wind, 250 predicted arrivals could be compared to 165 ICMEs, for VEX 121 predictions against 93 ICMEs and for MESSENGER 117 forecasts were compared to 87

ICMEs.

*Table 3.4.2: Percentage of correct hits of the ARRCAT predictions, meaning there is an entry in ICMECAT within +/- 1.5 days of a predicted arrival in ARRCAT. Fields with * mark "self-predictions"*

spacecraft	Wind	STEREO-A	STEREO-B	VEX	MESSENGER
HIA	30	31*	12	17	17
HIB	31	25	44*	25	28

Figure 3.4.13 demonstrates how the percentage of correct hits developed as a function of time (upper panel) and thus separation from Earth (lower panel). Here, only the percentage of correct hits at Earth / L1 are shown, for both HIA and HIB. We further use the time window of 1.5 days around the predicted impact for assessing if the prediction indeed lead to a hit. STEREO-B reached the L5 point at 60° separation from Earth in October 2009, and the percentage of correct hits during 2009 was better compared to 2008, where the mean separation

was about 30° heliospheric longitude.

However, surprisingly, the percentage did not decrease with angles larger than L5 but slightly increased as STEREO-A went behind the limb as seen from Earth and finally into conjunction. Lugaz et al. (2012) first described the possibility that using HI works for CMEs that propagate behind the limb as seen by an HI spacecraft, and this is consistent with our findings. However, the effect that the percentage of correct hits slightly increases with longitudinal separation needs to be investigated further. One possibility for the higher percentage might be that the higher CME frequency during solar maximum plays a role here. The current results imply that L5 is not a particular outstanding point for predicting CME hits and misses, but of course still very desirable because of its relative stability.

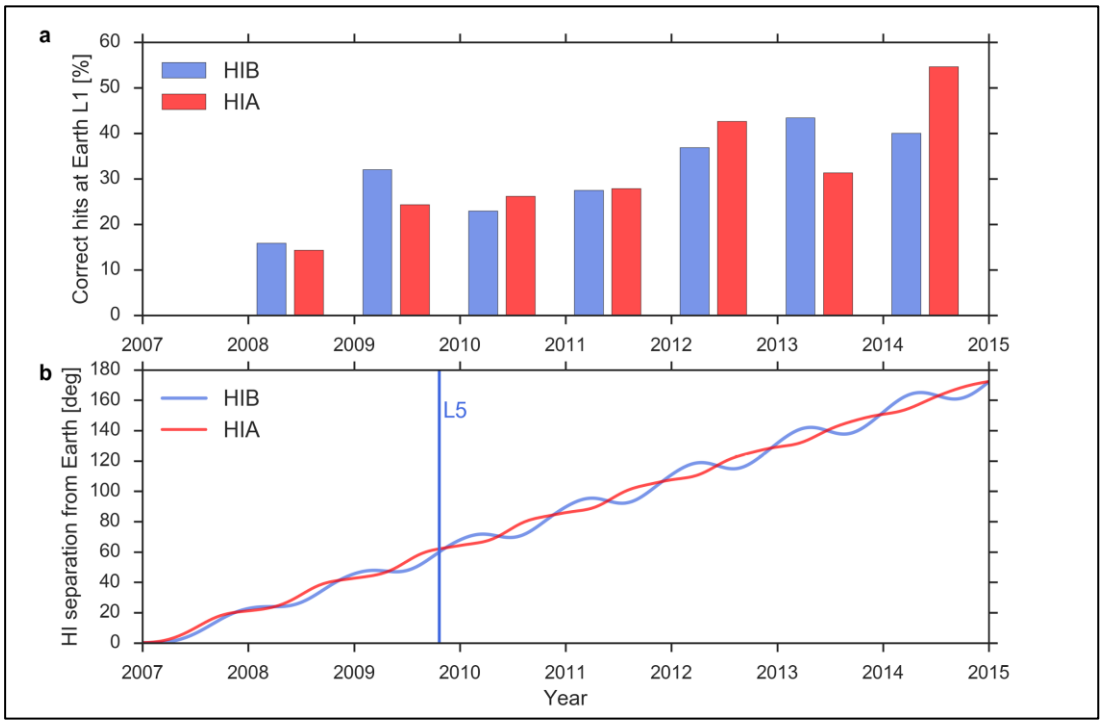

Fig. 3.4.13 - Correct hit percentage as function of time and longitudinal separation to Earth. (a) Yearly percentage of correct hits as function of time. (b) Separation of STEREO-A/B from Earth in heliospheric (HEEQ) longitude with time. The moment as STEREO-B passed L5 is highlighted as a vertical line.

(2) Comparing HI-derived CME arrival times/speeds with in-situ CME arrival times/speeds

Figure 3.4.14 demonstrates the arrival time differences for each spacecraft and HI-A/HI-B separately (left and right column, respectively). We show the Calculated (C) minus observed (O) arrival times in hours. Positive values stand for cases where the CME arrived earlier than the forecast implied, and negative values signify late CME arrivals. Again we use a time window of +/- 1.5 days around all predicted arrival times in ARRCAT. The ICME_START_TIME of the ICME that is closest to the predicted arrival is taken for the C-O calculation, and this time difference must be inside the time window.

Table 5.3: Mean and standard deviation of arrival time C-O, in hours

spacecraft	Wind	STEREO-A	STEREO-B	VEX	MESSENGER
HIA	3.2 +/- 16.3	1.0 +/- 23.4*	8.0 +/- 14.5	-2.1 +/- 11.9	3.2 +/- 18.1
HIB	0.8 +/- 17.4	6.8 +/- 16.6	7.7 +/- 14.7*	-0.7 +/- 13.7	3.8 +/- 12.9

All other ICMEs inside and outside this time-window are ignored. “Double hits”, so that one predicted arrival can be related to two ICME start times, is quite seldom but happens e.g. at Earth only for 12% (9%) of those

arrivals in HI-A (HI-B) that can be related to at least one ICME in the time window.

The total number of comparisons for HIA was 171, for HI-B 194. The average C-O is 2.4 +/- 17.1 hours for HIA, and 2.7 +/- 16.0 hours for HIB, so no significant difference. In comparison, Möstl *et al.* (2014) find an average C-O = -1.4 +/- 11.1 (their Table 3) for the SSEF30 technique. The difference is explained by the selection of events by these authors that quite clearly matched between HI and in situ, whereas here there is no such selection. Most values in Table 3.4.2 are positive, so the CME arrived slightly earlier than predicted.

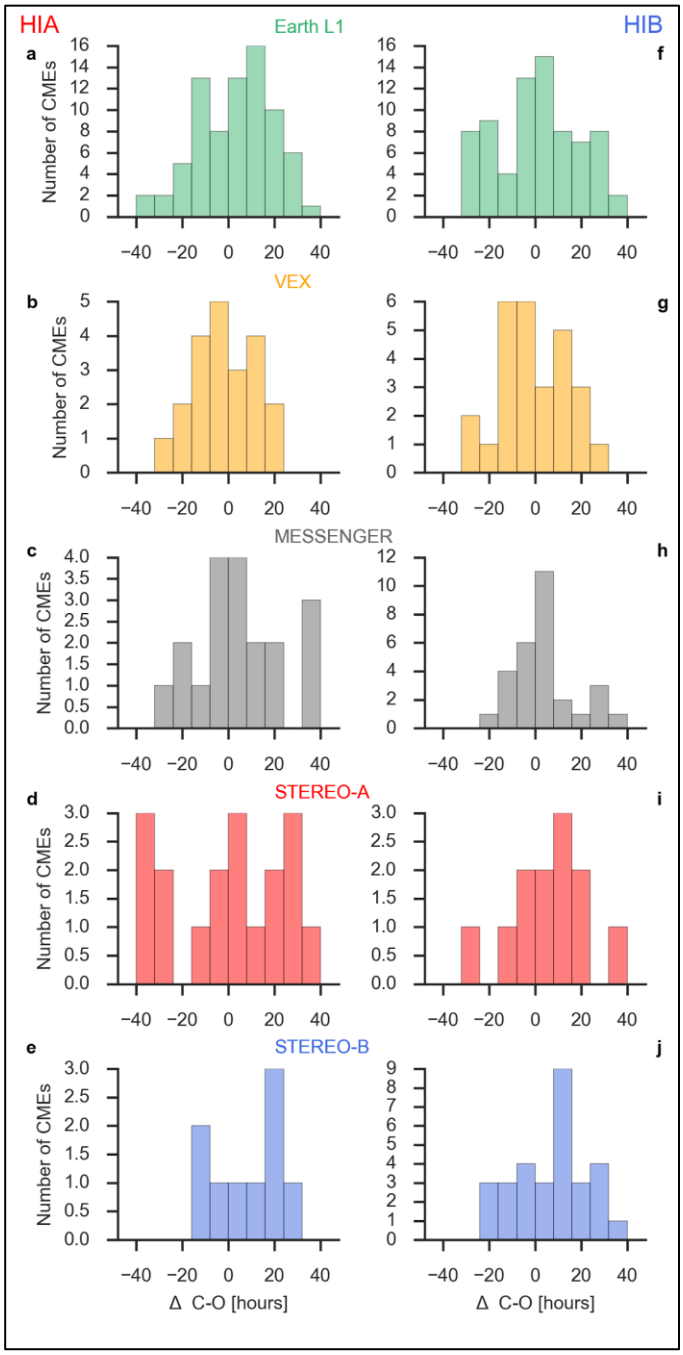

Fig. 3.4.14 - Histograms of calculated (C) minus observed (O) arrival times, in hours for each spacecraft. Left column shows observations based on HIA, right based on HIB.

Figure 3.4.15 demonstrates the calculated minus observed CME speed at Earth. It is seen that many events cluster around a speed difference of 0, but there is a positive tail to the distribution, which is a consequence of the constant speed assumption of SSEF30, overestimating the arrival speed (Möstl *et al.* 2014). The HI speed is corrected for the circular SSEF30 front (after Möstl & Davies 2013). The in situ speed for comparison is the

proton speed in the ICME sheath region. The differences are for HIA at Earth L1: 191 +/- 341 km/s, and HIB at Earth L1: 245 +/- 446 km/s. These results are very similar to Möstl *et al*. (2014) who quote 252 +/- 302 km/s. Because we do not have plasma speeds from VEX and MESSENGER we cannot do this comparison for < 1 AU.

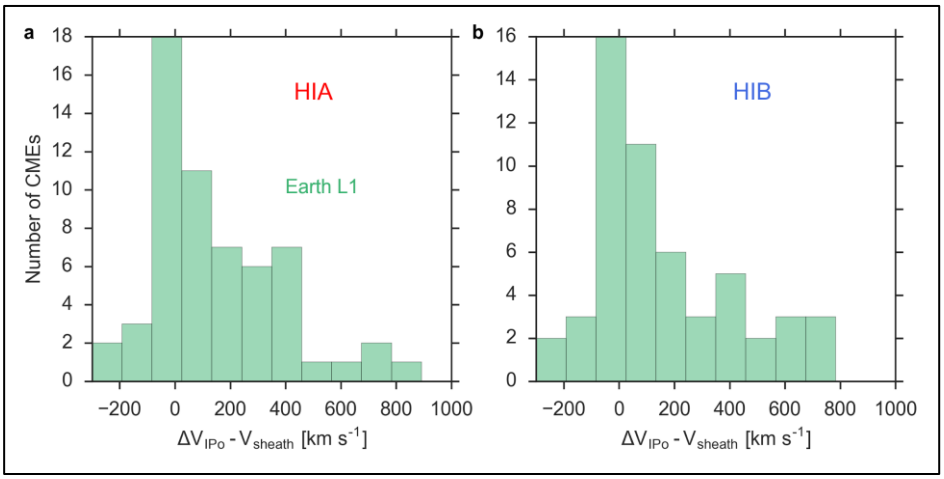

Fig. 3.4.15 - Difference of HI predicted speeds to ICME plasma speeds. (a) Calculated minus observed CME speed at Earth, for HIA. The HI speed is corrected for the circular SSEF30 front. The in situ speed is the proton speed in the ICME sheath region. (b) Same for HIB.

(3) comparing white-light HI morphology with in-situ flux rope orientation.

Figure 3.4.16 shows the outcome of an experiment where we tried to correlate the orientation from the in situ flux rope to the latitudinal extent of the CME in the HI FoV. The rationale behind this is to check whether the flux rope inclination, which is a decisive parameter for the resulting Bz field and thus geomagnetic storm strength (e.g. Bothmer and Schwenn, 1998), may be predicted from the CME morphology in HI. We show this for 2 techniques: Grad-Shafranov Reconstruction (orange) and Minimum Variance Analysis (blue). Here, we use the LINKCAT list (Deliverable 4.1) because the in-situ - HI connection must be as clear as possible. The correlation coefficients are -0.17 for GSR and -0.21 for MVA, so there is no connection between CME extent in latitude and the in-situ flux rope inclination. The expected relationship would imply a correlation of -1. This shows that the shape the flux rope may in general not be a well-shaped tube (e.g. Wood *et al.* 2010), or that the flux rope shape is not represented by the appearance of the CME in HI, or that the techniques to derive a local orientation of a flux rope are not sufficiently representative of the global CME shape (Al-Haddad *et al*. 2013).

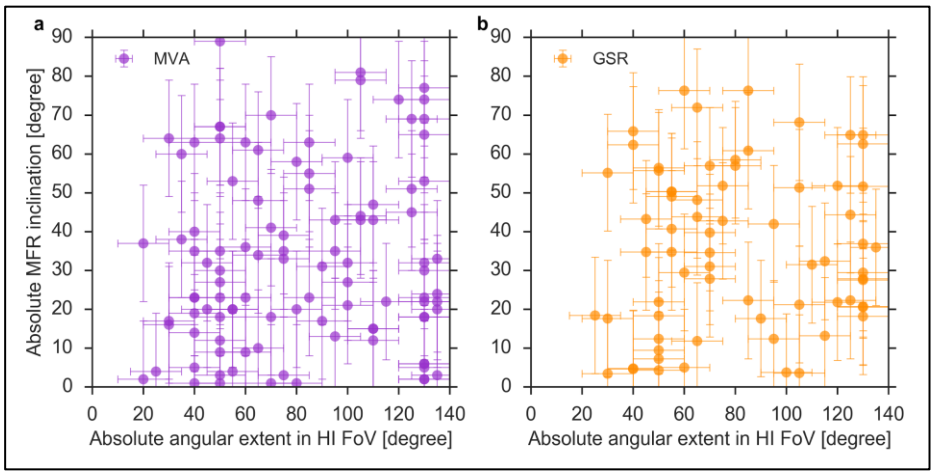

Fig. 3.4.16 - No correlation exists between the in situ flux rope inclination and the HI CME extent in latitude. Two techniques for the flux rope inclination are shown: (a) MVA and (b) GSR. The expected relationship would follow a linear decrease from top left to bottom right.

Conclusion

We have compared a large-scale number of about 1300 CME events observed with the STEREO/HI instruments with 668 in situ observed ICMEs. Thereby we have derived some fundamental results concerning geometrical modeling with the currently available SSEF30 technique. This is of major importance for a space weather mission carrying a heliospheric imager at the L5 or L1 points (Lavraud *et al.* 2016, DeForest *et al.* 2016).

We find that 1 out of 4 predicted impacts results in a clear ICME. This number might be considered low concerning the accuracy for a regular space weather forecast, however e.g. singular shocks in the in situ data which are results of ICME flank hits are ignored. In future work, the forecasted CME arrivals might be checked against the in situ data directly, not just the ICME lists, which would eliminate the identification of ICMEs which is always a subjective matter. Forecasting with HI also works well for locations at < 1 AU, as we find that the predicted arrival times match with similar accuracy compared for spacecraft positioned around 1 AU. This result might be expected too for Mars, though we could not yet test this as MAVEN entered its orbit around Mars in late 2014 just when STEREO went into conjunction. The predicted arrival time errors of around +/- 17 hours are very close to those reported by a comparison of Enlil and DBM forecasts at Earth (Vrsnak et al. 2014). Our sample for assessing the arrival time accuracy consists of 315 event (HIA: 143, HIB: 172).

Additionally, L5 is a good location for the prediction of CMEs with HI. But somewhat surprisingly, if the HI observing spacecraft is positioned further away from the Earth in heliospheric longitude, the hit/miss predictions do not get worse. Note, however, that this was already seen by Lugaz et al. (2012) and Möstl et al. (2014), though we can now base this conclusion on much better statistics. This has an implication for current operations with STEREO-Ahead: real time predictions with HI should be done even when the spacecraft is still behind the east limb of the Sun as seen from Earth. This means we do not have to wait to use HI until it passes L5 in July 2020 to make good predictions using the HI instrument. Even L1 could be a good location for a heliospheric imager: self-predictions of CMEs observed with HIA or HIB and later detected with the same spacecraft by the in-situ instruments measuring magnetic fields and plasma parameters show slightly better percentages of correct hits than those to other spacecraft.

We have actually only scratched the surface here concerning other possibly analyses. For hits and misses, Brier skill scores should be established. We have only considered false alarms (false positives) and correct predictions (true positives), not false negatives and true negatives. The SSEF30 modeling should be updated with the results from ElEvoHI (Rollett *et al*. 2016), as the constant speed of SSEF30 assumption runs into troubles in particular predicting the arrival speeds. ElEvoHI eliminates both assumptions of a circular front and constant speed. We expect that applying ElEvoHI to all CME tracks in the HIGeoCat will show improvements concerning the arrival time and arrival speed. Another major assumption that needs to be eliminated is the constant 60° full width of the CME. Future work should also focus on adding magnetic fields to predictions with heliospheric imagers, by bringing together a model such as FRi3D (Isavnin 2016) with ElEvoHI to make predictions of CME geomagnetic effects possible.

The final visualization of the HIGeoCAT and ICMECAT is now permanently available at the HELCATS website and:

Youtube: https://www.youtube.com/watch?v=Jr4XRzGCaaQ&t=1s

Figshare: doi.org/10.6084/m9.figshare.4602253.v1.

Comparisons with coronagraph and source region data

CORHITCAT is a catalogue of COR2 CMEs with the addition of a predicted arrival of each CME to a spacecraft (and its corresponding validation by cross-checking these predictions with an ICME catalogue). In more detail, CORHITCAT takes the input parameters from the Göttingen COR2 CME catalogue (KINCAT) (**https://www.helcats-fp7.eu/catalogues/wp3_kincat.html**) and applies the method of Rodriguez *et al.* (2011) to see if, based on the GCS fits (with parameters available in KINCAT), a CME should arrive at L1 or at either of the two STEREO spacecraft. In order to validate these predictions, they are compared to real ICME arrivals, by using the ICMECAT catalogue. To do so, we take the time when the ICME arrived at the spacecraft and propagate the ICME back to 15 Rs, assuming a constant velocity. If the time at 15 Rs matches with the CME time from KINCAT within a 12 hour time-window, we will call that a good hit (i.e. the CME-ICME are the same event).

The method employed in KINCAT uses the Graduated Cylindrical Shell (GCS) model (Thernisien *et al.* 2006, 2009). The model aims to reproduce the large scale structure of flux rope-like CMEs. It consists of a tubular

section forming the main body of the structure attached to two cones that correspond to the "legs" of the CME. Only the surface of the CME is modeled, there is no rendering of its internal structure. The model is applied to CMEs observed by SOHO/LASCO and STEREO/COR data. The following parameters are derived:

- outer shell height

- the CME direction of propagation in longitude and latitude (Φ and θ, respectively),

- the cross section of the CME legs (a),

- the tilt angle around the axis of symmetry (γ) and

- the half angle between the legs (α).

From the parameters provided by the model, one can then calculate the half angular width of CMEs in latitude and longitude, using the following formulas (Rodriguez et al. 2011):

$$\theta_w = \arcsin(\sin\alpha \sin\gamma) + \beta$$

$$\Phi_w = \arcsin\left(\frac{\sin\alpha\cos\gamma}{\cos\theta_w}\right) + \beta$$

Where β is the angular width of the CME legs cross section (β = arctan(κ), with κ = a/r), r represents the distance from the center of the Sun to the edge of the shell, Φw and θw represent the angular width of the CME in longitude and latitude, respectively. Then, by knowing the location of the different spacecraft (latitude and longitude) one can infer whether a CME should be detected at one or more of them.

The catalogue columns are defined in the following way:

- 1st column: Event number (from KINCAT)

- 2nd column: date and time of the last image in COR2 with full visibility of the CME, in the format yyyy-mm-ddThh:mm (from KINCAT)

- 3rd column: predicted hit on STEREO–B (0 or 1)

- 4th column: predicted hit on Earth (0 or 1)

- 5th column: predicted hit on STEREO–A (0 or 1)

- 6th column: longitude at which the CME propagates (from KINCAT),

- 7th column: CME angular width in longitude,

- 8th column: difference in longitude between the CME edge and L1,

- 9th column: latitude at which the CME propagates (from KINCAT),

- 10th column: CME angular width in latitude,

- 11th column: Earth latitude,

- 12th column: difference in latitude between the CME edge and L1,

- 13th column: the associated ICME (using ICMECAT_ID from ICMECAT),

- 14th column: time of the propagated-back ICME at 15 Rs

- 15th column: time difference between the real CME (from KINCAT) and propagated back ICME

- 16th column: validation of predicted hit on STEREO-B (0 or 1)

- 17th column: validation of predicted hit on Earth (0 or 1)

- 18th column: validation of predicted hit on STEREO-A (0 or 1)

Column 3-5: 0 means that the method predicts no hit, while 1 means that the method predicts a hit. Column 16-18: 0 means that no associated CME was found, while 1 means that an associated CME was observed either

by STEREO-B, Wind or STEREO-A.

LINKCAT contains currently the total 143 events from May 2007 to December 2013. It aims at connecting CME observations from their source at the Sun to interplanetary space, using HI observations to connect the different datasets (see Deliverable 4.1). The catalogue provides several parameters for each event. For the remote-sensing part, they include the back-projected launch time of the CME, the source type (flare or filament eruption), the Stonyhurst latitude and longitude of the source region, and the flare time. For the in situ part, they include the shock or density enhancement arrival time, the magnetic obstacle start and end times, and the CME speed.

The LINKCAT serves as the optimal catalogue for the basis of comparing the magnetic structure of the CMEs in situ and as inferred from remote sensing observations. We will describe shortly our on-going statistical analysis below.

The parameters we use from the catalogue to study the magnetic structure of the sources are the back-projected launch time (from HIGeoCat), the source type, and the source's latitude and longitude. To check if the provided launch time is correct we look backwards from the HI images to the COR2 and COR1 images, and then find the source on the solar disk. We focus on the Earth-directed events due to the availability of SDO observations of the source. When the source region is identified, we check if the source type and location correspond to the one reported in the LINKCAT catalog. An example of a CME event backtracked from HI, first to COR2, and then to COR1 is shown in Figure 3.4.17. The rightmost panel shows the identified source in SDO AIA 171 Å image.

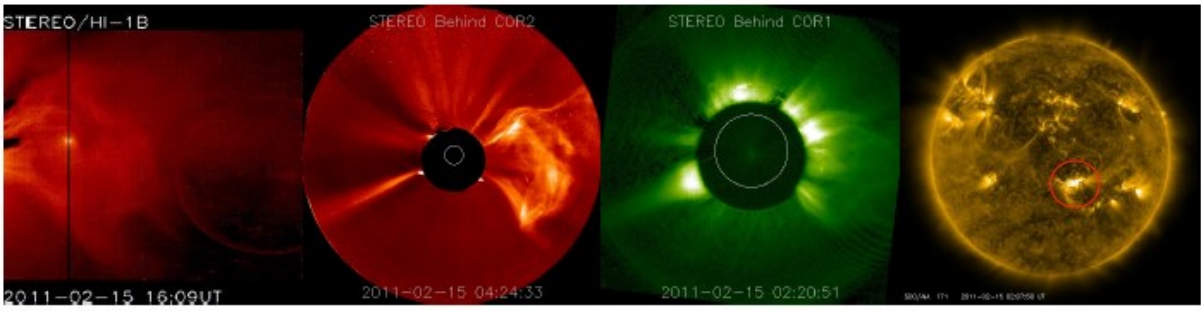

Fig. 3.4.17 - Magnetic structure analysis for the CME on 15 February 2011. Top row: examples of helicity sign proxies, from left to right: X-ray sigmoid, flare ribbons, and filament threads crossings. All proxies are right-handed. Mid row: determination of the orientation and direction of the axial field, from left to right: PIL orientation, PEAs orientation, and direction of the field from coronal dimmings. The axial field appears with a low inclination and directed eastwards. The proxies predict a NES-type flux rope.

When the magnetic structure of the erupting CME has been inferred, we make a first order validation of our results by comparing with in situ observations of the corresponding CME. The ICME time interval and its magnetic structure (e.g., from Grad-Shafranov modelling) are taken from the LINKCAT catalogue as derived in the ICMECAT catalogue. The paper by Palmerio et al. (2017) highlighted that a collection of several indirect proxies are needed to predict the flux rope type from remote-sensing observations for active region CMEs. In particular, such CMEs often lack clear filament association. However, the paper showed that the flux rope type was successfully estimated even for complex eruptions where the filament material erupted only partially and where the CME formed at higher altitudes, and the estimated flux rope matched well with the in situ structure. The Palmerio *et al.* (2017) paper was a case study of two events. A paper is now in progress where we perform a statistical analysis of about 20 events comparing their magnetic structure between the Sun and in situ. As described above, this study exploits widely the LINKCAT catalogue.

WP4 CONCLUSIONS:

WP4 had two main goals: (1) to establish the first linked catalog from CMEs, seamlessly connecting solar to in situ observations, in order to provide a dataset that serves as a basis to better understand the physics of solar eruptions, and (2) to test the predictive capability of STEREO/HI with the SSEF30 technique with in situ observations by various spacecraft around the terrestrial planets and the solar wind. Both aims have been achieved: the linked catalog is distributed online via the HELCATS website, an online repository (figshare), and

will be submitted in a journal publication (the HELCATS overview paper). The files are distributed in formats to be easily used by other researchers. The results on the assessment of HI predictions have been submitted to a journal (Möstl et al., 2017), and the catalogs we have used (ARRCAT and ICMECAT) as well as instructive animations are available via the HELCATS website, its gallery, and have been placed on figshare and youtube. These products are highly valuable for efforts to enhance the methodology of HI prediction (e.g. Rollett et al. 2016), which is of utmost importance in order to provide accurate daily forecasts based on data from a space weather mission to the Sun-Earth L5 point.

WP4 HIGHLIGHTS:

- Creation of the most comprehensive catalogue of in situ observed CMEs to date, containing over 650 events over 9 years of data from 5 spacecraft in the inner heliosphere (ICMECAT).
- First production of a catalogue of over 100 events that seamlessly links solar and in situ observations of CMEs in order to better understand the origin and evolution of geoeffective CME magnetic flux ropes (LINKCAT).
- Establishing the new state-of-the-art for predicting the arrival times and hit and miss classifications with a CME prediction model, using more than 1000 events, covering 2/3 of a solar cycle, and varifying the model predictions with 5 spacecraft at 3 different planets.

WORK PACKAGE 5 (WP5):

PRODUCING A DEFINITIVE CATALOGUE OF CIRs IMAGED BY STEREO/HI THAT INCLUES VERIFIED MODEL-DERIVED KINEMATIC PROPERTIES

WP5 ACTIVITY TYPE: UPS

WP5 DURATION: MONTHS 1 – 36

WP5 LEAD BENEFITIARY: STFC (1)

WP5 LEADER: Dr Alexis Rouillard

WP5 CONTRIBUTORS: UH (7)

WP5 OVERVIEW: The primary goal of WP5 is to provide a catalogue of the spatial and temporal evolution of Stream Interaction Regions (SIRs)/Co-rotating Interation Regions (CIRs) (and their substructures) observed by STEREO/HI in 3-D, following their complete formation process using different observations (mainly imaging but also in-situ) from the Sun out to 1 AU. This is a parallel activity to the CME cataloguing of other WPs. The output of the solar wind stream advanced catalogue is set-up as a facility, and optimized to help the space physics community in the search for clues on the origin, propagation, 3D morphology, and the planetary effects of CIRs and the slow solar wind.
[Relevant catalogue: CIRCAT]

WP5 TASK 5.1: CATALOGUING THE OCCURRENCE OF CIRs (CIRCAT) (TASK LEAD: UPS)

The large-scale structure of the solar wind measured in the ecliptic plane at solar minimum is to a large extent set by the recurring compression/rarefaction regions formed by the radial alignment of fast and slow solar wind. The compression regions are called Stream Interaction Regions (SIRs) when measured once in situ or Corotating Interaction Regions (CIRs) when measured over consecutive solar rotations (Jian et al. 2006). The advent of high-resolution heliospheric imaging allows us to track continuously the solar wind outflow between the Sun and 1 AU and to study the origin of the variable plasma output released from the Sun. Imaging from STEREO has shown that, contrary to the standard picture of a smooth spiral of density increase, SIR/CIRs have significant longitudinal variability associated with the continual release and subsequent compression of small-scale transients in the slow solar wind. STEREO has been monitoring the variable plasma output of the Sun systematically for the last 8 years, thereby offering just under a solar cycle of insightful observations.

Thus, the principal output of task 5.1 is deliverable D5.1, 'Establishing an online CIR catalogue'. Using J-maps and optimized running-difference images, we list the times of observations of each CIR in HI images, measure the number of small-scale transients entrained inside each CIR in the ecliptic plane, determine the minimum and maximum radial distance at which CIRs are observed, and establish a common timeline (first order catalogue) of remote-sensing and in-situ measurements of CIRs. From the CIR fitted trajectories, we provide an estimate of the arrival times of CIRs at Mercury, Venus, Mars, Earth, Saturn, thereby providing support to European-funded space missions around these planets. The instruments used include STEREO/HI and in-situ STEREO instrumentation, and in-situ instrumentation aboard Wind, ACE, Venus Express and Ulysses.

It is possible to track the Corotating Density Structures (CDS) in the Heliospheric Images by using J-maps constructed from running-difference images. In J-maps made with SECCHI-A, patterns of converging tracks appear at nearly every solar rotation and are most clearly visible during solar minimum years. As previously shown by Rouillard et al. 2008 and Davies et al. 2009, each track in this pattern is the white-light signature of a strong density inhomogeneity (or so-called `density blob') moving radially outward. Beyond about 0.3 AU (situated roughly between HI-1 and HI-2 fields of view), these inhomogeneities become entrained ahead of corotating high-speed streams. Because these density structures are emitted by a spatially limited source region at the Sun they rapidly form a spiral of density inhomogeneities in the interplanetary medium. This spiral is analogous to the Parker spiral formed by the interplanetary magnetic field, both trace approximately

the locus of plasma emitted by a single source region at the Sun.

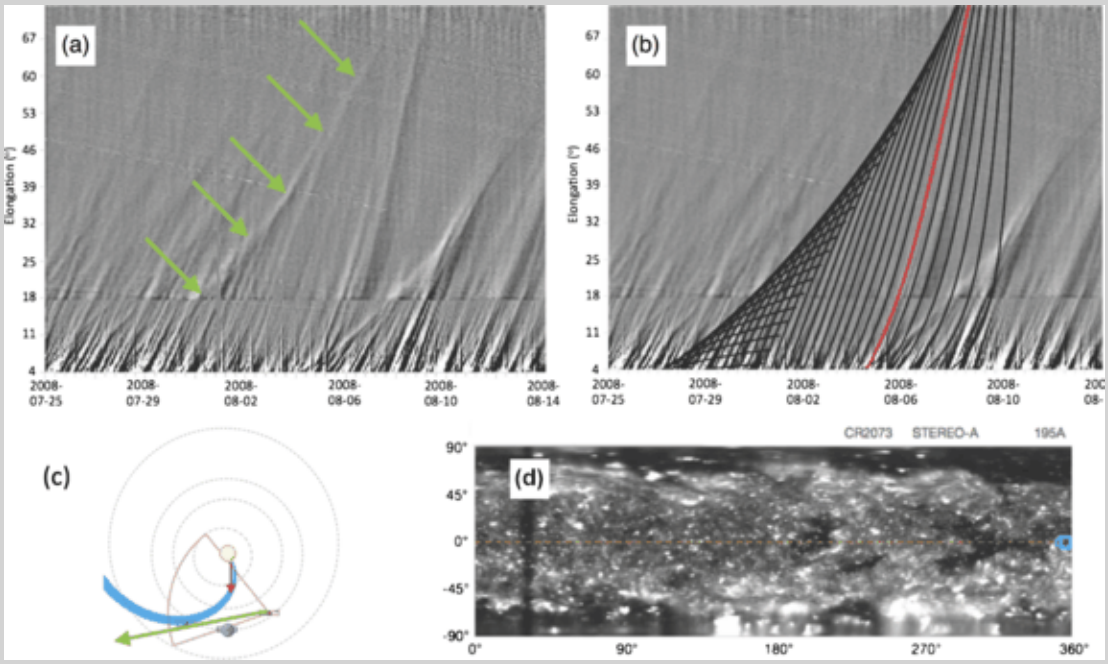

Fig. 3.5.1 - (a) Example of a J-map extending from 25 Jul to 14 Aug 2008. (b) The same J-map but overlaid with time–elongation profiles corresponding to a series of individual blobs that comprise a CDS. The red curve is the actual fit to one well-observed CDS blob (onset 2008-08-03T21:36:26 UT, Vb=358±10 kms−1, and ϕ=34°±3°). The black curves, reconstructed using this speed, simulate the elongation variations of a series of such blobs emitted at 8 hr intervals from the same region. (c) The orbital configuration at the onset date. (d) The coronal map for the Carrington rotation 2073 at a wavelength of 195 Å, derived from ST-A/EUVI images.

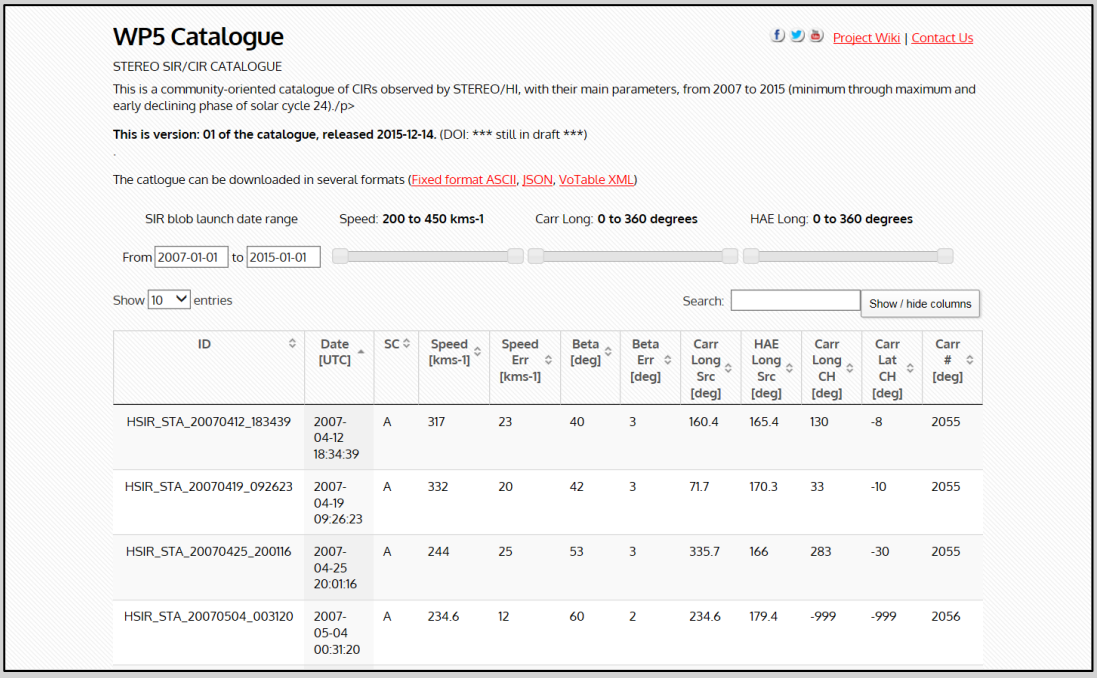

WP5 Catalogue

Project Wiki | Contact Us

STEREO SIR/CIR CATALOGUE

This is a community-oriented catalogue of CIRs observed by STEREO/HI, with their main parameters, from 2007 to 2015 (minimum through maximum and early declining phase of solar cycle 24)./p>

This is version: 01 of the catalogue, released 2015-12-14. (DOI: *** still in draft ***)

The catlogue can be downloaded in several formats (Fixed format ASCII, JSON, VoTable XML)

SIR blob launch date range Speed: **200 to 450 kms-1** Carr Long: **0 to 360 degrees** HAE Long: **0 to 360 degrees**

From 2007-01-01 to 2015-01-01

Show 10 entries Search: Show / hide columns

ID	Date [UTC]	SC	Speed [kms-1]	Speed Err [kms-1]	Beta [deg]	Beta Err [deg]	Carr Long Src [deg]	HAE Long Src [deg]	Carr Long CH [deg]	Carr Lat CH [deg]	Carr # [deg]
HSIR_STA_20070412_183439	2007-04-12 18:34:39	A	317	23	40	3	160.4	165.4	130	-8	2055
HSIR_STA_20070419_092623	2007-04-19 09:26:23	A	332	20	42	3	71.7	170.3	33	-10	2055
HSIR_STA_20070425_200116	2007-04-25 20:01:16	A	244	25	53	3	335.7	166	283	-30	2055
HSIR_STA_20070504_003120	2007-05-04 00:31:20	A	234.6	12	60	2	234.6	179.4	-999	-999	2056

Fig. 3.5.2 – The CIR catalogue on the HELCATS website (CIRCAT).

We have derived a catalogue listing the properties of 190 corotating structures well-observed by the STEREO-A/HI instrument images (from April 2007 to August 2014). The time-dependent evolution of the 3-D trajectory of each CDS was determined, the characteristic tracks left by these CDS in the J-maps were fitted manually by clicking on J-maps produced with HI-1 and HI-2 images from STEREO-A. An example of an ecliptic J-map, showing two distinct families of converging tracks observed during July and August 2008, is presented in panel

(a) of Figure 3.5.1. An example of a fit to a single CDS, spanning July and August 2008, is shown in panel (b) of Figure 3.5.1. This is explained in more detail, later, in the text relating to deliverable D5.2.

The CIR catalogue is located on the HELCATS website under the PRODUCTS tab at WP5. Figure 3.5.2 shows an extract from the catalogue.

WP5 TASK 5.2: DERIVING/CATALOGUING THE KINEMATIC VARIATION OF CIRs (TASK LEAD: UPS)

In this task, we are fitting the leading edge of each CIR/SIR in the STEREO/HI J-maps, derived at all available latitudes, to obtain the spatial/temporal evolution of each CIR over ~180^o longitude. The relevant deliverabale, D5.2 is entitled 'Fitting the leading edge of CIRs and determination of latitudinal extent', which, in practice tranlstes to deriving and cataloguing the kinematic properties of each CIR.

For each CDS, we fitted first the clearest tracks associated with individual density irregularities entrained by the SIR. We then used the fact that a CDS corotates during its passage in the heliospheric imagers, thereby leaving a characteristic pattern in the J-map. This pattern was then computed theoretically and superposed onto the real J-map. To determine the time-dependent 3-D location of each CDS we select a single reference track in each pattern, corresponding to a single blob, and fit its trajectory by assuming that it moves radially outward at constant speed (the so-called 'fixed-phi' approximation). It can be shown that the time variation of its elongation, α(t), can be described using the equation:

$$\alpha(t)=\arctan[V_b t\sin(phi)/\{r_A(t)-V_b t\cos(phi)\}], \qquad \text{Eq. 1}$$

here V_b is the radial speed of the blob, *phi* is its propagation angle relative to the observer (which equates to ecliptic longitude relative to the observer for a feature propagating in the ecliptic plane), and *rA(t)* is the radial distance of the observer from the Sun (the observer is ST-A in this case). The algorithm to trace this SIR pattern folds in a correction for the orbital motion of the spacecraft. This orbital motion changes the location of the viewpoint of the probe (STEREO-A) and can have an important effect when the SIR pattern is considered over a 180 degrees of corotation in the HI field of view lasting up to 18 days. Rearranging Equation (1) to express the blob speed in terms of α and phi, we can compute the minimal speed that a solar wind feature must have to cross two adjacent J-map bins during the 2-hour cadence. In this study we fit the apparent position of CDSs mostly inside a 10^o-60^o elongation window. We find that for typical longitudinal separations of the radially outflowing feature, phi=10^o, 45^o, and 60^o, the minimal speed must be ~30 kms^{-1} or ten times less than typical solar wind speeds. At phi=90^o, the minimal speed is higher for larger elongations but at these large heliocentric distances the blobs become undetectable. Overall, the time to cross two consecutive J-map bins is between 15 minutes and 1 hour at 300 kms^{-1} depending on the direction of propagation. The solar wind speeds we deal with in this work are never much less than 300 kms^{-1}. Consequently, the J-maps offer sufficient precision to track solar wind features with a precision of ~30 kms^{-1} and to compare with in situ measurements with 1-hour cadence.

An example of a fit to a single CDS, spanning July and August 2008, is shown in panel (b) of Figure 3.5.3. The red curve indicates the elongation variation of the fitted blob, emitted at 2008-08-03T21:36:26 UT. Its best-fit radial speed is V_b=358±10 kms^{-1} and it propagates at a best-fit longitude of *phi*=34^o ± 3^o relative to STEREO-A. The family of black curves in this panel are simulated (using Equation (1)), assuming regular release of a series of density structures at multiples of 8 hours relative to the release time of the blob associated with the red curve. These blobs cover the range of phi values decreasing from 180^o to 0^o with increasing time. The entire pattern comprises the CDS, and the elongation angle marking its outermost location at any one time (indicated by green arrows in panel a) is the time-varying location of the tangent to the overall spiral structure. This tangent is also indicated as a corresponding green arrow in panel (c), which shows the orbital configuration at the emission date of the reference blob. STEREO-A is represented by the red spacecraft symbol, STEREO-B by the blue symbol and the Earth by the blue sphere between two spacecraft. The combined field of view of the HI cameras on STEREO-A is delimited by red lines. The blue spiral represents the corotating Parker spiral arm, propagating radially outward with the same speed as deduced from fitting the time–elongation profile of the blob corresponding to the red curve in panel (b). The red arrow represents the trajectory of that blob (34o from the Sun; the STEREO-A line). Panel (d) shows the coronal map from the Carrington rotation 2073 at a wavelength of 195 Å, derived from STEREO-A/EUVI images. The back-projected source longitude of the CDS is at 352.2^o Carrington longitude (indicated by a blue circle). A V-shaped coronal hole is clearly visible at 300^o -

320^{o} longitude, to the east of the source location.

There are several factors that can affect the identification of CDSs in J-maps constructed from running-difference images. These include the following:

- Times when multiple CDSs pass through in the field of view at the same time. This can occur when the streamers are highly warped, for instance when the non-axisymmetric solar magnetic field becomes strong as solar activity increases.
- Times when multiple CMEs pass through the field of view at the same time as the passage of the CDS. This problem is important as solar maximum approaches (e.g. in the period 2011 – 2014). Given the high frequency of CMEs, it then becomes very difficult to identify CDSs in the images. We analyze this effect later in the paper.
- Times when the Milky Way passes through the field of view. This makes it extremely challenging to identify the passage of CDSs.

Consequently, there are a number of CDSs that are missed completely or misidentified when making such a catalog derived from the STEREO-A heliospheric imagery.

Once the trajectory of the best-defined small-scale transient (blob) is fitted for its radial speed and direction, we generate a pattern of converging tracks by using the following assumptions to model the entire CDS:

- the best-fit radial speed of the reference blob is common to all density inhomogeneities within the fitted CDS,
- the corotating structure is rotating with a fixed period of 25.38 days.

We ensure that the elongation variation of the tangent to the CDS (i.e. the locus of enhanced visibility) maps closely the envelope of the converging tracks. In fact, the fit is only validated if other tracks are well fitted, and all tracks converge toward the locus of enhanced visibility. Both of these criteria usually impose that the SIR be well observed by the heliospheric imagers over a large range of elongations (>40^{o}). SIRs that are poorly observed because (1) the white-light signature is too weak, (2) too many CMEs passed in the field of view are not fitted. We found that HI detects all S/CIRs passing in its field of view as CDSs at solar minimum but at solar maximum the many CMEs passing in the field of view 'hide' up to half of the passing S/CIRs. The reader is referred to Figure 3.5.1 as an illustration of the work discussed in this sub-section.

Figure 3.5.3 presents histograms of the best-fit speed (a) and phi angle (b) for the selected blob tracked within each CDS. The mean speed ⟨ Vb ⟩=311±31 kms^{-1} and mean angle ⟨ phi⟩=49^{o} ±20^{o} . The maximum fitted speed is 404 kms^{-1} and the minimum is 233 kms^{-1}. The range of speeds is roughly the same for both solar minimum (2007 – 2009) and solar maximum periods (2010 – 2014). No correlation was found between the level of solar activity and the average speed of CDSs. The Gaussian nature of the speed distribution has no physical basis a priori. As can be seen from panel (b) of Figure 3.5.3, the majority of fitted density blobs propagate at phi angles between 20^{o} and 60^{o}. From the STEREO-A perspective, these separation angles correspond to optimal visibility of the corotating spiral, because the line-of-sight in the ecliptic plane remains tangential to the spiral over a large range of elongations and density structures propagate close to the so-called Thomson sphere. This explains why there are only a few events with phi>90^{o} and no events at all with phi>130^{o} while the maximum possible value is close to 180^{o} (corresponding to a blob traveling away from the spacecraft).

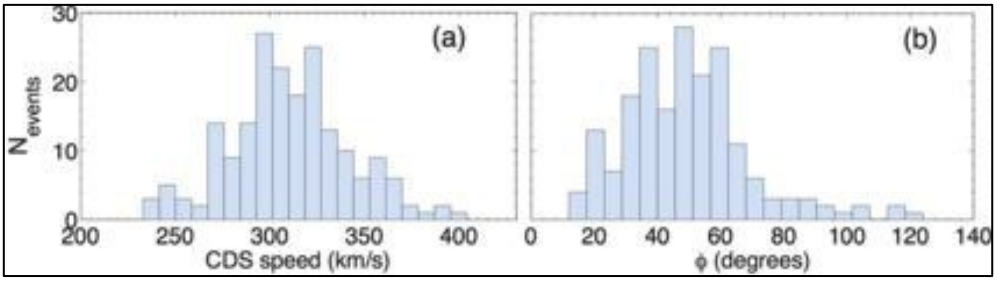

Fig. 3.5.3 - Distributions of CDS speeds (panel (a)) and phi angles (panel (b)) for all cataloged events observed between April 2007 and August 2014. These are derived by fitting the selected blob within each CDS. The mean speed is ⟨Vb⟩=311±31 kms^{-1} and the mean direction is ⟨phi⟩=49^{o} ±20^{o}

The catalogue currently extends from April 2007 to August 2014 (see HELCATS webste, PRODUCTS tab and WP5), it lists the following (see Figure 3.5.2):

- A unique SIR identifier, e.g. HSIR_A__20070419_191210
- The spacecraft making the white-light observations (STEREO-A or STEREO-B),
- The 'reference launch time' of the most clearly observed density irregularity embedded in the SIR along the ecliptic plane: Format: YYYY-MM-DDTHH:MM:SS,
- Rotation period of the SIR assumed fixed at 25,38 days,
- The radial velocity (in km/s) of the SIR along the ecliptic plane,
- The error in radial velocity (in km/s) of the SIR along the ecliptic plane,
- The longitudinal separation (called 'beta', in degrees) between the observer and the most easily tracked density feature embedded in the SIR along the ecliptic plane,
- The error in the longitudinal separation (in degrees) between the observer and the most easily tracked density feature embedded in the SIR along the ecliptic plane,
- The Carrington longitude (in degrees) of the SIR source (tracked along the ecliptic plane),
- The HAE longitude (in degrees) of the SIR source (tracked along the ecliptic plane),
- The Carrington longitude (in degrees) of the coronal hole in EUI identified near the source region of the SIR in Carrington coordinates,
- The Carrington rotation number of the identified source.

SIR Identifier	Observer	Reference launch time	CoRot. Period	Velocity	Err velocity	beta	err beta	Carr Source Long.	HAE Source Long.	Carr CH Long.	Carr. CH. La
	Observer		(days)	(km/s)	(km/sec)	(deg)	(deg)	(deg)	(deg)	(deg)	(deg)
HSIR_STA_20070619_155931	STEREO-A	2007-06-19T15:59:31	25,38	292	11	44	4	355,7	242,4	10	
HSIR_STA_20070624_073810	STEREO-A	2007-06-24T07:38:10	25,38	326	27	44	8	294,2	246,6	292	
HSIR_STA_20070628_073032	STEREO-A	2007-06-28T07:30:32	25,38	245	23	68	7	221,2	230,7	235	
HSIR_STA_20070711_083535	STEREO-A	2007-07-11T08:35:35	25,38	284	5	42	1	72,8	267,3	102	
HSIR_STA_20070718_203106	STEREO-A	2007-07-18T20:31:06	25,38	323	7	54	6	323	263,4	295	
HSIR_STA_20070729_125707	STEREO-A	2007-07-29T12:57:07	25,38	287	4	32	1	203,6	295,7	203	
HSIR_STA_20070806_035723	STEREO-A	2007-08-06T03:57:23	25,38	279	27	67	8	71,1	271,7	105	
HSIR_STA_20070814_182817	STEREO-A	2007-08-14T18:28:17	25,38	288	17	90	18	297,1	259,4	NaN	NaN
HSIR_STA_20070823_013231	STEREO-A	2007-08-23T01:32:31	25,38	277	9	31	2	242,6	322,7	243	
HSIR_STA_20070903_192613	STEREO-A	2007-09-03T19:26:13	25,38	266	12	53	3	68,3	315,1	NaN	NaN

Fig. 3.5.4 - A sample of the CIR catalogue data available online on the HELCATS website.

The orbital configuration of STEREO and SOHO during this period is presented in the polar view of the ecliptic plane depicted in Figure 3.5.5(c). The STEREO spacecraft were 140° ahead and behind the Earth and separated by 80° from each other. The location of a CIR that passed through the Field-of-view (FOV) of the HI instruments, and will be presented later, is shown in Figure 3.5.5(c) as a blue spiral. We will demonstrate that this CIR was induced by the giant coronal hole seen in Figure 3.5.5(a). Over several days, the CIR, the coronal hole and the north-south oriented neutral line corotated from the longitude of Earth to that of STEREO-A. Hence, they passed through the FOVs of LASCO and SECCHI, giving us the opportunity to study the variability of the corona and the solar wind from multiple vantage points and with different instruments. The CIR was detected by the in-situ instruments on board the STEREO and L1 spacecraft during several Carrington rotations.

Figure 3.5.6 shows six time-elongation maps (J-maps) constructed using HI-1/2A running-difference data (Davies et al. 2009) at three different Position Angles (PAs) during the passage of the CIR of interest, from 2013 May 28 to June 06. Most of the tracks that are visible on these maps are the signatures of outward-moving blobs entrained by the CIR.

We identified each separated track in each J-map as a blob and assigned it a theoretical trajectory, which is overplotted as a red solid line in the right hand panels. This theoretical trajectory is calculated assuming a constant velocity and direction of propagation. The computed velocity is 400 kms^{-1}, which is the velocity of the slow wind part of the CIR measured in-situ. The direction of each blob is determined by the Carrington longitude of the neutral line, given by the PFSS extrapolation of the photospheric magnetic field (Figure 3.5.5).

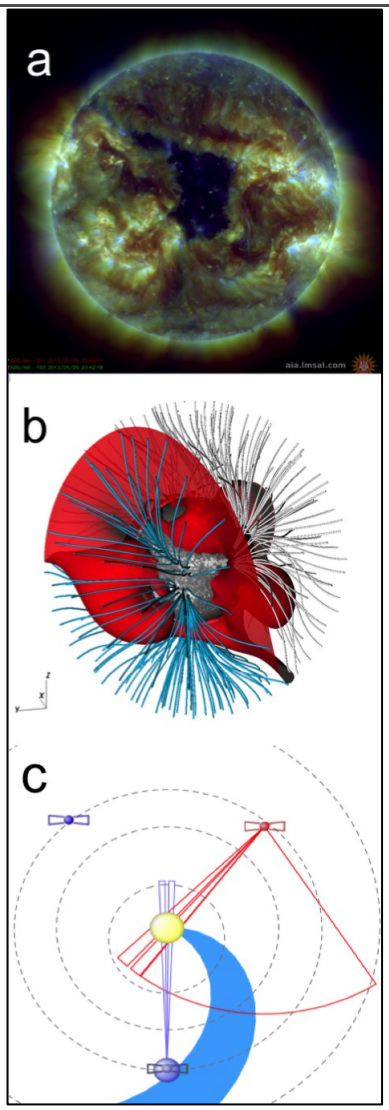

Fig. 3.5.5 - Top: AIA image of the solar corona (193 Å) on 29 may 2013. Middle: PFSS reconstruction of the coronal magnetic field for solar rotation 2137. The red sheet is the neutral sheet and each line colour corresponds to a different polarity of the magnetic field lines. Bottom: polar map of the ecliptic plane with the position of Earth (blue dot), Sun (yellow dot), STEREO-A (red butterfly) and B (blue butterfly), the field of view of STEREO HI-A (red triangle), COR2-A (red double triangle) and C2 (blue double triangle) and the CIR (blue spiral) on 2013/06/03. This plot was generated with propagation tool.

The initial condition is chosen such that the theoretical trajectory and the corresponding trace cross, at the same time, an arbitrary height of 20 solar radii. This trajectory is projected into the J-map using Equation 1 of Rouillard et al. (2008). The theoretical trajectories are accurate representations of the actual observed traces. This confirms that the CIR-entrained blobs are back-traced to the neutral line, as shown by P lotnikov et al. (2016). The result of this analysis is exploited further in Deliverable 5.3 to study the coronal origin of streamer blobs and to determine for the first time the source location of streamer blobs.

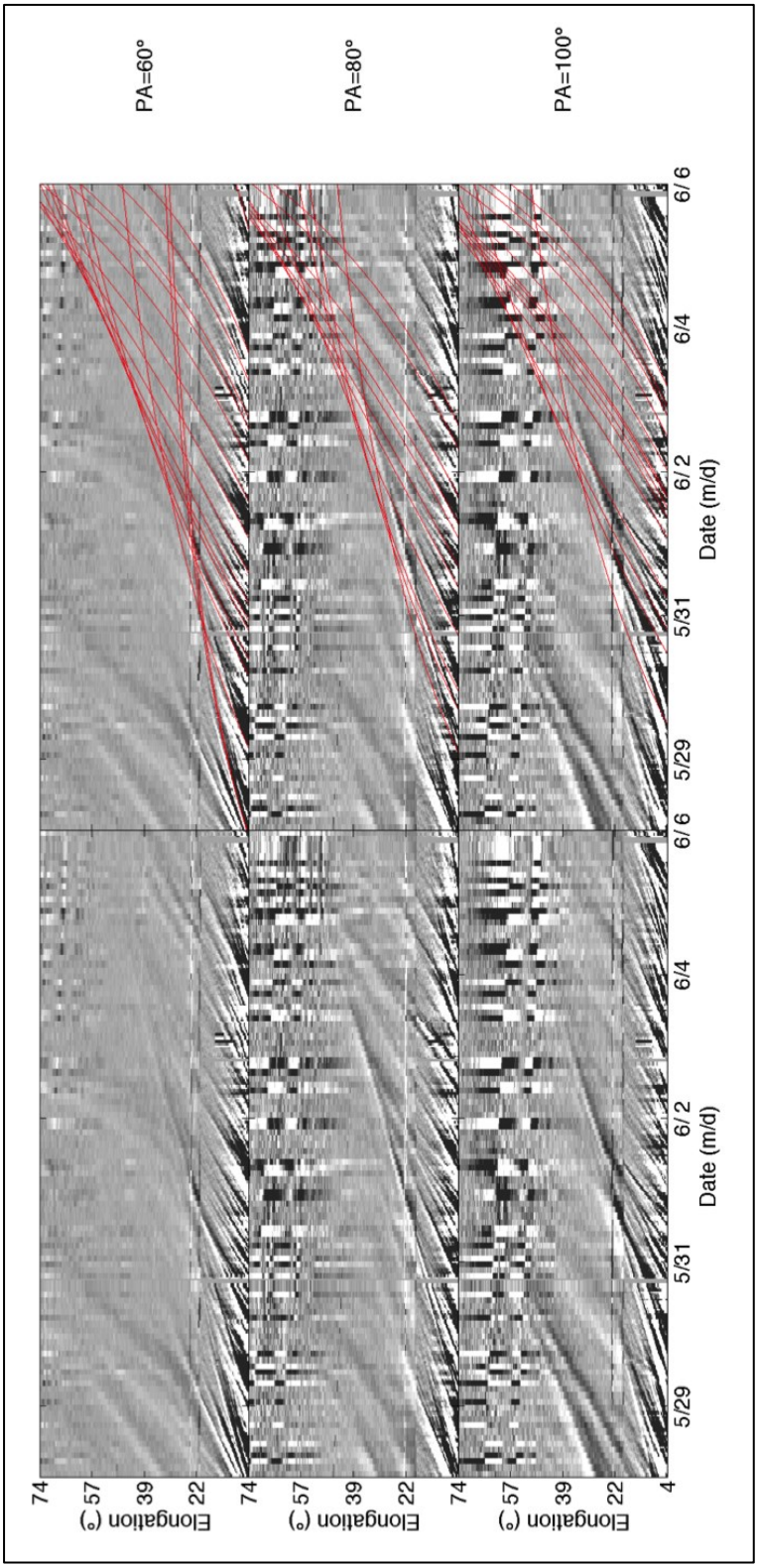

Fig. 3.5.6 - left: J-maps of HI-A at 100° (top), 80° (medium) and 60° (bottom) position angle during the passage of the CIR, from 2013 May 28 to June 06. The right hand plots are copies of the same J-maps as the left hand plots with the theoretical blob trajectories plotted as red solid lines.

WP5 TASK 5.3: COMPARING BACK-PROJECTED CIR TRACKS WITH CORONAL SOURCES (TASK LEAD: UPS)

Using the derived trajectories and kinematic properties of CIRs and their small-scale transients, in task 5.3, we are determining, for each CIR observed in white-light images, if there is an associated coronal hole observed in EUV. For each CDS fitted from task 5.2, we record the back-projected emission time (at the solar surface) of the blob that produces the reference track in the ecliptic J-map. By fitting its trajectory, we also derive the heliocentric ecliptic longitudinal separation of this small-scale transient with respect to the STEREO-A spacecraft (phi) and its average radial speed Vb. Because the fitting process also 'folds in' a fit by eye to the entire pattern of converging tracks, Vb also represents the 'average' radial speed of the entire CDS. By back-projection, we also obtain an estimated source location for the fitted blob, from which, when combined with the launch time, we can assign to it a Carrington rotation number. Since we are analyzing a corotating structure, the source location of the fitted blob is the source location of all inhomogeneities constituting the CDS. Using this estimate of the source location, we can use EUV images to identify the location of the closest equatorial coronal hole.

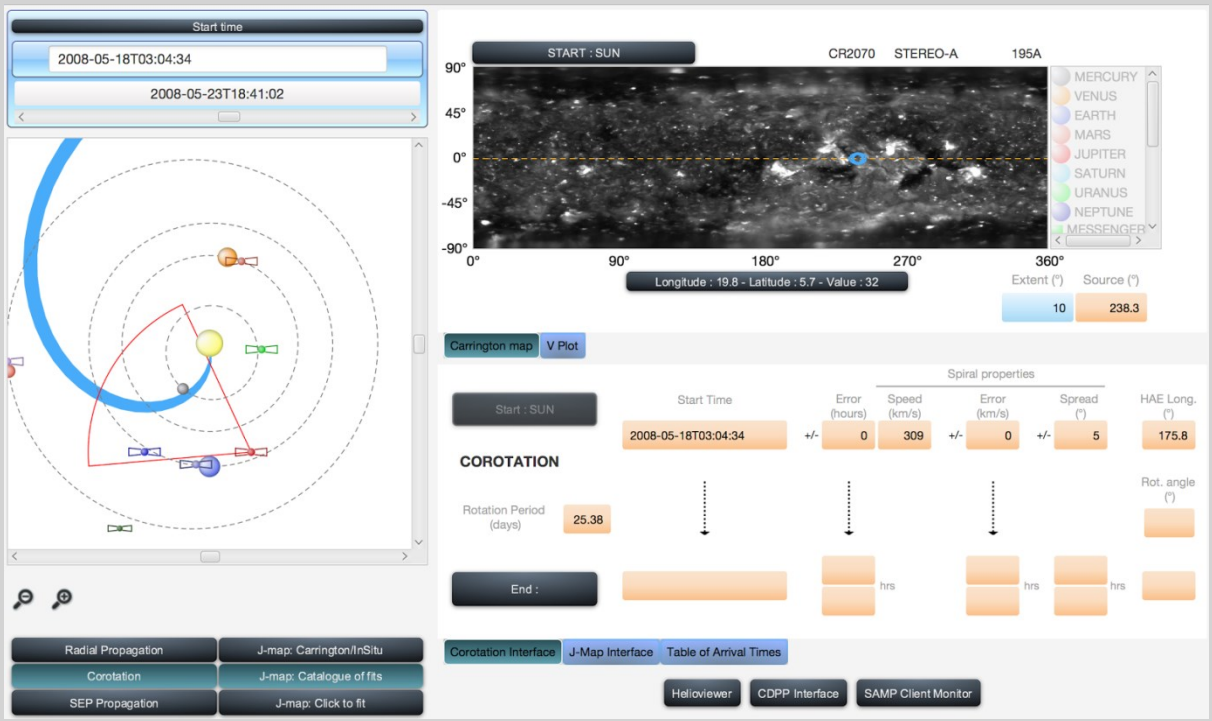

Fig. 3.5.7 - Panel view of the propagation tool used to carry out the source region analysis. The CIR spiral corresponds to the CIR detected by SECCHI-A between 14 and 28 May 2008. The Carrington map presented in the top-right hand part of the panel is a map constructed from EUVI-A images taken at 195 Angstrom and shows the association between the CIR source region (blue circle inside blue oval) and the coronal hole.

In this first statistical analysis of the solar origin of CDSs, we simply visually inspected Carrington maps constructed from 195 Å EUVI images from both STEREO-A and STEREO-B for the presence of coronal holes, the westward edges of which are separated by less than 30° of longitude from the estimated source location of each CDS. It should be borne in mind that back-projecting radially to the solar surface, as we did, inherently ignores the complexity of the lower corona. The Carrington longitude of the directly back-projected coronal source region was cataloged for every CDS. Figure 3.5.7 presents the tool used to analyse the source location of a CDS listed in the catalogue. This CDS was associated with a clear coronal hole located Eastward of its source location identified in a Carrington map constructed from EUVI images (top right-hand part). For only 20 % of CDSs was no coronal hole identified in the vicinity of their source location. The general presence of coronal holes to the east of the source location of ecliptic CDSs is strongly suggestive that such CDSs are mostly associated with the entrainment and compression of density inhomogeneities by high-speed (coronal-hole) streams. This is confirmed later in the current paper by the systematic comparison of the predicted arrival times of our identified CDSs with in situ measurements. For those events associated with coronal holes, we

also carried out the reverse analysis by locating the western boundary of the coronal hole and checking whether, for an average radial speed of ~300 kms^{-1}, we would predict the presence of an associated CDS in an ecliptic J-map. This was done for several events and gave good agreement with the results from the analysis of the J-maps.

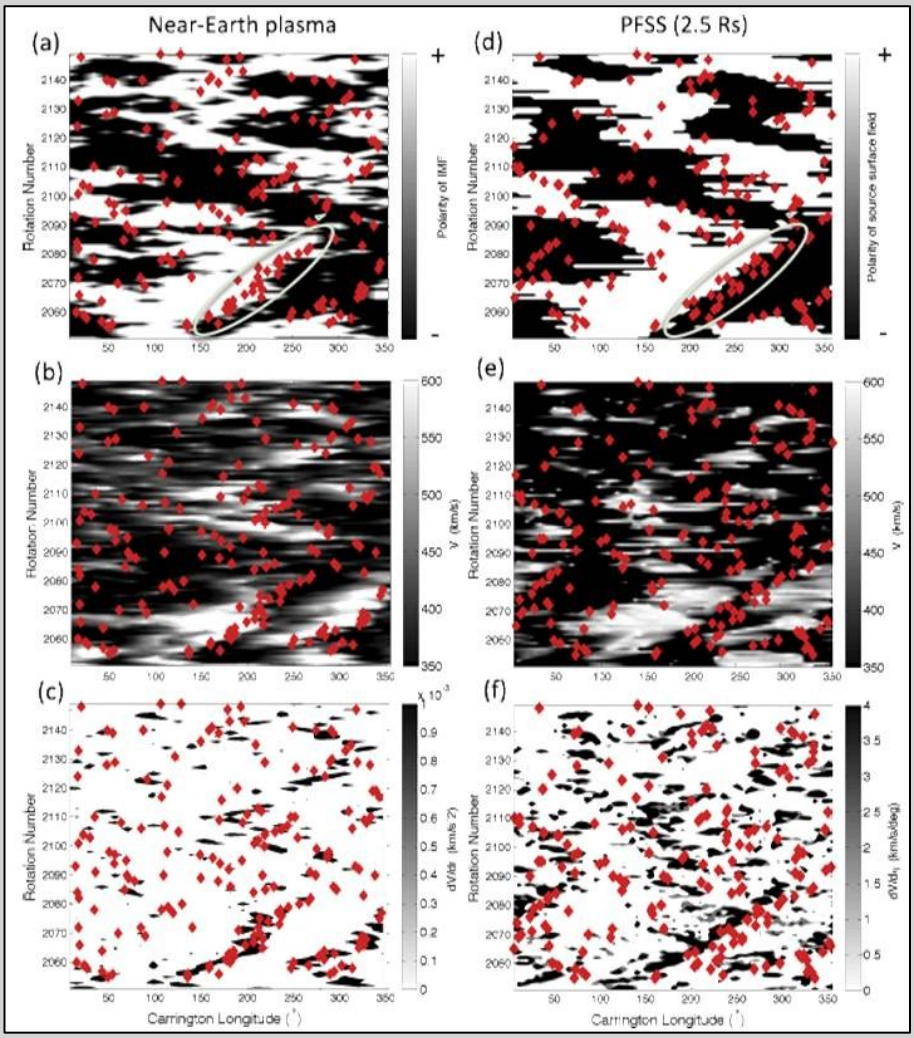

Fig. 3.5.8 - A series of contour plots of in situ measurements of the near-Earth (L 1) plasma (panels (a) – (c)) and of the solar magnetic field from a PFSS model (panels (d) – (f)). All panels are presented in the same format, with Carrington longitude running along the X-axis and Carrington rotation number along the Y-axis. The red diamonds indicate the estimated Carrington rotation number versus longitude of each CDS in our catalog. Note that time runs from high to low values of Carrington longitude (right to left along the X-axis) and low to high Carrington rotation number (bottom to top along the Y-axis).

To analyze the origin and evolution of CDSs over the solar cycle, and interpret the observations shown earlier, we present a series of contour plots in Figure 3.5.8 of in situ measurements of the near-Earth (L 1) plasma (panels (a)–(c)) and of the solar magnetic field derived using a PFSS model (panels (d)–(f); Wang and Sheeley, 1992). All contour plots are presented in the same format, with Carrington longitudes running along the X-axis and Carrington rotation number along the Y-axis. Carrington rotation numbers range from 2051 to 2150 i.e. from January 2007 to May 2014. We remind the reader that, on these stack plots, time runs from high to low values of Carrington longitude (right to left along the X-axis) and from low to high numbers of Carrington rotation number (bottom to top along the Y-axis). All measurements correspond to magneto-plasma parameters (described below) either directly measured in (left-hand columns) or extrapolated to (right-hand column) the ecliptic plane. The red diamonds overlaid in each panel show the estimated Carrington rotation number versus longitude of each CDS in our catalogue.

Panel (a) shows the polarity of the interplanetary magnetic field derived from the OMNI dataset (King and Papitashvili, 2005), converted from RTN coordinates to azimuth angle, φIM. We consider that all field orientations that are within 90° of the average Parker spiral orientation azimuths of 45° and 315° have negative and positive polarity, respectively. We have shifted the times of in situ measurements backward by 5 days to roughly account for propagation time to 1 AU. In this way we have associated to the resulting 'solar date' of the measurement, a Carrington rotation number and a longitude. The resultant data, displayed in panel (a), demonstrates the well-known sector structure of the interplanetary magnetic field as well as showing the transitions between polarities that mark the passages of the heliospheric current sheet. This panel shows that a magnetic field sector structure comprising between two and four sectors existed in the ecliptic plane throughout this weak solar cycle. The red diamonds correspond to the predicted Carrington rotation number versus longitude of all cataloged CDSs (i.e. the results from the previous section).

Examination of the locations of these red diamonds show that CDSs occur most frequently at locations where the interplanetary magnetic field polarity reverses, i.e. at the heliospheric current sheet; this is particularly clear during the solar minimum years (see the region bounded by the green oval) but is also visible at solar maximum. Panel (b) enables comparison of the CDS arrival time with the radial solar wind speed measured in situ. The red diamonds tend to cluster in those regions where the solar wind speed increases (i.e. changes from black to white) rather than decreases (changes from white to black). This is more clearly seen in panel (c), which presents the radial gradient in the solar wind speed. Panels (b) and (c) confirm the association between CDSs and SIR/CIRs demonstrated in the previous section. Interestingly, there are rare cases of CDSs occurring on the rarefaction side of coronal holes, where the solar wind speed decreases with decreasing Carrington longitude (e.g. between 100° and 120° longitude, between rotations 2070 and 2080). These occur, nevertheless, on a magnetic sector boundary. We will discuss these events later.

Since we include the Carrington longitude and estimated launch time of each CDS in the catalog, we can also compare these parameters with reconstructions of the coronal magnetic field. We apply the potential field source surface (PFSS) technique of Wang and Sheeley (1992) to magnetograms taken by the Wilcox Solar Observatory (WSO). Panel (d) shows the resultant polarity of those magnetic field lines threading the source surface set at 2.5 $R_\odot$ that are connected to the Carrington coordinates of Earth. The PFSS-derived sector structure is in very good agreement with the sector structure derived from in situ measurements. Again there is a clear tendency for CDSs to cluster around the neutral line (e.g. region bounded by the green oval). This provides further evidence for a close association between CDS and polarity inversions near the Sun. Nevertheless, there is evidence, both in the panels presenting the in situ data and the PFSS output, of the rare occurrence of CDSs occurring far from the neutral line; these could be investigated in future studies.

For completeness, we also predicted the speed of the solar wind streaming out of flux tubes reconstructed using the PFSS model. To do this, we computed the flux tube expansion factor FS, the amount by which the magnetic flux tube expands in solid angle between the photosphere and the source surface (Wang and Sheeley, 1990), for each flux tube connected to the Earth. Wang and Sheeley (1990) showed that the expansion factor is anti-correlated with the solar wind speed, V. To perform this analysis, we used the following relationship between the expansion factor and the solar wind speed, which has been shown to reproduce roughly the solar wind speed measured near 1 AU (Rouillard, Lockwood, and Finch, 2007):

$$V=280+350\times\exp(F_s/14)^2 \qquad \text{Equation 2}$$

Panel (e) of Figure 3.5.8 displays the predicted solar wind speed at the source surface (2.5 R_s) and panel (f), the longitudinal gradient −dV/dphi in the predicted solar wind speed (the negative sign in the latter expression being related to the decrease in Carrington longitudes with time). This longitudinal gradient will be manifested, as the Sun rotates, in a radial solar wind gradient in the interplanetary medium (e.g. panel (c)). The red diamonds cluster predominantly in slow solar wind regions (panel (e)), with a significant fraction lying close to the boundary with rising solar wind speed. Just as for panels (b) and (c), there are cases of CDSs originating within the predicted source regions of high-speed solar wind but still near the sector boundary (as shown in panel (a)).

The clearest relationship seen in the right-hand contour plots is between CDS location and the magnetic sector boundary. To test this correspondence more quantitatively, we show (as a histogram in Figure 3.5.9) the distribution of the angular separation, Δγ, between the PFSS neutral line and the recorded CDS source locations at the Sun. Half of the 190 cataloged in-ecliptic CDS events are separated by less than 10° from the neutral line. However, most of our cataloged CDSs occurred at solar minimum, when the neutral line tends to be less warped than at solar maximum, and therefore when the separation between sources in the ecliptic plane and the neutral line would be expected to be small. Hence, in order to test the significance of this result we compared the distribution of observed Δγ values with one that would result from a random distribution of the same number of source locations. We find that the peak in Δγ for randomly distributed sources also occurs in the [0°--10°] bin but is only around half the size of the peak in the observed Δγ distribution. From this we can conclude that there is an overall strong tendency for CDSs to originate near the coronal neutral line.

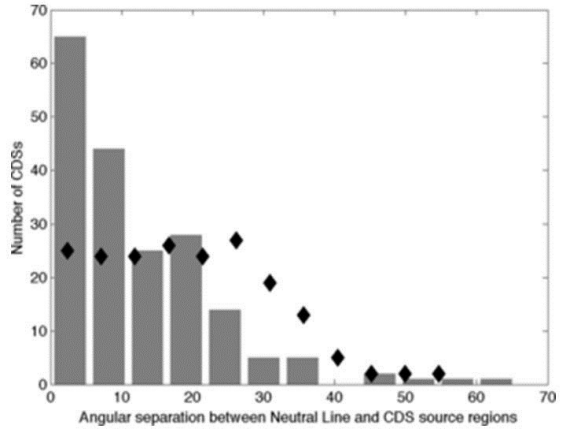

Fig. 3.5.9 - Distribution of the angular separation, Δγ, between the PFSS neutral line and the recorded CDS source location at the Sun. The distribution resulting from random source locations (instead of fitted CDS source locations) is plotted using black diamonds.

In addition, with the model developed for WP6, we can compare the source region of CDSs and the distribution of fast and slow solar wind in the low corona including boundaries where fast solar wind emerges eastwards of the slow solar wind. The difference with the approach presented before is that the solar wind generated comes now from a physics-based model rather than an empirical relation. The details of the simulation work are given in the deliverables of WP6.

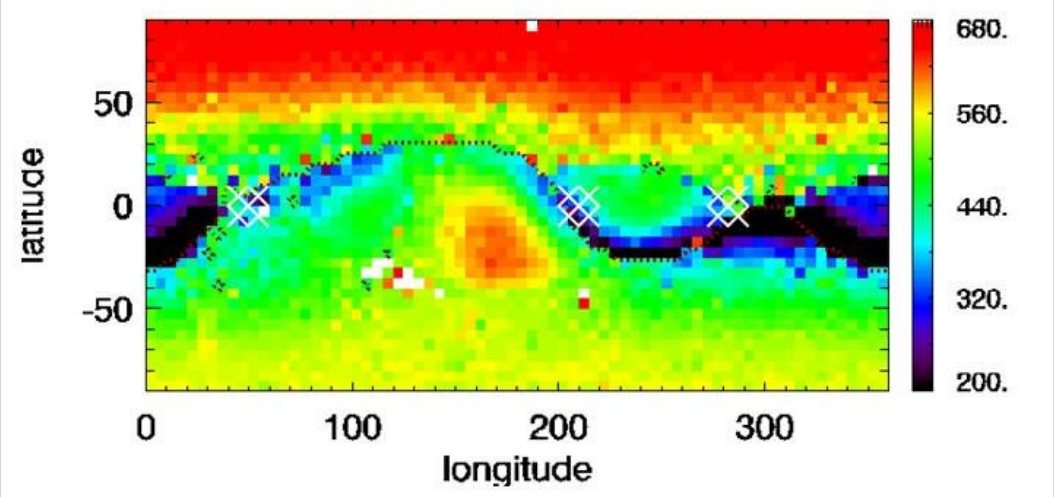

Fig. 3.5.10 - A map of simulated solar wind speeds (in km/s) in a Carrington format at 21.5 R_s. The longitudes of the source location of CIRs are overplotted on the map as white crosses. These maps are available at https://stormsweb.irap.omp.eu/doku.php?id=windmaptable

We provide to users a comparison of the source location of CDSs with the distribution of solar wind speeds plotted in a Carrington map format. As can be seen in an example map shown in Figure 3.5.10, the source location of CIRs are systematically located where fast and slow solar winds originate at adjacent locations.

We have carried out a multipoint analysis of small transient structures released from the north-south tilted helmet streamer into the slow solar wind over a broad range of position angles during Carrington Rotation 2137. This CIR was introduced in Deliverable 5.2. Combining the remote-sensing observations taken by the Solar-TErrestrial RElations Observatory (STEREO) mission with coronagraphic observations from the Solar and Heliospheric Observatory (SoHO) spacecraft, we show that the release of streamer blobs, which subsequently move away from the Sun, is associated with the concomitant formation of transient structures collapsing back towards the Sun previously named 'raining inflows'. This is the first direct association between outflowing blobs and raining inflows, which locates the formation of streamer blobs above the helmet streamers and gives strong support that the blobs are released by magnetic reconnection.

C2 has observed a large number of inflows during solar cycle 23 [Sheeley et al., 2007, 2014]. Some extended inflows, known as falling curtains, were associated with outflowing counterparts in the C3 FOV and sometimes in the C2 FOV [Sheeley & Wang, 2002]. Related to these are so-called in/out pairs, which are combined inflowing and outflowing plasma, mostly associated with Coronal Mass Ejections (CMEs) [Sheeley & Wang, 2002]. A third category of inflows — raining inflows — has been detected in the C2 FOV. Such raining inflows manifest as a multitude of density structures falling back towards
the Sun when a highly tilted coronal current sheet or neutral line passes in the plane of sky (POS). No clear outflowing component could be associated with these raining inflows [Sheeley et al., 2007, 2014]. Either there was no corresponding outflowing component or its brightness fell below the detection threshold of the C3 coronagraph. In this paper, we make use of the complementary instrumentation offered by the SECCHI package [Howard et al., 2008] on board the twin STEREO spacecraft [Kaiser et al., 2008], and in particular the highly sensitive Heliospheric Imager (HI) instruments to search for a potential outflowing component. The SECCHI package on each STEREO spacecraft consists of an inner coronagraph (COR1) that observes the corona between 1.4 and 4 solar radii, an outer coronagraph (COR2) that observes between 2.5 and 15 solar radii and the HI instrument, which observes from the outer edge of the COR2 FOV out to 1 AU and beyond.

HI has been successfully used to track streamer blobs over an extended range of heliographic longitudes, and in particular blobs that have been compressed by CIRs (Deliverable 5.2). Such compression counteracts, at least in part, the strong radial expansion experienced by these structures as they propagate outward [Rouillard et al., 2008; Sheeley et al., 2008]. The heights imaged by HI1 are well beyond those imaged by the C2 coronagraph, in regions where no inflows have ever been observed. The COR2 instrument, on the other hand, is better suited to observe both inflows and outflows, and covers the gap between the C2 and HI1 FOVs with a higher sensitivity than C3 at low heights, where blobs are still dense enough to be clearly observed with a coronagraph. Of the two coronagraphs, C2 is better suited than COR2 to observe inflows because the latter typically form at mid heights in the C2 FOV and therefore the inflowing motion can be captured in multiple consecutive images.

Over a long time scale, the total number of inflows of all kinds is well correlated with solar activity [Sheeley & Wang, 2014]. This explains why few raining inflows have been reported with STEREO, as the mission has operated thus far during the least active solar cycle of the space era. On the short time scale, the total inflow rate is better correlated with the gradient of the non-axisymmetric quadrupolar component of the coronal magnetic field [Sheeley & Wang, 2014]. The solar corona achieved a topology such that this component was important during Carrington rotation 2137 (May to June 2013), with a highly tilted neutral line, making it a favorable period to observe raining inflows.

The period analysed corresponds to the same event as the one presented in Deliverable 5.2 Figure 3.5.11 presents a sequence of running-difference images from some of the remote-sensing instruments onboard STEREO-A and SOHO. The coronagraphs and HI instruments detected multiple streamer blobs, over the broad range of latitudes spanned by the north-south oriented neutral line. Using STEREO coronagraph observations, Sheeley et al. (2009) showed that streamer blobs imaged by a detector looking at a helmet streamer side-on are much narrower than those blobs that are observed by a similar detector looking at a helmet streamer from

a face-on perspective. With the latter configuration, blobs tend to appear more reminiscent of magnetic loops (see also Rouillard et al., 2011).

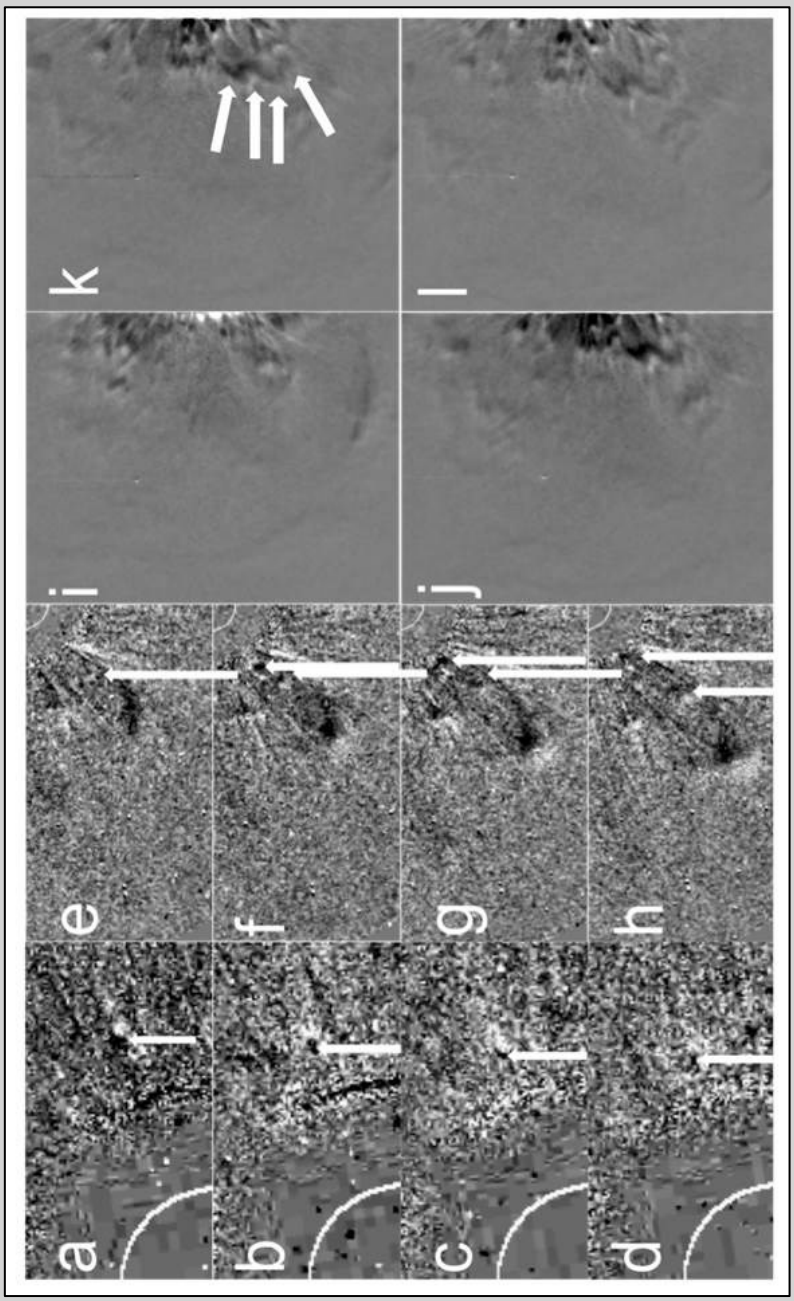

Fig. 3.5.11 - (a-d): Sequence of images of a portion of LASCO C2 from 2013/06/03 06:24:05 to 07:36:05 showing a raining inflow with the white arrow. (e-h): Sequence of images of a portion of SECCHI COR2-A from 2013/05/29 12:54:00 to 14:24:00 showing an in/out pair with the white arrows. (i-l): Sequence of images of a portion of SECCHI HI1-A from 2013/05/30 14:49:01 to 22:09:01. The white arrows in 3k signal a filamentary structure as an example.

The structures imaged by HI-1 have loop-like aspects, but are far more numerous over all observed latitudes than observed in previous studies. The loop-like structures appear to form larger-scale filamentary structures in the HI1-A images extending over a broad range of latitudes. One such filamentary structure is indicated by a series of white arrows. Analysis of the variability along an east-west oriented streamer/neutral sheet (i.e. as a function of longitude) is difficult with images taken from a vantage point in the ecliptic plane because white-light features are integrated along the line of sight. By contrast, images of a north-south oriented neutral

sheet allow us to study, at a single point in time, the distribution of streamers blobs over an extended surface area of the neutral sheet. In agreement with Sheeley and Rouillard (2010), the tangent to the CIR manifests as a C-shaped density enhancement on the anti-sunward side of the HI1-A FOV.

In the coronagraph images, we can observe these same structures during the earlier phase of formation. Figure 3.5.12(e-h) shows an example of one of the blobs observed by COR2. This blob is associated with an inflow, also imaged by COR2. To the best of our knowledge, this is the first observation of an inflow detected by STEREO remote-sensing instrumentation. When the neutral line passes into the POS of SOHO, C2 observes some raining inflows in addition to the blobs. As explained in Section 1, magnetic reconnection has been suggested as a viable mechanism to release streamer blobs, but so far this is unsupported by observational evidence.

Figure 3.5.12 shows six time-elongation maps (J-maps) constructed using HI-1/2A running-difference data at three different Position Angles (PAs) and taken out of Deliverable 2.1. during the passage of the CIR of interest, from 2013 May 28 to June 06 (Davies et al. 2009). Most of the tracks that are visible on these maps are the signatures of outward-moving blobs entrained by the CIR.

We identified each separated track in each J-map as a blob and assigned it a theoretical trajectory, which is overplotted as a red solid line in the right hand panels (see Deliverable 5.2). This theoretical trajectory is calculated assuming a constant velocity and direction of propagation. The computed velocity is 400 km/s, which is the velocity of the slow wind part of the CIR measured in-situ. The direction of each blob is determined by the Carrington longitude of the neutral line, given by the PFSS extrapolation of the photospheric magnetic field. The initial condition is chosen such that the theoretical trajectory and the corresponding trace cross, at the same time, an arbitrary height of 20 solar radii. This trajectory is projected into the J-map using Equation 1 of Rouillard et al. (2008). The theoretical trajectories are accurate representations of the actual observed traces. This confirms that the CIR-entrained blobs are back-traced to the neutral line, as shown by Plotnikov et al. (2016).

Since the blobs are already visible at low coronal altitudes (Sheeley et al., 1997), some of the traces observed in HI, likely start in the coronagraphs. In order to track them down to their origin, we combined the J-maps derived from COR2 and the lower part of HI1. Figure 3.5.13 shows the STEREO-A J-maps from 125° (upper panel) and 80° PA (lower panel) that combine COR2-A data with observations from the near-Sun part of the HI1-A FOV. The J-maps cover the estimated time of passage of the neutral line through the left limb of the STEREO-A POS, from 2013 May 29 to June 01. Many of the outflowing blobs seen by HI1-A during this period can be traced back to inflows seen by COR2-A, and every inflow is associated with an outflowing blob observed first by COR-2A and then by HI-1A. Figure 3.5.14 constitutes the first ever direct observation of the association between raining inflows and the streamer blobs that are released in the slow solar wind and subsequently entrained by a CIR. The separation between the outflowing blobs and the inflows occurs typically at an altitude between 5 and 6 solar radii from the center of the Sun.

The height of this separation makes COR2 much better suited than C3 to observe it. The separation occurs close to the inner edge of C3 FOV, where coronagraphs have most visibility issues, and close to the middle of COR2 FOV. It would not be possible to observe this separation in C2 because, at most, one or two frames of the outflowing part would be available at the outer edge of the C2 FOV, where signal to noise ratio is low.

If the raining inflows, traditionally observed by C2, are related to the outflowing blobs observed by HI-A, originating at the neutral line, we would expect to observe raining inflows when the neutral line is at the POS of SOHO. According to the PFSS extrapolation, the neutral line is at the SOHO POS between 3 and 4 June, while some blobs are still observed by HI-A.

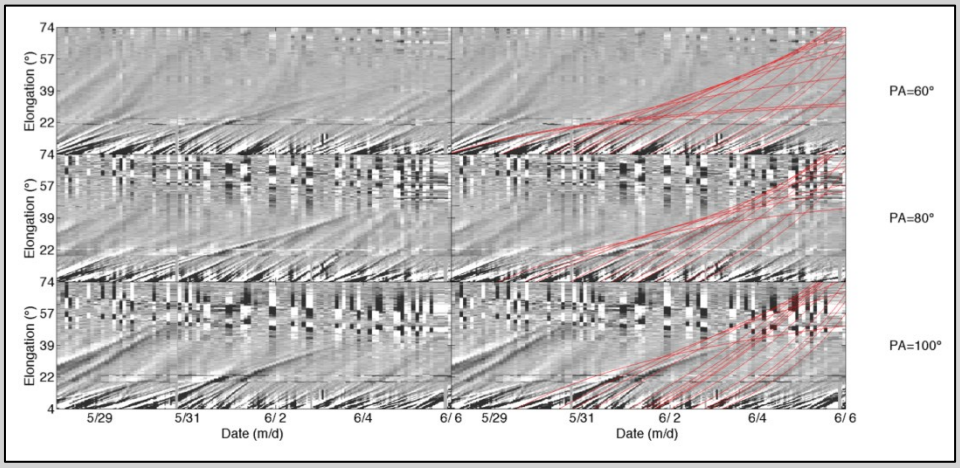

Fig. 3.5.12 - left: J-maps of HI-A at 100° (top), 80° (medium) and 60° (bottom) position angle during the passage of the CIR, from 2013 May 28 to June 06. The right hand plots are copies of the same J-maps as the left hand plots with the theoretical blob trajectories plotted as red solid lines

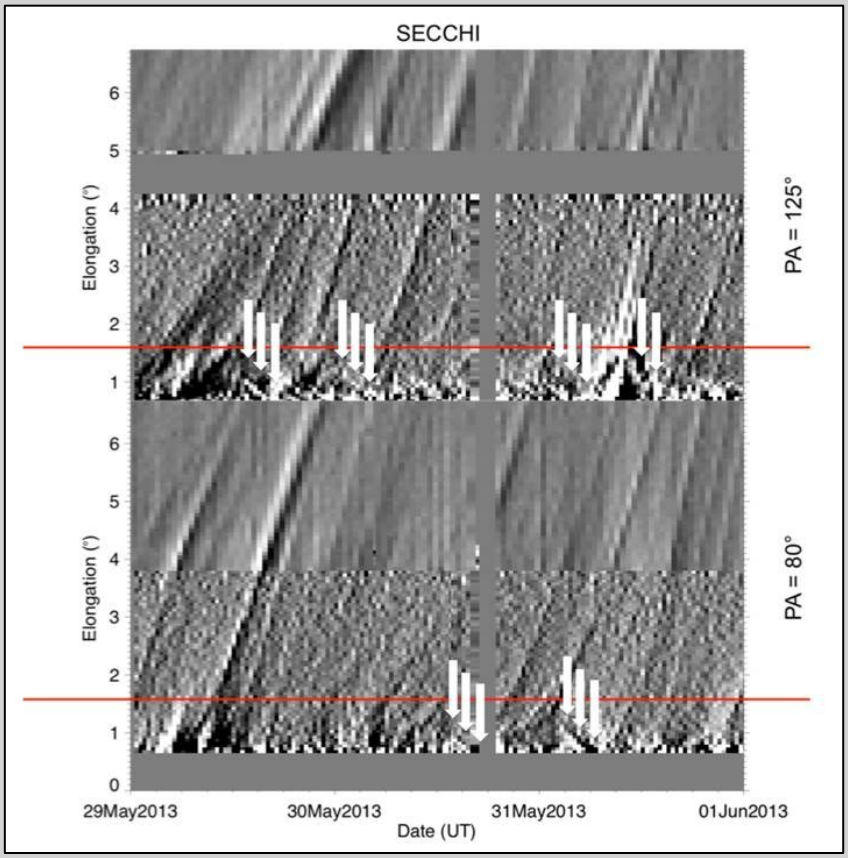

Fig. 3.5.13 - J-map of SECCHI COR2-A and HI1-A during the passage of the CIR of May/June 2013 at position angles 125° and 80°. The arrows point some of the inflows associated to outflowing blobs. The red line stands for the outer edge of LASCO C2.

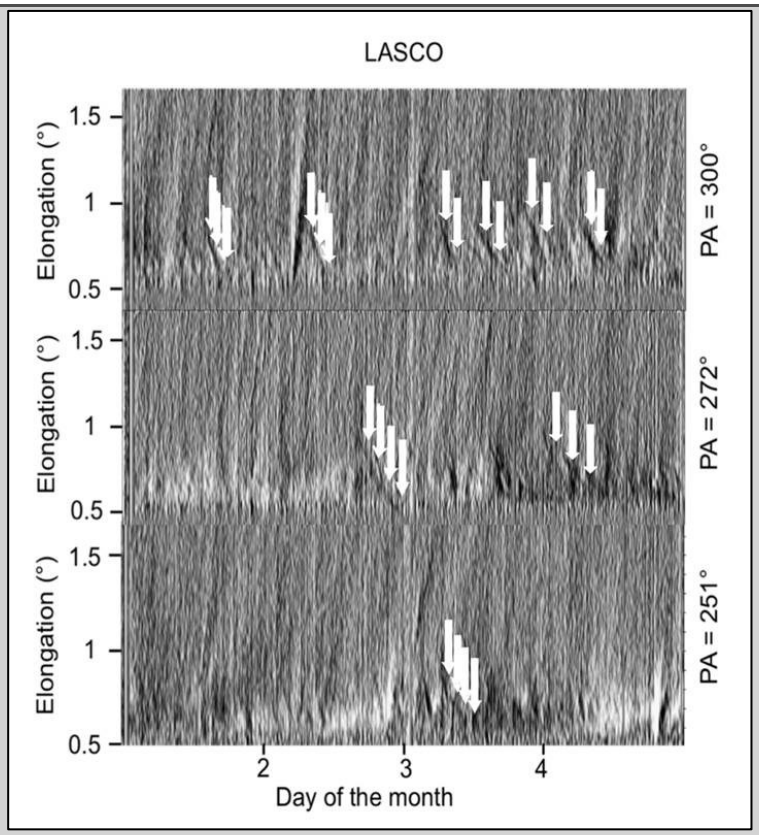

Fig. 3.5.14 - J-map of LASCO C2 during the passage of the CIR of May/June 2013 at position angles 300°, 272° and 251°. The arrows point the signature of some of the raining inflows.

Figure 3.5.14 presents three J-maps derived from LASCO C2 running-difference data at three different PAs around the estimated time of passage of the neutral line through the right limb of the POS of SOHO (2013 June 01 to 05). Raining inflows are seen at all PAs at a rate of 3 to 5 inflows per day or about every 6 to 8 hours. As usual, the raining inflows are not clearly associated to discernable outflows in C2 data, or in C3 data, but their periodicity is similar to that of the blobs clearly detected at higher altitudes by HI during the same period of time and consistent with the periodicities of blobs observed in previous studies (eg Rouillard et al., 2010a). Similarly to the inflows observed with COR, they typically approach the Sun with average velocities around 100 km/s, accelerating at their early life and decelerating below 1° elongation.

Some of the streamer blobs observed by HI were also observed by COR2. J-maps constructed using COR2 show the first clear link between these blobs and coronal inflows (Figure 3.5.13). The separation between the outflowing blob and the raining inflow occurs typically around 5-6 solar radii, well above the location of helmet streamers. These inflows are clearly observed by COR2 when the coronagraph observes the streamer, and its associated neutral line, passing through its POS. By letting that streamer rotate into the SOHO POS, we see many more inflows in the C2 images than in COR2 in the form of raining inflows (Figure 3.5.14). A close association had been already found between raining inflows and the coronal neutral line (Sheeley et al., 2001). Here we link these dynamical processes with the continual outflow of transient structures typically measured in the solar wind with HI. The co-existence near 5-6 solar radii of oppositely directed magnetic field and the bursty nature of outflow/inflow occurrence supports the idea that magnetic reconnection is the key mechanism for the formation of streamer blobs, generating a continual stream of outwardly-moving blobs in the form of loops and twisted magnetic fields and of inwardly collapsing magnetic loops.

It has been both argued that the entire slow solar wind might be made of a continuous release of transients [e.g. Einaudi et al., 2001; Lapenta and Knoll, 2005; Antiochos et al., 2007] or may be composed of two components, one transient and one resulting from a continual wind flow heated and accelerated for instance by wave-particle interactions at highly expanded flux tubes [e.g. Wang et al., 2009]. In-situ measurements also

suggest two different types of slow solar wind [Kasper et al., 2007, Stakhiv et al., 2015, 2016]. Our results suggest that a transient part is formed above the helmet streamers as a consequence of magnetic reconnection. We note that Solar Probe Plus and Solar Orbiter will soon obtain unprecedented imaging of the tip of streamers providing the observations necessary to quantify, in detail, the contribution of small-scale transients to the slow solar wind. Magnetic reconnection is a ubiquitous mechanism in space and astrophysical plasmas. The same mechanism that explains magnetic reconnection during bursty bulk flows in the Earth's magnetotail has been proposed to occur in the solar corona (Birn & Hesse, 2009; see also Linton & Moldwin, 2009). Here, we show that magnetic reconnection is taking place at small temporal and spatial scales at high coronal altitudes (and not only in association with pulses of Poynting flux in solar flares), thus bringing further evidence for an analogy to the recurring substorm process at Earth.

WP5 TASK 5.4: COMPARING FORWARD-PROJECTED CIR TRACKS WITH IN-SITU MEASUREMENTS (TASK LEAD: UPS, CONTRIBUTOR: UH)

In this WP, we are tracking small-scale transients to 1 AU and making a list of predicted impacts at points in the heliosphere where in-situ measurements are taken. The work focuses on two deliverables, D5.4 (Imagery/in-situ comparison) and D5.5 (Analysis of in-situ data), exploiting the results of deliverables D5.2, D3.1 and D3.2, analysing the relation between the speed of the CDS and the in-situ measurements.

CDS Propagation and Validation Versus In-situ Measurements

Figure 3.5.15 compares the solar cycle variation in the number of CDSs cataloged in the current study from ecliptic J-maps and the number of SIR/CIRs detected in situ at 1 AU from STEREO-A (Jian et al., 2013), as well as showing the number of CMEs identified in the HI-1 images from STEREO-A. The number of cataloged CDSs is above 30/year in 2007 – 2009 (i.e. during solar minimum), roughly the same as the number of SIR/CIRs identified in situ during the same period. The numbers of CDSs and SIR/CIRs diverge between 2010 and 2014, with a much lower number of CDSs (only 17 per year) being identified at solar maximum. One of the principal reasons for this drop in the occurrence rate of CDSs is due to the difficulty in their identification, and accurate characterization, in J-maps, during times when many CMEs pass through the HI field of view; at solar maximum a number of CDSs are “hidden” by the high number of CMEs crossing the field of view of the HI cameras (red curve).

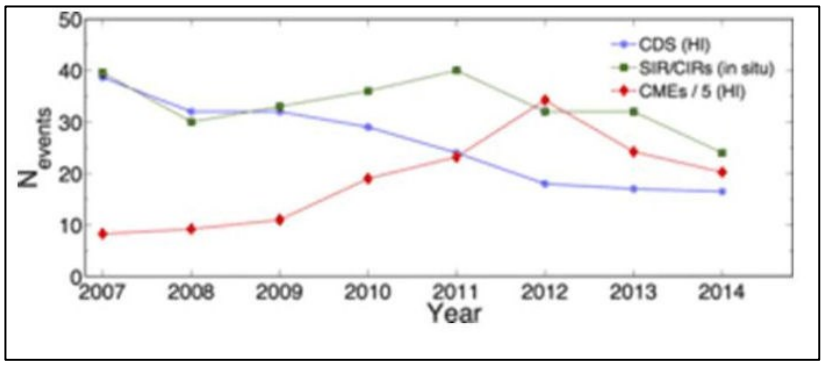

Fig. 3.5.15 - Occurrence per year, from 2007 to 2014, of CDSs, SIRs/CIRs, and CMEs. CDS occurrence, from our catalog, is plotted with blue stars, the occurrence of in situ SIRs/CIRs, from L. Jian’s ST-A catalog (Jian et al., 2013), is plotted with green squares, and red diamonds show the total number of CMEs detected in HI-1 images from ST-A (divided by 5 here for convenience). The latter was taken from the HELCATS website http://www.helcats-fp7.eu. Incomplete years 2007 and 2014 are weighted accordingly.

To determine the nature of a sample of the identified CDSs, we estimated their arrival times at a number of probes making in situ measurements of the interplanetary plasma, namely ACE, Wind and the STEREO spacecraft themselves. The cadence of in situ plasma measurements we used was of 1 hour, being comparable to HI-2 images cadence (2 hours). This analysis was carried out for a subset of 61 events that occurred during 2007 and 2008. Focus was placed on the solar minimum period, when both the white-light images and in situ data are easily interpretable due to the low occurrence rate of CMEs. The impact time at each in situ probe of every CDS observed during that period was predicted and a comparison with the in situ measurements

undertaken. Since running-difference images reveal variations in plasma density, we compare our estimated CDS arrival times with the closest peak in density measured in situ. The density peak corresponding to a SIR/CIR detected in situ is usually located on the slow solar wind side of the stream interface, since the slow solar wind tends to be denser than the fast solar wind. Moreover, the highly dense heliospheric plasma sheet that is advected by the slow wind can find itself entrained and compressed by high-speed streams during their transit to 1 AU, enhancing the density asymmetry between the slow and fast solar wind plasma on either side of the stream interface.

The first question to address is whether the predicted passage of a CDS over an in situ observatory occurs simultaneously with the observed passage of a SIR/CIR, the latter being a region of interaction between fast, tenuous, hot solar wind on one side and slow, dense, cold wind on the other. The fast and slow solar wind streams are separated by a stream interface where plasma density and transverse pressure maximize (e.g. Jian et al., 2006). The magnetic field, and the bulk solar wind ion speed, density and temperature, are used to identify the in situ passage of a SIR/CIR. Typical SIR/CIRs are identified in situ by the following signatures (Borovsky and Denton, 2010):

- A transition in the radial component of the solar wind speed from slow (~300 kms $^{-1}$) to fast (500-700 kms^{-1}).
- A deflection in the flow around a stream interface.
- A peak in plasma density very close to the stream interface, on the slow-wind side.
- An amplification in the magnetic field in the compression region (i.e. at the plasma density peak).
- An enhancement in the following characteristic speeds: sound, Alfvénic and magnetosonic speed, in the compression region.
- A rapid increase in the ion specific entropy ($T_i/n^{2/3}$) at the stream interface.

Comparison with In-situ Measurements

Figure 3.5.16 presents the in situ data taken by STEREO-A and STEREO-B spanning, in each case, the predicted arrival time of the CDS identified in Del. 5.1 and 5.2. At both spacecraft, a SIR/CIR is clearly identified in situ, close to the central time of each figure. SIR/CIR arrival is marked by an increase in magnetic field, a density enhancement, and a transition from cold, slow (~300 km.s−1), dense plasma to hot, fast (~600 km.s−1), tenuous plasma. The predicted arrival times at the two in situ observatories, based on the analysis of the HI data from ST-A, are indicated by vertical red lines. Predicting the time at which the CDS would encounter ST-A and ST-B is done by adding, to the launch time of the fitted blob, the time required for its source region to corotate (at fixed solar rotation period of 25.38 days) to the longitude of the in situ observatory and the time taken for such a feature to propagate (at its fitted speed) out to the heliocentric distance of that observatory. The mean predicted speed, ⟨Vb⟩=358±10 km.s−1, is close to the slow solar wind speed measured at ST-A and ST-B prior to the arrival of the stream interface. In both cases, the predicted arrival time is slightly later than the in situ detection time of the stream interface (by 6 hours for STEREO-A and 2 hours for STEREO-B). It should be noted that the method's uncertainty in the predicted arrival time (corresponding to the uncertainty in the fit of the time–elongation profile of the reference blob) is of the order of ±3 hours if the uncertainty in the mean speed is propagated over 1 AU. An analogous comparison was done using ACE and Wind data. For this particular CDS, the predicted arrival time is several hours after the in situ detection of the stream interface at all of the probes considered.

We present, in the upper panel of Figure 3.5.16, the in situ measurements made by STEREO-B around the predicted impact times of five CDSs with the arrival time of each CDS being marked by a red vertical line. The proton density and the radial solar wind speed are plotted over a time window extending from 1 February to 31 March 2008. The bottom panel of the figure a shows ST-A J-map with signatures of these five different CDSs, which correspond to four different SIR/CIRs detected in situ during this time period (top panel). The second CDS (indicated by the second dashed arrow) has no SIR/CIR counterpart in situ at STEREO-B. Each SIR/CIR is followed by a long-lasting high-speed stream. Before the arrival of the first SIR/CIR (02-02 to 10-02), multiple magnetic flux ropes are detected in situ, each of which is associated with a CME clearly identified near the Sun (first dashed arrow). The associated J-map is complex, with multiple CME tracks crossing the (albeit still clear) CDS signature. The in situ signature suggested to be associated with the second CDS is the most interesting, as it does not correspond to that of a typical SIR/CIR or even have a strong density peak at STEREO-B (STEREO-B was situated, at this time, at a heliographic latitude of −5.6^{o}). For this event, we find in the heliospheric imagery that the compression by the high-speed stream mainly occurs south of the ecliptic plane; the weak CDS detected in the ecliptic by HIis likely the signature of the northern boundary of the SIR/CIR. The

associated SIR/CIR is, however, detected by ST-A in situ (at a heliographic latitude of −7.2◦). Because the ecliptic transients associated with this event experience no significant compression during their outward propagation, their brightness decreases rapidly as they propagate outward and their J-map signature is weak. The third and fourth CDSs have typical SIR/CIR signatures in situ (see e.g., Borovsky and Denton, 2010).

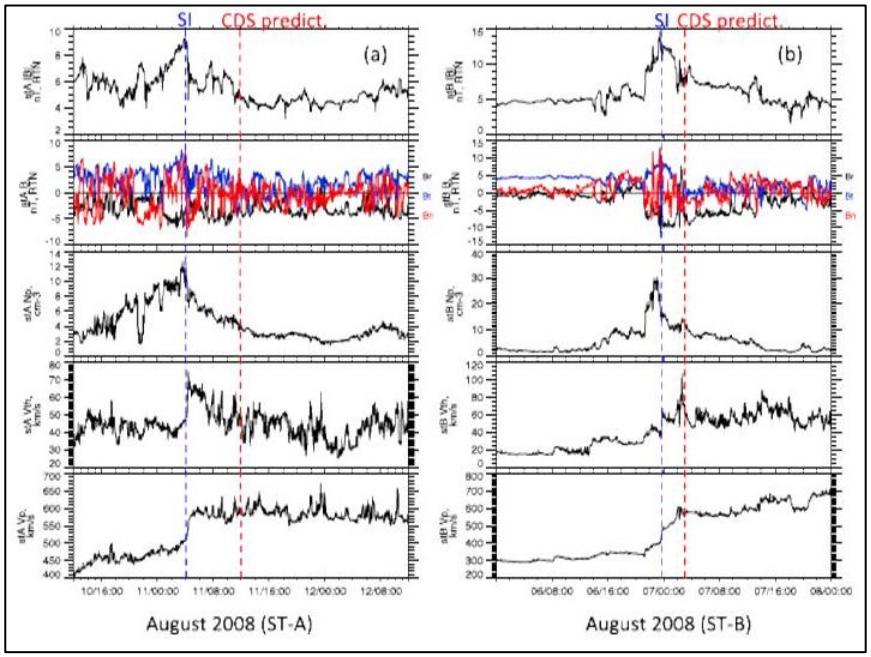

Fig. 3.5.16 - In situ data from ST-A (a) and ST-B (b) showing the SIR/CIR corresponding to the CDS fitted in Figure 3.5.1. From top to bottom: Magnetic field amplitude |B|, components of magnetic field [Br,Bt,Bn], proton density, thermal velocity, and bulk solar wind speed. The red vertical lines indicate the predicted arrival times of the CDS at ST-A and ST-B from the ST-A J-map analysis, which yields Vb=358±10 kms−1. The in situ speed at the predicted time of arrival at both ST-A and ST-B is ∼600 kms−1 (i.e. in this case the predicted arrival time is too late, such that it lies on the fast wind side of the stream interaction region). Note that at the time of peak density (at the stream interface; indicated by the blue vertical lines), the solar wind speed is intermediate between the fast- and slow-wind speeds.

Long-Term Variations in the prperties of CDSs

To illustrate the connection between CDSs and SIR/CIRs during solar minimum, Figure 3.5.17 presents STEREO-A measurements of the proton density (upper panel) and the radial solar wind speed (lower panel) from April 2007 to December 2008. This period corresponds to the deep solar minimum, with very few CMEs emerging from the corona. The recurrent pattern of fast (>600 kms^{-1}) then slow solar wind (<400 kms^{-1}) is clearly visible in the lower panel. Very few of the large density increases are not associated with a predicted CDS impact. For these events, we find that either the J-map was of insufficient quality to permit the definitive identification of a CDS or that the density peak measured in situ was associated with the passage of a CME rather than a SIR/CIR. Red vertical lines in the upper panel (density) indicate the predicted impact times of all CDSs cataloged during this interval. The black stars in the lower panel show the fitted CDS speeds (Vb) at the predicted impact times. The fitted speeds are clearly close to the slow solar wind speed. Remarkably, the time variation of the fitted speeds follow closely the time variation in the speed of the slow wind ahead of the SIR/CIRs detected in situ. For these reasons, we conclude that these CDSs, at least, are mainly associated with the outward propagation of SIR/CIRs and with the formation of strong density enhancements in the interplanetary medium. Moreover, during their transit from the Sun to 1 AU, the CDSs appear to propagate with a speed close to that of the slow solar wind rather than the typical average speed of stream interfaces located inside SIR/CIRs (which tends to be some 100 kms−1 faster than the slow solar wind speed).

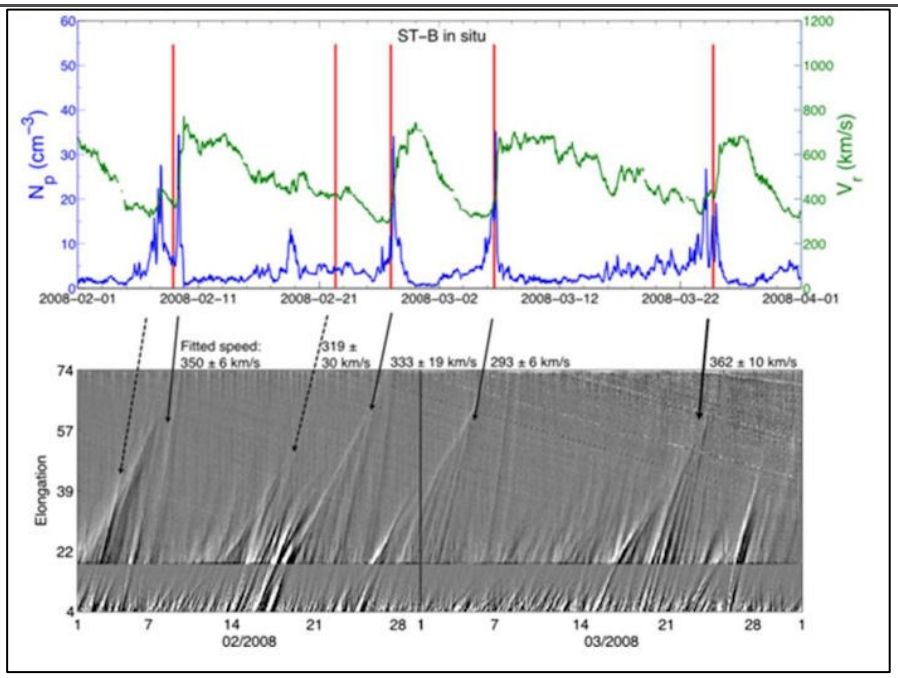

Fig. 3.5.17 - Illustration of a series of SIR/CIRs detected in situ at ST-B (upper panel) and their corresponding signatures in ST-A HI J-maps (bottom image). The blue and red time series presented in the upper panel correspond to the density Np and the solar wind speed Vr. Vertical red lines indicate the predicted arrival times at ST-B of the five CDSs shown in the ST-A J-maps (in the bottom panels). Black arrows indicate HI signatures of the in situ CDS predicted events. The first black arrow does not correspond to a CDS but presumably to a CME.

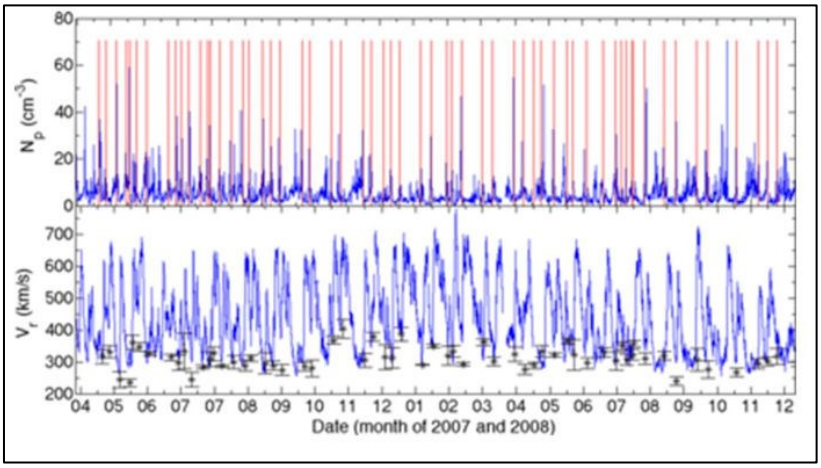

Fig. 3.5.18 - STEREO-A in situ measurements of the proton density (top panel) and the radial solar wind speed (bottom) from April 2007 to December 2008. Red vertical lines indicate the predicted CDS arrival times. Black stars in the lower panel, with corresponding error bars, are the predicted CDS speeds from J-map analysis, plotted at the predicted arrival times. Quiescent density values do not exceed 10 cm−3 while strong peaks reveal the presence of local strong compression regions. The speed values oscillate between 300 kms−1 (slow solar wind) and 700 kms−1 (fast wind).

A closer look at Figure 3.5.18 shows that the predicted CDS arrival times do not coincide exactly with times of the SIR/CIR density peaks detected in situ. The time of passage of the in situ density peak of the SIR/CIR associated with each CDS (this association was done by eye) was recorded for every event, as was the corresponding difference between the predicted and measured arrival times (Δt=tpred−tpeak). Figure 3.5.19 presents histograms of Δt for STEREO-A (panel (a)) and STEREO-B (panel (b)). Statistically there is a tendency for the predicted impact time to be later than the in situ arrival time of the density peak (corresponding to positive values of Δt). This is consistent with our observation that the CDS speed tends to be lower than the in situ speed of the SIR/CIR. The mean values of the time differences for STEREO-A and STEREO-B (denoted by

⟨ΔtA⟩ and ⟨ΔtB⟩) are +6.5 hours and +2.4 hours, respectively; standard deviations are of the order of 19 hours in each case. Note that the minimum absolute value of |Δt| is 2 minutes and the maximum value is 3 days. The most probable absolute values of ΔtA and ΔtB are 9 hours and 11 hours, respectively. Assuming that the density peak corresponds to the location of the stream interface, Δt>0 will tend to mean that the arrival time of the CDS is predicted to lie in the faster solar wind regime downstream of the interaction region while Δt<0 will tend to mean that the CDS is predicted to arrive in the slower solar wind regime upstream of the stream interface.

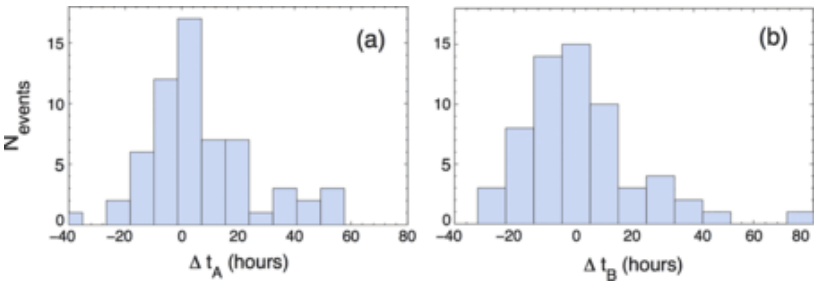

Fig. 3.5.19 - Histograms of differences between the predicted CDS arrival time and the time of the density peak detected in situ Δt=tpred−tpeak for ST-A (a) and ST-B (b). All events cataloged during 2007 and 2008 were used to generate these plots. This period corresponds to the deep solar minimum.

In Figure 3.5.20 we compare the distribution of the in situ radial solar wind speed at the predicted CDS impact times with that of CDSs speed (panels (a) and (b)). We also plot the distribution of the differences between the in situ radial solar wind speed measured at the time of the density peak associated with (i.e. nearest in time to) each predicted CDS arrival and the CDS speed (panels (c) and (d)). CDS speeds, derived from the analysis of the STEREO-A J-maps, form a distribution centered at 311 kms^{-1} with a half-width of 30 kms^{-1}. The distribution of in situ speeds measured at STEREO-A at the predicted CDS arrival times spans a range of speeds extending from 300 kms^{-1} (slow wind) to >600 kms^{-1} (fast wind). The same is true for STEREO-B. The broad nature of this distribution, extending up to the speed of the fast solar wind ($\triangle V \geqslant 100$), is a consequence of the distribution in arrival time errors, $\triangle t$, shown in Figure 3.5.19. The relatively large errors in the predicted CDS impact time relative to the stream interface move it into the slow-wind regime for Δt<0 (upstream of the stream interface) and into the fast wind for Δt>0 (downstream of the stream interface). This distribution shows a tendency to measure a significantly faster in situ solar wind than the CDS predicted speed, due to aforementioned tendency for a larger part of the predicted CDS arrival time to be later, even, than the arrival of the density peak and hence in the fast solar wind regime. As illustrated in panels (c) and (d) of Figure 3.5.20, when the times of the in situ density peaks are considered instead, the distribution of ΔV becomes narrower, centered around 50 kms^{-1} for STEREO-A and 100 kms^{-1} for STEREO-B. There are no more events exceeding ΔV=200 kms^{-1}.

Fig. 3.5.20 - Histograms of differences between in situ radial solar wind speed measured at the predicted CDS impact times and the CDS radial speed from our ST-A catalog (a), (b), and between in situ radial solar wind speed measured at the time of the associated SIR/CIR density peak and the CDS radial speed from our ST-A catalog (c), (d). Left and right panels are based on ST-A and ST-B in situ measurements, respectively

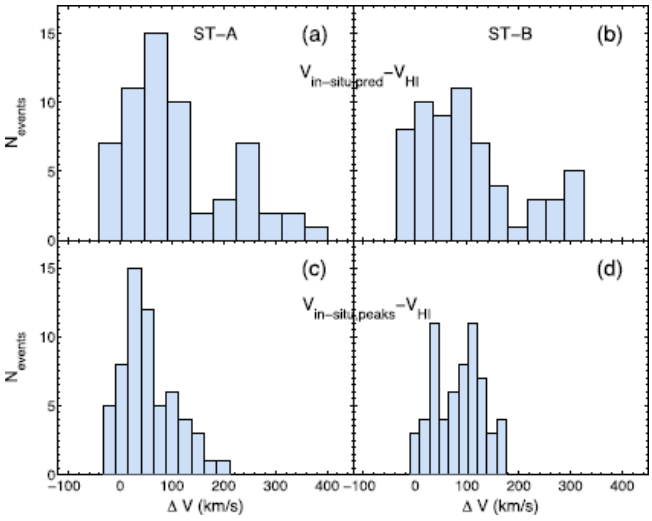

Comparison with In-situ Catalogues for SIR/CIRs

In situ catalogues of SIR/CIRs have been produced using ACE and Wind datasets for the interval spanning the years 1995 to 2009 (Jian et al., 2006; Jian, Russell, and Luhmann, 2011) and using STEREO datasets for the years 2007 to 2014 (Jian et al., 2013, catalogue updated online). These catalogues provide a comprehensive list of SIR/CIRs and their physical properties (including the solar wind speed before and after the stream interface, as well as the maximum values of the density, pressure and magnetic field). The information contained within the STEREO SIR/CIR catalogue (which includes 248 events from STEREO-A and 231 from STEREO-B) is compared here with our predictions.

The first point to note is that we see fewer events in total (190) than are detected in situ over the same period. As shown in Figure 3.5.15, over the solar minimum period (2007 – 2009) roughly the same number of events were imaged in HI as were detected in situ (30 – 40/year). At solar maximum far fewer CDSs were imaged by HI (17/year) while the frequency of SIR/CIRs detected in situ remained almost unchanged. This discrepancy is, as has been discussed at length above, attributed to the increasing number of CMEs at solar maximum. Next, we compare the CDS speeds with the minimum solar wind speed measured ahead of the SIR/CIR compression region and also with the speed at the stream interface itself. To this end, Figure 3.5.21 displays the distributions of the speeds of our 190 cataloged CDSs (in red) and of the minimum speed of the slow solar wind measured ahead of the SIR/CIRs, detected by STEREO-A (black; Jian et al., 2013). Generally, the two distributions seem to be in good agreement, with the mean CDS speed of 311 kms^{-1} being comparable with the mean minimum slow solar wind speed of 325 kms^{-1} (expressed as Vmin in the catalog of Jian et al. (2013)5). In contrast, the mean speed at the stream interface itself, the latter identified as the location of maximum transverse pressure Pt in Jian et al. (2006) is 424 kms^{-1} at STEREO-A and 404 kms^{-1} at STEREO-B. The latter values lie close to 411 kms^{-1}, which corresponds to the average speed of the in situ density peak closest to the predicted arrival time (see Figure 3.5.21). This provide further hints that (1) the CDS speeds are globally those of the slow solar wind just ahead the stream interface at 1 AU and (2) the closest density peaks to the predicted impact times lie very near the stream interface.

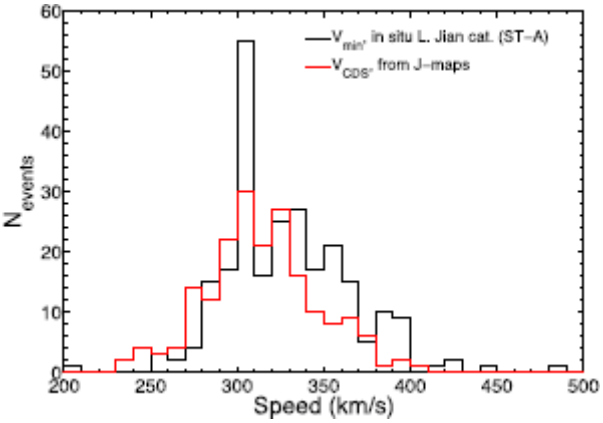

Figure 3.5.21 - Distributions of the derived CDS speed (red histogram) and of the minimum solar wind speed (black histogram) prior to the arrival of the stream interface at STEREO-A. The latter are taken from the in situ catalog of SIR/CIRs derived by Jian et al. (2013), but only for STEREO-A.

STEREO-A CDS Catalogue from 2007 to 2014

Here we summarize the catalogue of CDS events and the results of their propagation to a number of in situ observatories. The STEREO-A HI CDS catalog from April 2007 to August 2014 includes 190 events. For each CDS, the information provided in this catalog is: the launch time of the fitted blob; its speed Vb ; its direction φ relative to STEREO-A; the Carrington rotation number of the CDS; the Carrington longitude of the CDS source location; the predicted impact times at different probes near 1 AU (STEREO-A, STEREO-B, Wind and ACE). The catalog covers the ascending phase of Solar Cycle 24, from solar minimum (2007 – 2009) to solar maximum (~2012--2014). As was illustrated in Figure 3.5.15, the number of well-identified CDS events detected by HI on STEREO-A appears to be anti-correlated with the number of CMEs observed by HI. As the number of CDSs falls, from ~40/year in 2007 to 17/year in 2014, the number of CMEs rises from 40/year in 2007 to a maximum of several 100/year in 2012, after which it decreases slightly. CME activity prevents the systematic identification of corotating structures in HI imagery. Figure 3.5.22 presents the density (top) and radial speed (bottom) of the solar wind measured in situ at the STEREO-A spacecraft, from 2007 to 2014. Predicted arrival times (red vertical lines: top panel) and speeds (red stars: bottom panel) of all cataloged CDSs are over-plotted. During the first half of the period under consideration (2007 – 2010), density structures that are not associated with

predicted CDS arrival are rare, and the fitted speeds follow well the slow solar wind variations. Note that the uncertainty in the arrival time at 1 AU is about 11 hours. By contrast, between 2011 and 2014 the number of fitted CDSs decreases markedly. This is because of the difficulty of observing "clean" CDS signatures (a well-constrained fit requires the clear identification of the tracks of several individual blob tracks, as well as a clear envelope) due to high level of CME activity

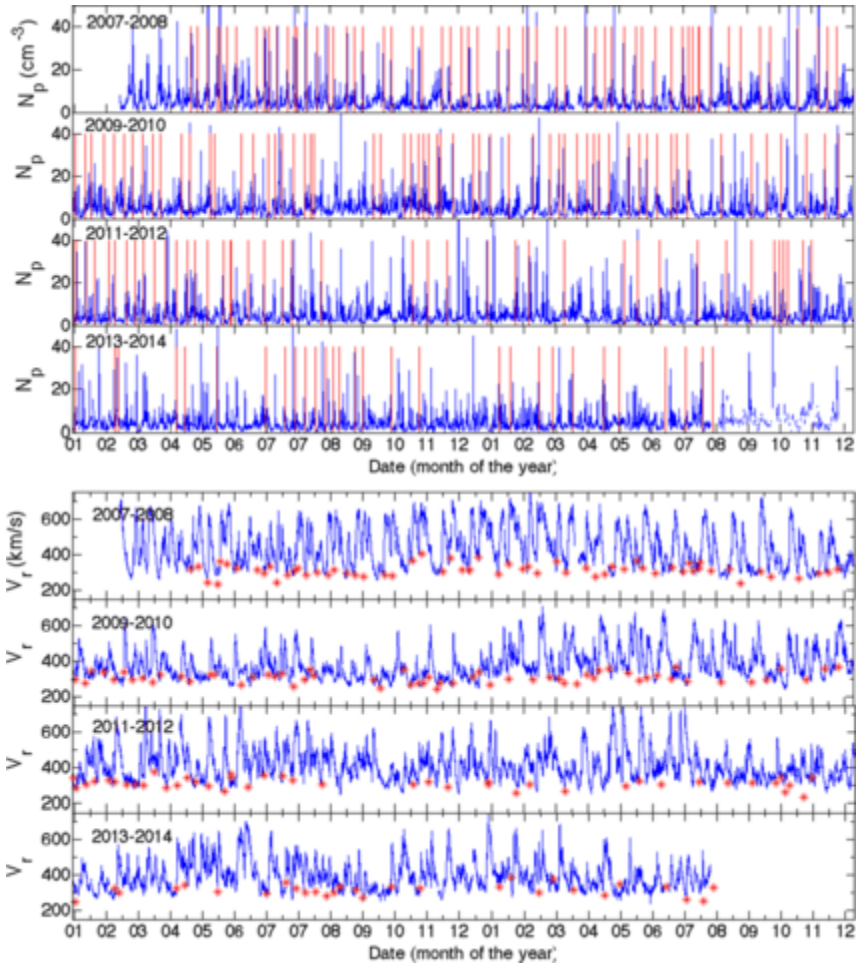

Fig. 3.5.22 - In situ proton density (top) and radial solar wind proton speed (bottom) as measured by the ST-A spacecraft from 2007 to 2014. Over-plotted are predicted impact times of all cataloged CDSs at ST-A (top figure: red vertical bars) and fitted CDS speeds (bottom: red stars).

Conclusions

To summarise CDSs are most clearly imaged in the heliosphere during solar minimum, when the heliospheric images are not too perturbed by the presence of CMEs. Their derived speeds correspond to that of the slow solar wind throughout the solar cycle (see also Conlon et al. 2015). Comparison with in situ data shows that CDS speeds are not those of the stream interface measured at 1 AU, nor of the stream interfaces tracked via IPS (Bisi et al., 2010). We note that IPS is sensitive to density fluctuations and therefore particularly sensitive to the shear regions generated at the stream interface. We conclude that, for most of their propagation, CDSs are therefore associated with density variations in the background slow solar wind. Recent analysis of Helios observations near 0.3 AU has revealed that the densest solar wind is associated with the heliospheric plasma sheet and propagates with a speed of less than 300 kms^{-1} over 8 % of all observations (Sanchez-Diaz et al., 2016). Additionally, SIR/CIRs are rarely well formed at these heights. Therefore, we conclude that the CDSs tracked in this study must undergo little compression, and therefore little acceleration, below 0.3 to 0.5 AU (roughly halfway through the field of view of SECCHI imagers). However, by the time they reach 1 AU, CDSs

tend to arrive at any observing spacecraft close to the peak in density associated with SIR/CIR passage. We hence conclude that between 0.5 and 1 AU, the CDSs are rapidly caught up by ensuing high-speed streams.

Analysis of the in-situ signature of small-scale transients

In order to identify the in-situ signatures of small-scale transients in the solar wind we first determined the spatial and temporal scales of these transients using heliospheric imagery (Deliverables 5.1-5.4). This was achieved through a spectral analysis of the brightness variations caused by the outflow of these transients and detected remotely by the heliospheric imagers onboard STEREO-A. The latest analysis is reported in a HELCATS paper submitted to the Astrophysical Journal: Sanchez-Diaz et al. (2017), and we refer the reader to this analysis for further details on the followed methodology. In this paper the space and time scales of the release of density inhomogeneities from a highly tilted neutral line were determined with a spectral and wavelet analysis of heliospheric images.

The interpretation of the work done in Deliverables 5.1-5.4 and in Sanchez-Diaz et al. (2017) led to the cartoon picture sketched in Figure 3.5.23 on the topology of these transients released in the Heliospheric Current Sheet (HCS). In this schematic, we show the spatial distribution of small transients at a given time. Panel a shows a latitudinal cut of the density enhancement associated with one small transient. The average density inhomogeneity, that we call a blob, has major and minor axes with dimensions of 12 R_s and 5 R_s, respectively. Figure 3.5.23b shows, at a given time, the spatial distribution of small transients along the Parker spiral in a plane of constant heliographic latitude. The stream interface would consist on a succession of flux rope structures with higher magnetic field and lower density and structures with high density and low magnetic field (gray areas in Figure 3.5.23c). The brightness enhancements observed in running-difference images are unevenly spaced in time with the periodicity alternating between 9h (from the leading to the rearing edge of the same density structure) and 11h (from the rearing edge of a density structure to the leading edge of the next one). During the period of study presented in this paper, 4 brightness enhancements should be observed every 29h in running-difference images, i. e., 3.3 per day. Note that this number is consistent with the periodicities of streamer blobs in coronagraph images found by Wang et al. (1998) and Song et al. (2009).

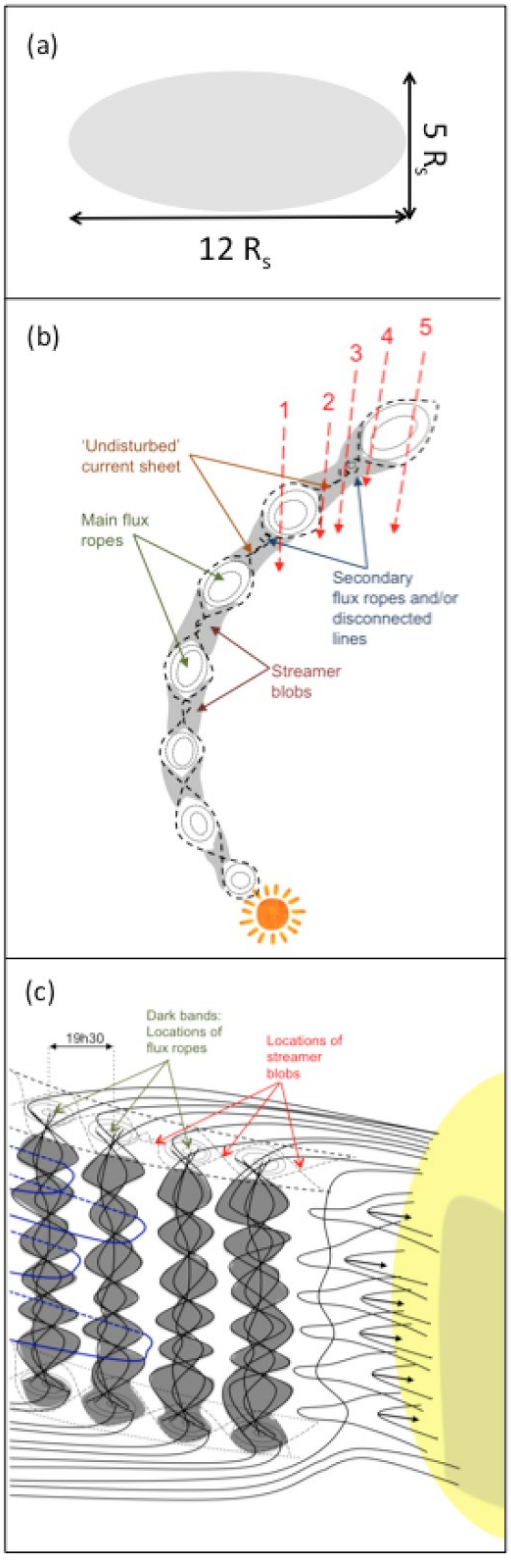

Figure 3.5.23 - (a) Shape and size of the latitudinal cut of the density enhancement (blob) associated to a small transient. (b) Polar map of the ecliptic plane with blobs released by an exactly corotating source in dark gray. The Sun, on the bottom left corner, is not to scale but the size of the blobs and distances are. The black arrows sketch different possible types of trajectories for a spacecraft relative to the position of blobs (c) Meridional view of the upper corona with its magnetic structure. The Sun, on the right side, is not to scale.

Figure 3.5.23c shows, at a given time, on a plane of constant heliographic longitude, the latitudinal and radial distribution of small transients released by a highly tilted neutral line. The common origin of outflowing small transients and raining inflows found in Tasks 5.2-5.4 suggests that magnetic reconnection is at the origin of outward moving density enhancements (Sanchez-Diaz et al. 2017). For this reason, we expect high-density regions to be associated with weak magnetic fields (such bright bands are shown in the LAT-map of Sanchez-Diaz et al. 2017). Dark bands (low density regions) observed in Sanchez-Diaz et al. (2017) likely represent enhanced magnetic-field structures with a magnetic flux rope topology.

In-situ measurements can be considered through a range of possible trajectories of a spacecraft crossing a north-south oriented HCS in the ecliptic plane, shown by the red arrows in Figure 3.5.23(c). The paths indicated include the following:

Trajectory 1: The spacecraft crosses the sector boundary by first intersecting a magnetic flux rope and then the high-density blob with highly variable magneto-plasma properties associated with the reconnection outflows.

Trajectory 2: The spacecraft crosses a clean heliospheric current sheet crossing associated with a high density region where the HCS has had time to reform before the next flux rope is released. The expected signature is that of an inversion of the magnetic field polarity and a clean sector boundary marked by a switch in the pitch angle of suprathermal electrons. The region surrounding the HCS could be a narrow peak of elevated densities right at the polarity inversion.

Trajectory 3: The spacecraft crosses the blob, the signature would be a broad density enhancement lasting several hours correlated with weaker magnetic fields. The magnetic field structure may be highly variable corresponding to smaller scale flux ropes embedded in high-density region.

Trajectory 4: The reverse scenario to trajectory 1, the spacecraft crosses the edge of the magnetic flux rope and the edge of a blob (trajectory 4). In this scenario, the in-situ measurements would exhibit first those of a flux rope crossed near the edge and then the signature of a blob.

Trajectory 5: The spacecraft crosses crosses the magnetic flux rope replacing the heliospheric current sheet with no signature of a blob.

We note that the longitudinal separation between two consecutive blobs is 12°, which corresponds to 19h30 for a typical solar rotation. This time is much longer than the typical time spent by a spacecraft in the HPS when crossing the neutral sheet. Therefore, it is unlikely that a spacecraft orbiting at constant heliographic latitude at near 1AU can measure two blobs during a single crossing of a highly tilted neutral sheet.

The above described results set the context for analyzing the in-situ measurements corresponding to the crossing of highly tilted heliospheric current sheets and for identifying the in-situ signatures of blobs. We carried out a survey of in-situ data to search for crossings of a highly tilted HCSs during the STEREO era. Our criteria were in addition that no CME was directed at the spacecraft during the 5 days that preceded the intersection of the HCS. This was checked using a combination of the HELCATS catalogues provided by WP3 (KINCAT), WP4 (ARRCAT, ICMECAT) and WP6 (SIMCAT). The event list is shown in Table 3.5.1.

All HCS crossing are marked by significant increases in the density of the solar wind that we associate with the passage of the HPS. We investigated the properties of the suprathermal particles measured during the passage of these HPSs. As shown by previous authors, the passage of the HPS is frequently associated with complex signatures in the pitch angle of suprathermal electrons suggesting that magnetic field lines have undergone connectivity changes in the corona. Table 1 confirms this picture, it shows that all but three of our identified crossings were associated with either counter-streaming electrons or heat flux dropouts lasting several hours. These two signatures are traditionally associated with the passage of either magnetic loops or disconnected loops, respectively (Pagel et al. 2005, Crooker & Pagel 2008). Such magnetic structures differ from the signature that one expects for Parker spirals convected out by the background solar wind, they suggest passages of transient structures convected out in the slow solar wind (Kilpua et al. 2009) and that magnetic reconnection is occurring continually in the source region of the HPS as suggested by the schematic

drawn in Figure 3.5.23.

Table 3.5.1 - Figure 3.5.24. List of small transients measured in-situ at crossings of north-south oriented HCSs during solar cycle 23. The first column show the Carrington rotation of the measurement, the second column the name of the spacecraft, the third column the date and time of the HCS crossing, the fourth column whether the HPS was a single density peak (1) or had double-peaked structure (2) and the fifth column reports the traces measured in the pitch angle distribution of suprathermal electrons. D stands for heat flux drop-out and BDE for bidirectional electrons.

Carrington rotation	Spacecraft	HCS crossing	Density peaks	strahl signature
2092	STEREO-B	25/01/10 01:00	2	D (before), BDE
2092	WIND	31/01/10 01:30	1	no
2093	STEREO-B	24/02/10 13:30	2	D
2094	STEREO-A	03/04/10 19:00	2	D, BDE (after)
2107	STEREO-B	20/02/11 19:00	1	BDE
2107	WIND	28/02/11 21:30	2	D
2107	STEREO-A	03/03/11 11:45	1	BDE
2109	STEREO-A	04/05/11 21:30	1	D, BDE
2110	STEREO-B	20/05/11 05:45	2	-
2111	STEREO-A	28/06/11 03:45	2	D,
2112	WIND	18/07/11 04:15	1	no
2114	STEREO-B	04/09/11 19:15	2	D, BDE
2133	STEREO-A	02/05/13 22:00	2	D
2138	STEREO-A	09/07/13 05:45	2	D
2139	STEREO-B	16/07/13 13:45	2	D
2139	WIND	25/07/13 14:45	2	no
2139	STEREO-B	04/08/13 19:15	2	D

We used the list given in Table 3.5.1 to test the validity of the schematic shown in Figure 3.5.23 through an analysis of individual HCS-HPS crossings measured in situ. We present in Figure 3.5.24 examples of four of the five types of trajectories that we think a spacecraft can encounter when passing through a north-south oriented HCS-HPS system. Trajectory 5 not shown here was also found in the in-situ data (see for example Rouillard et al. 2009).

Common properties to all crossings: The sector boundary is crossed in all four cases because the pitch angle of suprathermal electrons has switched between 0 and 180 degrees. The spacecraft have crossed the HCS

because the sign of the Bx and Bx components of the interplanetary magnetic field has also changed between positive and negative polarities. In all cases the solar wind density increases significantly for several hours during the sector boundary crossings. We identify this density enhancements as the HPS crossing; it is fully consistent with the expected passage of the dense blobs typically observed in HI images. Three of the four events shown in Table 3.5.1 exhibit counter-streaming electrons or heat flux dropouts. There is even a case of a drop in the flux of suprathermal electrons during the entire blob passage during trajectory 3.

Comparing the schematic shown in Figure with the different signature of the hour trajectories shown in Figure 3.5.24, we see that:

Trajectory 1: The probe encounters, first, the edge of a magnetic cloud and after the density enhancement associated with the blob. The HPS identified as the blob is associated with a depletion of the suprathermal strahl, partially coincident with an even stronger density enhancement. In this particular case, magnetic disconnection from the Sun is complete in 3D space because the strahl disappears at pitch angles and in all energy bands. The magnetic cloud conserves the polarity of the preceding ambient solar wind. It is, therefore, attached to one hemisphere of the Sun but has probably reconnected its other leg (see schematic in Figure 3.5.23).

Trajectory 2: The probe encounters a clean HCS crossing with a gradual increase in plasma density (as we enter the HPS) ended by a correlated change in the sign of the magnetic field and the pitch angle of suprathermal electrons. There are only very brief periods of counter-streaming electrons detected inside the HPS. Figure 1 suggests that these clean HCS crossing should be rare and correspond to regions where the HCS as reformed temporarily before the next flux rope is released.

Trajectory 3: The probe encounters the sector boundary (switch of pitch angle) and enters a very dense structure exhibiting highly variable magneto-plasma parameters. The entire structure appears partially disconnected from the Sun because the flux of suprathermal electrons is greatly reduced. The multiple peaks in density are correlated with drops in the magnetic field strength. Magnetic structures are measured between consecutive peaks and we associate those to additional smaller transient structures formed in along the X-line that follows the release of a magnetic flux rope into the HCS.

Trajectory 4: The probes encounters first the HPS marked by counter-streaming electrons or equivalently magnetic loops connected at both ends to the Sun, we associate this signature as the end of a blob. Immediately after the blob passage, a magnetic flux rope intersects the spacecraft exhibiting rotations in the By and Bz components.

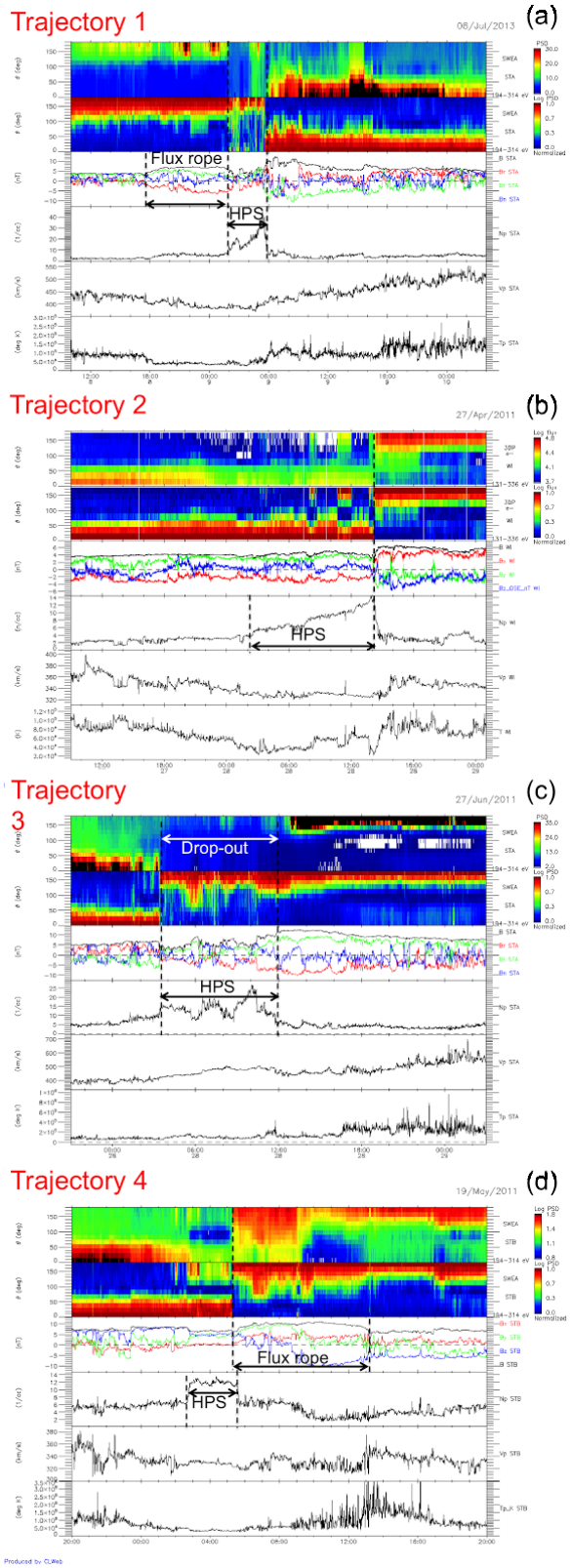

Figure 3.5.24 - In-situ data of STEREO-A (a, c), STEREO-B (d) and WIND (d) during the crossing of four different north-south oriented HCSs. Each one of the three panels corresponds to each of one of the possible trajectories a probe can trace for such a crossing. Each panel shows (from top to bottom), as a function of time, the pitch angle distribution of suprathermal electrons, the pitch angle distribution of suprathermal electrons normalized for each point in time, the interplanetary magnetic field in RTN coordinates, the proton density, the proton bulk speed and the proton temperature. The black dashed lines delimitate the location of the HPS, the blue shaded areas highlight the location of blobs. The initials MC stands for magnetic cloud. Plots generated with CLweb @IRAP.

WP5 CONCLUSIONS:

The activities of WP5 were to mirror the CME-reated activities of the other WPs, exploiting the STEREO/HI data to develop a catalogue of CIRs and to determine their parameters, and making the resulting catalogue freely available to the community to enable future research on SIR/CIR physics. The work has included the back and forward projection of HI transients to make comparisons to solar source and in-situ signatures, as described in detail, above. The completeness of the work produced, in its comparison of soure, heliospheric and in-situ data is unprecedented in the study of these solar wind structures, providing a potential for major advances over the coming years and a facility that will enable the definition of a long-term benchmark. The WP provided the first characterisation of blob emission during solar maximum, determined where blobs form in the solar corona and provided a basic picture of the 3-D topology heliospheric current sheet perturbed by the continual release of small-scale transients.

WP5 HIGHLIGHTS:

- Creation of the first CIR catalogue based on HI imagery.
- First determination, in 3D, of where blobs form in the solar atmosphere and how they are released.
- First determination of the 3-D structure of the variable heliospheric current sheet.

WORK PACKAGE 6 (WP6):

INITIALISING ADVANCED NUMERICAL MODELS BASED ON THE KINETIC PROPERTIES OF STEREO/HI CMEs AND CIRs

WP6 ACTIVITY TYPE: UPS

WP6 DURATION: MONTHS 7 – 36

WP6 LEAD BENEFITIARY: UPS (1)

WP6 LEADER: Dr Alexis Rouillard

WP6 CONTRUBUTORS: GMU (Third-party)

WP6 OVERVIEW: The primary goal of WP6 is to transform the catalogues of CMEs and CIRs observed by HI, accomplished in WP2/3 and WP5, into more advanced catalogues of simulations results of CIRs and CMEs. This advanced database will provide to the space community a set of simulation results optimised by assimilating direct images of the solar wind into Enlil simulations. The delivery of these advanced catalogues will enhance forefront research on the 'background' solar wind (fast and slow solar wind) and on the spatial and temporal evolution of CIRs and CME shocks, and will provide unique material to study and interpret particle radiation measurements in the inner heliosphere.
[Relevant catalogues: SIMCAT (Solar Wind), SIMCAT (Solar Wind + Fast CMEs, SIMCAT (Solar Wind + all CMEs]

WP6 TASK 6.1: ASSIMILATING HI IMAGES TO MODEL THE BACKGROUND SOLAR WIND (TASK LEAD : UPS, CONTRIBUTOR : GMU)

In this task the combination of the catalogues of CIRs derived in WP5, J-maps derived from HI images and movies will be compared with synthetic J-maps and movies of CIRs derived from numerical simulations of the background solar wind. Specifically, this work relates to deliverable D6.1. The aim was to divide events in two classes: Class 1 for which a good correspondence is immediately obtained between simulated and observed height-time maps and Class 2 for which J-maps differ significantly. We compared how well Enlil predicts the in-situ measurements of CIRs for these two classes of events separately. We then modified the coronal input of Enlil of the second class of events until synthetic and observed J-maps were in good agreement.

We carried out the analysis on two years of data (2012-2013), we employed a catalogue of real HI J-maps produced by the HELCATS consortium along the ecliptic plane. This catalogue of J-maps was incorporated through WP8 in the propagation tool and was used in WP5 to produce the catalogue of Corotating Density Structures (CDSs) (in the form of CIRs/SIRs: Deliverables of 5.1 and 5.2).

For the synthetic J-maps, we used results of Enlil simulations initiated using GONG magnetograms and the Wang-Sheeley-Arge relation for the background solar wind and including the DONKI CME catalogue for CMEs. Even though this task focuses on assessing the value of HI images to validate/invalidate ENLIL simulations of the background solar wind, we decided to carry out the analysis in a real context and kept CMEs in the simulations. The accuracy of the CME simulations was therefore not critical and we did not include the HECLATS CME catalogue that was still being prepared in WP2 and 3. The ENLIL simulations of CIRs and CMEs produced 3-D density cubes and we converted those simulations into synthetic J-maps that could be immediately compared with real J-maps. ENLIL simulations were also run to specific spacecraft so that real and modelled in-situ parameters could also be compared. In order to compare the real and simulated J-maps, and in preparation for the output of deliverable 6.2 and 6.3 we modified the IRAP propagation tool so that it could read these new simulations. Synthetic and real J-maps can now be immediately compared in the rich data environment of the propagation tool (propagationtool.cdpp.eu).

We analysed all SIRs/CIRs observed in imagery, measured in situ and modelled numerically by ENLIL in 2012-2013, we choose this time period because it combined short periods of quiet solar wind conditions and also more disturbed solar wind conditions due to CME activity. We kept in mind that CIR detection in HI depends on the variability of the background slow solar wind associated with the continual release of small blobs as clearly demonstrated in Deliverables 5.3 and 5.4. The speed of CIRs derived by HI is influenced by the speed of the slow wind and does not reflect the speed of the interface between fast and slow solar wind (see results of WP5). The main conclusion of Deliverable 6.1 is that heliospheric images such as those measured by STEREO-A provide information on the location of CIRs in the ecliptic plane that are useful to evaluate the accuracy of the ENLIL simulation. The images also provide an estimate of the speed of the slow solar wind ahead of the CIR that can be used to validate or invalidate simulations of the slow solar wind speed but imagery provides no information or constraint on the speed of the fast solar wind that compresses that slow solar wind to form a CIR.

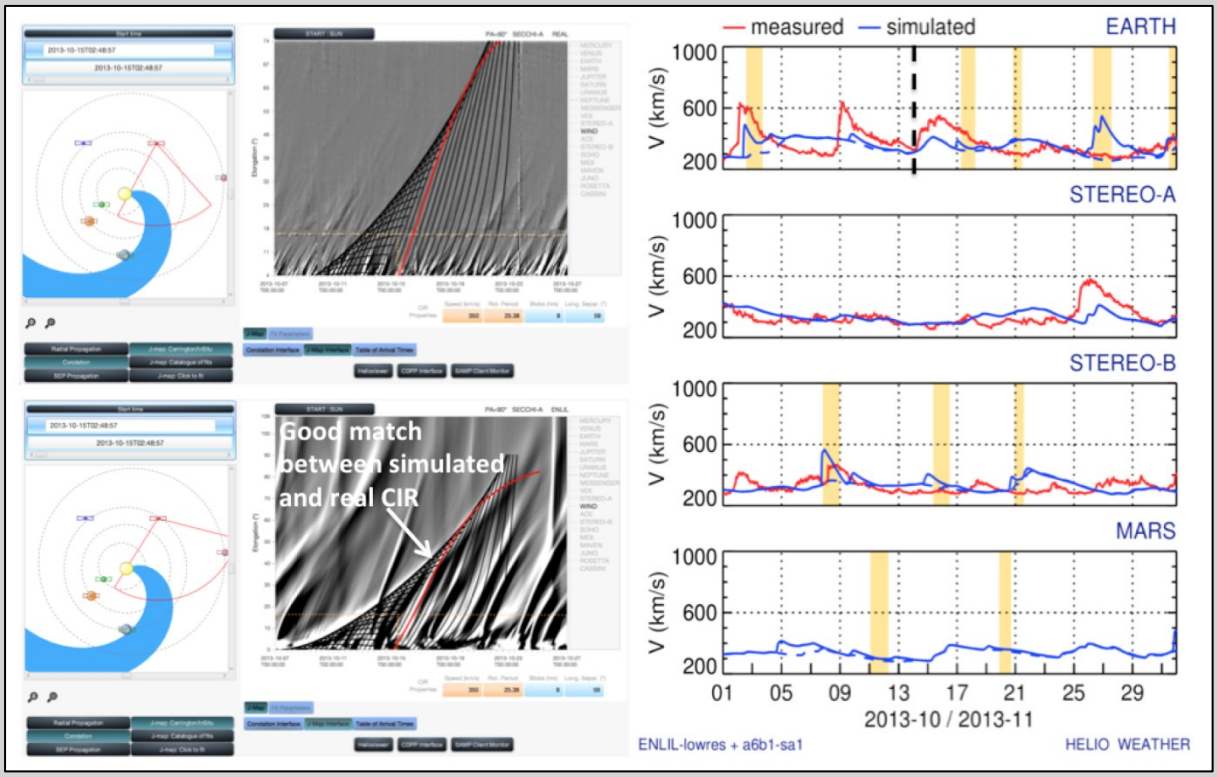

Fig. 3.6.1 - Left-hand panels: the standard propagation tool interface with a view of the ecliptic plane and a real J-map (top) and the modified propagation tool with the simulated J-map (bottom). Right-hand panels: comparison of real and simulated solar wind speeds.

Figure 3.6.1 presents the datasets used to carry out the analysis. There are two snapshots of the propagation tool on the left-hand side of the propagation tool. The top left-hand panel shows the analysis of a real J-map following the methodology of Deliverable 5.1. The bottom left-hand panel presents the analysis of the synthetic J-maps through a version of the propagation tool modified for the present analysis. The right-hand panels present a systematic comparison between measured and simulated solar wind speed values at Earth, STEREO-A, STEREO-B and MARS (the same was done for density, not shown here). This combination of figures allows comparison of the real and synthetic CIR patterns. Indeed by fitting the real CIR pattern following the methodology of Deliverable 5.2 and 5.3 and superposing this fitted pattern onto the simulated J-map, it is possible to detect differences

- in the timing of the pattern (i.e. the simulated CIR forms Eastward or Westwards of the real CIR),
- in the rotation rate of the simulated and real CIR,
- in the radial speed of the plasma carried out by the real and simulated CIRs.

Main results: using this interface, we found that:

(1) when CIR patterns in simulated and real J-maps are clearly visible and the onsets of the pattern of converging tracks match well, the arrival of the Enlil-simulated CIR and the in-situ CIR measurements math reasonably well. Figure 3.6.1 illustrates this finding with one CIR event. The interface of the propagation tool with the real J-maps shows the presence of the converging tracks that we use to locate the CIR in the ecliptic plane. The pattern shown corresponds to a CIR located by Plotnikov et al. (2016) and listed in the HELCATS CIR catalogue (described in detail in WP5). The same pattern is also observed in the interface with the synthetic J-maps produced by the Enlil model. The HI and Enlil patterns of converging tracks match reasonably well for these two events. We then compared the predicted impact times of the CIR located with HI observations (see WP5) and the CIR modeled by Enlil at Earth where in-situ measurements were available. For the CIR presented in Figure 3.6.1, the Earth was impacted by the CIR at the time of the observed CIR pattern and is therefore in-situ measurements taken near Earth are most appropriate. Indeed for this comparison we wish to avoid long propagation times between the occurrence of the CIR tracks in J-maps and the time of CIR passage in situ that would contribute additional uncertainties in the arrival times. The predicted arrival time of the HI-modeled CIR is shown as the vertical dashed line, the modeled solar wind speed is plotted in blue. The arrival times of the HI-modeled and Enlil-modeled CIRs are very close. The amplitude of the high-speed stream of that CIR is very different between the Enlil prediction (blue) and the in-situ measurements (red), this is discussed in the next paragraph.

(2) Even with a good match between the simulated and measured patterns of converging tracks and good timing of the real and simulated CIR in situ, the maximum speed measured in the high-speed that follows the interaction region can have very different speeds. This is also illustrated in Figure 3.6.1. The CIR event is clearly observed as converging tracks in the measured and simulated maps with both patterns matching very well, but when the comparison is made with the in-situ data, the measured and simulated high-speed streams are very different. This is because the bulk of the density increase that creates the converging patterns of tracks in both HI and Enlil J-maps occurs mainly in the slow solar wind. The latter is inherently more dense and when compression sets in, an asymmetric density distribution forms on either side of the stream interface with denser compression on the slow solar wind side. In turn this creates a stronger signal in white-light images and J-maps. This effect is enhanced in the real slow wind due to the additional entrainment of streamer blobs (Plotnikov et al. 2016). Hence the comparison of simulated and real patterns of converging tracks cannot provide information on the high-speed stream that will follow, this information must determined with other techniques.

(3) Interestingly there are cases (we found about 5 for the period analysed) where Enlil misses CIRs completely both in the synthetic J-map and the modeled in situ signature but in contrast when HI detects the CIR clearly in the J-map. In this case the predicted arrival time of the CIR from HI (vertical dashed line) matches the arrival time of the CIR measured in situ. This is illustrated in Figure 3.6.2, where this is clear CIR pattern in the real J-map that corresponds to a real CIR in-situ. But analysis of the synthetic J-map shows that there is no CIR pattern corresponding in the synthetic J-maps and of course no CIR simulated at the predicted impact at Earth.

(4) The HI J-map can also detect if the corotation of the CIR is too slow in Enlil simulations. To remove the effect of latitudinal gradients, we concentrated on the CIR formed by the giant coronal hole analysed in Deliverable 5.3. This equatorial coronal hole occupied a broad range of latitudes that covered the latitudes of the various in-situ spacecraft and as shown in Figure 3.6.3 of Deliverable 5.2 led to a north-south excursion of the neutral line. For this event, Figure 3.6.3 reveals that the CIR passage at Earth leads the passage of the simulated CIR by a shorter duration than when it passes at STEREO-A after corotating some 12 days later. Two vertical dashed lines marking at each spacecraft the onset of the speed increase of the simulated (solid blue line) and measured data (solid red line). Since the maximum speed of the simulated and measured CIRs at the same at both STEREO-A and Enlil, we associate this increase timing difference to the corotation rate of the CIR being too slow in Enlil. This is confirmed by the separation of the tracks observed in the J-maps (white arrows) in the bottom panel as the CIR corotates between the Earth and STEREO-A.

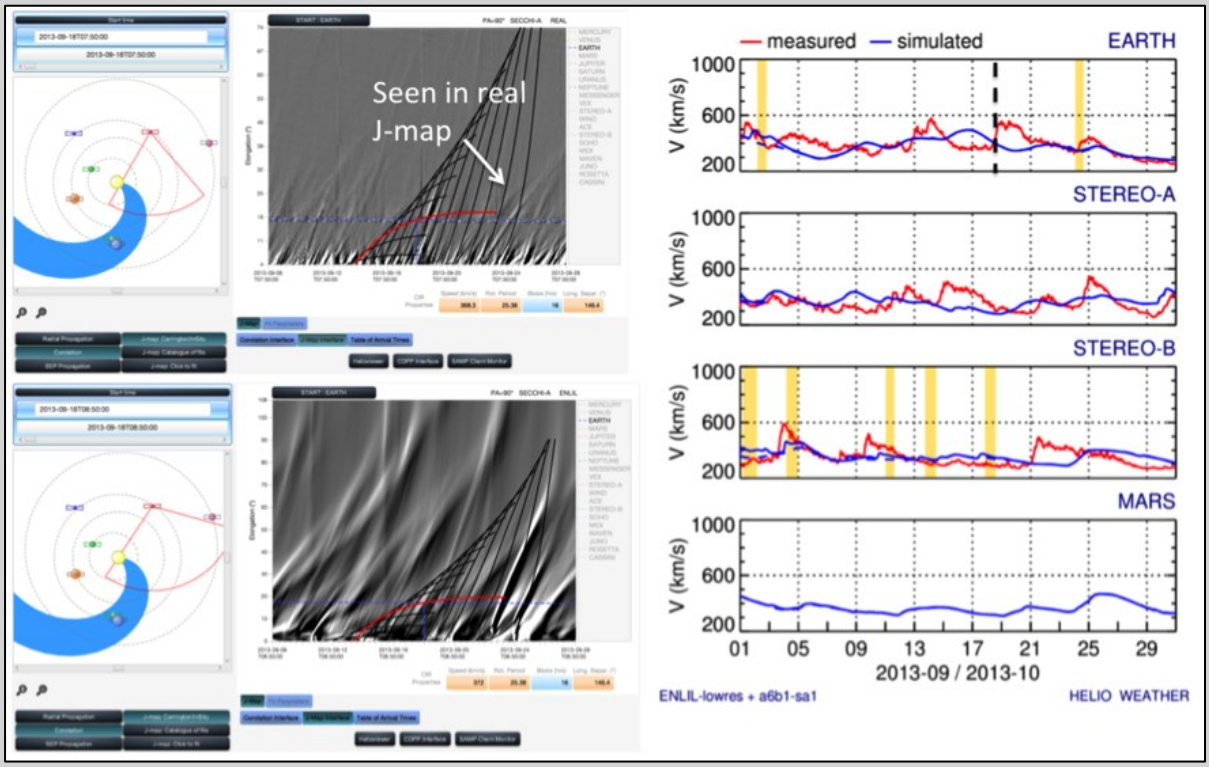

Fig. 3.6.2 - Same format as Figure 3.6.1.

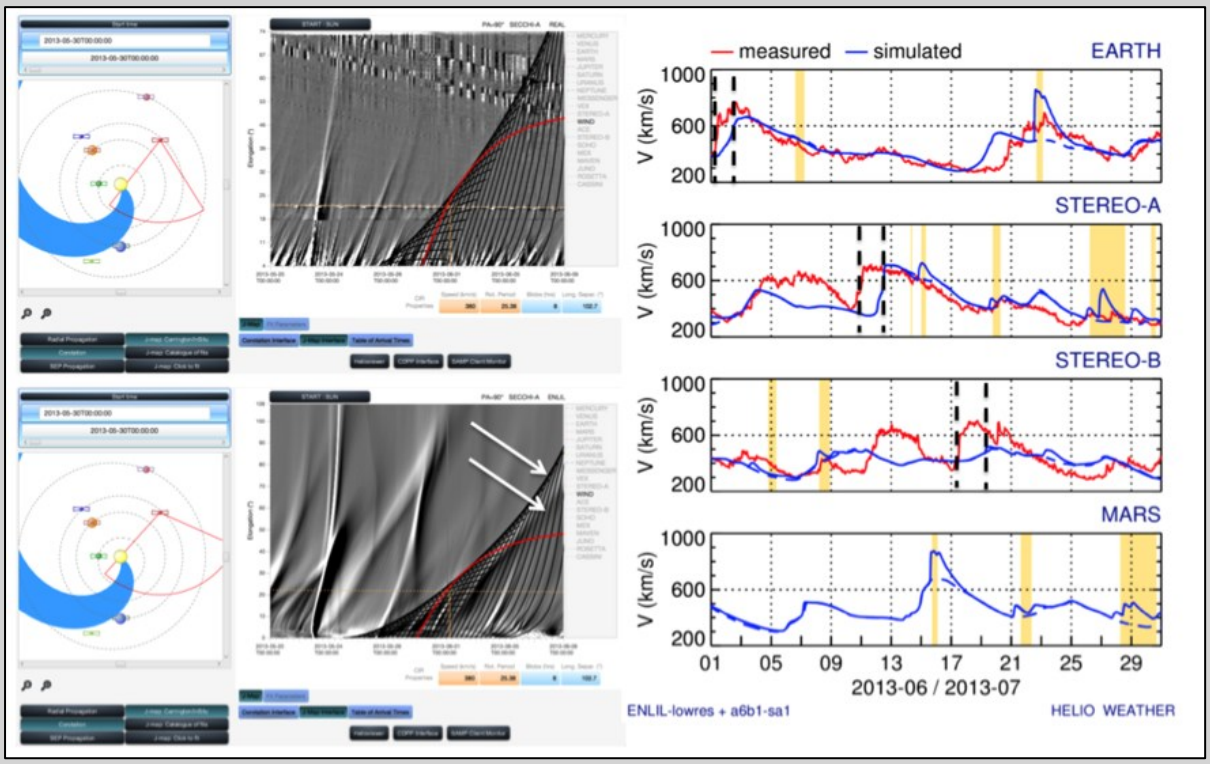

Fig. 3.6.3 - same format as Figure 3.6.1.

We conclude that heliospheric imagery provides great potential to validate the accuracy of simulations of CIRs. Since the compression region is stronger in the slow solar wind upstream of the stream interface, the observed

and modeled patterns of converging tracks are biased towards slow solar wind speeds. This was confirmed in WP5 through the extensive analysis of CIRs observed by HI. Therefore HI can only validate the location of the interaction region but provides no information on the amplitude and duration of the high-speed stream that follows. In addition HI can also detect if the interaction region has a faster or slower corotation speed than usually assumed in numerical simulations. Finally, when a simulation misses out a CIR passage completely due to bad coronal input, HI can provide a safeguard by bringing the necessary observation to confirm and locate that CIR.

WP6 TASK 6.2: ASSESSING THE USE OF HI TO INITIALISE ENLIL (TASK LEAD: UPS, CONTRIBUTOR: GMU)

The task we set ourselves to accomplish was comprised of the following:

- To derive a new method to produce solar wind parameters at the inner boundary of models simulating the interplanetary medium (21.5 R_s),
- To put in place a methodology that would allow the use of HI observations to evaluate the accuracy of the inner boundary conditions put into MHD models simulating the interplanetary medium (here Enlil),
- That the method is sufficiently fast that it can produce a catalogue of solar wind simulations from the corona to Earth-like distances and beyond.

To address the requirements of the HELCATS project and potentially deliver a new European space-weather asset, we developed a new solar wind model (MULTI-VP) which adopts a new approach to modelling the solar wind in 3D. This approach lies in between those of the traditional MHD global-scale models and of the more specialized uni-dimensional models. The model consists of computing many 1D wind solutions which sample the whole solar atmosphere (or any smaller sub-domain of interest). The individual 1D solutions are based on a previous mature uni-dimensional wind model (Pinto et al. 2009; Grappin et al. 2010), modified in order to take the full magnetic flux-tube geometry (expansion, inclination and amplitude of the field) and different heating functions. The background magnetic field geometry is currently obtained via potential field source-surface extrapolation (PFSS) from publicly available magnetogram data, but the model is ready to use any other data source (real data, coronal reconstructions or modeled data). The three-dimensional structure of the solar wind is then derived from this large set of contiguous uni-dimensional wind solutions, and take into account the heating and acceleration of the solar wind between the surface of the Sun and the top of the corona. MULTI-VP operates, typically, under the following workflow (see Figure 3.6.4):

1. Choice of a magnetogram data source. The source magnetograms can be full Carrington maps (e.g from Wilcox Solar Observatory - WSO - or from adaptative/ forecast magnetograms (for example, from HMI or ADAPT, at much higher temporal cadences).

2. Choice of a coronal field reconstruction method. We reconstruct the coronal magnetic field and sample out an ensemble of open magnetic flux tubes extending from the surface of the Sun up to about 30 Rsun and covering all latitudes and longitudes of interest (see Figure 3.6.4).

3. Computation of field-aligned wind profiles for each one of the sampled flux tubes. The wind model takes full account of the magnetic field amplitude, areal expansion and inclination in respect to the vertical direction along the flux tubes. The model includes a simplified chromosphere, the transition region (TR) and the corona (more details are given below).

4. Assemble the wind profiles and map the wind speed, temperature, density and magnetic field amplitude at all the positions desired (see Figure 3.6.4). We routinely produce maps at 21.5 R_s (see Figure 3.6.5) which can be used to initiate heliospheric propagation models (such as Enlil and EUHFORIA). This framework was designed to be fully modular, such that any of the points above can easily be replaced by other data sources and models depending on the scientific application, and as newer methods become available.

5. Using the 3-D density cube generated by MULTI-VP we create synthetic images of the corona to compare the simulated coronal structure (streamers/pseudo-streamers) with the observed structures in real

coronagraphic and heliospheric images (background subtracted; see Figures 3.6.6, 3.6.7, 3.6.8). The discrepancies in the locations of the simulated and modeled coronal structures is either due to the MULTI-VP model or to the PFSS reconstruction. We have then two approaches: either we change the magnetogram used in PFSS for one from another observatory or we change some parameters in MULTI-VP (heating function).

6. Once the solar wind output from MULTI-VP is produced, models simulating the interplanetary medium can propagate the wind to 1AU. We use the Enlil model for this task. It is then possible to convert the simulated 3-D density cubes into synthetic heliospheric images that are then converted to J-maps (see Deliverable 6.1). We can compare the locations of simulated and observed CIRs to evaluate the accuracy of the solar wind simulation (see methodology in Deliverable 6.1).

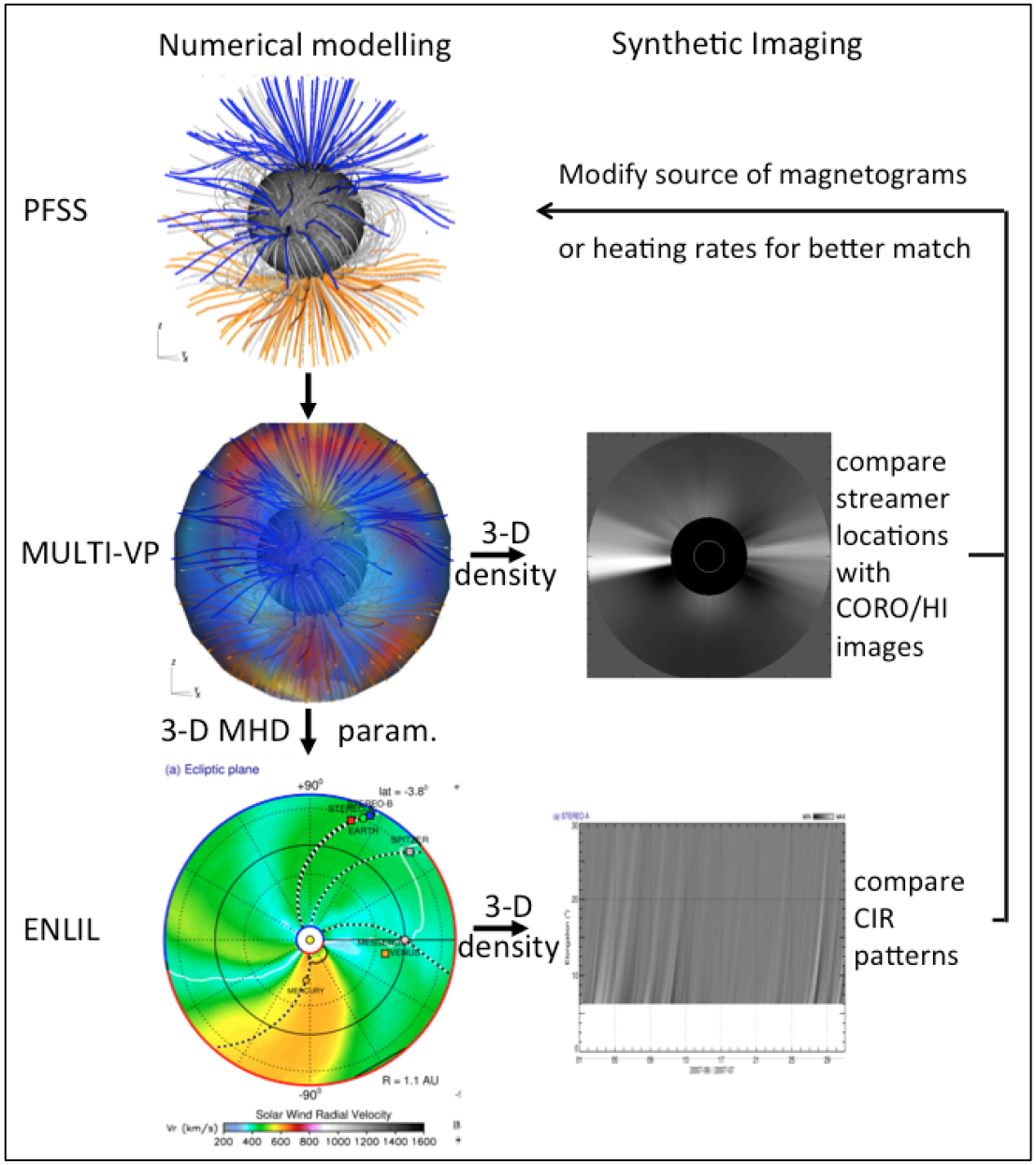

Fig. 3.6.4 - The setup followed in the present Deliverable to evaluate the accuracy of the background solar wind simulations with coronal and heliospheric imaging.

This framework was designed to be fully modular, such that any of the points above can easily be replaced by other data sources and models depending on the scientific application, and as newer methods become

available.

The new HELCATS MULTI-VP code

We present and discuss the design, implementation and testing of the new solar wind model, called MULTI-VP. The model calculates the dynamical and thermal properties of the solar wind from the chromosphere up to about 30 Rsun, and can cover the totality or a fraction of a spherical domain representing the three-dimensional open-field corona. In this task, we use Potential Field Source-Surface extrapolations from WSO synoptic maps covering several Carrington rotations both at solar minimum and at solar maximum (CR 2055 - 2079 and CR 2130 - 2149). We set a constant source-surface radius RSS = 2.5 R_s for the PFSS extrapolations and use the polar-field correction of Wang & Sheeley (1992). We trace an ensemble of open magnetic field lines starting from the source-surface down to the solar surface with a standard angular resolution of 5°. Each field-line is, at first, assigned a purely radial expansion above the source-surface. This leads to an interplanetary magnetic field amplitude which is very variable within each magnetic sector, much unlike the amplitudes measured by space probes in the interplanetary field (which are remarkably uniform everywhere except near polarity inversions close to heliospheric current sheets). We correct for this by adding an additional flux-tube expansion profile which smoothly (and asymptotically) transforms the very non-uniform source-surface field at r = RSS into a uniform field at about r = 12 R_s. The correction conserves the total open magnetic flux. Its effects on the properties of the wind flow are thoroughly discussed in Pinto et al. (2016).

The baseline model used to compute the solar wind profiles follows closely the strategy described in Pinto et al. (2009), albeit with a number of modifications. The numerical code solves the system of equations describing the heating and acceleration of a wind stream along a given magnetic flux-tube

$$\begin{aligned}
&\partial_t \rho + \nabla \cdot (\rho \mathbf{u}) = 0 \ , \\
&\partial_t \mathbf{u} + (\mathbf{u} \cdot \nabla)\, \mathbf{u} = -\frac{\nabla_s P}{\rho} \\
&\quad - \frac{GM}{r^2} \cos(\alpha) + \nu \nabla_s^2 u \ , \\
&\partial_t T + \mathbf{u} \cdot \nabla_s T + (\gamma - 1)\, T \nabla \cdot \mathbf{u} = \\
&\quad - \frac{\gamma - 1}{\rho} \left[\nabla \cdot F_h + \nabla \cdot F_c + \rho^2 \Lambda(T) \right] \ ,
\end{aligned}$$

where ρ is the mass density, u is the wind speed, and T is the plasma temperature. The wind profiles are computed on a grid of points aligned with the magnetic field (with curvilinear coordinate s), α is the angle between the magnetic field and the vertical direction (cf. Li et al. 2011; Lionello et al. 2014b), and r represents the radial coordinate (distance to the center of the Sun). The ratio of specific heats, γ, is 5/3. More details on the numerical scheme can be found in Pinto et al. (2016).

The terms Fh, Fc denote the mechanical heating flux and the Spitzer-H□arm conductive heat flux, which are both field-aligned. The radiative loss rate is Λ(T). The mechanical heating flux Fh parametrizes the coronal heating processes, and is assigned a phenomenological form inspired on that suggested be Withbroe (1988), but depending on the basal magnetic eld amplitude, on the total flux-tube expansion ratio f, and on the curvilinear coordinate s:

$$F_{\mathrm{h}} = F_{\mathrm{B0}} \left(\frac{A_0}{A} \right) \exp\left[-\frac{s - R_\odot}{H_{\mathrm{f}}} \right]$$

The heating coecient FB0 is proportional to the basal amplitude of the magnetic field, and Hf represents an arbitrary damping length which is inversely proportional to the total expansion ratio. The three-dimensional geometry of the coronal magnetic field is given directly by PFSS extrapolations and is represented in Fig. 3.6.5 for Carrington rotations 2056 (at the end of solar cycle 23, during the solar minimum of 2008) and 2123 (1.5 years before the peak of cycle 24). The former is characterized by equatorial streamers covering all longitudes, large coronal holes rooted at the poles, and a well dened heliospheric current sheet (HCS) which remains close

to the ecliptic plane (albeit with a noticeable warp). The latter shows, in contrast, the presence of high-latitude streamers and of large coronal holes rooted close to the equator and a double-lobed HCS. The figure also shows that the resulting slow and fast wind distribution relate to the large-scale geometry of the magnetic field, with slow wind conned to low latitudes during solar minimum and with slow and fast wind streams mixed up in latitude during solar maximum.

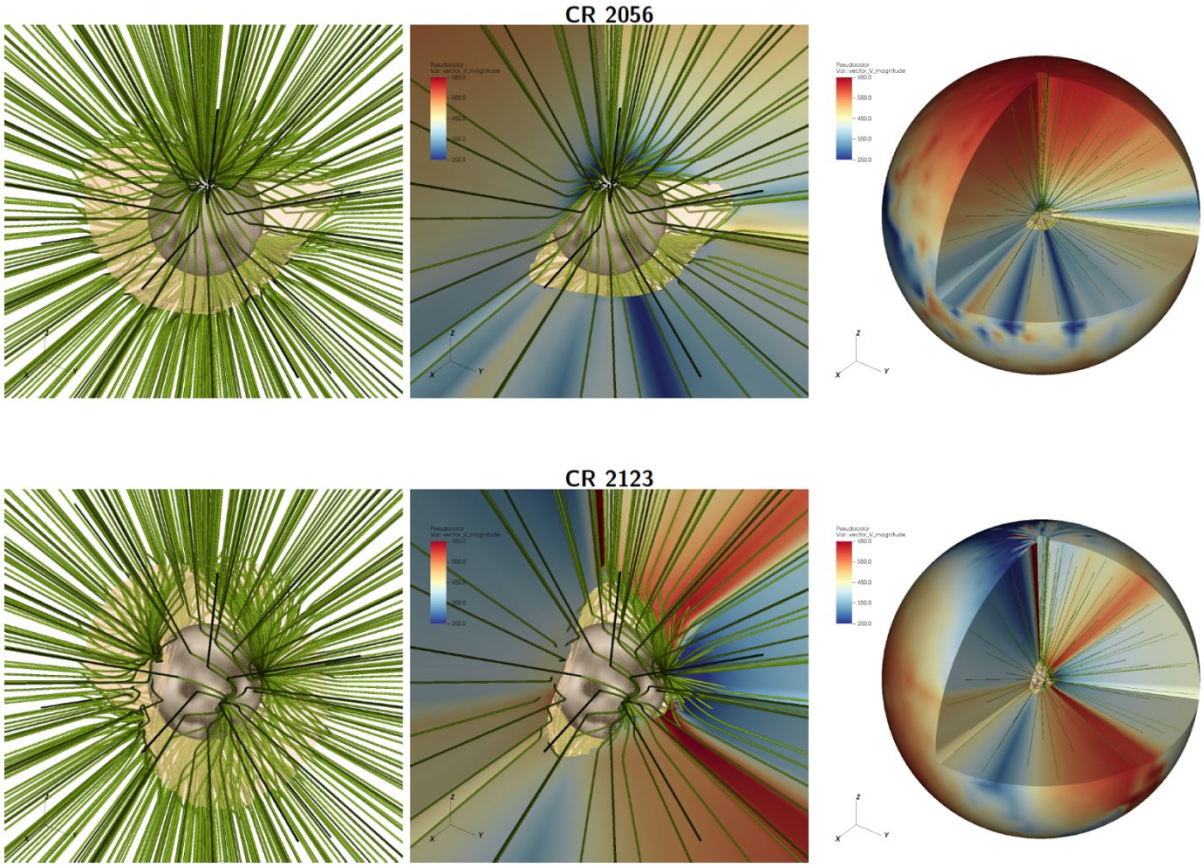

Fig. 3.6.5 - Illustration of the operation of MULTI-VP. The first row corresponds to CR 2056 (April - May 2007, close to solar minimum) and the second one to CR 2123 (April - May 2012, close to solar maximum). The first column shows the input WSO magnetogram rendered in gray-scale over the surface of the Sun and a sample of the magnetic field lines obtained via PFSS extrapolation used to initiate the model. The transparent yellow surface indicates the coronal hole boundaries (the closed-field regions are excluded from the domain). The second column shows a close-up of the wind speeds in the low corona, represented in colour-scale (from dark blue at 250 km/s to dark red at 650 km/s). The third column shows the same information at global scale (truncated at a radius of 15 Rsun and with one octant removed).

Figure 3.6.6 shows a sequence of maps of the wind speed, plasma temperature and density at 21.5 Rsun for several Carrington rotations. The vast majority of the wind streams are close to their asymptotic state at this height, the exceptions being those on the lower tail of the wind speed distribution, such as the very slow 200 – 250 km/s flows appearing on the 4th row of the figure (cf. Sanchez-Diaz et al. 2016). Slow wind flows tend to concentrate on the close vicinity of the HCS, but also occur in the regions surrounding pseudo-streamers. The plasma temperature is generally well correlated with wind speed, while the plasma density anti-correlates, which is consistent with space-borne measurements in the interplanetary medium (cf. Elliot et al, 2012). The velocity and density maps shown for solar minimum show a close resemblance to those obtained via global MHD simulations in (e.g, Yang et al, 2012), but with the band of slow wind being much thinner due to the absence of spurious cross-field diffusion (unavoidable in large-scale MHD computations). At solar maximum, the distribution of fast and slow winds shows a more intricate configuration with stronger contrasts between neighboring wind streams. The combination of the magnetic field amplitude of the corona with the obtained

wind speeds and densities lets us furthermore deduce the distribution of the characteristic magneto-hydrodynamical phase speeds important for characterising the medium through which CME propagate.

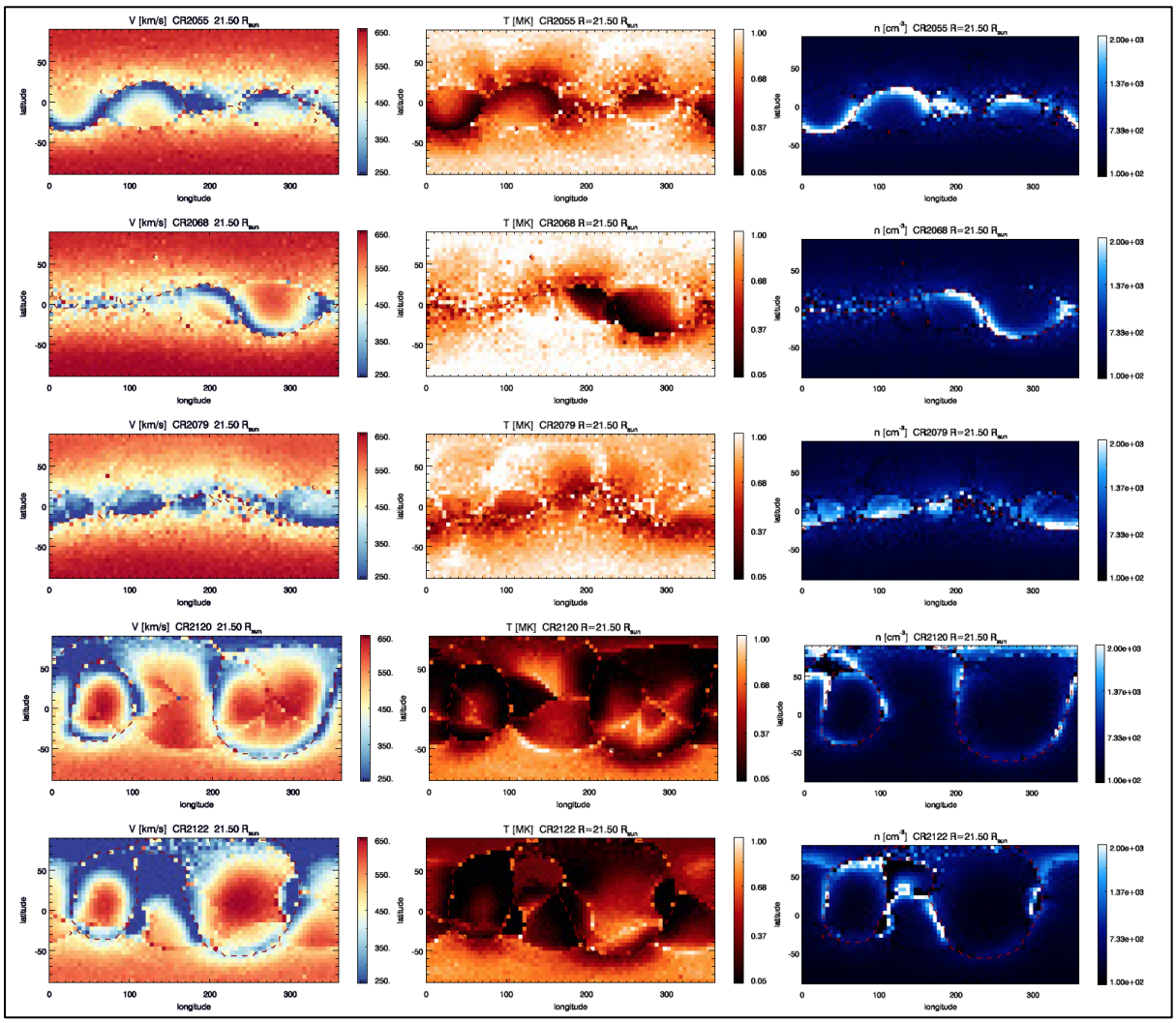

Fig. 3.6.6 - Carrington maps of the computed wind speed, temperature and density for several Carrington rotations (2055, 2068, 2079 and 2136) at r=21.5 Rsun. The dark-red dashed line shows the position of the heliospheric current sheet (HCS).

To conclude, MULTI-VP adopts a new and very promising approach which complements the past and present efforts on modelling the solar wind at global scales using full 3D MHD and on modelling the heating and transport processes at smaller scales on the wind flow. MULTI-VP computes detailed solutions of the background solar wind on a arbitrarily large bundle of open flux-tubes extending from the bottom of the chromosphere up to the high corona (typically up to 30 Rsun). The model is able to sample large regions of the solar atmosphere (up to a full spherical domain) with more detailed thermodynamics and with significantly smaller computational requirements than the current full MHD global models. MULTI-VP is furthermore unaffected by numerical resistive effects such as the spurious broadening of the HCS. We currently compute the state of the whole corona in about 6 hrs with moderate angular resolution (5x5 degrees) and with a moderate number of allocated computing cores. But the total execution can be significantly reduced, as the model is nearly perfectly scalable (in respect to parallel computing), and real-time operation can be envisaged. The downsides of the MULTI-VP strategy are that it relies on coronal field reconstruction methods (or any other more or less realistic magnetic field model), it neglects cross-stream effects on the wind, and is only well defined for stationary flows.

Calibration of the model with with coronagraphic and heliospheric observations

We used the FORWARD tool-set (Gibson et al. 2016) to deduce the white-light emission from our wind model and to build synthetic images of the corona. Figure 4 shows synthetic white-light polarised brightness (WLpB) images of the corona obtained from our simulations for Carrington rotations 2079 and 2136 sided by SoHO/LASCO-C2 images at the corresponding dates. The synthetic images were NRGF-filtered to enhance the contrast of the coronal features and ease the qualitative comparison. We found that the positions and widths of the main features are very well matched by our simulations for configurations typical both of solar minimum and solar maximum. The main differences between the synthetic and the real coronagraph images relate to the low angular resolution of the magnetograms we have used (5x5 degrees), meaning that we cannot capture the finer structure of the streamers and pseudo-streamers, and the absence of transient events (the magnetic and wind models are stationary). The lack of angular resolution is well visible for example on the coronal features at the equator (both east and west) on the first set of images in the figure (for CR 2079). The CME visible on the LASCO-C2 image on the bottom row shows is of course absent on the corresponding synthetic image. We note furthermore that some of the streamers are not strictly aligned with the vertical direction in the C2 images, which probably corresponds to a temporary deflection due to CME activity (see e.g. Rouillard et al. 2012). The corresponding features on the synthetic images are perfectly aligned with the vertical direction.

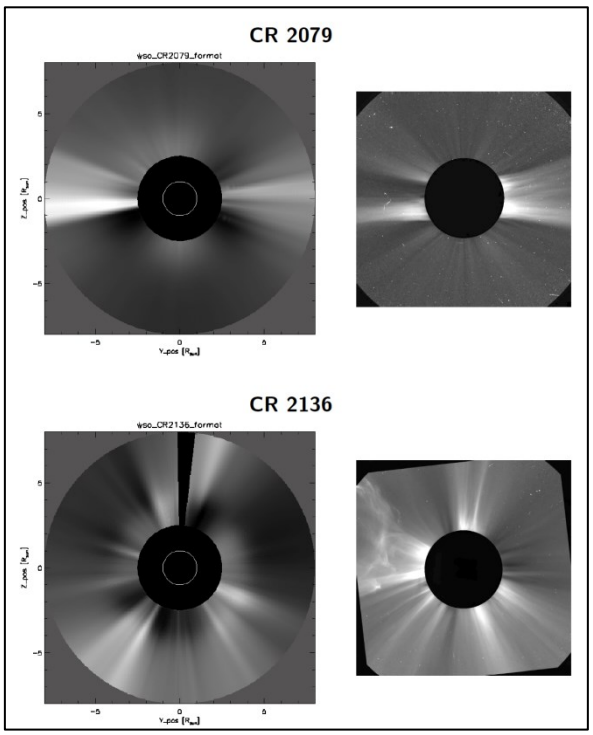

Figure 3.6.7 - Synthetic NRGF-filtered (left panel) and SoHO/LASCO-C2 (right) white-light images of the corona at solar minimum (top row) and solar maximum (bottom row).

Figures 3.6.8 and 3.6.9 show Carrington maps of synthetic WLpB built using west limb cuts at two different heights (r = 7 and 13 R_S) sided be real maps using STEREO-B/COR2 data. Once again we observe that the main features of the WL maps are very well reproduced (positions, slopes and widths) in our simulations, except for the signatures of coronal transients (CME) which appear as vertical traces in the COR2 maps.

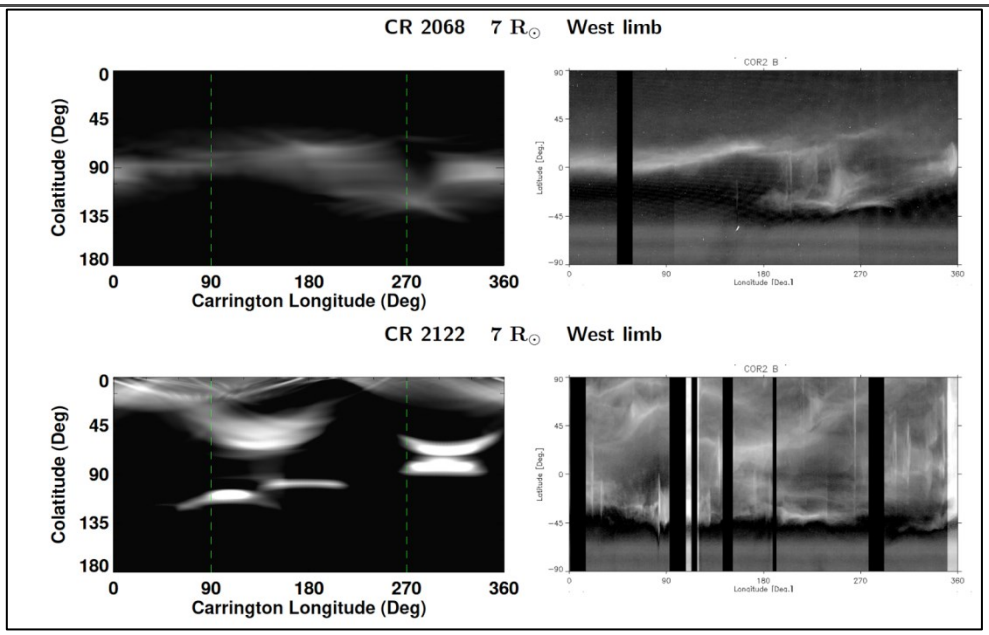

Fig. 3.6.8 - Synthetic white-light west-limb Carrington maps at 7 R (left panels) and SECCHI STEREO-A/B white-light images of the corona (right panels).

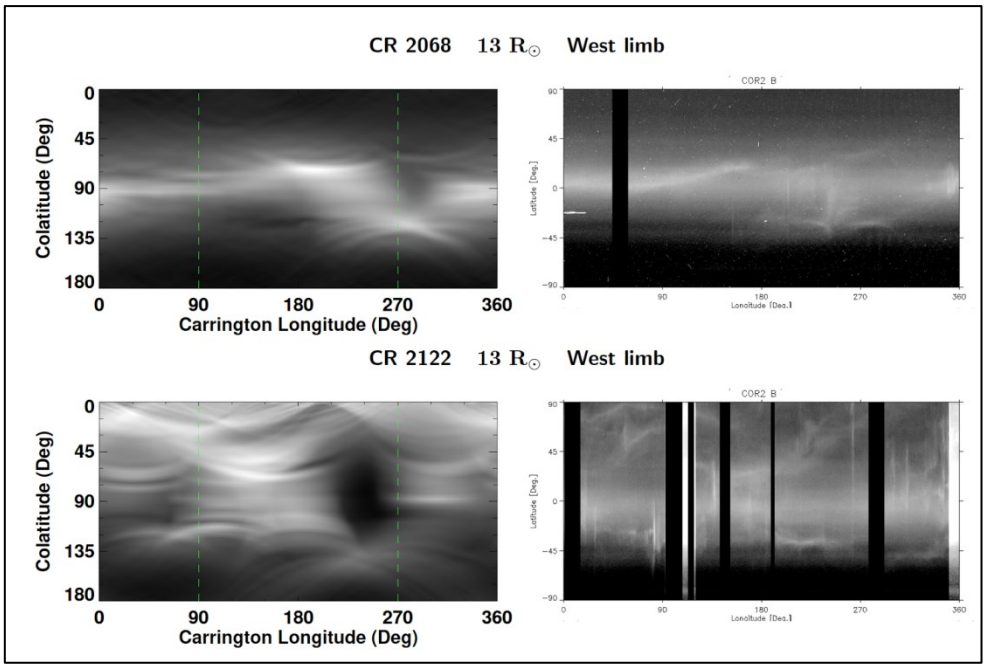

Fig. 3.6.9 - Synthetic white-light west-limb Carrington maps at 13 R_{sun} (left panels) and SECCHI STEREO-A/B white-light images of the corona (right panels).

Using heliospheric imaging from deliverables 5.2 and 5.3 to validate MULTI-VP

We evaluated how useful HI images would be to validate the modeled solar wind. As demonstrated in Work Package 5, HI can be used to locate the boundaries between fast and slow solar wind that form Corotating Interaction Regions. The occurrence of such boundaries on the database of solar wind simulation maps produced for HELCATS was systematically compared with the locations of CIR sources determined in Deliverable 5.3. This is shown in Figure 3.6.10, where we find that CIRs source locations (white markers) tend

to form where fast solar solar sources form immediately eastwards of the slow solar wind source (the streamer belt).

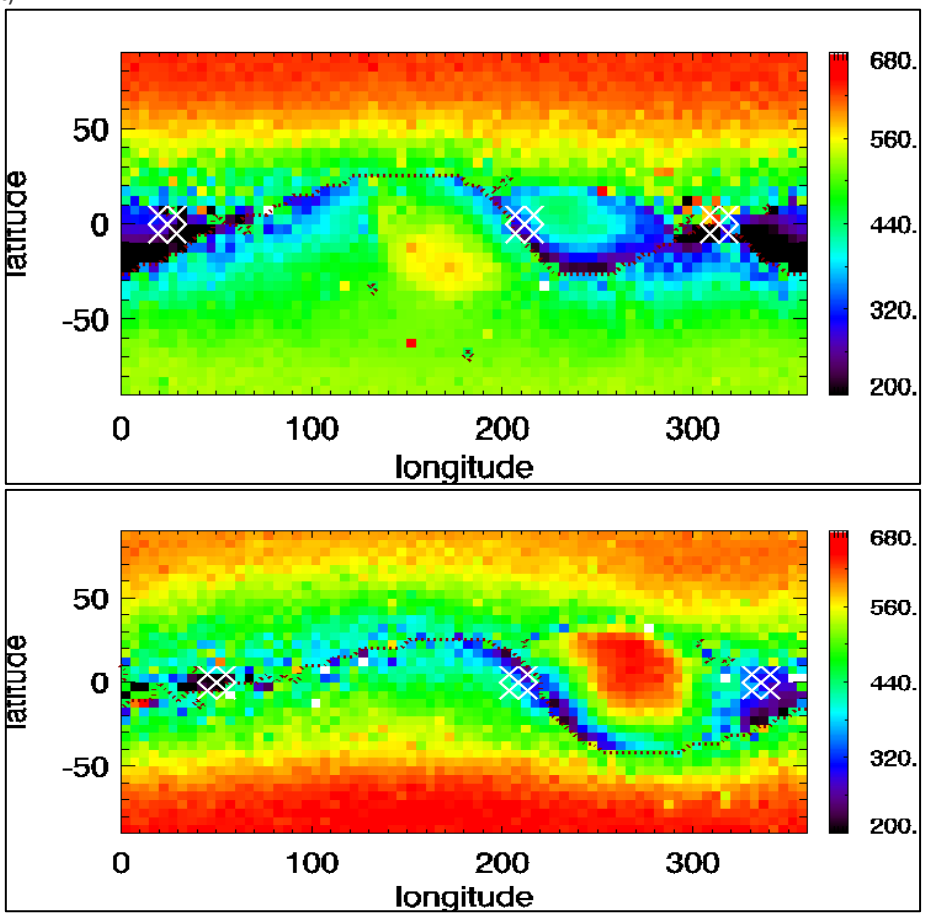

Fig. 3.6.10 - The solar wind speed modeled by MULTI-VP at 21.5 Rsun In a Carrington map format, CR 2061 (top) and 2066 (bottom), The source longitudes of the CDS located by Plotnikov et al. (2016) are marked by white arrows.

Coupling MULTI-VP with the ENLIL solar wind model

MULTI-VP can model the solar wind up to 30 R_{sun}, and we accomplished the propagation of the wind flow up to 1 AU (and beyond) with the help of an MHD model of the interplanetary medium (such as Enlil or EUHFORIA). The lower boundary of these models sit at r = 21.5 R_{sun}, and so we chose to produce systematically wind maps at the same height (such as those in Figure 3). MULTI-VP supplies the full set of physical boundary conditions required to initiate the model Enlil, hence providing an efficient method for coupling the coronal to the interplanetary media. Enlil was the model of choice to perform this task at the time when the HELCATS project was proposed.

We defined an intermediate data format to act as interface between MULTI-VP and Enlil, which consists on a re-write the wind maps produced by MULTI-VP (wind speed, density, temperature and magnetic field amplitude at 21.5 R_{sun}) in a flexible and human-readable text format. The data files contain a header which identifies:

1. the source wind model (MULTI-VP) and its main setup parameters (typically, magnetogram source, date or Carrington rotation used,
2. the map grid dimensions and coordinate ordering adopted,
3. full descriptors of the numerical records in the file, including names of the physical quantities, their ordering and dimensions,
4. a list of control parameters, used to verify if the data was well read.

This self-descriptive scheme ensures the portability of the data for future applications. We also planned transcribing this scheme into standard formats more widely used by the community (e.g: FITS, CDF or HDF5). Different representations of the same data, such as maps with different grids and angular resolution, are kept separately and can be recombined as multi-block grids after reading.

The full wind maps were built initially at a coarse angular resolution (5x5 degrees) and limited to a latitudinal range of 60 to -60 degrees, providing the first set of boundary conditions which let us run Enlil at its low resolution configuration. After inspection of the first results, we refined the most relevant regions of the domain (down to 2x2 degrees), notably a 24 degree wide latitudinal band around the solar equator. Furthermore, we also tested against magnetic field extrapolations from a different source of magnetographic data. We chose a few publicly available NSO-GONG magnetograms for carrington rotations matching some of the previous runs. These maps have a higher angular resolution than the WSO maps we used before (of 1x1 degrees close to the equator) and are built using different instruments. We downgraded the NSO-GONG maps to the previous 5x5 degree angular resolution and cross-calibrated them against the WSO maps. We kept the higher resolution NSO-GONG for the tasks 6.3 and 6.4.

Figure 3.6.11 shows one example of speed and density maps assimilated by Enlil as lower boundary conditions. The figure also shows the latitudes and longitudes of planets Mercury, Venus, Earth and Mars, and of spacecraft STEREO A and B at the corresponding time.

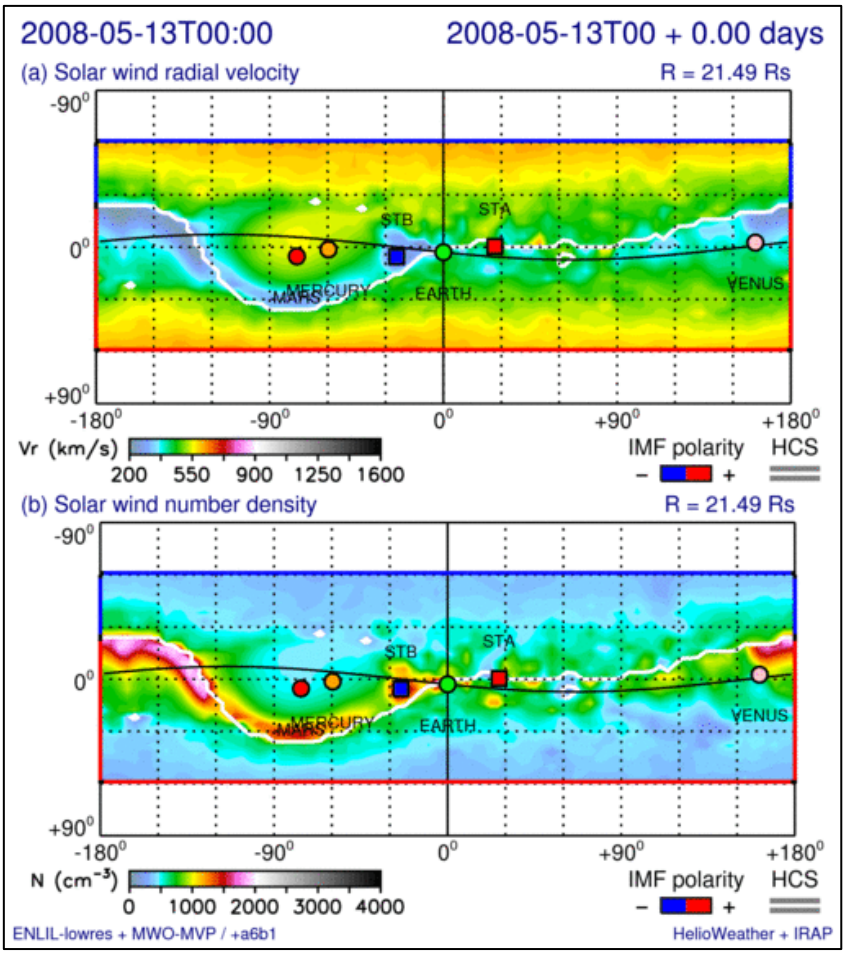

Fig. 3.6.11 - Input boundary conditions (top: solar wind speed, bottom: solar wind density) to the Enlil model coming from the MULTI-VP code.

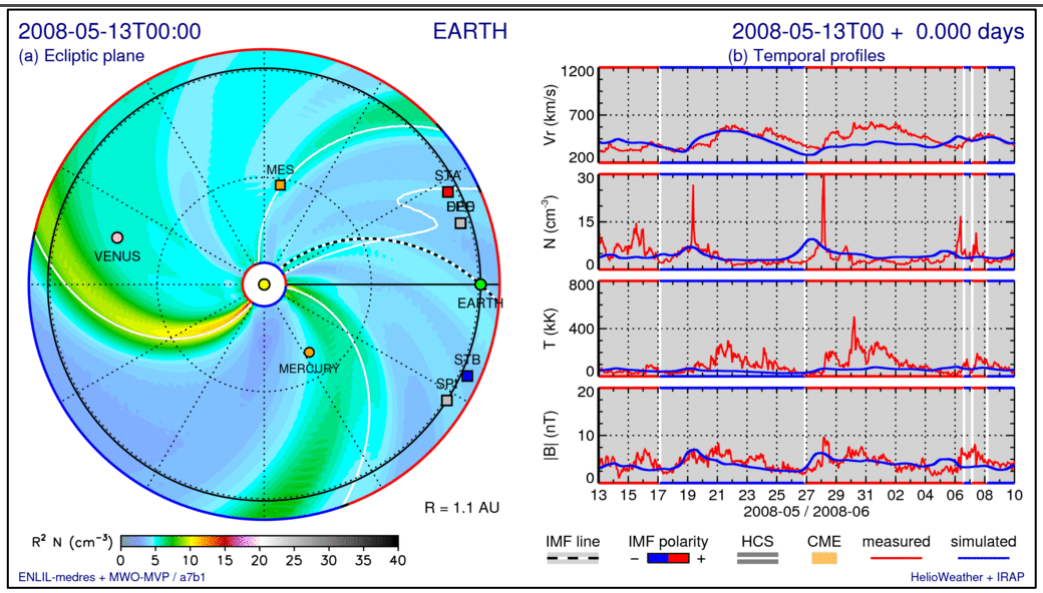

Fig. 3.6.12 - Results of propagation the solar wind from MULTI-VP to 1 AU and beyond. Left-hand panel shows the distribution of densities in the ecliptic plane. Right-hand side: Simulations of solar wind speed (Vr), density (N), temperature (T) and magnetic field strength (B) at Earth.

An example of the solar wind parameters simulated by Enlil from 21.5 R_s (= 0.1 AU) to 1 AU using MULTI-VP date is shown in Figure 3.6.12. This Enlil run corresponds to the first series of coupled runs, before any adjustment to the MULTI-VP code was made. In other words, it corresponds to the left branch of the scheme in Figure 3.6.4 before the outer feedback loop between Enlil and PFSS / MULTI-VP was enabled. These first results are a milestone, and represent the first remarkable representation of the solar wind speed and densities at 1 AU based solely on physical principles (without resorting to heuristic or semi-empirical laws).

MULTI-VP was, at this point, already optimised to reproduce well the white-light observations of helmet streamers made by coronagraphs and heliospheric images (cf. the inner feedback loop in Figure 3.6.3). The good match between the observed and simulated densities follows from this initial calibration procedure. The helmet streamers are the densest structures observed in the corona, and correspond to the brightest features in images of Figure 3.6.7. After propagation, they generate strong density signatures at 1 AU well visible in the time-series plotted on the right-hand side of Figure 3.6.12.

The figure also shows that the use of standard PFSS extrapolation to reconstruct the magnetic field of the corona underestimates globally the magnitude of the magnetic flux in the interplanetary medium. This was corrected in the second calibration step, after these first Enlil simulations were performed.

Figure 3.6.13 illustrates the method used to generate synthetic white-light J-maps for the fields of view of heliospheric imagers using MULTI-VP+Enlil simulations. This combo computes 3-D density cubes of the interplanetary medium, taking solar rotation into account. A map of the wind density in the ecliptic plane at all azimuths is shown in the top left-hand panel. The bottom left-hand panel shows the temporal evolution of the solar wind density as they would be measured at differents points (Earth, STEREO A and B). We then run a model that simulates the effect of Thomson scattering on the solar wind electrons. We compute the brightness of the corona as viewed from STEREO-A and STEREO-B's perspectives. Once synthetic images are produced (top-right hand panel), we compute the difference between consecutive images to produce running-difference images. To produce the synthetic J-ms, we then extract bands of pixels at the Position Angle (PA) of the Earth, and plot these bands vertically with time (bottom-right hand panel). Figure 3.6.14 shows two examples of synthetic J-Maps we obtained via this technique, one for the field of view of STEREO-A and the other one for the field of view of STEREO-B.

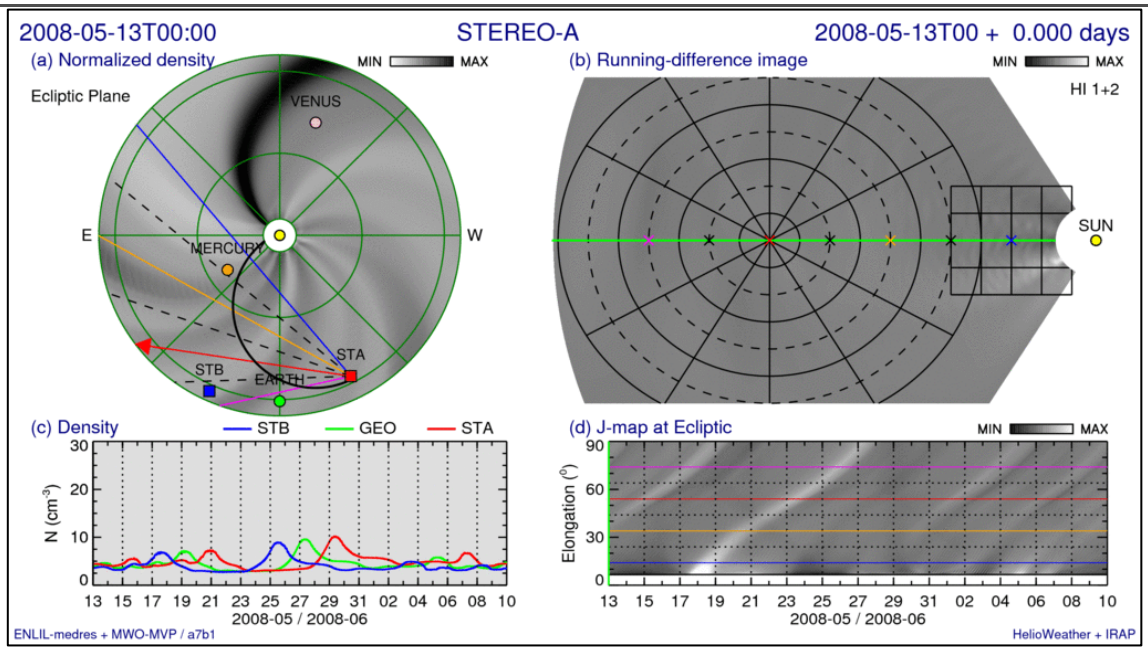

Fig. 3.6.13 - The procedure to produce synthetic white-light images and J-maps with ENLIL simulations.

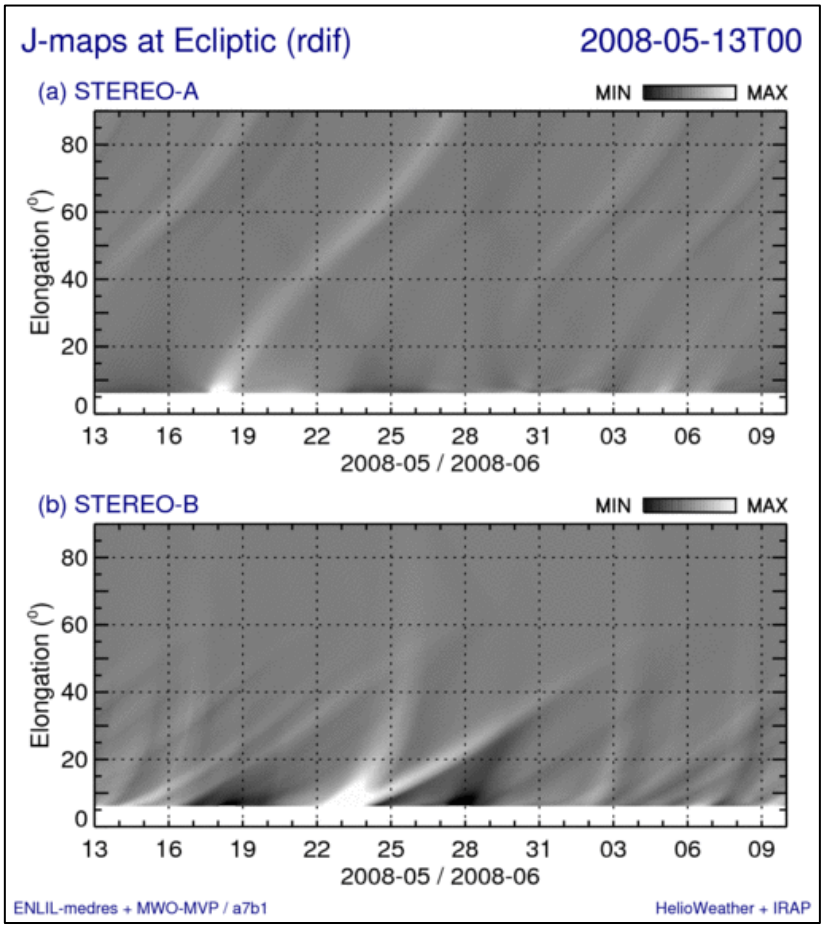

Fig. 3.6.14 - Synthetic J-maps produced from MULTI-VP and Enlil combined for the fields of view of STEREO A and B.

Production of the optimised database of simulations

The set of solar wind simulations we performed provide new estimates of the state of the background solar wind which are based only on physical principles and are more complete than the methods currently in use. We compared systematically the results we obtained by combining MULTI-VP and ENLIL with the results obtained via current standard techniques relying on semi-empirical scaling laws.

We proceed by testing the output of our model against in-situ measurements of different spacecrafts and against white-light J-Maps and coronal/heliospheric imagery. We adopt immediately the solar wind solutions that provide better predictions than the classical methods. We then re-iterate and re-calibrate the runs that did not produce the best results (see scheme in Figure 3.6.4). The improvements to the model consist mostly of small adjustments to the magnetic field extrapolation, to the heating parameters and to the geometry of the grid used by the simulations. This calibration process leads to considerable improvements of the MULTI-VP model and to increasing the efficiency of the coupling with Enlil. The background solar wind database was produced this way and was made available via the IRAP STORMS website (stormsweb.irap.omp.eu) and on the HELCATS website.

WP6 TASK 6.3: CONTINUAL ASSIMILATION OF HI DATA IN ENLIL AND COMPARISON WITH STANDARD IMPLEMENTATION TECHNIQUES (TASK LEAD: UPS, CONTRIBUTOR : GMU)

The aim of this task was to produce the catalogue of simulations of the interplanetary medium (SIMCAT) based on accurate input conditions of the background solar wind and on the catalogues of CMEs produced in WP3. We completed this task in a number of different ways.

1. Preparation of the CME input for the ENLIL simulations: The CME catalogues produced in WP3 (HiGeoCAT) using different assumptions on the geometry of CMEs (fixed phi, self similar, harmonic mean) provide the launch time, direction of propagation (in Heliocentric Earth Equatorial coordinates: HEEQ), speed (km /s) and extent (for the self similar technique it is fixed at a half angle of 30 degrees).

All these CMEs were fitted using heliospheric imagery, therefore the catalogues:

- include potentially the same CME in the field of views of HI-A and HI-B: duplications between the two catalogues can be removed by using the combined CME list provided in WP2 that identifies the CMEs seen simultaneously in both HI-A and HI-B.

- do not include the CMEs propagating through regions that are not imaged by the HIs, the latter is not an issue to synthetic J-maps to be compared with real J-maps constructed with HI images. Nevertheless, to be more useful to scientists that may potentially be interested in CMEs that are not imaged by HI, we decided to derive a new CME catalogue that also includes CMEs not imaged by HI. In order to achieve this, we used the Database of Notifications, Knowledge, and Information (DONKI) CME list (DONKICAT) derived using coronagraph images from SoHO and STEREO. This list is maintained by scientists at NASA Goddard Space-Flight Center.

The HELCATS HiGeoCAT catalogues produced in WP3 provides CME properties for the period April 2007 to January 2017 with a gap between September 2014 and November 2015 associated with the superior conjunction of the STEREO spacecraft. This large gap also justified the use of a complementary CME catalogue based on SoHO observations to derive an uninterrupted CME catalogue covering nearly the entire solar cycle. DONKICAT starts in June 2010 and runs continuously until January 2017.

A more comprehensive catalogue of CMEs was therefore produced especially for this task in order to simulate all CMEs imaged and fitted by different teams using coronagraphs and heliospheric imagery. This list was produced by:

- combining the STA and STB CME lists of WP2 (1414 CMEs),

- removing the 240 events from the STEREO-B CME list that were already observed and listed in the STEREO-A,
- adding all CMEs measured by DONKICAT (1594 CMEs) that erupted 6 hours before or after a CME listed in HELCATS HiGeoCAT.

We derived the new catalogue based on the Fixed-Phi (FP) and Self-Similar Expansion (SSE) HiGeoCAT as they cover the two extreme cases of different geometries. Hence we have two catalogues of CMEs to input into ENLIL a HiGeoCAT-SSE-DONKI and HiGeoCAT-FP-DONKI catalogue. The combined HiGeoCAT-SSE-DONKI catalogue gives the properties of 3457 CMEs shown in Figure 3.6.15.

The numerical code ENLIL (Sumerian god of wind and storms) is a research tool for simulations of corotating and transient solar wind disturbances. The physical model is based on ideal magnetohydrodynamics (MHD) and the numerical scheme is an explicit high-resolution TVD Lax-Friedrichs scheme (Odstrcil and Pizzo 1999).

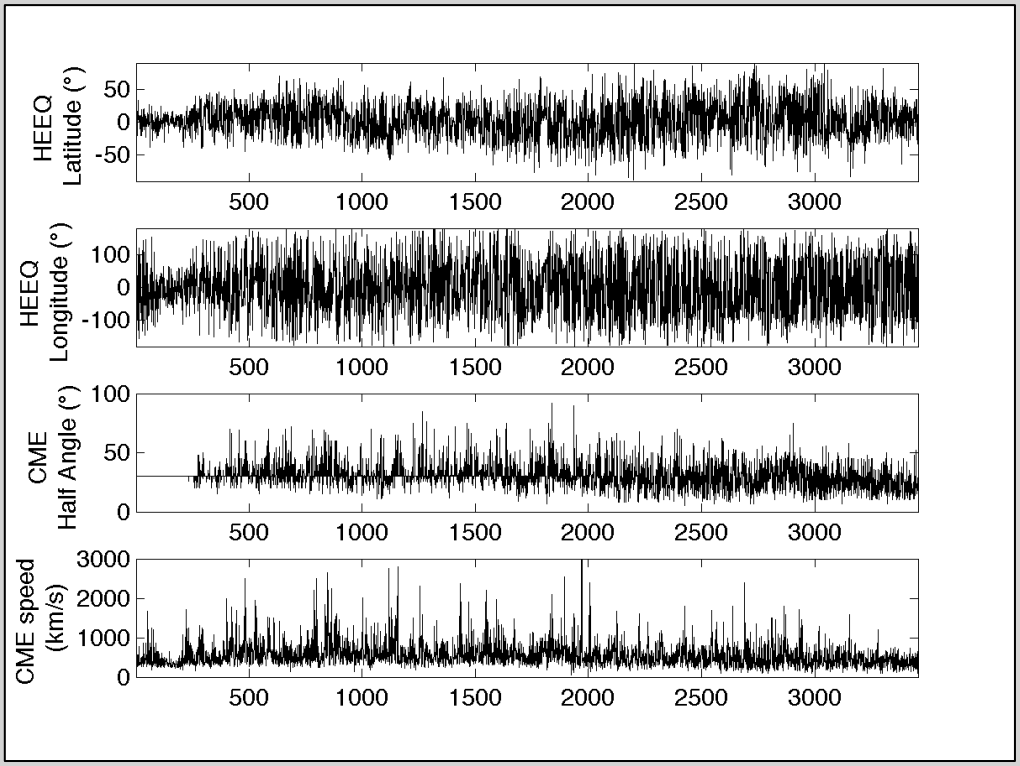

Figure 3.6.15 - The combined HELCATS-DONKI catalogue of all CMEs employed for the simulations. From top to bottom: the latitudes and longitudes of the direction of propagation, half angle and speed of the CMEs provided by the HELCATS HiGeoCAT Self-Similar Expansion and the DONKI catalogues.

Half angle: There are a number of different assumptions between the different techniques employed that are visible in Figure 3.6.15. The SSE techniques assumes for instance that all CMEs have a 30 degree half angle whereas the DONKI catalogue makes no such assumption and fits the angular width of CMEs observed in coronagraph images with on the CME cone model. The median of all half angles given in the DONKI catalogue is very close to 30 degrees. In the third panel of Figure 3.6.15, the half angle is fixed at 30 degrees by the HiGeoCAT-SSE catalogue before the DONKI catalogue begins (June 2010). The Fixed-Phi technique does not assume nor provides a half angle hence it is a free parameter that we also set at 30 degrees when incorporating the HiGeoCAT-FP into our combined catalogue.

CME Speeds: The CME speeds derived by the HiGeoCAT-SSE and HiGeoCAT-FP are representative of the CME speeds in the interplanetary medium once acceleration effects have been attenuated by the weakening of the magnetic forces acting the CME flux rope. The CME parameters provided by DONKI are derived using real-time coronagraph observations from spacecraft and a geometric triangulation algorithm. The measurements are an

approximation of the true 3D speed and width of the CME at 21.5Rs. However, often the coronagraph derived measurements are inferred from just a few data points, and some CMEs may be missed due to real-time data gaps.

To prepare the files for the ENLIL simulations we computed the times of passage of each CME at 21.5Rs starting from the launch time and assuming a constant speed from the solar surface.
Background solar wind:

The background solar wind was simulated with three inputs:

- the standard Wang-Sheeley-Arge (WSA) model based on the flux expansion factor of magnetic flux tubes derived from the results of the PFSS and Schatten-Current Sheet models. The magnetograms were updated every Carrington rotation and were obtained from GONG-NSO.
- the time-dependent version of the Wang-Sheeley-Arge model run on GONG-NSO magnetograms updated daily,
- the MULTI-VP model developed in Task 6.2 and run on magnetograms from the Wilcox Solar Observatory.

2. Combined solar wind and CME simulations:
The two catalogues of CMEs HiGeoCAT-FP/DONKI and HiGeoCAT-SSE/DONKI produced in this task were then injected as hydrodynamic ejecta into the ENLIL 3-D MHD model. 3457 CMEs were simulated over nearly the entire solar cycle 24 (April 2007-January 2017) covering the deep solar minimum (April 2007-September 2009) as well as solar maximum (peak of sunspot activity measured on April 2014). Figure 3.6.16 presents the simulated solar wind at Earth for the year 2010 based on the results of ENLIL simulations with the WSA-GONG model and the HiGeoCAT-FP/DONKI CME catalogue.

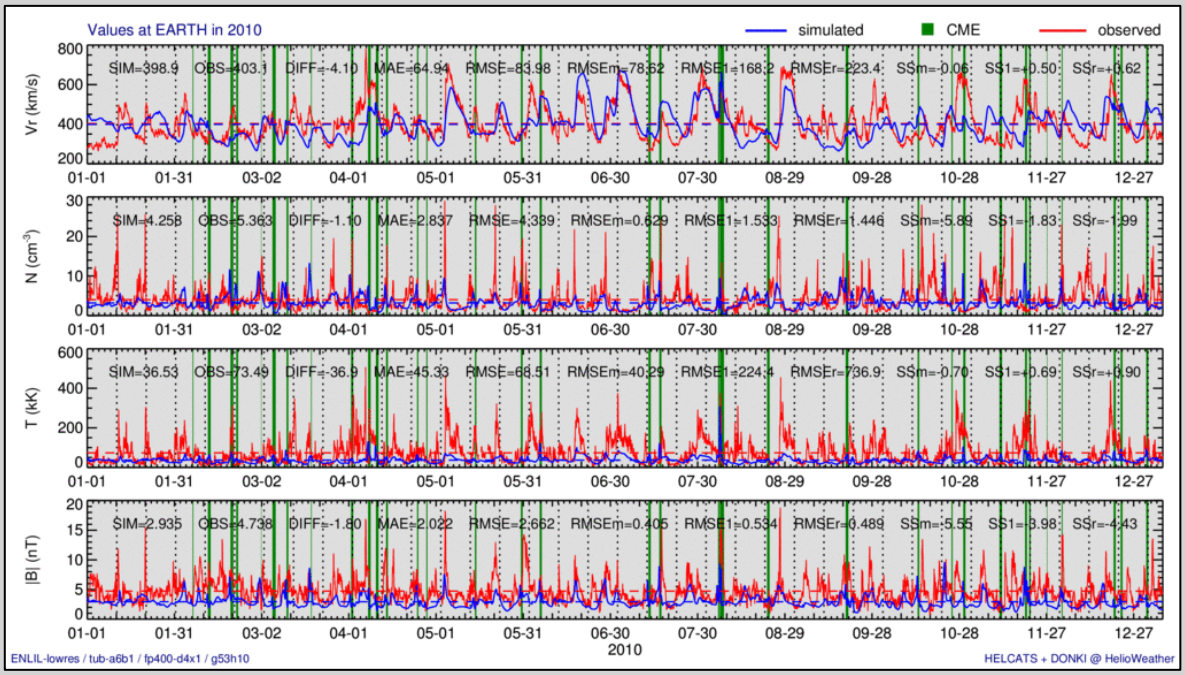

Figure 3.6.16 - A comparison of simulation results from the ENLIL model (blue) with in-situ measurements made near Earth (red) for the year 2010. The boundary conditions were from the WSA solar wind and the HiGeoCAT-FP CME catalogue. From the top to bottom: the solar wind speed (km/s), the density (cm^{-3}), temperature (kK) and magnetic field strength (nT). The vertical green lines correspond to times when CMEs were launched in the ENLIL model along any direction (not necessarily along the Sun-Earth line).

We derived two catalogues of CME simulations with CME speeds greater than 400 km/s and with all CMEs. Figure 3.6.16 presents a zoomed-in view of Figure 3.6.16 for the month of April 2010. A CME impacted Earth

on 5 April 2010, this CME was studied in detail in Rouillard et al. (2011). The event, erupted near central meridian on 3 April 2010 and was imaged by both STEREO spacecraft. The HELCATS CME IDs are HCME_A__20100403_01 and HCME_B__20100403_01. As we can see in Figure 3.6.17, the event impacted Earth (Measured Arrival Time in Figure 3.6.17) several hours (15 hours) before the simulated arrival time for this particular ICME.

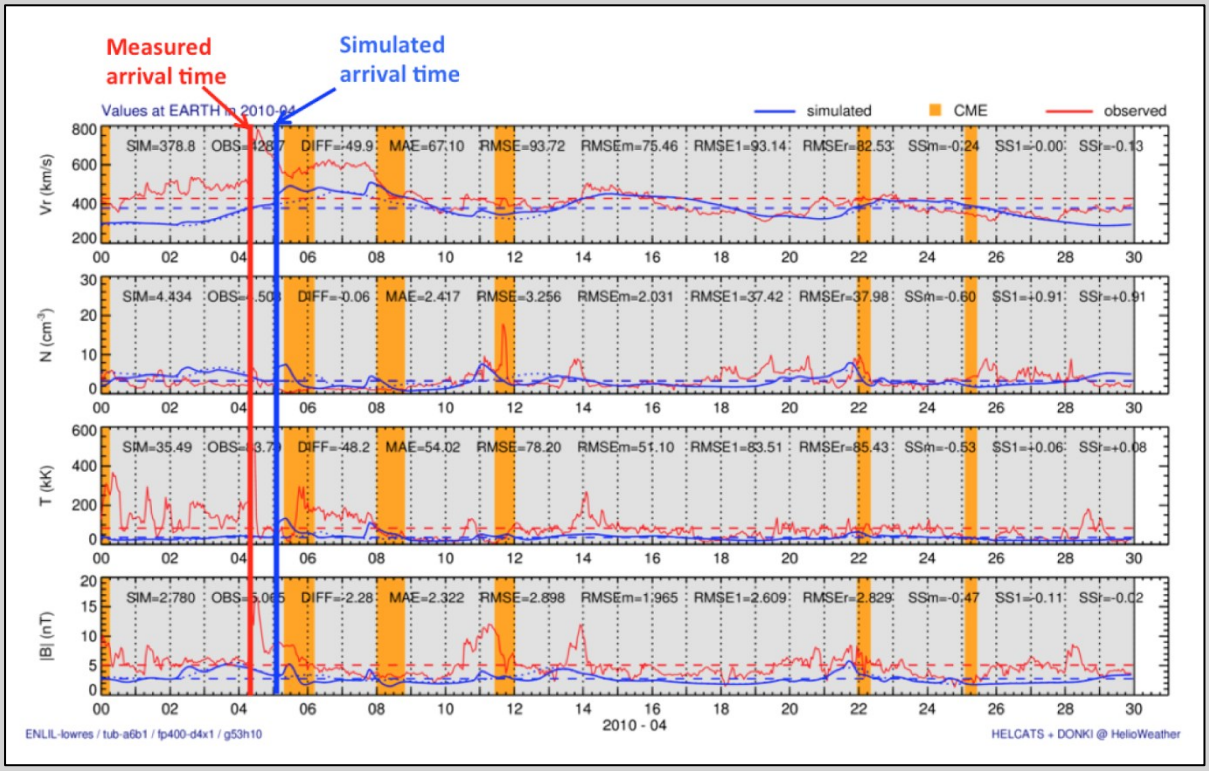

Figure 3.6.17: a zoomed-in view of Figure 2 to illustrate the signature of an ICME measured in situ and simulated by the numerical setup WSA-GONG and HiGeoCAT-FP/DONKI.

The HELCATS catalogue of simulations (SIMCAT) consists in movies of MHD parameters in the ecliptic plane, synthetic images, plots of in situ measurements at all planets and probes situated in the inner heliosphere, these are illustrated in Figure 3.6.18 and 3.6.19 for two CMEs simulated in December 2008 and the same CME as shown in Figure 3.6.15. The datacubes of simulated densities can be exploited to produce synthetic images expected from the STEREO-A and -B spacecraft. An example is shown in the middle panel of Figure 3.6.18 where we display simulated HI-1/2 images and synthetic J-maps (see report on Tasks 6.1 and 6.2 for more details). These dataproducts can be compared with the real images and movies made available via the official FP7- HELCATS website.

To complete this deliverable we created movies shown in the bottom panels of Figure 3.6.18 and 3.6.19 showing when and how different spacecraft taking in-situ measurements are connected to the CME-driven shocks. These movies cover the entire simulated period (2007-2017) and will be highly useful for scientist studying the origin of energetic particles. Indeed an enhanced flux of energetic particles measured at a spacecraft could be linked to the spacecraft's connectivity to a CME-driven shock modeled in SIMCAT.

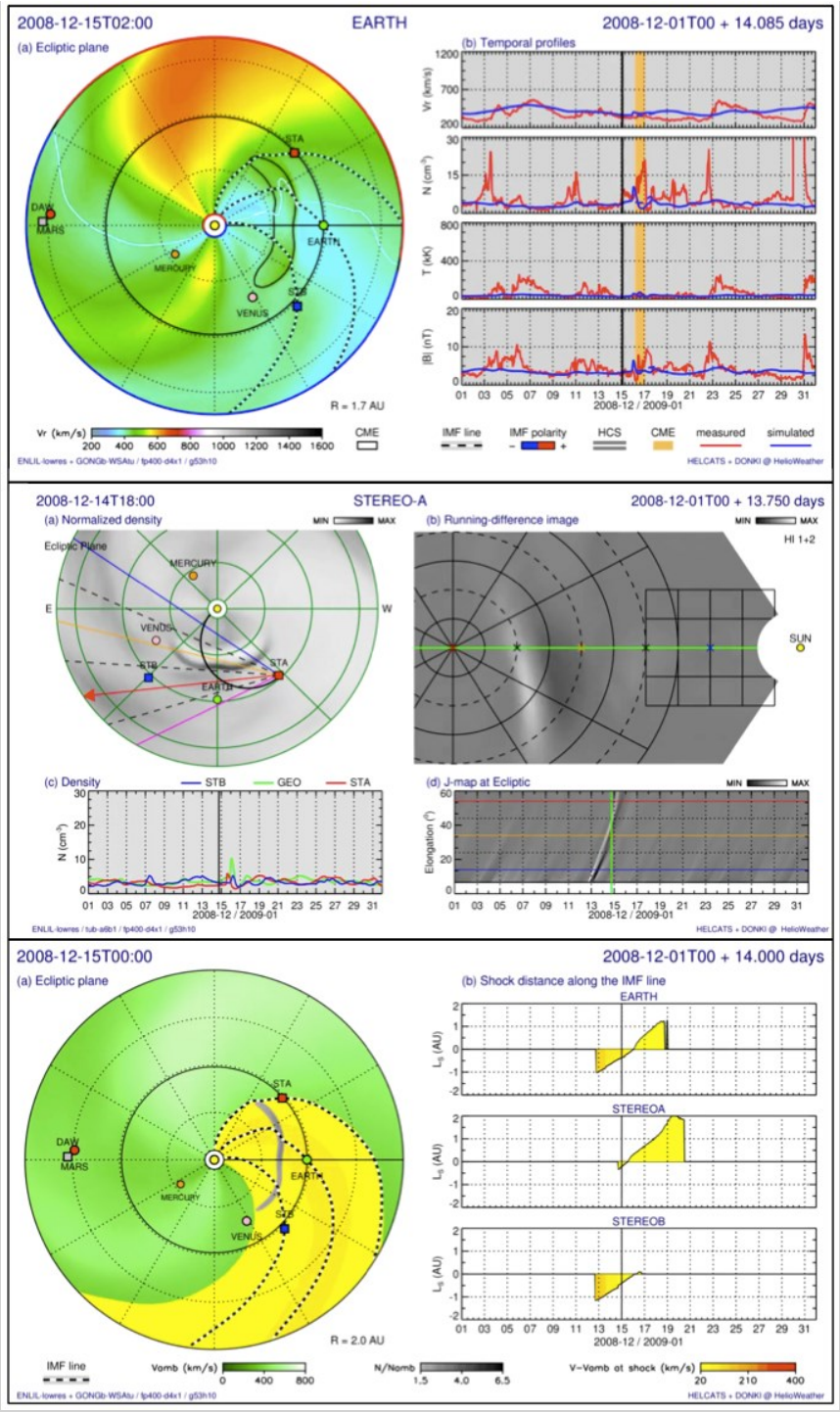

Figure 3.6.18 - Example of data products made available via the HELCATS SIMCAT. Top: a composite of images showing (left) the distribution of plasma speed in the ecliptic plane and the modeled in-situ signature near 1AU (repeat of Figure 3.6.17). Middle: distribution of solar wind density in the ecliptic plane (left), simulated STA images and expected J-maps (right). Bottom: images and plots giving the times and regions of the ecliptic plane that are magnetically connected to a CME-driven shock.

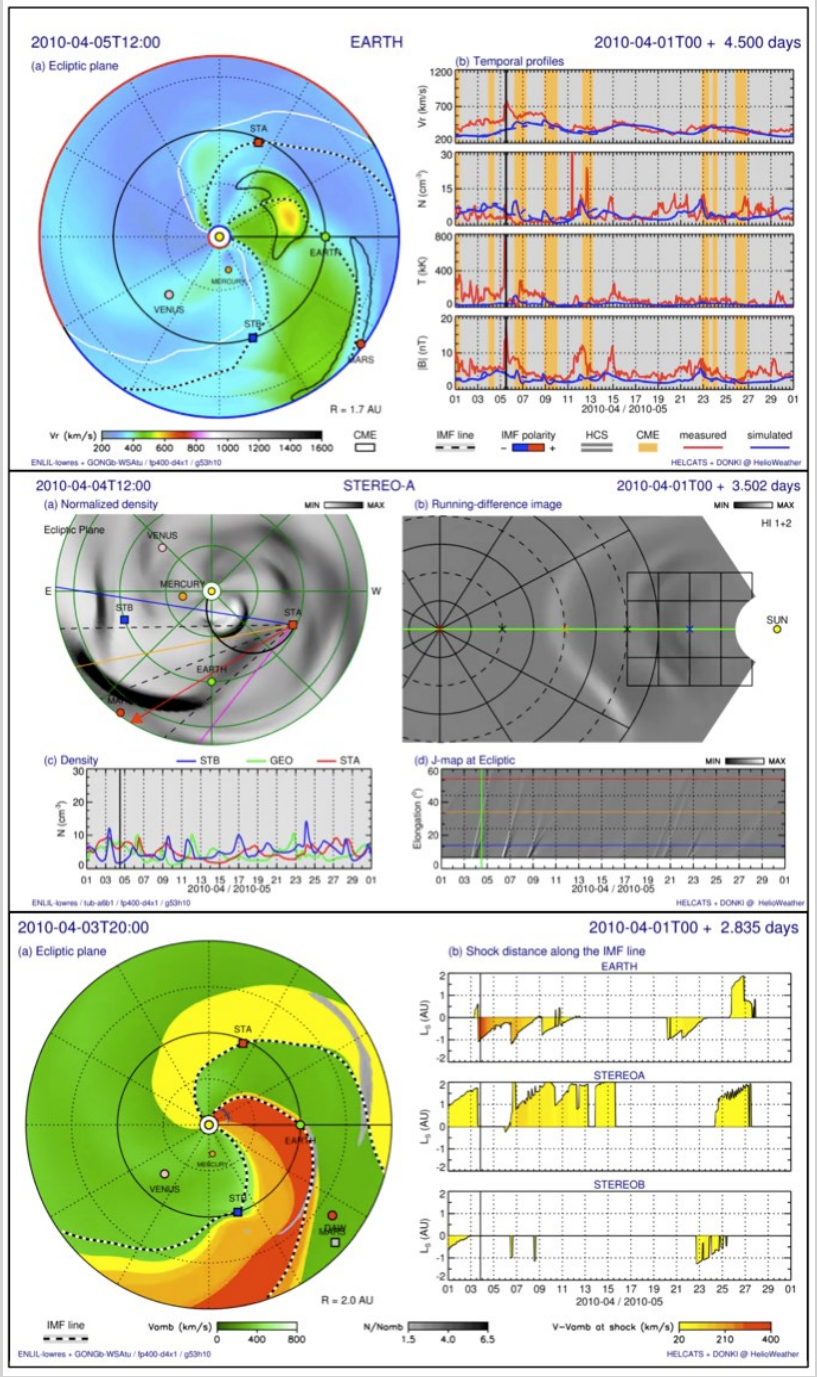

Figure 3.6.19 - same format as Figure 3.6.18 but for the 2010-04-03 event.

Access to the SIMCAT catalogues:

The SIMCAT catalogue consists of three different catalogues and can be accessed via the official HELCATS website (https://www.helcats-fp7.eu/) under WP6 dataproducts.

The background solar wind simulations based on the MULTI-VP solar wind coronal model but without CMEs are stored at: https://stormsweb.irap.omp.eu/doku.php?id=windmaptable

The combined background solar wind with the HELCATS-DONKI CME catalogues for all CMEs with speeds greater than 400 km/s are accessible at:

http://helioweather.net/archive/

The combined background solar wind with the HELCATS-DONKI CME catalogues of all speeds are accessible at: https://ccmc.gsfc.nasa.gov/community/HELCATS/

WP6 TASK 6.4: ASSESSMENT OF THE USE OF HI/ENLIL FOR SPACE-WEATHER FORECASTING (TASK LEAD: UPS, CONTRIBUTOR : GMU)

1. Fitting the kinematic variation of the CME using HI J-maps:

The HI-1 and HI-2 cameras image the solar wind typically above 20 solar radii. In this task we assume that a spacecraft located along the orbit of STEREO-B is providing science-grade images of the solar wind in real time. As the CME propagates through the HI fields of view, we get updated information on the position of the CME along the Sun-Earth line. We investigate here how this information can be assimilated in different models to improve the forecasting of CME arrival times at 1AU.
At the heights of the solar atmosphere imaged by the HIs, the motion of CMEs is no longer dictated by magnetic forces but is rather dominated by the drag force generated by the interaction between the CME and the solar wind. The equation of motion becomes:

$$a = -(v-w)|v-w| \quad \text{(Eq. 1)}$$

where the drag parameter and the wind speed w are supposed to be constants (Vršnak et al., 2007, 2012). We see that the acceleration or deceleration of the CME is controlled by the difference in speed between the CME and the solar wind.
We can express the position and speed at any point of the CME trajectory with the following analytical solutions to the equation of motion:

$$v = w + v_i - w1 + |v_i - w|(t-t_i) \quad \textit{(Eq. 2)}$$

$$r = v_i - w|v_i - w|(1+|v_i - w|(t-t_i)) + w(t-t_i) + r_i \quad \textit{(Eq. 3)}$$

where v_i is the speed of the CME at time ti when the CME crosses the inner boundary at a radial distance of r_i. Hence, the speed v and radial distance r of the CME at any time $t>t_i$ is defined by the initial conditions (v_i, t_i) at sayri=21.5 Rs, and the background solar wind speed *w*assumed to be constant for r_i>21.5 Rs.
Based on the hypothetical detection of a flare on the solar disk and on the propagation of a Halo CME by the SOHO coronagraphs, we assume that a CME is roughly directed at Earth. Imaging equipment such as the one available on STEREO-B provides live information on the progression of the CME through the coronagraphs. Based on the estimated direction of propagation, the measured elongation of the CME can be converted into a radial height and we mark the time when the CME passes roughly at r_i=20 Rs (or r_i=21.5 Rs in what follows to match the inner boundary of ENLIL). The images provide a rough estimate of the speed (v_i) of the CME at that height (r_i). Additional crucial information from HI on the propagation of the CME can be exploited as it propagates towards the Earth. We want to use that information to infer not only the varying speed of the CME but also the speed of the solar wind into which the CME propagates so that we can refine continually the ENLIL simulation of the propagating CME.

We decide to update our model every 6 hours by estimating the position of the CME at control points at radial distances $r_c=r(t_c)$. This 6-hour time interval is sufficiently long to allow significant changes in the CME position in the imagers and is sufficiently short to use two control points during very fast historical CMEs that propagate to 1AU in 16-17 hours.

The value of $r_c=r(t_c)$ obtained from the imagers can be used to update the value of the initial speed such that a CME influenced by the drag force passes by the control point r_c at time t_c:

$$v_i = w + r_c - r_i - w(t_c-t_i)|r_c-r_i-w(t_c-t_i)|\, e|r_c-r_i-w(t_c-t_i)|-1(t_c-t_i) \quad \text{(Eq. 4)}$$

The value of the solar wind speed has uncertainties given by its variance Var(w). We can compute the associated uncertainties in the initial speed :

$$Var(v_i) = Var(w)1-e|r_c-r_i-w(t_c-t_i)|2 \quad \text{(Eq. 5)}$$

The previous calculation uses only a single point, if instead we decide to exploit the information provided by all control points in the time interval of available observations. This approach provides not only the initial speed (v_i) of the CME but also the speed of the wind stream interacting with the CME. In this multi-point approach, we seek the parameters vi and w such that it minimizes the cost function:

$$F= \text{sum}(r(t_c,v_i,w)-r_c^2) \quad \text{(Eq. 6)}$$

As the CME passes 21.5 Rs we can estimate v_i, using that initial value for the minimization leads to local minima and it can be a poor solution if this estimate is not accurate. To solve this we have regularised the cost function:

$$F= \text{sum}(r(t_c,v_i,w)-r_c^2+|v_i-v_e|) \quad \text{(Eq. 7)}$$

where ve is the estimate of vi and is a control parameter. The greater alpha the more we trust our estimate.
Case studies based on the drag model: we considered two past events that were directed at Earth: the fast 03 April 2010 (HELCATS CME event ID HCME_A__20100403_01) and the slower 12 December 2008 December (ID: HCME_A__20081212_01). The results of using the drag-based model by considering a single control point (Equ. 4) and multiple control points (Equ. 7) are shown for the two events in Figure 3.6.20, 3.6.21 and 3.6.22.

Figure 3.6.20 displays a height-time map that results from the fitting technique. The blue height-time curve in this Figure was derived by the optimisation carried out through the regularization of the cost function such that the curve passes by all red points. The arrival times given in Table 3.6.1 correspond to the intersection of the blue curve with the horizontal dashed curve (distance of the Earth).

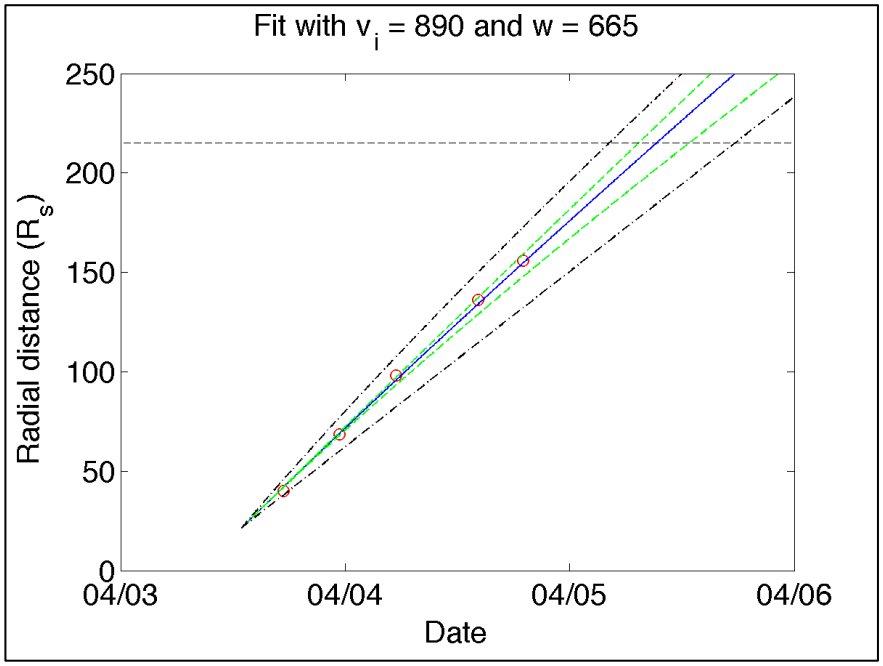

Figure 3.6.20 - A height-time map displaying as red circles the positions of the 2010 April 3 CME measured in the HI field of view every 6 hours as 'control points'. The radial distance of the Earth is shown as a horizontal dashed line. The blue curve is the optimized height time map based on the multi-point drag-based model. The green and black curves show the uncertainty associated with changes in the parameters of the cost function: the green curve shows a 20% change in the wind velocity while the black line is 20% change in the initial velocity.

Event ID : HCME_A__20100403_01
Time at 21.5Rsun : 3 april 2010 12:57UT
Arrival time measured in situ: 5 april 2010 08:26UT

Time of control point	Alpha	Vi calculated (km/s) (single point)	Predicted arrival time (single point)	Vi calculated (km/s) (multi-points)	w calculated (km/s) (multi-points)	Predicted arrival time (multi-points)
17:26 3/04/10	10.6	831	20:53 05/04/10	831	500	20:53 05/04/10
23:23 3/04/10	18.5	976	17:27 05/04/10	895	506	13:34 05/04/10
05:27 4/04/10	26.8	1128	14:44 05/04/10	939	534	11:13 05/04/10
14:12 4/04/10	36.9	1245	13:03 05/04/10	949	557	10:12 05/04/10
19:00 4/04/10	41.8	1303	12:15 05/04/10	954	558	09:59 05/04/10

Table 3.6.1: Two left-hand columns: the times and elongations of the CME measured in HI and used as control points. Middle column: the derived initial speed. Right-hand columns: the estimated arrival time of the CME at Earth based on the drag-based model fitted on a single control point and all control points simultaneously.

As we can see in Table 3.6.1, the prediction of the arrival time of the CME at Earth improves, i.e. getting closer to the measured arrival time of the sheath ahead of the associated ICME at 08:26 UT on 5 April 2010, as additional images of the CME are obtained by the HI cameras for both fitting techniques. The two techniques have identical estimates in the first row because both fit only two points: the initial point (r_i , v_i, t_i) and the first control point (r_c, v_c, t_c) at 20:53 UT. At the second control point, the multi-point technique predicts already an impact at 08:36 UT within 10 minutes of the actual impact time and remains within 1 hour of that predicted impact time for all additional control point. The fitting of a single (latest) control point in addition to the initial point produces forecasts that are gradually approaching the arrival time. In addition the background solar wind speed into which the CME (and measured in situ near Earth) is propagating is also correctly inferred by the multi-point technique around 550 km/s.

We repeated this analysis on the 12 Dsecember 2008 event which impacted the Earth on 16 December 2008 at 9:00UT, the predicted arrival times are shown in Table 3.6.2. For this event, the estimated time of passage at the inner boundary of r_i = 21.5 Rs is 17:48 UT on 12 December 2008.

For this much slower event, the two techniques reach reasonable estimates of the arrival time (within 5-6 hours) some two to three days before impact. However the solution does not converge smoothly towards the correct arrival time like the much faster 2010 April event. In addition both techniques tend to overestimate the speed of the CME and of the background solar wind. This less accurate fitting could be related to the fact that the CME is neither much faster nor slower than the ambient solar wind and therefore the drag force is not acting strongly to change the CME speed, hence our optimisation technique is carried out on a straight line rather than a smoothly varying function.

Event ID : HCME_A__20081212_01
Time at 21.5Rsun : 12 December 2008 17:48 UT
Arrival time measured in situ: 16 December 2008 07:50 UT

Time of control point	Alpha	Vi calculated (km/s)	Predicted arrival time (single point)	Vi calculated (km/s)	w calculated (km/s)	Predicted arrival time (multi-points)
22:57 12/12/08	9.625	560	13:22 15/12/08	560	500	13:22 15/12/08
05:55 13/12/08	13.75	466	01:37 16/12/08	479	501	23:40 15/12/08
12:29 13/12/08	18.125	453	03:33 16/12/08	463	506	01:52 16/12/08
18:38 13/12/08	21.4375	423	07:56 16/12/08	448	541	02:31 16/12/08
01:36 14/12/08	25.9375	416	08:50 16/12/08	447	480	00:19 16/12/08
06:31 14/12/08	29.8125	426	07:25 16/12/08	443	548	02:38 16/12/08
14:43 14/12/08	34.9375	417	08:42 16/12/08	442	446	02:54 16/12/08
22:06 14/12/08	39.625	413	09:13 16/12/08	441	540	03:17 16/12/08
02:37 15/12/08	44.6875	444	04:50 16/12/08	436	476	06:54 16/12/08

Table 3.6.2: Same format as Tabe 3.6.1.

2. Using HI to initialise ENLIL:

The previous section presented a new technique to fit the kinematic evolution of the CME as it transits from 21.5 Rs to Earth in the HI images. We can use the updated estimates of the CME and background solar wind speed to relaunch ENLIL every 6 hours (i.e. every time a control point is acquired).

The standard forecasting mode for ENLIL at NOAA SWPC uses daily updated solar wind maps instead of wind maps computed for a full rotation. Like for SIMCAT, CMEs are injected as hydrodynamic ejecta inside the simulation domain at 21.5Rs. Figure 3.6.21 displays the result of computing the arrival time of the CME based on the assumption that it was directed at Earth, using the average transit speed of the CME computed in the HELCATS catalogue and daily updated solar wind maps based on GONG magnetograms. Clearly the simulated CME arrival time is too late. This is likely due to a too slow solar wind ahead of the CME (the background solar wind is slowing the structure down).

To illustrate further the effect of the speed of the background solar wind on the CME motion, we neglect the detailed structure of the solar wind stream and run ENLIL with an isotropic solar wind. In this set of simulations there are no Corotating Interaction Regions forming and the background wind is blowing at the same speed in all latitudes and longitudes. Figure 3.6.22 shows in the same format as Figure 3.6.21 the results of two simulations assuming a fast (750km/s; top panels) and a slow (300 km/s; bottom panels) background solar wind. Comparison with in-situ measurements shows that the assumed background solar wind speed is either too high or too low ahead of the CME with an associated drag force that is too low and too high, respectively.

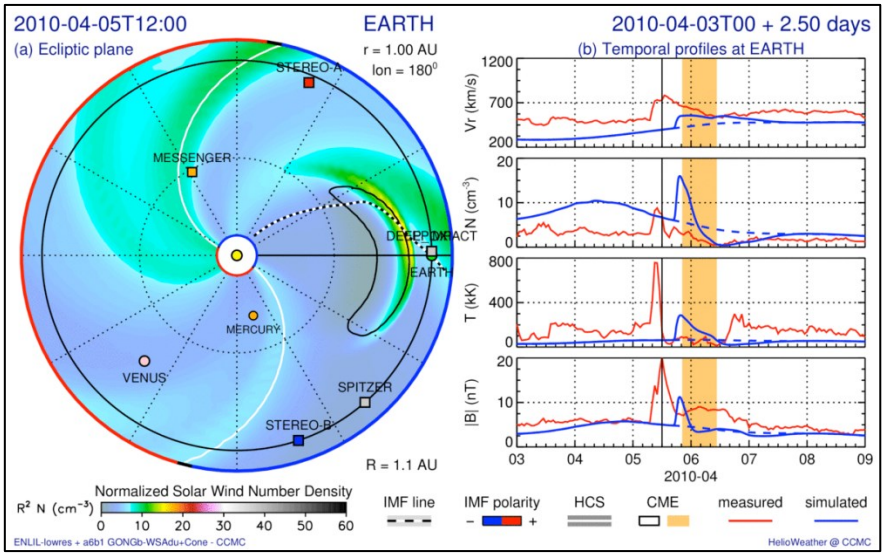

Figure 3.6.21 - A composite of images showing (left) the distribution of plasma speed in the ecliptic plane and (right) the modeled in-situ signature near 1AU (blue lines). From the top to bottom: the solar wind speed (km/s), the density (cm^{-3}), temperature (kK) and magnetic field strength (nT). The red lines are the measured OMNI solar wind parameters.

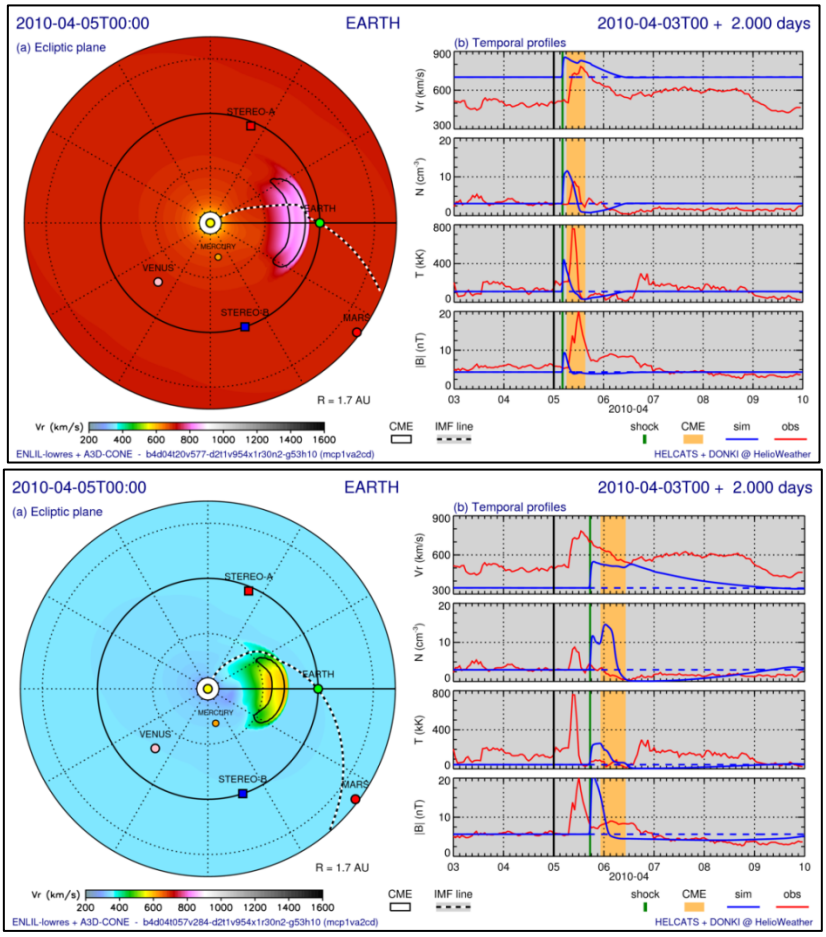

Figure 3.6.22 - same format as Figure 3.6.21 but with a fast background solar wind of 700 km/s (top panels) and a slow solar wind of 300 km/s (bottom panels). The background solar wind density in the simulation was adjusted to match that of the background solar wind measured in situ ahead of the CME.

In order to accurately forecast the CME arrival time it is therefore crucial to determine not only the CME speed but also the background solar wind speed into which the CME is propagating. Other parameters that also play a role in the CME propagation and arrival time at 1AU are the background solar wind density, the energy equation used in the simulations, and the size of the hydrodynamic ejecta injected in the simulation to simulate the CME. In principle HI images can provide information on the solar wind density ahead of the CME and also on the latitudinal extension of the CME injected in the simulation (see Rouillard et al. 2011, Temmer et al. 2011 for more details), however in the present report we concentrate on assimilating HI data to improve the kinematic properties of the wind and the CME.

To improve the forecast, we use the fitting method presented in the previous section to estimate the solar wind speed (w in Table 3.6.1) ahead of the CME each time a control point is used in HI images to fit the kinematic properties of the CME.

Each time we obtained a new update on the solar wind speed from our fitting technique, we adjusted the ENLIL background wind speed so that the terminal speed at 1AU matched the fitting speed. The HI fitting technique also provides an updated CME speed at the inner boundary that we also exploited (vi in Table 3.6.2). Hence each time a control point was used to fit the CME kinematics, we relaunched ENLIL with a new w and a new vi.

Figure 3.6.23 shows the results of a simulations based on the Vi and w values given in the first row of Table 3.6.1 for a CME speed of vi= 831 km/s and a background solar wind speed of w=500 km/s. As we can see the simulated background solar wind speed and the CME speed match better the speeds measured in-situ. The arrival time of the CME is also closer to the measured arrival time than for the simulation results shown in Table 3.6.1.

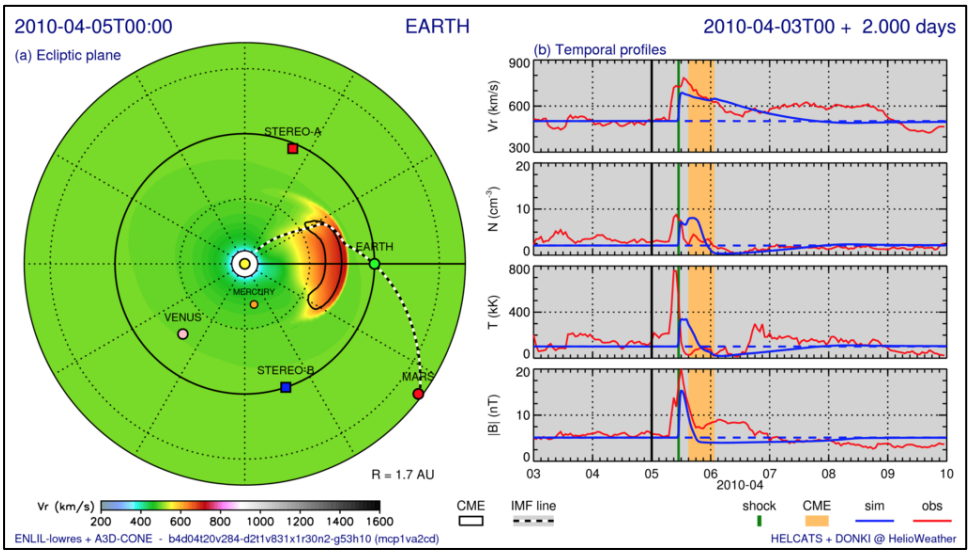

Figure 3.6.23 - In the same format as Figure 3.6.22 but for an axi-symmetric solar wind stream.

We pursued this exercise until the last available control point is used (last row of Table 3.6.1) giving a CME speed at 21.5Rs of vi= 954 km/s and a solar wind speed of w=558 km/s. The results of this simulation are shown in Figure 3.6.24. As we can see the simulated arrival time matches closely the measured arrival time. The background solar wind speed ahead of the CME is however slightly overestimated by 20-30 km/s. Providing that the solar wind density and temperature and magnetic field are modeled reasonably well upstream of the shock, ENLIL provides in addition to an estimated arrival time a prediction of the shock strength upon CME impact.

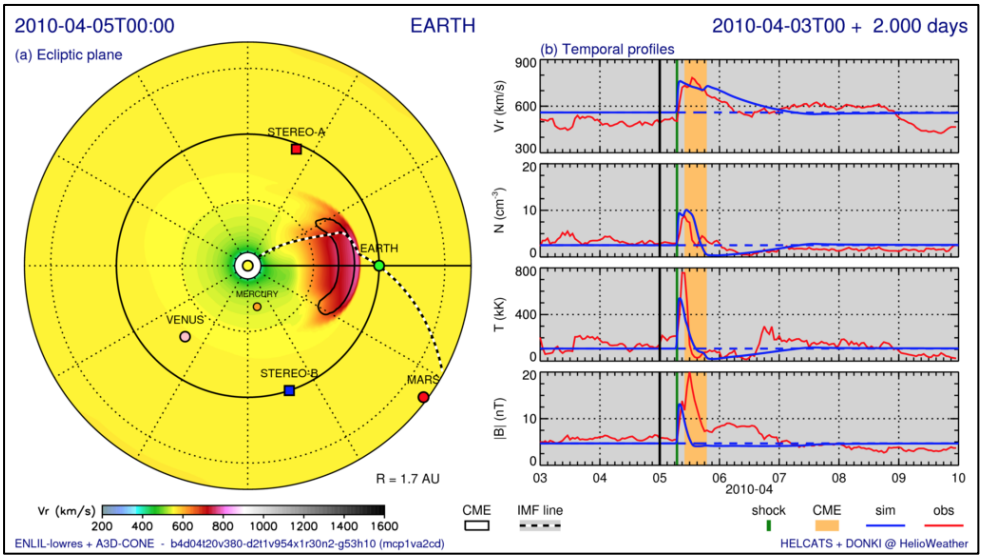

Figure 3.6.24 - same format as Figure 3.6.22 exploiting all available control points given in Table 3.6.1.

We note that using all control points given in Table 3.6.1 results in the last forecast being made at 19:00 UT on 4 April 2010 just 12 hours before the CME impact. However we note that the accuracy of this last forecast would have been achieved already at 05:27 UT on 4 April 2010, or 27 hours before the actual impact.

WP6 CONCLUSIONS:

In **Task 6.1** we showed that heliospheric imagery provides great potential to validate the accuracy of simulations of CIRs. Since the compression region is stronger in the slow solar wind upstream of the stream interface, the observed and modeled patterns of converging tracks are biased towards slow solar wind speeds. This was confirmed in WP5 through the extensive analysis of CIRs observed by HI. Therefore HI can only validate the location of the interaction region but provides no information on the amplitude and duration of the high-speed stream that follows. In addition HI can also detect if the interaction region has a faster or slower corotation speed than usually assumed in numerical simulations. Finally, when a simulation misses out a CIR passage completely due to bad coronal input, HI can provide a safeguard by bringing the necessary observation to confirm and locate that CIR.

In **Task 6.2** we developed a new coronal solar wind model based on fluid equations and simulating the plasma motion from the chromosphere to the corona. Because the model solves for the energy exchanges that occur at the base of the solar corona, it is able to model realistically the mass flux expelled in the solar wind and notably the density of the solar corona. In turn this allowed us to simulate white-light images and compare those with real heliospheric images. We developed a methodology to evaluate the accuracy of our model using imagery. We also coupled the model to the ENLIL interplanetary solar wind model and thereby also simulated the solar wind measured in situ. We produced a database of solar wind simulations called SIMCAT (Solar wind).

In Task 6.3 we delivered the most accurate and most comprehensive database of CME simulations. The simulations were optimised by exploiting the techniques and catalogues developed in the HELCATS project and also from other community-led efforts. These catalogues of simulations will be useful to scientists studying the propagation of CMEs in the interplanetary medium, the formation of shocks and their potential link to energetic particles or to scientist interested in planetary space weather.

In **Task 6.4**, we presented a new method to forecast the arrival time of CMEs based on the assimilation of information provided heliospheric images as they become available during the propagation of a CME. This technique is based on the widely used drag-based model (Vršnak et al., 2007, 2012) but modified to fit the updated position of the CME as it propagates to 1AU. Updated locations of the CME provide a more precise computation of the evolving speed of the CME and the background solar wind ahead of the CME. Combining this technique with ENLIL simulations, we can assimilate continually updated information from HI to improve

the forecasted arrival time of the CME and its shock at 1AU. This technique shows great promise but needs to be tested on a wider range of CME types. Indeed we have found that application of the technique on a slow CME (undergoing smaller speed variations) provides less accurate results. This is likely a consequence of a weaker interaction between the CME and the background solar wind speed.

WP6 HIGHLIGHTS:

- Development of the most advanced coronal solar wind model coupled to ENLIL.
- Provision of the most complete catalogue of solar wind and CME simulations covering nearly an entire solar cycle (SIMCAT).
- First assessement of the usefulness of HI images to initialize CMEs in ENLIL.

WORK PACKAGE 7 (WP7):

ASSESSING THE COMPLEMENTARY NATURE OF RADIO MEASUREMENTS OF SOLAR WIND TRANSIENTS

WP7 ACTIVITY TYPE: RTD

WP7 DURATION: MONTHS 10 – 36

WP7 LEAD BENEFITIARY: IMPERIAL (6)

WP7 LEADER: Dr Jonathan Eastwood

WP7 CONTRIBUTORS: STFC (1); ROB (5)

WP7 OVERVIEW: Work package 7 of the HELCATS project had two main goals. The first was to identify and analyse potentially-geoeffective solar wind events that are observed by both HI and IPS, and use IPS to augment the HI observations. The second was to identify and analyse solar wind transients that are observed by both HI and in radio, and add value to the HI data by establishing/cataloguing the relationships between them. Task 7.1 (Identifying and analysing potentially-geoeffective solar wind events that are observed by both HI and IPS) was performed by STFC. Task 7.2 (Identifying and analysing solar wind transients that are observed by both HI and in Type II radio burst emission) was performed by IMPERIAL and ROB. Three deliverables were identified: D7.1: Catalogues of EISCAT and LOFAR IPS data events and of S/WAVES events, both extending throughout the STEREO HI Mission timeline; D7.2: Report of initial comparison between IPS events and HI events; D7.3: Report of initial comparison between solar radio-burst events and HI events. D7.1 was the joint product of the two work tasks, whereas D7.2 and D7.3 were the result of T7.1 and T7.2 respectively. All the tasks and deliverables were successfully achieved as described here.
[Relevant catalogues: RADCAT, IPSCAT]

WP7 TASK 7.1: IDENTIFYING AND ANALYSING POTENTIALLY GEOEFFECTIVE SOLAR WIND EVENTS THAT ARE OBSERVED BY BOTH HI AND IPS (TASK LEAD: STFC)

Interplanetary scintillation is a technique whereby radio emission from distant, compact, astronomical sources is used to probe the properties of the solar wind. In particular, the turbulent solar wind medium causes scintillation of the signal. By cross-correlating the frequency power spectra of a given source measured by two spatially separated receivers on the ground, the Cross-Correlation Function (CCF) is formed where specific features in CCFs can be attributed to known phenomena moving away from the Sun through the corona and inner heliosphere. IPS therefore provides a potentially powerful way to augment the HI dataset, and so the goal of this task was to examine this in more detail.

Construction of IPSCAT

It should first be recognised that IPS data are not typically uniformly available. This is because the radio-telescope systems used here typically run on a campaign basis only for observations of IPS. It was therefore first necessary to establish the data availability working from the catalogues of CMEs and CIRs/SIRs provided by WP2 and WP5, respectively. This used all the IPS data available at STFC during the STEREO mission (primarily from the radio-telescope systems of EISCAT/ESR, MERLIN, and occasionally, LOFAR) and focussed on identifying intervals where multi-site IPS observations were available and where CCFs could therefore be constructed.

Following this preparatory work, the next step was to develop a catalogue of CMEs and CIRS/SIRS observed using IPS by analysing the measured CCFs. Peaks in the CCF provide velocity estimates for features crossing the IPS line of sight. For automation of identifying CCF features, we developed feature-finding tools for the resulting analysed IPS data from which CCFs were able to be produced. This provides an idea of whether or not a CME, SIR/CIR, or ambient streams were being observed in an automated fashion. All IPS data and CCFs were calculated in an automated mode in order for the assessment to be space-weather oriented as a quasi-

operational system. This involves fitting a function to the CCF (as shown in Figure 3.7.1), and calculating three parameters: the fractional residual (r), the depth of the minimum at or near to zero time lag (z), and the asymmetry of the CCF (a).

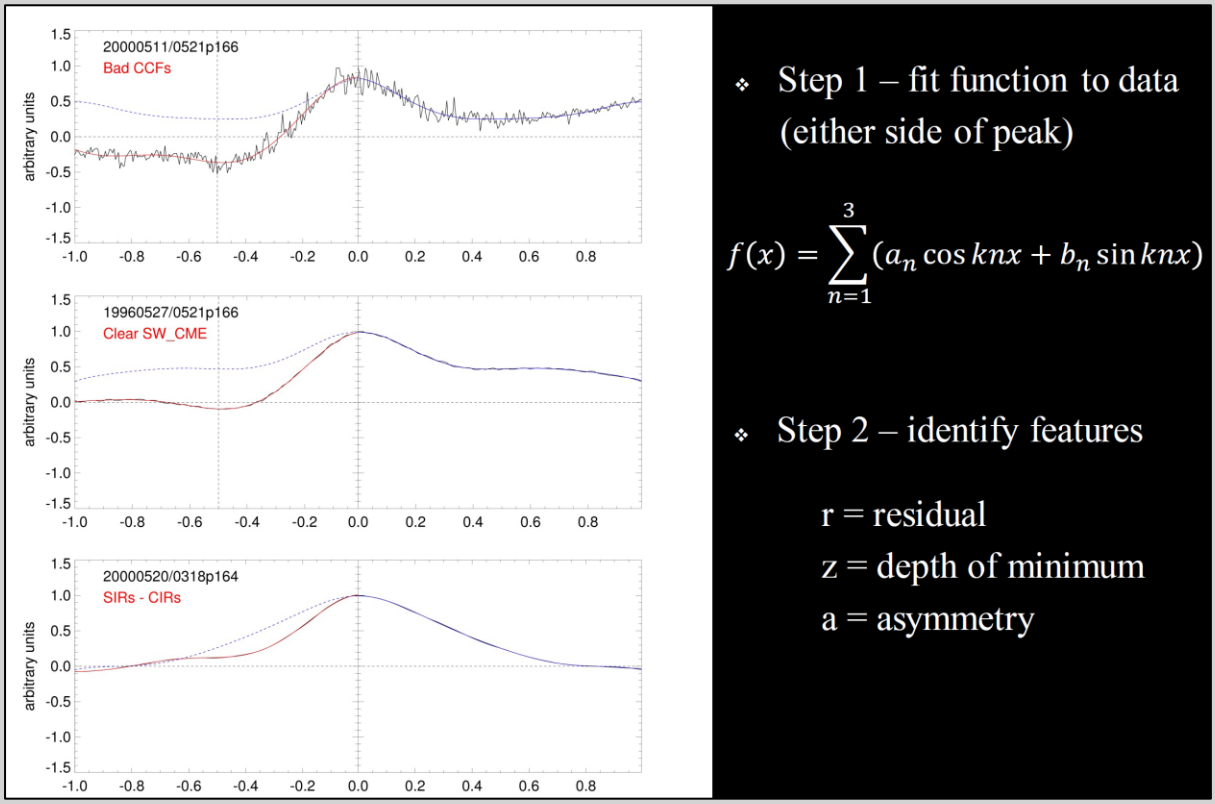

Figure 3.7.1 - (left hand panels). Three examples of CCF data are shown in black. The red and blue lines show the fit to the left and right hand sides of the CCF. Any difference in the red and blue lines reflect asymmetry in the underlying CCF.

The parameters are used to diagnose the CCF in the following way:

- If r ≥ 2%, then the CCF is considered to be bad data (see top left panel of Figure 3.7.1)
- If r < 2% and z < 0, then there is a negative lobe and a CME is identified (see middle left panel of Figure 3.7.1
- If a > 10%, then a SIR/CIR is identified – this value is the residual between the function fitted either side of the peak as a measure of asymmetry (see bottom left panel of Figure 3.7.1)

If none of these criteria are satisfied, then nothing is identified. However, the interpretation of IPS data must be performed with care. The strongest or best-identified feature(s) in manually inspected CCF(s) are not always the one(s) that provides the highest amount of correlation in the CCF primary peak identified by the automated technique. For example, if multiple features are crossing the line of site, these features can be removed from a CCF if the geometry is not adequately set up. A manual investigation of each of the CCFs was therefore also undertaken to check and verify the results, and to assess that the automated procedure performed adequately.

Having identified CME and SIR signatures in the IPS data, images were created showing the IPS P-Point, IPS observing line of sight, and any features detected in the WPs 2, 3, or 5 catalogues, projected onto the ecliptic for a notional comparison. HI images were also prepared with the P-point (the IPS point of closest approach) included. However, IPS information comes from the entire line of sight through the inner heliosphere (and corona) and not just from the P-Point; this emphasises the need for the ecliptic-plane-projecting images.
Finally, to connect the IPS data back to the HELCATS catalogues and the HI data, the following automated criteria were used to relate IPS identified features to HI-identified features. A CME was matched to the IPS data if the projection of the P-Point into the ecliptic is within 1.5 CME radii of the centre of the CME – this uses the SSE model with a half-width of 30° as noted. For multiple CMEs that satisfy the first criterion, the one closest (spatially) to the Sun is used. An SIR/CIR was matched to the IPS data if the projection of the P-Point

into the ecliptic is within 0.1 AU of any of the SIR/CIR features identified in CIRCAT.

The initial comparison of all the IPS results to the HI catalogues:

- 374 manual CME and/or SIR features identified in total;
- 120 automated CME and/or SIR features identified in total;
- Generally, CME signatures seen in IPS and not identified in the HI imagery are due to the criteria used to identify a CME in the HI imagery; and
- Generally, CME/SIR signatures not detected in the IPS but noted in the HI catalogues is due to either the feature not crossing a sufficient portion of the IPS line of sight (or not crossing at all) or due to the geometry of the observation – indicating the need for several simultaneous observations of IPS from different observing sites to provide a combination of available baseline geometries.

nitial comparisons show that while IPS and Heliospheric Imaging have some significant overlaps in terms of features being detected (either manually or automatically), there are also some significant differences. Most differences seem to be in relation to three factors:

- The CMEs observed by the HIs have to be ≥ 20° in PA width (so smaller CMEs and larger CME-like blobs are explicitly excluded from the HI catalogues but still detected by IPS;
- The automated CCF feature-identification tools are not overly robust and can only cater for a number of different shaping/feature scenarios; and
- The automated CCF analyses leading to noisy/noisier CCF shapes that provide less-accurate results than full, careful, manual analyses would often provide.

The HELCATS IPS catalogue IPSCAT is accessible via the HELCATS web site at https://www.helcats-fp7.eu/catalogues/wp7_ipscat.html. At the time of writing, the catalogue is version 01 (first full release) released 2017-04-26 and covers the period from 20 April 2007 through 03 October 2012 where only STEREO and IPS CCF results were available from IPS campaign periods (1,299 entries at time of writing) at the same time. Clicking on any particular entry in the catalogue brings up images corresponding to Figure 3.7.3 and 3.7.4.

IPSCAT is summarised in the report prepared as Deliverable 7.1 'Interplanetary Scintillation (IPS) Catalogue', issue 1.2, 2017-04-27.

Case study and initial comparison of IPS events and HI events:

IPSCAT event IPS_20070421_1530 provides a useful illustrative example of how IPS can be used in conjunction with HI data. In this event, both manual and automated CCF-feature identifications indicated that a CME was present somewhere along the line of sight. This observation uses EISCAT data from the Kiruna and Sodankylä sites forming a projecting baseline on the sky of around 188km almost parallel to the assumed radial outflow. The observations were of radio source J0318+164 and were made on 21 April 2007 with a start time of 15:30UT when the source was located off the East limb of the Sun.

Figure 3.7.2 shows the CCF for this event. There is a good correlation with a negative correlation near the zero time lag; this negative correlation is indicative of a CME crossing the IPS line of sight. Note also the dominance of only a single speed which can be attributed to the CME speed and is comparable to the speed given for this CME in the WP3 catalogue.

Figure 3.7.3 and Figure 3.7.4 show the IPS data in the context of the HI data. Figure 3.7.3 shows the location of the IPS P-point for this event relative to the HI measurements. A faint backend part of the CME is seen along with a potential SIR in the movies and other versions of HI imagery. Figure 3.7.4 shows the ecliptic-plane-projecting image for this event. In this example, IPS is sensitive to the CME and does not seem to detect the SIR – but the 3-D geometry would need to be further investigated to understand why this is the case.

This aspect of Task 7.1 is summarised in Deliverable 7.2 'Report of initial comparison between IPS events and HI events'. Manuscripts reporting the main results from the analysis are being prepared for publication.

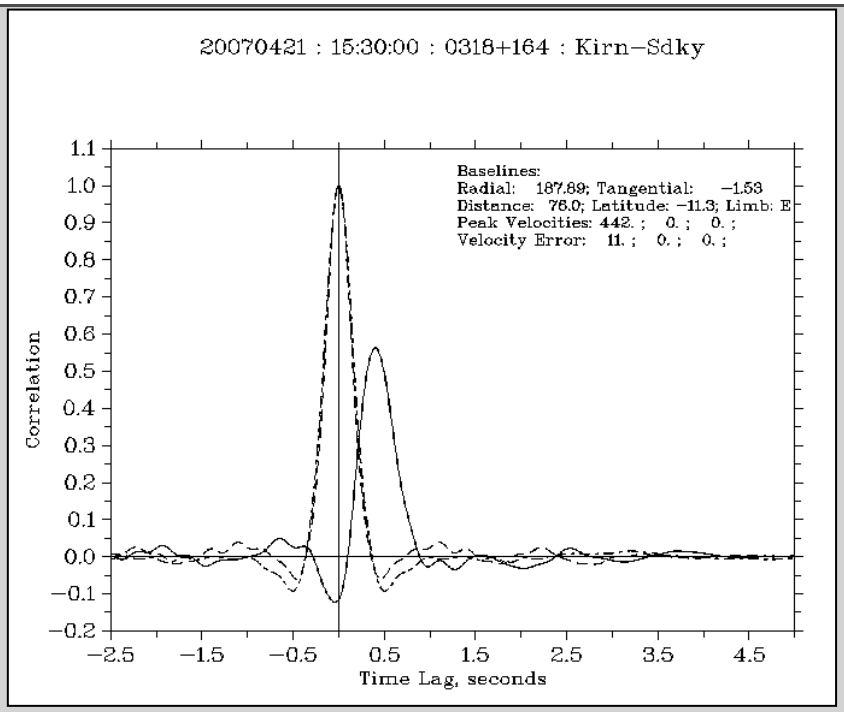

Figure 3.7.2 - IPS correlation functions for IPS_20070421_1530. The non-solid lines are the auto-correlation functions of each of the observing sites for this observation, which have a correlation of 1.0 at zero time lag. The solid line is the cross-correlation whereby the peak in the CCF provides a measure of the speed of the plasma crossing over the two observing lines of sight.

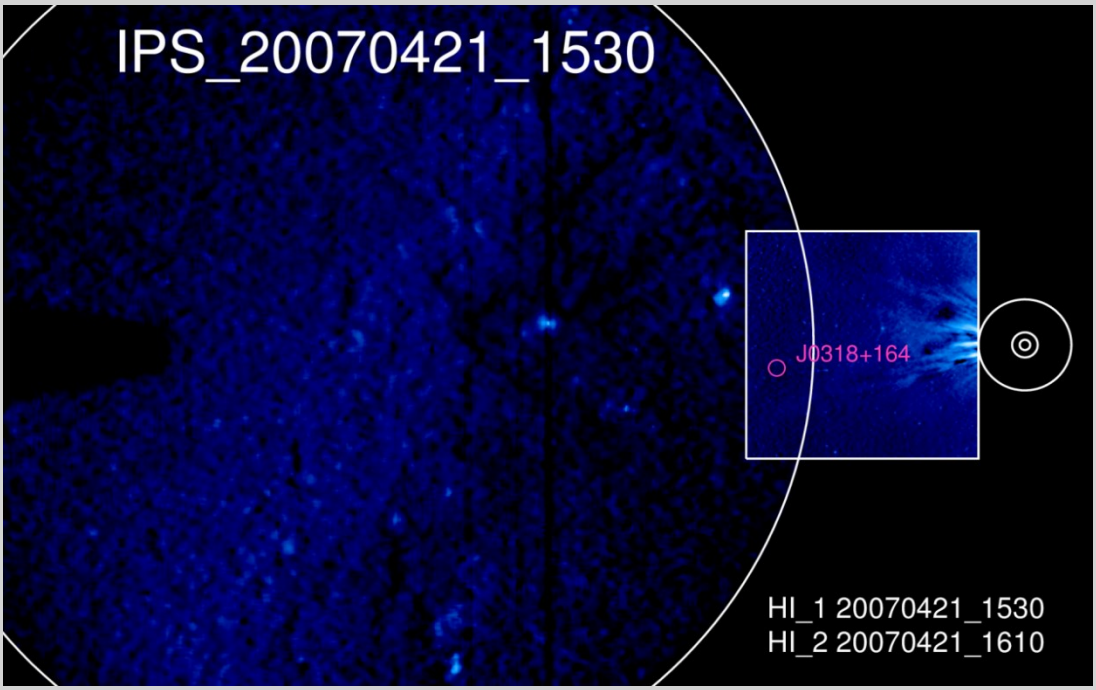

Figure 3.7.3 - The combined HI-1 and HI-2 fields of view (with the fields of view outer edges of the COR2, COR1, and the radius of the Sun descending inward, shown to scale) of the STEREO-A spacecraft showing the projection of the IPS P-Point for radio source J0318+164 (CTA21).

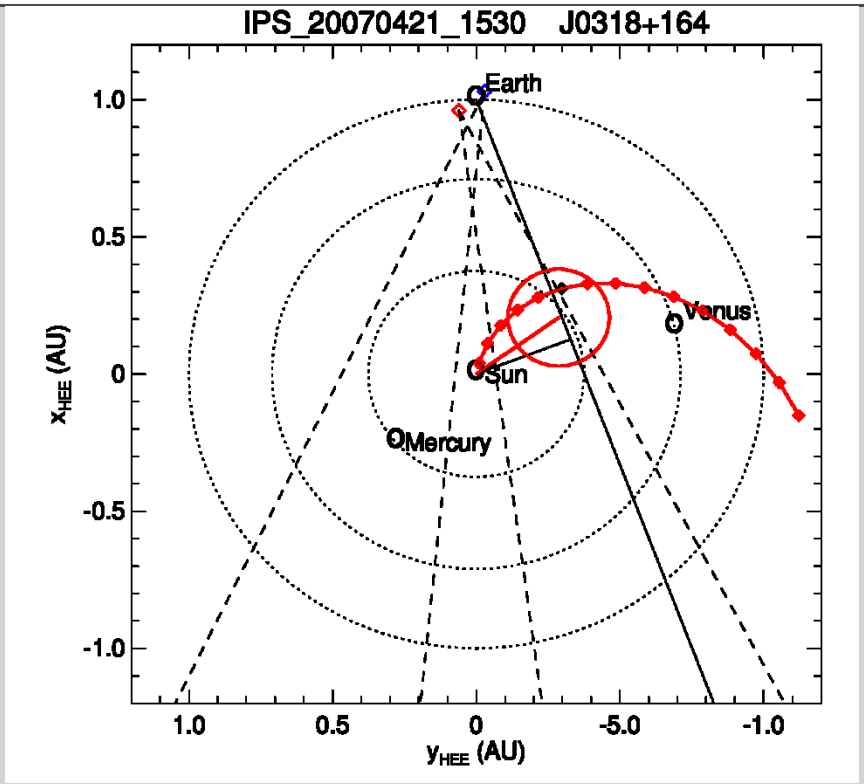

Figure 3.7.4 - The HELCATS WP7-developed ecliptic-projection image showing the in-ecliptic geometry of the Earth, Sun, Mercury, and Venus (all as black circles), STEREO-A (red diamond), STEREO-B (blue diamond), HI-1 fields of view (dashed lines), IPS line of sight projected into the ecliptic (solid black line originating from the Earth) along with its P-Point intersection (solid black line originating from the Sun), the WP2/WP3 CME (red circle - this is a 30° half-width CME projected into the ecliptic), and the WP5 SIR trace (red curved line with red diamond markers).

WP7 TASK 7.2: IDENTIFYING AND ANALYSING SOLAR WIND TRANSIENTS THAT ARE OBSERVED BY BOTH HI AND IN TYPE II RADIO BURST EMISSION (TASK LEAD: IMPERIAL)

Solar radio emission covers a broad frequency domain corresponding to different distances from the Sun. So-called type II radio bursts appear as emission which slowly drifts in time, from high to low frequencies. Generally they are produced at CME-driven shock waves (in the corona and interplanetary space), by fast electrons beams [Gopalswamy et al., 2000; Reiner et al., 1998]. Radio observations provide an alternative view of CME-driven shocks, and already with the two-point measurements of the STEREO spacecraft, the location of radio emission in space can be triangulated via direction finding techniques [Krupar et al., 2014; Krupar et al., 2012]. Combining STEREO solar radio-burst, coronagraph and HI observations enables unique studies of the propagation of shock waves and their drivers (CMEs), as well as the interaction of fast CMEs, all the way from the corona to 1 AU. A key advantage of space-based radio measurements is their effectiveness in tracking CME-driven shocks and therefore also indirectly tracking CMEs through the interface between the coronagraph and HI fields of view [Harrison et al., 2012].

Construction of RADCAT

The primary goal of this task was to develop a joint catalogue of CMEs observed in STEREO/HI, taken from the HICAT catalogue (WP3), and associated Type II radio observations from S/WAVES and Wind/WAVES data, on board the STEREO and Wind spacecraft, respectively. To accomplish these goals, the first requirement was to survey the radio data in the context of the main HICAT event list provided by WP2/3.

The onset time of each event in the WP3 HI catalogue was used to produce a catalogue of radio data survey plots. These were then examined individually for the signatures of slowly drifting radio emission. Shock associated radio emission is usually very intermittent and its interpretation can't be automated. Consequently, we examined the data visually several times, with the results cross-checked and repeatedly refined (work done by Krupar at IMPERIAL and Magdalenic at ROB). The radio catalogue provides the following information for each spacecraft: (1) the date and time of the first and last observation of radio emission; (2) the low and high

frequency cut-off of the observed radio emission; (3) the number of components of emission – either 2 (fundamental and harmonic), 1 (fundamental or harmonic), or 0 (indicating that the number of components is unclear); (4) the quality of the emission, rated on a scale of 0 – 5 where 0 indicates that no associated radio emission was observed, and 5 indicates that very clear radio emission was observed. This process is illustrated in Figure 3.7.5, which corresponds to Event ID: HCME_A__20131102_01 and exhibited a quality factor of 5 at both STEREO spacecraft. Panel (a) shows the radio data from STEREO-A. To specifically compare the radio measurements with the CME kinematics derived from WP3, we first converted the radial distances yielded by the SSEF technique to frequencies using the electron density model of Sittler and Guhathakurta [1999]. We then over-plotted the predicted signal drift for fundamental and harmonic emissions, assuming the emission was produced at the CME leading edge (indicated by black solid and dashed lines, respectively). The actually observed radio emission is denoted by the boxed areas. Panel (b) shows the results of the subsequent direction finding analysis.

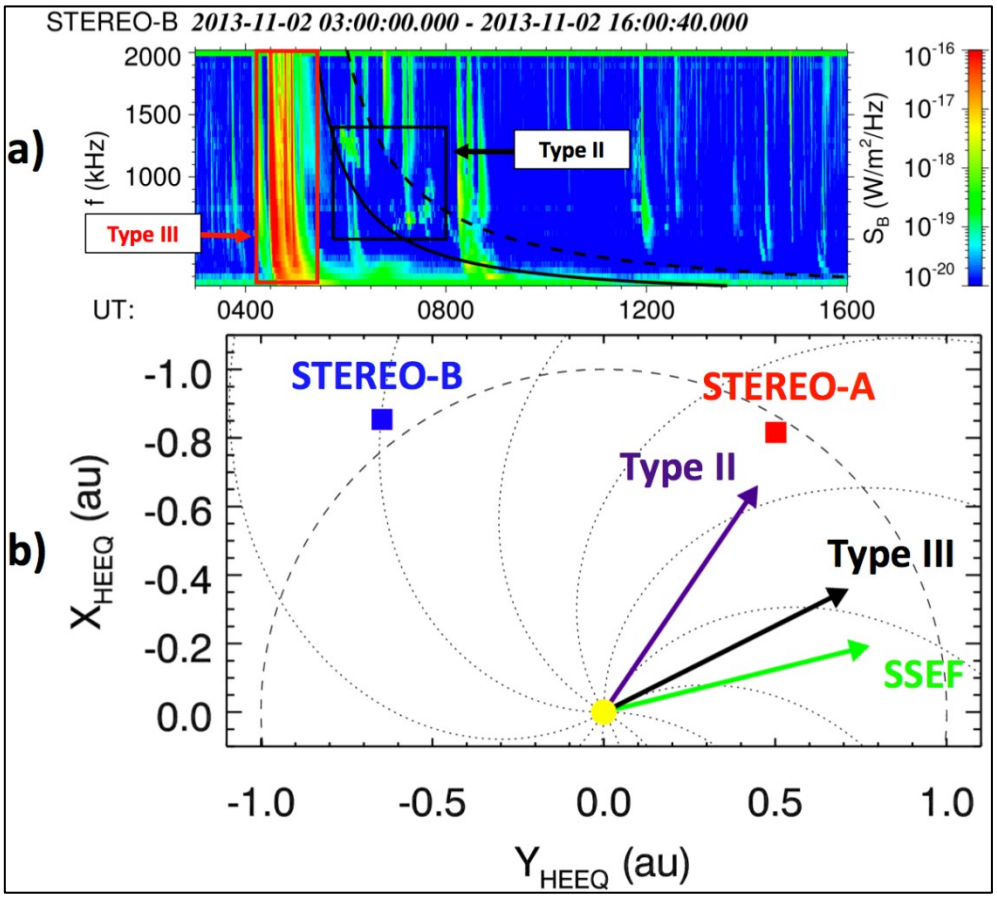

Figure 3.7.5 - (a) Radio emission measured by STEREO-A associated with HELCATS Event ID: HCME_A__20131102_01. (b) Direction finding analysis.

The initial comparison of all the S/WAVES results to the HI catalogues shows that there are 156 events with slow drifting radio emissions out of 1210 CMEs. Some initial statistics are shown in Figure 3.7.6.

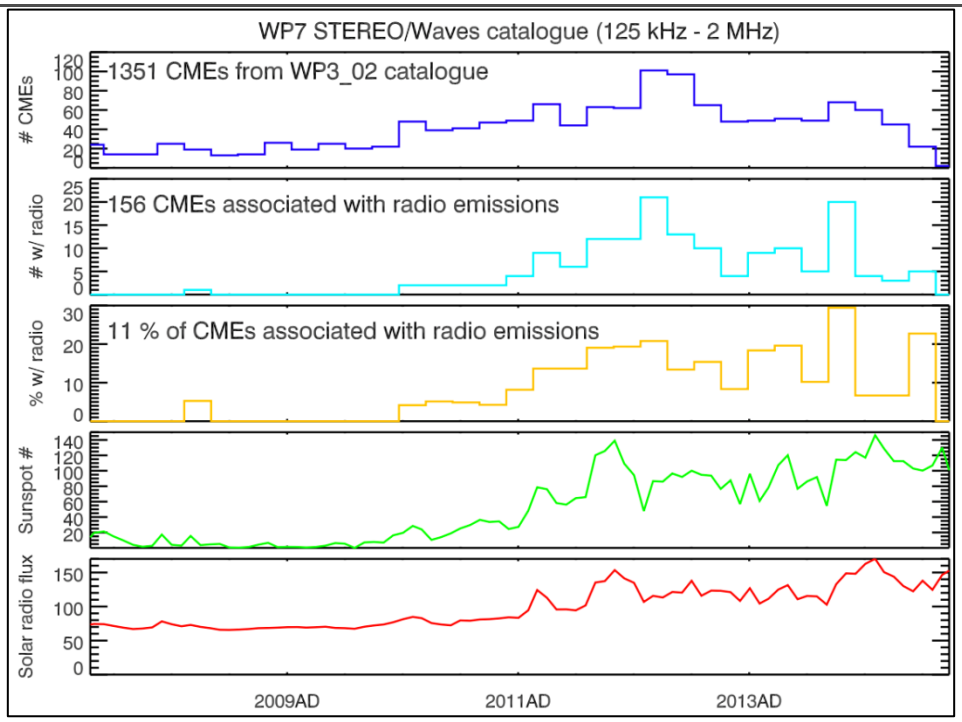

Figure 3.7.6 - RADCAT statistics of slowly drifting radio emission identified in association with CMEs listed in the HICAT catalogue.

The HELCATS radio catalogue RADCAT is accessible via the HELCATS web site at https://www.helcats-fp7.eu/catalogues/wp7_cat.html. At the time of writing, the catalogue is version 03 released 2016-10-19 and covers the period from April 2007 through September 2014. Clicking on any particular image in the catalogue brings up images showing the radio emission as shown in Figure 3.7.7

.

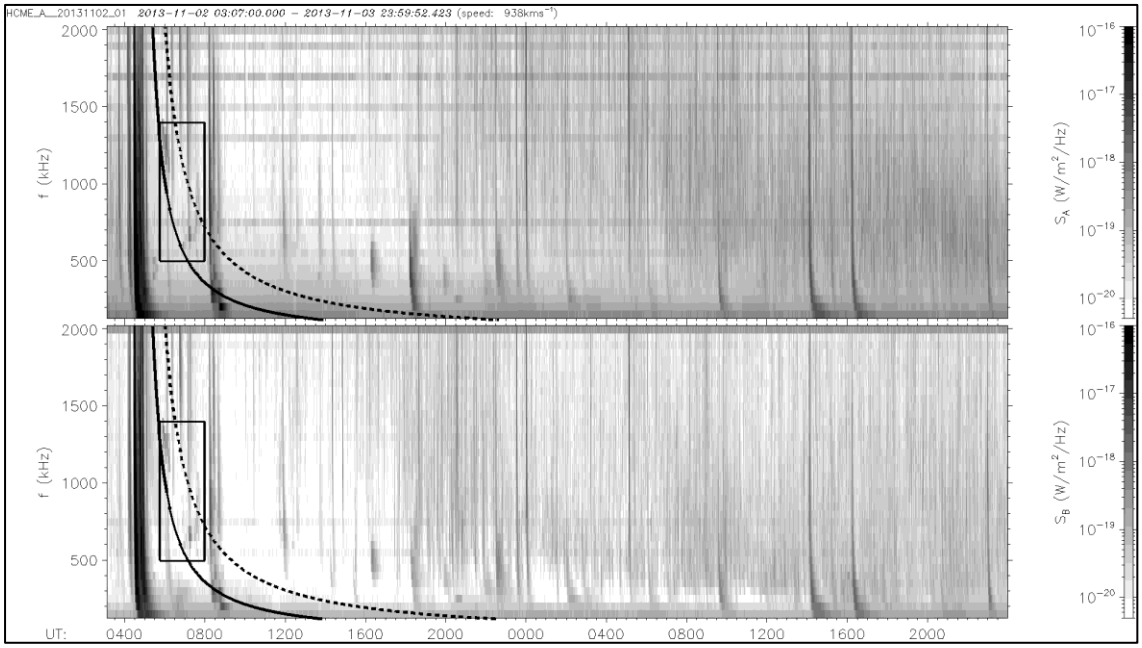

Figure 3.7.7 - Example of radio spectrogram summary plot available on the HELCATS website. This plot is of event HCME_A__20131102_01 shown in Figure 3.7.5.

RADCAT is summarised in the report prepared as Deliverable 7.1 'Solar radio burst catalogue', issue 1.0, 2017-01-08.

Case studies and initial comparison of IPS events and Hi events:

A first HELCATS case study has recently been published [Krupar et al., 2016]. The publication presents analysis of the type II radio emission observed on 29-30 November 2013, associated with a CME that was launched from the Sun in the direction of STEREO-A. This CME was uniquely well observed with: coronagraph observations from three satellites (STEREO A/B and SoHO); STEREO-HI observations; multi-point radio measurements enabling triangulation of the shock associated radio emission; and in situ measurements made by STEREO-A and MESSENGER in the vicinity of Mercury. In this study it was possible to measure the CME kinematics applying radio, coronagraph, heliospheric imaging, and in situ detection, allowing in depth analysis.

Figure 3.7.8 shows the height-time profile of the CME derived from multiple data sources. In this well-observed event there was very good agreement between radio (height time from density model) and the coronagraph GCS modelling (cross-over to WP3), the HI SSEF modelling (cross-over to WP2) and the in situ measurements (cross-over to WP4). Unfortunately no ground based radio data were available for this event given its location on the backside of the Sun relative to the Earth. This proved to be a general problem, with more CME-related slowly drifting radio emission being observed later in the mission (cf. Figure 3.7.6).

In this case study it was found that the goniopolimetry (direction finding) gives the correct direction and qualitative behaviour, but the apparent height is in disagreement with the other data sets. The cause of the discrepancy in apparent height remains to be determined. Nevertheless, the radio data can be used to accurately constrain the kinematics of this CME. A further point of interest is that the main radio emission arises from CME flanks, which has implications for how the production of radio emission by CME shocks occurs. Further analysis of the RADCAT dataset is ongoing to examine this result on a more statistical basis.

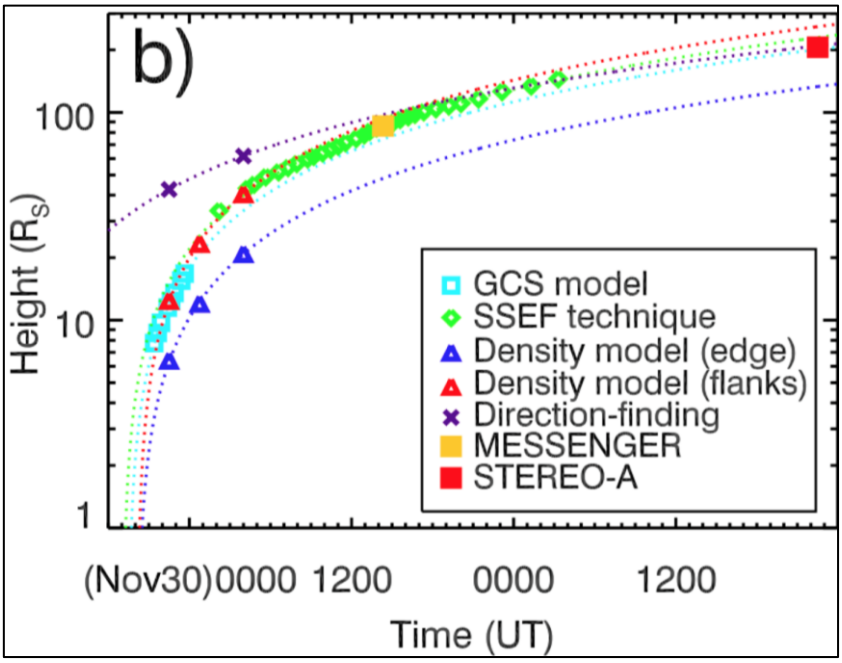

Figure 3.7.8 - CME height time profile derived using coronagraph and heliospheric imager white light imaging, radio measurements, and in situ measurement at Mercury and STEREO-A. The data could be combined to gain a nearly complete experimental characterisation of the CME [Figure taken from Krupar et al., 2016].

A second case study considers the radio emission seemingly associated with the complex interaction of two CMEs, successively launched from the same active region (NOAA AR 11158), on February 14 and February 15, 2011 [J. Magdalenic et al., to be submitted]. The studied continuum-like radio emission has a particular morphology and might be considered as a continuation of the decametric type II radio emission associated with the second CME, or as a continuation of the type III radio bursts associated with a flare from NOAA AR 11158. The radio triangulation study provided us with the 3D source positions of the continuum-like emission

and the associated type II burst, which were compared with the reconstructed positions of the interacting CMEs. Since results of the study indicate that the continuum-like radio emission is neither continuation of the type III radio bursts nor the radio signature of the CME-CME interaction, different scenarios for the generation of the continuum-like radio emission are discussed.

This aspect of Task 7.2 was to be summarised in Deliverable 7.3 ('Report of initial comparison between solar radio-burst events and HI events'). In fact D7.3 takes the form of the peer-reviewed journal publication 'An analysis of interplanetary solar radio emissions associated with a coronal mass ejection' Krupar et al., Astrophys. J. Lett., 825, L5, 2016. This open access article provides a complete description of the event summarised above and shown in Figure 3.7.8.

WP7 CONCLUSIONS:

In this work package we have assessed the complementary nature of radio measurements of solar wind transients. This has focussed on (a) using interplanetary scintillation data to remotely sense the motion of CMEs and SIRs in the interplanetary medium and (b) using low frequency radio signals emitted from the CME shock front to calculate kinematic information associated with the CME. The analysis shows that both have considerable potential to augment coronagraph and heliospheric imaging white light observations.

In Task 7.1 the complementarity of IPS was examined. The IPS and HI data sets provide good complementarity, especially for the manual CCF IPS feature identifications, but the automation described here holds promise. We note that not all HI events were observed in IPS radio data. This was most often due to either the lack of an appropriate source in the HI field of view, or the more practical problem of unavailability of the necessary radio telescope systems. In the latter case, new upcoming systems (e.g. the Square Kilometer Array) provide a very promising way to further develop IPS, and IPSCAT should play a crucial role in improving the general understanding of the efficacy of IPS and its utility.

In Task 7.2 the complementarity of low-frequency radio, and Type II radio emission was examined. The construction of RADCAT further demonstrated that not all CME-driven shocks emit detectable radio emission, but individual case studies highlight the potential utility of the data, with potential for space weather applications in the future. Again RADCAT should be of interest to the community in understanding the fundamental plasma physics that causes radio emission, and will be of use in preparing for the upcoming Solar Orbiter and Solar Probe Plus missions.

WP7 HIGHLIGHTS:

- Completion of catalogues of both IPS data and S/WAVES data
- Augmentation of catalogues with images that are available on the HELCATS website as described here
- Automation of IPS data analysis pipeline with potential future application to space weather monitoring
- New knowledge regarding flank radio emission from CME shocks [Krupar et al., 2016].

WORK PACKAGE 8 (WP8):

DISSEMINATION

WP8 ACTIVITY TYPE: OTH

WP8 DURATION: MONTHS 1 – 36

WP8 LEAD BENEFITIARY: STFC (1)

WP8 LEADER: Dr Chris Perry

WP8 CONTRUBUTORS: UPS (3)

WP8 OVERVIEW: WP8 oversees the logistics of the dissemination of products and information to the project, the Commission and the wider community. The internal project and public websites (accessible at www.helcats-fp7.eu) provide the principal tool for distribution of work results and for keeping track of other dissemination activities. The work has been divided into the following five tasks that are described in more detail in the subsequent task descritpitons.

8.1. The publication of the project results and conclusions to the open research community. This has primarily related to the publication of results from WP2 to WP7 in the professional literature and maintenance of the publication list on the website. It has also included the submission of the underlying catalogues generated by the project to an open scientific data repository that will provide long-term, sustainable and citeable, access to these key outputs.

8.2. The annual open meetings and presentations at scientific meetings have provided an important path to dissemination and engagement with the broader scientific community. A local organising committee was established for each of the annual meetings to handle the specific meeting logistics while the presentations and conclusions have been collected and posted on the website for future reference.

8.3. The installation of documents, catalogues and presentations onto the website. This has included the initial specification of standard formats and identifiers for consistent delivery of the catalogue information. Templates have been produced to provide a common look and feel for project documentation.

8.4. Submission of the catalogues and supporting information for inclusion in community facilities has been an important task both for the long-term sustainability of the work outputs but also to minimise the barriers to community access to these results via access through familiar systems and interfaces.

8.5. The dissemination of appropriately targeted information to the public and policy makers is an important engagement activity. It has been used to highlight the relevance and broader societal and economic impacts of the types of heliospheric event identified and analysed by HELCATS, with particular relevance to Space Weather and improved forecasting

WP8 TASK 8.1- PUBLICATION OF RESULTS AND CONCLUSIONS (TASK LEAD: STFC)

This task focuses on providing support for publication of work results relevant to the project in peer reviewed journals and elsewhere. This has included central support for open access publications costs and maintenance of the project publication list. The full list of publications, talks and posters that have been generated by the project can be found on the website at under the OUTREACH/publications tab (or directly

at https://www.helcats-fp7.eu/publications/publications.html). The current publication statistics (not yet finalised) are provided in Table 3.8.1. See section 4 for more details o n publication strategy and output.

Table 3.8.1 –Publication and presentation statistics

Publication Type	Number
Published/Accepted	31
In Preparation/Submitted	16
TOTAL PAPERS	47
Conference Talks	19
Conference Posters	40

From the project outset a priority has been given to ensuring the accessibility, citability and sustainability of not just the published results and conclusions but also the underlying work results, namely the catalogues. This has included standardisation of catalogue formats and presentation which is covered in WP8.3 and the incorporation of catalogues into established facilities (WP8.4). In order to address the issue of citablitiy and sustainability some intermediate versions and all final versions of the catalogues, together with associated descriptions and documentation, are being deposited in an open access science data repository. The service selected by the project for this purpose is fig**share** (**https://figshare.com/**) which provides all necessary services, such as long-term reliable storage and citeable DOI referencing, without charge for open access data (Figure 3.8.1).

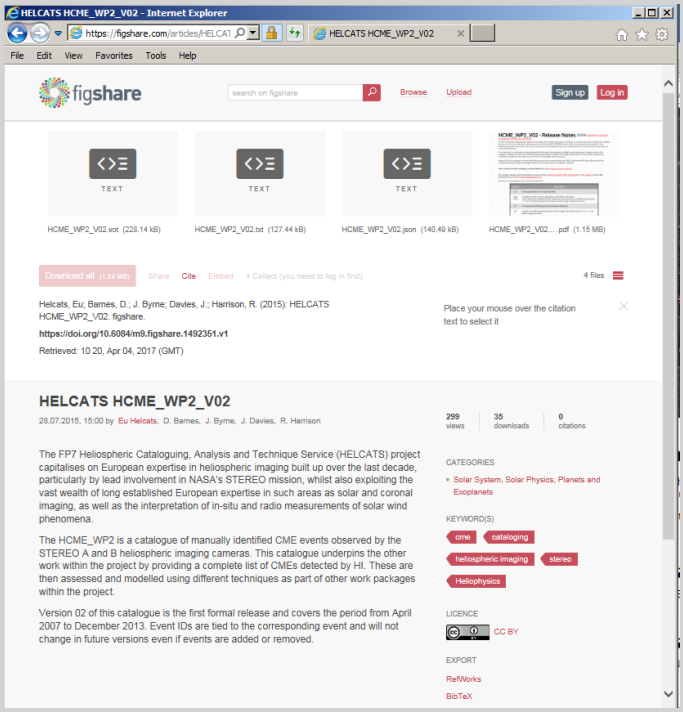

*Fig. 3.8.1 –Example of one of the HELCATS catalogues accessible via fig**share**.*

WP8 TASK 8.2 – ANNUAL OPEN MEETINGS WITH THE SCIENCE COMMUNITY AND PRESENTATION AT MAJOR SCIENCE MEETINGS (TASK LEAD: STFC)

The three annual open meetings that have been held during the progression of the HELCATS project have been an important pathway for dissemination of the project results to the wider community. They have included key presentations from the HELCATS team and from the wider community. The organisation of the

meetings has been undertaken by a local organising committee. The program and presentations from the meeting are accessible either directly or via links on the main HELCATS website.

The **first annual meeting** entitled « Heliospheric Imaging a new era of space science and space weather observations » was held in Gottingen (19-22 May 2015). It was a dedicated HELCATS meeting consisting of about 50 participants from within the project and the broader community including both science and application areas such as space weather service providers. The meeting was an excellent springboard from which to advertise the early results, get initial feedback from outside the project, and to ensure the correct focus for the remainder of the project.

The **second annual meeting** was undertaken as a special session entitled « Heliospheric Cataloguing, Analysis and Technique Service (HELCATS) » as part of the Variability of the Sun and Its Terrestrial Impact (VarSITI) general symposium meeting held in Bulgaria (6-10 June 2016). The meeting was well aligned with the goals of the HELCATS project and with a participant list of well over 150 it provided a scale of access to the HELCATS community that would have been difficult to achieve with a dedicated meeting. It provided the perfect forum in which to present theworking results of the project.

The **thrid (and final) annual meeting** was held as a session of European Geosciences Union (EGU) genereral assembly held in Vienna (23-28 April 2017). With its very large and broad community participation it is the perfect venue in which to present the near-final outputs of the project and to encourage the ongoing use of the results, tools and services that have been implemented during HELCATS.

In addition to the project initiated meetings members of the consortium have regularly participated in community conferences and meetings as demonstrated by the numbers of conference talks and posters listed under task 8.1

WP8 TASK 8.3 – INSTALLATION OF RELEVANT DOCUMENTS, CATALOGUES, PUBLICATIONS ON THE PROJECT WEBSITE (TASK LEAD: STFC)

This task has dealt with the dissemination of project information during the course of the project. The website, which was set-up and maintained under task 1.1 has been actively utilised from the start of the HELCATS project with basic information, meeting information, documents, reports and minutes of meetings and teleconferences. Task 8.3 has been responsible for the overall organisation, design and styling of the website descirbed in the document HELCATS_STFC_D1_1 which was submitted to the comission as part of the overall website deliverable (D1.1). This task is therefore develops the web content that is then loaded as part of 1.1.

The web based dissemination activities consist of three core parts :

- **The public web site**
- **The internal project Wiki**
- **Social media feeds**

It is the first of these that has formed the primary means of ongoing dissemination during the project. Contents are divided in to a number of sections as shown in Figure 3.8.2.

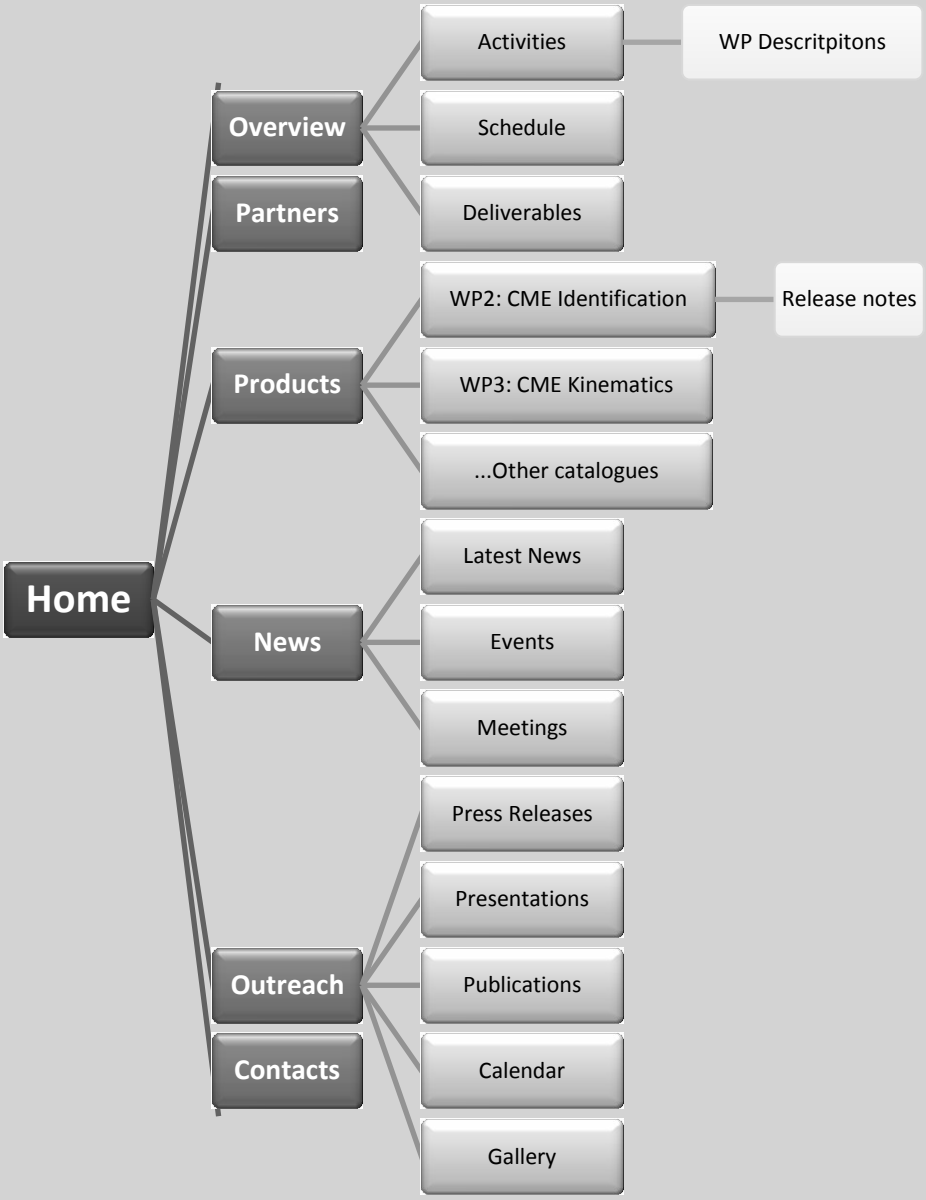

Fig. 3.8.2 –The organisation of the public HELCATS website.

An important task in ensuring the usability of the catalogues has been to define the standards that are to be used for these data products and a standard look and feel for their presentation via the web site. The baseline has been that catalogues are provided in three formats (ASCII, JSON and VOTable). The ASCII format was defined within the WP responsible for their production and follows a simple fixed format or space delimited scheme. Files of this type were then delivered to task 8.3 for conversion to JSON (which is ideal for dynamic web display) and VOTable (which has additional metadata making it well suited for long term access). By following this workflow commonalities in the format translation pipelines could be exploited which otherwise would have required duplication amongst many of the consortium institutes. This also simplified the process of the construction of the dynamic tableview pages used to display these catalogues on the website, examples of which can be found in many of the preceeding WP reports.

An important early decision made by the project was to use a standard event identifier nomenclature. This was implemented for the WP2 HICAT and frozen such that any subsequent updates to the catalogue would not change the ID to event linkage. This ID was then used by all relevant downstream catalogues (see Figure 3.8.3) such as the WP3 HIGeoCAT, the WP4 LINKCAT and the WP7 RADCAT to name a few. This has provided a robust basis on which to undertake join operations between catalogues generated within different WP

and even those that have been created based on different versions of the master HICAT.

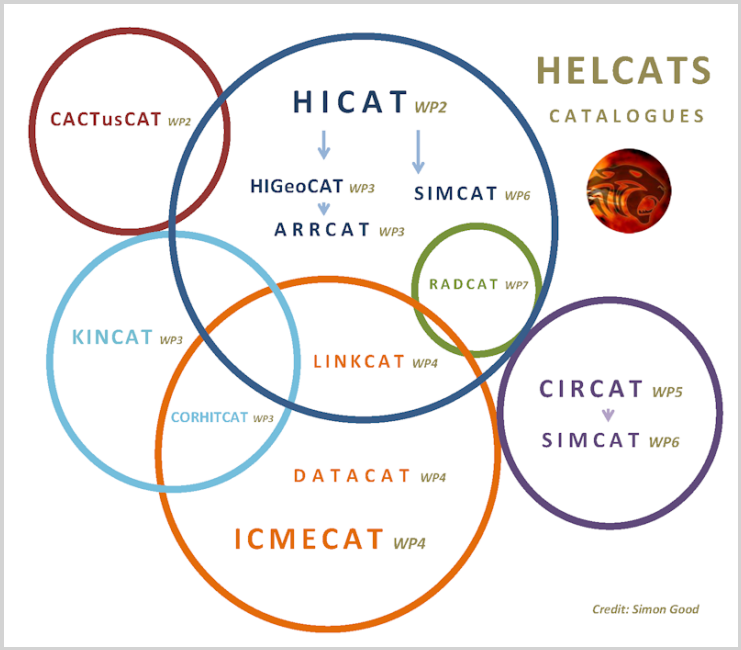

Fig. 3.8.3 –Overview of the HELCATS catalogues (credit: Simon Good).The use of standard data formats and a common event identifier simplifies catalogue interoperability

The benefits of this approach are that it has been possible to use the catalogues directly with third party catalogue processing and display tools such as TOPCAT (linked from the tools menu on the website) Figure 3.8.4. Thus improving accessibility to users who are already familiar with these tools and providing functionalities that would not have been possible to develop within HELCATS with the available resources.

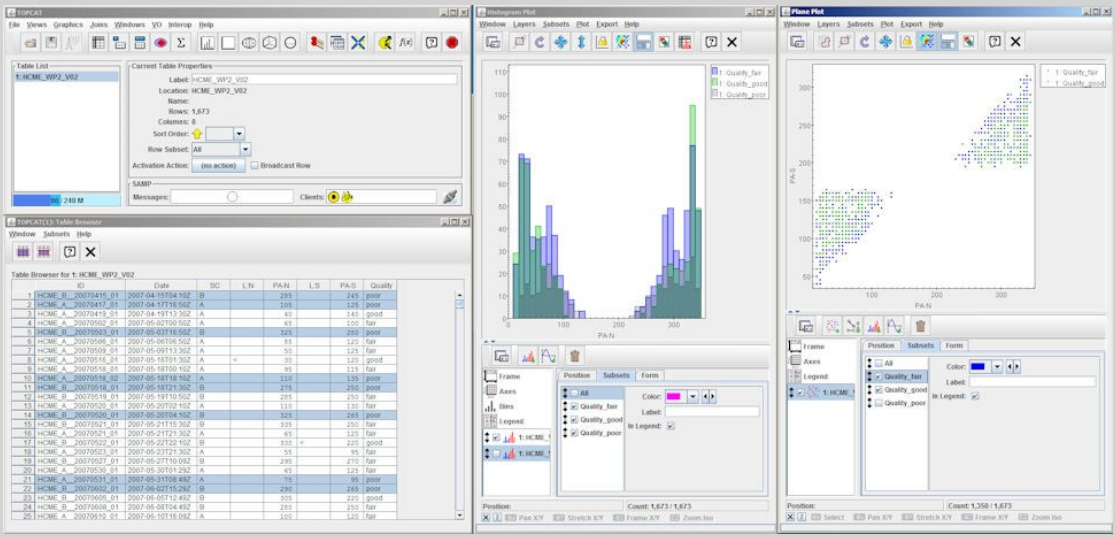

Fig. 3.8.4 –Example of one of HELCATS catalogues (VOTable version of WP2 HICAT) viewed within the standard TOPCAT tool

Guidance is also provided on the website on how Python can be used to load the JSON version of the catalogues directly from the web in a few lines of code. Making it straightforward to integrate the latest version of the HELCATS results into existing processing pipelines.

While the focus of this task has been on standardisation of the catalogue products it was also responsible for the production of standard documentation templates (accessible via the website wiki) to help provide consistent formatting and look and feel amongst the project documentation.

WP8 TASK 8.4 - INTEGRATE WITH RELEVANT, ESTABLISHED COMMUNITY FACILITIES AND WEBSITES (TASK LEAD: STFC)

The catalogues and related products discussed in the previous task are key outputs from the project. They provide one of the best multi-technique assessments of CME identification and propagation that has ever been undertaken. We have therefore been keen to incorporate these results into established community facilities where they can be utilised long after the project itself has completed.

Work has been completed on the integration of the current versions of the catalogues into the widely used tools provided by IRAP including the propagation tool (and 3D-View) which have been reported in the section on task 6.1. This has included the provision and integration of the HELCATS j-maps (deliverable D8.7) and the CME catalogue as shown in Figure 3.8.5.

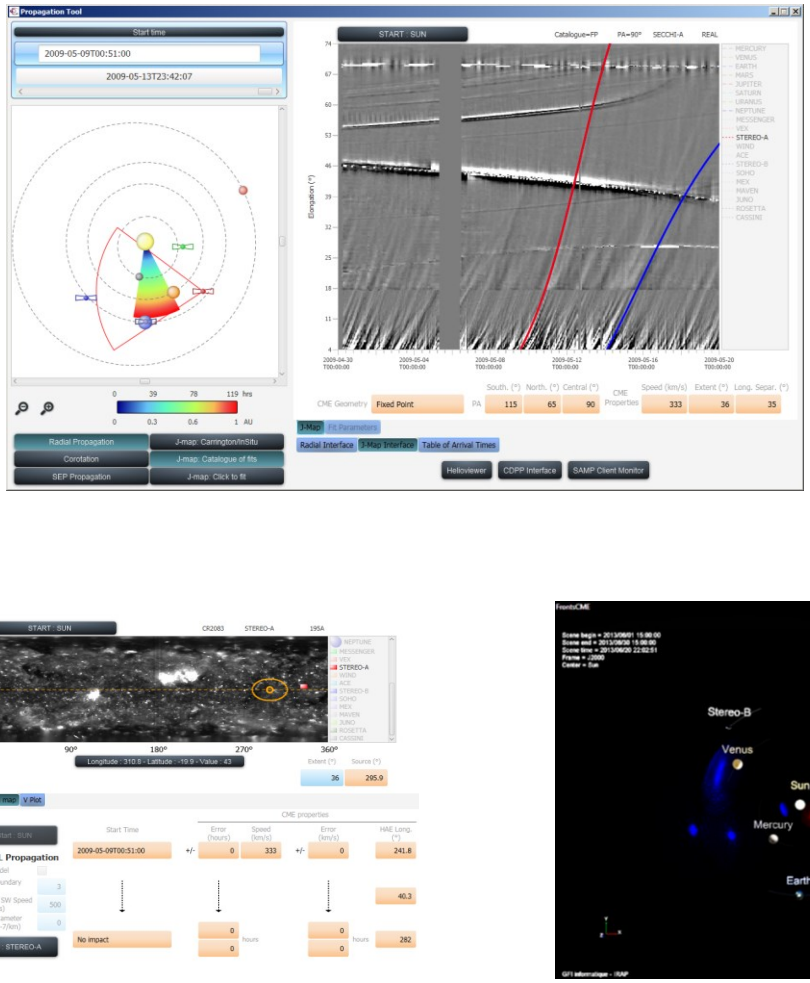

Fig. 3.8.5 –Example of j-maps within the IRAP Propagation Tool (top and bottom left) and incorporation of the CME kinematics (HIGeoCAT) within the IRAP 3Dview tool (bottom right)

Discussions have been held with the EU HELIO project on the integration of the final version of the HICAT within the HELIO Event Catalogue system and with the UK Solar System Data Centre. This transition is straightforward via the ue of the VOTable version of the catalogue which has the necessary metdata already incorporated to semi-automate the ingestion process.

WP8 TASK 8.5 – DISSEMINATION OF INFORMATION TO THE PUBLIC AND POLICY MAKERS (TASK LEAD: STFC)

The website is openly available to the public with information about the project and access to most of the project documentation and activities. The website includes news items, events, tweets and information on meetings. There is much background information for the non-professional, interested reader.

The HELCATS team members are very active in 'live' space projects (e.g. STEREO, Cluster, Hinode) and in space weather activities, such as ESA's Space Situational Awareness (SSA) space weather programme. The HELCATS project has been widely discussed, especially in space weather fora, because it is seen as pioneering and spearheading the assessment of HI observations along with associated data and modelling methods in a way that can have a major influence on future space weather strategic applications. Many members of the Steering Committee, including the Coordinator and the Scientific and Technical Managers, are actively involved in SSA projects. In the UK this has involved close involvement with the Met Office, which is now an established space weather forecasting facility for the UK Government. These activities have come to a critical point within the last year with the completion of initial Phase-0 studies on a space weather operational demonstrator mission to the Legrange L5 point. A key rationale for such a mission is to move away from the Sun-Earth line to provide a side-on view of CMEs propagating towards the Earth via wide angle white light heliospheric imaging. The results of the HELCATS study are providing a vital input to the assessment of potential improvements in forecasting capability that are expected to result from some a mission in the future.

WP8 DELIVERABLES:

WP8 has eight associated deliverables, which are defined and their status outlined, in Table 3.8.2. The dissemination levels indicate, in this case, whether the deliverable is publically available (PU) or available only to the project, the project Officer and reviewer (PP).

Table 3.8.2: The HELCATS deliverables for WP1

No.	Title	Lead Beneficiary	Nature	Dissemination Level	Delivery Date (m)	Status/Comment
D8.1	Publication in the professional scientific literature	STFC	Other	PU	36	Publication list on the web site. Catalogues available on figshare
D8.2	Annual open meeting	STFC	Other	PU	36	Links to meeting website and presentations on the website
D8.3	Attendance/presentations at major science meetings	STFC	Other	PU	36	List of presentations on the web site
D8.4	Posting information on the website	STFC	Other	PU	36	See the website
D8.5	Integration with	STFC	Other	PU	36	Catalalogues

	community facilities and websites					integrated with Propagation tool, available on figshare, plans for inclusion in EU HELIO
D8.6	Production of press releases, public	STFC	Other	PU	36	Kick-off press release. Other announcements via social media
D8.7	Integrate the J-map associated catalogues produced in HELCATS to the propagation tool	UPS	Other	PU	36	Propagation tool has been updated
D8.8	Integrate Carrington Map associated catalogues in the propagation tool	UPS	Other	PU	36	Propagation tool has been updated

WP8 CONCLUSIONS:

WP8 has successfully ensured that the outputs from the main production work packages (WP2 to WP7) were made available in an efficient, standardised and easily accessible way to the wider scientific community. This has been achieved through the use of the project website whilst the long term sustainability and access has been guaranteed by registering the key products in an open access science archive service run independently of the project. Support has been provided for the effective communication of the HELCATS conclusions and results both through three very successful workshops and through publications in the relevant peer reviewed science literature and at science workshops and conferences.

4 CONCLUDING REMARKS: IMPACT, LEGACY, LESSONS LEARNT

The HELCATS project has delivered what it set out to deliver. The core effort, related to the setting up and development of the catalogues, the employment of appropriate models, and the formal reporting of the activities through the defined deliverables, has been completed. The project telecons, meetings and open meetings were held as defined at the start of the project. Those deliverables that were to be delivered on completion of the project have now been completed. No aspect of the formal statement of work has not been completed.

The STFC management team and the Steering Committee take pride in the fact that the products that have been developed are unique; there is no other unified, extensive, global catalogue and analysis facility of heliospheric CMEs and CIRs/SIRs and, thus, we believe that we have delivered something that will provide a step-change in the study of solar transients in the heliosphere, enabling many lines of research for the wider community.

So, our efforts at the end of the project and into the future are to ensure that the ground-breaking facilities for research into solar transients in the heliosphere, provided by HELCATS, is well advertised and well exploited. Our strategy for this is outlined below.

IMPACT

From the comments, above, it is clear that we envisage a clear and significant scientific impact from the HELCATS project. In particular, the new access to extensive statistical studies, to mechanisms to link phenomena from Sun to Earth, as well as readily available access to data and to catalogued information will undoubtedly enhance many aspects of heliospheric research. The number of publications already in the open literature is testament to this. In terms of the applied side of that research, specifically for space weather, not only will the catalogues enable space-weather related research, the techniques and models applied to the HELCATS project, in particular, when making comparisons and validation, can be applied directly to space weather activities. The details of these are given in the WP descriptions but, to ensure that this has been considered fully, we defined the UK Met Office as a formal 'interested third party' to the HELCATS project. We believe that the project has provided assessments and tools that will be central to the development of space weather application in Europe.

Another impact of the project is the training and development of the young scientists (detailed below) and the influence that the HELCATS project has on the research they take forward. The uniqueness of the project plus its applicability to the emerging space weather programme in Europe (in particular the ESA SSA space weather programme) has provided excellent training for that emerging field. In parallel, the collaborations that have developed in the conceptual phase of HELCATS and in the running of the project have cemented new cross-disciplinary collaborations in heliospheric research.

LEGACY

The HELCATS team have always been fully aware of the need for a legacy plan, to ensure that the successful delivery of HELCATS includes a strategy to ensure that the products and findings are exploited fully into the future. We have been well aware of past EU projects that have not been particularly well set-up to deliver benefits for the wider community into the future, and this is something that we have taken great pains to avoid. Our plan has always included a number of elements that amount to a legacy policy with regard to the continuation of the catalogues and access to them, to the post-project state of the website, to publications – especially what we regard to be key project publications, to the development of people, in particular young scientists, and to the public. These are detailed below, and are consistent with our original proposal.

1. Catalogues and the HELCATS website

The catalogues produced by the HELCATS project will continue to be available through the HELCATS website. The website will be maintained under the auspices of the UK Solar System Data Centre (UKSSDC) at RAL (STFC). The NASA STEREO project continues and the HI PI team at RAL will maintain and continue to expand the HICAT

and HIGeoCAT catalogues as the official event lists of the HI project, adding new events as the mission progresses. Benefiting from the development work of HELCATS, the HI Post Launch Support operation at RAL will ensure that this is done. On completion of the mission these catalogues will be a formal facility within the UKSSDC for public use. However, we do not anticipate termination of STEREO in the foreseeable future, especially in the light of its value for space weather application. It is important to note that, as the Principal Investigator team for the STEREO/HI instruments, the RAL group has defined HICAT and HIGeoCAT as the definitive event lists to the wider heliospheric physics research community; they are the benchmark catalogues that the community will now use.

The website has been a working website for the project and, on completion of the project will be transitioned to a legacy portal for the HELCATS project information, as well as access to the catalogues and publications. The web address with remain as www.helcats-fp7.eu and it will be hosted at RAL.

Formal ownership or responsibility for maintaining these facilities and access to them will be taken up by the RAL STEREO/HI team within the RAL Space Physics and Operations Division.

2. Publications and presentations

The HELCATS website will provide access to the project publication list, containing all publications that related to the development of the project and to exploitation of the results of the project during its lifetime.

In terms of publication strategy, the project team regard the publication, on completion of the project, of key papers as being of critical importance for advertising the results of HELCATS, the facilities available and the future legacy. The final production of these will follow on immediately from completion of this report, though these papers are in a near-final in-preparation stage at this time. Submission prior to the completion of the project would have been counter-productive; our aim was to ensure that the catalogues were complete and final links accurate. These papers will be submitted to relevant professional journals, and made available on the website. This includes a definitive HELCATS project publication, and two publications that describe and detail the HICAT and HIGeoCAT catalogues and their results, especially with the presentation of the statistical analysis of CMEs in the heliosphere. Other papers will be included, and the intention has been to draft these as the project is completed so they include the important and up to date information on the data-sets themselves, access to data and final results. Whereas the HELCATS website is the shop-window or 'one stop shop' for the study of CMEs and CIRs/SIRs in the heliosphere, those key papers will provide the public advertisement of the facility and its exploitation. Those key papers will be widely distributed and they will be highly visible on the website.

The exploitation of the HELCATS catalogues will be intimately associated with the continued research relating, in particular, to the STEREO project. As a result, HELCATS will feature widely in the future analysis and exploitation of STEREO and the publications listed on the STEREO webpages. We anticipate extensive use of the HELCATS facilities in much the same way that the CDAW catalogues are associated with the SOHO mission research activities.

HELCATS publications are given in section 5 of this report and summarised in Table 4.1. In section 5, the key papers are shown in italics and, if they include definitive work on particular catalogues, these are indicated.

Table 4.1: HELCATS-related publications (see section 5 for details)(status as of 1 June 2017)

Year	Number of papers*
2014	**3**
2015	**7**
2016	**16**
2017 (up to June 1st)	**5**
In preparation and submitted	**16**
Total	**47**

[* Only full papers included, not published abstracts]

The HELCATS project, progress and results have been presented at a wide range of national and international meetings. These include oral and poster presentations, as listed in section 5. As an illustration, the team gave 19 oral presentations in international conferences in seven different countries. In the same period, 40

HELCATS posters were presented. It was the active engagement and interest of the community at such meetings that stressed to the Steering Committee that holding the final Open Workshop in Vienna at the EGU meeting would be beneficial from a community point of view.

3. People

The HELCATS project is a collaboration of eight European groups that are front-runners in heliospheric research. The STFC management team and the Steering Committee are made up of individuals with a wide-ranging expertise in solar, heliospheric and space environment sciences, including space weather, along with instrumentation and modelling interests. That collaboration has spawned research activities that are crossing traditional disciplinary boundaries. Thus, the spirit of the HELCATS concept has been to develop a strategic approach for the field by opening new multi-disciplinary approaches. The legacy of this will live on as the scientific collaborations develop between the groups and beyond. This is well illustrated by the publications that have been produced to date.

In particular, we have recognised that HELCATS is valuable for the training of the next generation and have been particularly sensitive to the employment of young scientists who, it is hoped, will continue to develop the field or will move into related areas. In this respect we feel that HELCATS has been particularly successful. Guided by the senior players in the project, a large portion of the work has been undertaken by the younger scientists who were employed on the project, and they have had the opportuinity to present and publish their work. We identify them below. These are all scientists that completed their PhDs within the last few years or are doing their PhD studies at this time. Only a few of them were 100% funded by HELCATS and some of the PhD students were not funded by HELCATS but contributed through their supervisors. Thus, we have a spectrum of involvement, from research through to substantial modelling or cataloguing work:

Julius Achenbach, UGOE – Student at Göttingen, finishing up his masters degree with the HELCATS team, worked on the programming of the CME database.

Dr David Barnes, STFC – Employed at RAL from 2014, working on the HICAT and HIGeoCAT development and analysis. Completed his PhD in 2016 and is now in a permanent position at RAL.

Dr Peter Boakes, UNIGRAZ – Employed as postdoc on the HELCATS project in Graz. He recently moved on to work on the Rosetta/MIDAS project.

Dr Eckart Bosman, UGOE – Worked on forward modelling (GCS), finishing in January 2017 to take up a position in Graz.

Anthony Bourdelle, UPS – A SUPAERO/Master student, did an internship at UPS and then at RAL, working on the HELCATS project. He is now doing a PhD at ONERA, the French aerospace lab in Toulouse.

Bram Bourgoignie, ROB – Early career IT position working on the CACTus software.

Dr Jason Byrne, STFC - Came as a postdoc to RAL from the University of Hawaii (also formally from Trinity College Dublin), to work on HELCATS, as a young, established solar physicist. Worked on the catalogue development and analysis. Left in 2016 to work at the UK Post Office.

Dr Eoin Carley, TCD – Worked as postdoc on TCD solar associations. Left to take up Marie-Curie Fellowship and now a Postdoc at TCD.

Dr Andy Davos, ROB – Employed on project as postdoc until June 2016. Left science afterwards.

Dr Simon Good, IMPERIAL – Taken up short term contract to replace Vratislav Krupar to the end of the project, from February to April 2017.

Skralan Hosteaux, ROB – First year PhD student working on HELCATS project at ROB.

Dr Alexey Isavnin, UH - Obtained his PhD at Helsinki in 2014 and worked as a postdoc directly on the HELCATS project on issues related to the in-situ analysis and modelling.

Dr Vratislav Krupar, IMPERIAL – Employed as a postdoc to work on the radio analysis work at Imperial College, from 2015-2016. Has taken up a position at the NASA Goddard Space Flight Center, USA.

Michael Lavarra, UPS - Did a six-month internship and is now doing his Masters project after graduating from SUPAERO. He will begin a CNES-funded PhD under Alexis Rouillard's supervision starting in September

on modelling the solar wind.

Niclas Mrotzek, UGOE – PhD student working at Göttingen, working on GCS modelling. Nearing submission.

Dr Sophie Murray, TCD – Worked at TCD and the UK Met Office before returning to TCD to work on the HELCATS project and the H2020 FLARECAST project.

Erika Palmerio, UH – Has worked extensively on the HELCATS catalogues within the UH group, now working towards her PhD. Also visiting ROB for one month during Spring 2017.

Dr Rui Pinto, UPS - Did his third postdoc with UPS and will continue on a 1-year space-weather project funded by CNES with Alexis Rouillard in the coming months.

Dr Illya Plotnikov, UPS - Was hired after his PhD (in astrophysics) to work on the HELCATS project. He learnt about heliophysics with UPS, obtained French nationality last year, and will start a 3-year postdoc at Princeton in September 2017.

Adam Pluta, UGOE – PhD student working at Göttingen, nearing submission.

Dr Martin Reiss, UNIGRAZ – Worked on HELCATS during the last two months, specifically on the WP4 publication and is applying to work at the NASA Goddard Space Flight Center, USA.

Eduardo Sanchez-Diaz, UPS - Completing his PhD thesis, involving HELCATS exploitation, that he will submit in July and defend in November. He has two HELCATS papers published, one will soon be submitted and one is in preparation.

Dr Pietro Zucca, TCD – Worked as a postdoc on the TCD solar association and inverse modelling activities. Now employed as a Postdoc at the Observatoire de Paris.

4. The public

HELCATS is a project that is geared towards enabling extensive exploitation of heliospheric phenomena such as CMEs and CIRs/SIRs. So, its prime aim is to deliver to the scientific research community and, in turn, to provide a valuable resource for space weather application. However, we have always been aware of the need to deliver to the public that ultimately funded the project and, we are aware, has an interest in matters relating to space.

The HELCATS website is publically available and includes basic descriptions of the project, aimed at the general reader, as well as a gallery and links to associated material (e.g. the STEREO project). We have also released occasional press releases (see the website for details) and HELCATS has been included in many public talks given by the team. However, the principal public deliverable is a final report on the project, to be delivered on completion of the project. This public report contains basic information on the project, detailing links to the website and other relevant sites, and including images (and links to movies). The public report is a formal deliverbale (D1.9); it will be distributed widely. *Despite completion of the project at the end of April (at the EGU meeting), the release of this public report and any associated press material has been delayed by the call, in the UK, of a General Election. As a Government laboratory RAL/STFC, we are formaly 'in purdah', meaning that we cannot communicate with the media (to avoid any implication of matters that might relate to the political parties in the UK). Thus, the formal release to the media will take place after the June election.* This was reported at the HELCATS Final Review in April.

The current final report will be made available (wth any sensitive information removed) for the public and scientific community, through the website.

We anticipate that shorter versions of the report will be used to report on completion of the project through, for example, the RAS Astronomy and Geophysics magazine and similar journals.

LESSONS LEARNT

The HELCATS project has been an extremely rewarding activity with the principal lessons learnt being associated with the ability to accelerate the advancing of the field through the active collaboration of a wide range of disciplines. Whilst the HELCATS concept was being developed, prior to the FP7 submission, the team

were of the view that whereas many space-related FP7 projects were providing portals for access to data from a range of space instruments, the aims were often not particularly focused and a number of projects were providing very similar products. We always felt that HELCATS provided a particular focus, on the identification, cataloguing and modelling of transients in the heliosphere and that this focus not only made the project unique, it gave it a clear scientific aim that was both manageable and valuable.

With hindsight, a number of activities on the administrative side could have been improved. For example, we defined the 18 month milestone and the end of the project as the two financial reporting periods. Thus, for each we required a financial report associated with a report on progress of the project. Noting that we also had full project annual reports at 12 and 24 months, this called for rather more, full, formal reports on the project than was anticipated. We tackled this by requesting that one of the annual reports could be converted to the production of the definitive HELCATS paper (which is in effect a full report but for publication purposes). Noting also that the financial reports, by necessity were generated after the milestones, it might have been better to disconnect the annual project reports and the financial reports, to be delivered as separate documents a few months apart.

Having said that, the communication structure of monthly telecons, bi-annual and annual meetings ensured that the groups were well integrated and that the project ran smoothly. With the number of deliverables and actions, it was essential to maintain good minutes of meetings and lodge them on the Wiki area of the website.

A particular lesson for us relates to the activity at the completion of the project. Many deliverables, such as the final catalogues were formally to be delivered in month 36, and a number of reports at about the same time. This does mean that our desire to publish the definitive HELCATS paper plus a few key project papers on the catalogues could really only be finalised right at the end of the project or the weeks after. Early publication could easily result in incomplete information. The decision was made early to not finalise those publications until month 36.

We believe that our approach to the legacy of the project is critical, having witnessed past projects pass into obscurity. We feel that the formal links to the UKSSDC and the STEREO project, ensuring that the catalogues and website are maintained into the foreseeable future, will enable the benefits of HELCATS to be widely exploited. In this respect, we would be happy to provide a legacy report to the EU some six months after the completion of the project, to demonatrate that the legacy strategy is working, and would suggest that such a legacy report some time after the completion of any such project would be valuable.

5 PUBLICATIONS & PRESENTATIONS

5.1 HELCATS Publications

We list here publications that relate to the activities of the HELCATS project or that have resulted from exploitation of the HELCATS project results or methods. Key project papers are shown in italics. Papers particularly associated with specific catalogues indicate the relevant catalogues in square brackets. Note that several of the 'in preparation and submitted' papers were identified early in the project as publications to produce on completion of the project (to ensure presentation of the complete results, links etc…). Most of these are in a near-final form at this time and will be submitted within 60 days of the completion of the project.

In preparation/submitted: [16 papers]

HELCATS – Heliospheric Cataloguing, Analysis and Techniques Service
Davies, J.A., Harrison, R.A., Barnes, D., Perry, C.J., Bothmer, V., Eastwood, J., Gallagher, P., Kilpua, E., Möstl, C., Odstrcil, D., Rodriguez, L., Rouillard, A.
2017, In preparation. ***[Definitive HELCATS project paper referring to all catalogues]***

Coronal Mass Ejections in the heliosphere: I. Cataloguing and analysis of events recorded by the STEREO Heliospheric Imagers for the period 2007—2014
Harrison, R.A., Davies, J.A., Barnes, D., Byrne, J.P., Perry, C.J., Bothmer, V., Eastwood, J., Gallagher, P., Kilpua, E., Möstl, C., Rodriguez, L., Rouillard, A.
2017, In preparation ***[HICAT]***

Coronal Mass Ejections in the heliosphere: II. A catalogue of kinematic properties derived from single-spacecraft geometrical modelling
Davies, J.A., Barnes, D., Harrison, R.A., Byrne, J.P., Perry, C.J., Bothmer, V., Eastwood, J., Gallagher, P., Kilpua, E., Möstl, C., Rodriguez, L., Rouillard, A.
2017, In preparation ***[HIGeoCAT]***

Coronal Mass Ejections in the heliosphere: III. A catalogue of kinematic properties derived from stereoscopic geometrical modelling
Barnes, D., Davies, J.A., Harrison, R.A., Perry, C.J., Bothmer, V., Eastwood, J., Gallagher, P., Kilpua, E., Möstl, C., Rodriguez, L., Rouillard, A.
2017, In preparation ***[HIjoinCAT]***

The application of heliospheric imaging to space weather operations: lessons learnt from published studies
Harrison, R.A., Davies, J.A., Biesecker, D.A., Gibbs, M.
2017, submitted to Space Weather

Multipoint analysis of CME-CME interaction
Isavnin, A., Kilpua, E.K.J., Möstl, C., Palmerio, E., Pomoell, J., Winslow, R.,
2017, in preparation

Automatic detection of Coronal Mass Ejections (CMEs) in Heliospheric Imager data: an automatic CME catalogue for STEREO-HI
Rodriguez, L., Pant, V., Mierla, M., Willems, S. et al.
2017, In preparation ***[CACTusCAT]***

Statistical Survey of Slow Drifting Radio Emissions at Long Wavelengths Associated with Heliospheric Imaging Observations
Krupar V. et al,
2017, In preparation ***[RADCAT]***

Space weather monitor at the L5 point: a case study of a CME observed with STEREO B
Rodriguez, L., Zhukov, A., West, M., Mierla, M.
2017, In preparation

Coronal magnetic structure of Earthbound CMEs and *in situ* comparison
Palmerio, E., Kilpua, E. K. J., Bothmer, V., Isavnin, A., Möstl, C., Green, L. M., James, A. W., Davies, J. A., and Harrison, R. A.
2017, In preparation

Cataloguing the solar wind from the surface of the Sun to 1 AU
Pinto, Rouillard, Odstrcil, et al,
2017, In preparation ***[SIMCAT]***

Connecting Coronal Mass Ejections to their Solar Active Region Sources
Murray, S. A., Zucca, P. , Carley, E., Gallagher, P. T., Guerra, J. A., Hong, S. et al
2017, In preparation ***[LOWCAT]***

The magnetic connectivity of coronal shocks to the visible solar surface during long-duration gamma-ray events
Plotnikov, I., Rouillard, A.P., Share, G.H.,
2017, submitted to Astron. & Astrophys.

The time and spatial scales of density fluctuations released in the slow solar wind,
Sanchez-Diaz, E., Rouillard, A.P., Davies, J.A., Lavraud, B., Pinto, R.
2017, In Preparation, to be submitted to Astrophyiscal J. ***[CIRCAT]***

Large-scale structure of the heliospheric plasma sheet inferred from in-situ data
Sanchez-Diaz, E., Rouillard, A.P., Kilpua, E., Lavraud, B.
2017, In Preparation, to be submitted to J. Geophys. Res. ***[CIRCAT]***

3-D modelling and multipoint analysis of magnetic flux ropes from the Sun to 1AU
Rouillard, A.P., Lavarra, M., Bourdelle, A., Kunkel, V.
2017, In Preparation, to be submitted to Astrophys. J. ***[SIMCAT]***

Published/Accepted: [2017 – 5 papers to date, 2016 – 16 papers, 2015 – 7 papers, 2014 – 3 papers]

Predictions of solar coronal mass ejections with heliospheric imagers verified with the Heliophysics System Observatory
C. Möstl, A. Isavnin, P. D. Boakes, E. K. J. Kilpua, J. A. Davies, R. A. Harrison, D. Barnes, V. Krupar, J. P. Eastwood, S. W. Good, R. J. Forsyth, V. Bothmer, M. A. Reiss, T. Amerstorfer, R. M. Winslow, B. J. Anderson, L. C. Philpott, L. Rodriguez, A. P. Rouillard, P. Gallagher and T. L. Zhang
2017, Space Weather – in press. ***[HIGeoCAT, ARRCAT, ICMECAT]***

A propagation tool to connect remote-sensing observations with in-situ measurements of heliospheric structures
Rouillard, A. P.; Lavraud, B.; Genot, V.; Bouchemit, M.; Dufourg, N.; Plotnikov, I.; Pinto, R. F.; Sanchez-Diaz, E.; Lavarra, M.; Penou, M.; Jacquey, C.; Andre, N.; Caussarieu, S.; Toniutti, J.-P.; Popescu, D.; Buchlin, E.; Caminade, S.; Alingery, P.; Davies, J. A.; Odstrcil, D.; Mays, L.
2017, In press. arXiv:1702.00399 ***[CIRCAT]***

Observational Evidence for the Associated Formation of Blobs and Raining Inflows in the Solar Corona
Sanchez-Diaz, E., Rouillard, A. P., Davies, J. A., Lavraud, B., Sheeley, N.R., Pinto, R.F., Kilpua, E., Plotnikov, I., Genot, V.
2017, Astrophys. J Lett. 835, L7 ***[CIRCAT]***

Determining the Intrinsic CME Flux Rope Type Using Remote-sensing Solar Disk Observations
Palmerio, E., Kilpua, E. K. J., James, A. W., Green, L. M., Pomoell, J., Isavnin, A., & Valori, G.,
2017, Solar Phys. 292, 39

A multiple flux-tube solar wind model,
Pinto, R.F., Rouillard, A.P.
2017, Astrophys. J. 838, 89 ***[SIMCAT]***

Automated Detection Of Coronal Mass Ejections In STEREO Heliospheric Imager Data
Pant, V., Willems, S., Rodriguez, L., Mierla, M., Banerjee, D., Davies, J.
2016, Astrophys. J. 833, 80 ***[CACTusCAT]***

Deriving the Properties of Coronal Pressure Fronts in 3D: Application to the 2012 May 17 Ground Level Enhancement
Rouillard, A.P., Plotnikov, I., Pinto, R.F., Tirole, M., Lavarra, M., Zucca, P., Vainio, R., Tylka, A.J., Vourlidas, A., De Rosa, M.L., Linker, J., Warmuth, A., Mann, G., Cohen, C.M.S., Mewaldt, R.A.
2016, Astrophys. J. 833, 45.

FRiED: A Novel Three-dimensional Model of Coronal Mass Ejections
Isavnin, A.,
2016, Astrophys. J. 833, 267.

Prediction of Geomagnetic Storm Strength from Inner Heliospheric In Situ Observations
Kubicka, M., Möstl, C., Rollett, T., Boakes, P.D., Feng, L., Eastwood, J.P., Törmänen, O.,
2016, Astrophys. J. 833, 255.

Sun-to-Earth Characteristics of the 2012 July 12 Coronal Mass Ejection and Associated Geo-effectiveness
Hu, H., Liu, Y. D., Wang, R., Möstl, C., & Yang, Z.,
2016, Astrophys. J. 829, 97.

ElEvoHI: a novel CME prediction tool for heliospheric imaging combining an elliptical front with drag-based model fitting
Rollett, T., Möstl, C., Isavnin, A., Davies, J. A., Kubicka, M., Amerstorfer, U. V., Harrison, R. A,
2016, Astrophys. J. 824, 131.

Interplanetary Coronal Mass Ejections observed by MESSENGER and Venus Express
Good, S.W., Forsyth, R.J.
2016, Solar Phys. 291, 239.

Erratum: "ElEvoHI: A Novel CME Prediction Tool for Heliospheric Imaging Combining an Elliptical Front with Drag-based Model Fitting ApJ 824, 2, 131",
Amerstorfer, T., Möstl, C., Isavnin, A., Davies, J. A., Kubicka, M., Amerstorfer, U. V., Harrison, R. A.,
2016, Astrophys. J. 831, 210.

Comparison of magnetic properties in a magnetic cloud and its solar source on April 11-14 2013
Vemareddy, P., C. Möstl, T. Rollett, W. Mishra, C. Farrugia, and M. Leitner,
2016, Astrophys. J. 828, 12.

An Analysis of Interplanetary Solar Radio Emissions Associated with a Coronal Mass Ejection
Kruper, V., Eastwood, J.P., Kruparova, O., Santolik, O., Soucek, J., Magdalenić, J., Vourlidas, A., Maksimovic, M.,

Bonnin, X., Bothmer, V., Mrotzek, N., Pluta, A., Barnes, D., Davies, J.A., Martínez Oliveros, J.C., Bale, S.D.
2016, Astrophys. J. Lett. 823, L5 ***[RADCAT]***

Thermal and non-thermal emission from reconnecting twisted coronal loops
Pinto, R.F., Gordovskyy, M., Browing, P.K., Vilmer, N.
2016, Astron. Astrophys. 585, A159, 14

3-D views of the expanding CME: from the Sun to 1AU
Rouillard, A.P.
2016, Highlights of Astronomy, 16, 106.

The very slow solar wind: properties, origin and variability
Sanchez-Diaz, E., Rouillard, A.P., Lavraud B., Segura, K., Tao, C., Pinto, R., Sheeley, N. R., Plotnikov, I.,
2016, J. Geophys. Res: Space Phys. 121, 4, 2830.

Coronal mass ejection-related particle acceleration regions during a simple eruptive event,
Salas-Matamoros, C. Klein, K.-L., Rouillard, A.P.
2016, Astron. & Astrophys. 590, A135.

Flux-tube geometry and solar wind speed during an activity cycle
Pinto, R.F., Brun, A.S., Rouillard, A.P.
2016, Astron. & Astrophys. 592, A65.

Long-term tracking of corotating density structures using Heliospheric Imaging
Plotnikov, I., Rouillard, A.P., Davies, J.A., Bothmer, V., Eastwood, J.P., Gallagher, P., Harrison, R.A., Kilpua, E., Möstl, C., Perry, C., Rodriguez, L.
2016, Solar Phys. 291, 1853. ***[CIRCAT]***

Strong coronal channelling and interplanetary evolution of a solar storm up to Earth and Mars
Möstl, C., Rollett, T., Frahm, R.A., Liu, Y.D., Long, D.M., Colaninno, R.C., Reiss, M.A., Temmer, M., Farrugia, C.J., Posner, A., Dumbović, M., Janvier, M., Démoulin, P., Boakes, P., Devos, A., Kraaikamp, E., Mays, M.L., Vršnak, B.
2015, Nature Communications 6, 7135.

Statistical study of magnetic cloud erosion by magnetic reconnection
Ruffenach A., B. Lavraud, C. J. Farrugia, P. Demoulin, S. Dasso, M. J. Owens, J.-A. Sauvaud, A. P. Rouillard, A. Lynnyk, C. Foullon, N. P. Savani, J. G. Luhmann and A. B. Galvin
2015, J. Geophys. Res.: Space Physics, 120, 43.

Radial Evolution of a Magnetic Cloud: MESSENGER, STEREO, and Venus Express Observations
Good, S. W., Forsyth, R. J., Raines, J. M., Gershman, D. J., Slavin, J. A., Zurbuchen, T. H.,
2015, Astrophys. J. 807, 177.

Propagation of the 7 January 2014 CME and Resulting Geomagnetic Non-Event
Mays, M. L., Thompson, B. J., Jian, L. K., Colaninno, R. C., Odstrcil, D., Mostl, C., Temmer, M., Savani, N. P., Taktakishvili, A., MacNeice, P. J., Zheng, Y.
2015, Astrophys. J. 812, 145.

Investigating Alfvénic wave propagation in coronal open-field regions
Morton, R.J., Tomczyk, S., Pinto, R.
2015, Nature Communications 6, 7813.

Soft X-ray emission in kink-unstable coronal loops
Pinto, R. F.; Vilmer, N.; Brun, A. S.
2015, Astron. & Astrophys. 576, A37, 16.

Statistical study of magnetic cloud erosion by magnetic reconnection
Ruffenach A., B. Lavraud, C. J. Farrugia, P. Demoulin, S. Dasso, M. J. Owens, J.-A. Sauvaud, A. P. Rouillard, A. Lynnyk, C. Foullon, N. P. Savani, J. G. Luhmann and A. B. Galvin
2015, J. Geophys. Res., Space Phys. 120, 43.

Combined Multipoint Remote and in situ Observations of the Asymmetric Evolution of a Fast Solar Coronal Mass Ejection
Rollett T., C. Mostl, M. Temmer, R. A. Frahm, J. A. Davies, A. M. Veronig, B. Vrsnak, U. V. Amerstorfer, C. J. Farrugia, T. Zic, and T. L. Zhang,
2014, Astrophys. J. 790, L6.

Connecting Speeds, Directions and Arrival Times of 22 Coronal Mass Ejections from the Sun to 1 AU
Möstl, C., Amla, K., Hall, J. R., Liewer, P. C., De Jong, E. M., Colaninno, R. C., Veronig, A. M., Rollett, T., Temmer, M., Peinhart, V., Davies, J. A., Lugaz, N., Liu, Y. D., Farrugia, C. J., Luhmann, J. G., Vrsnak, B., Harrison, R. A., & Galvin, A. B.,
2014, Astrophys. J. 787, 119.

HELCATS - Heliospheric Cataloguing, Analysis and Techniques Service
EU Space Research, Into Space report
2014, ISBN 978-92-79-34024-6, doi 10.2769/88565, page 113.

5.2 HELCATS Presentations

We list here presentations made on behalf of the project as oral or posters at national and international meetings:

Oral presentations:

12th European Space Weather Week, Ostend, Belgium – 23-27 November 2015
[R. Harrison et al., presentation on HELCATS overview and highlights in session on Recent Advances in Space Weather Science]
[Rodriguez, S. Willems, V. Pant, M. Mierla, A. Devos. (oral), Automatic detection of CMEs in STEREO-HI data]

European Geosciences Union General Assembly, Vienna, Austria – 12-17 April 2016
[E. Sanchez-Diaz et a., presentation 'Properties of the very slow solar wind']
[P. Boakes et al., presentation 'HELCATS Prediction of planetary CME arrival times']

Solar Orbiter SWT-18, April 13, 2016, Alcala, Spain
[V. Krupar, oral 'Tracking CME-driven shocks using radio measurements']

First VarSITI General Symposium, June 6-10, 2016, Bulgaria
[R. Harrison et al., HELCATS - Heliospheric Cataloguing, Analysis and Techniques Service]
[D. Barnes et l., A Catalogue of geometrically-modeled coronal mass ejections observed by the STEREO heliospheric imagers
[V. Bothmer et al., Deriving/cataloguing CME kinematics from modelling multipoint observations]
[I. Plotnikov et al., Long-term tracking of corotating density structures using heliospheric imaging. Catalogue update]
[R.F. Pinto et al., Simulating and cataloguing the background solar wind from 1 to 21 solar radii]

CESRA 2016: Solar radio physics from the chromosphere to near Earth, 13-17 Jun 2016 Orleans, France
[V. Krupar et al., oral, 'Radio triangulation of solar radio emissions: STEREO/Waves measurements']
poster 'HELCATS: Radio Burst Measurements']

Irish National Astronomy Meeting, 2016 September 9, Dublin, Ireland
[Murray, S. A., et al. (oral), 'HELCATS: Connecting Coronal Mass Ejections to their Solar Region Sources']

13th European Space Weather Week, Ostend, Belgium – 14-18 November 2016
[R.A. Harrison, 'Highlights and results from the FP7 HELCATS (Heliospheric Cataloguing, Analysis and Techniques Service) project']

American Geophysical Union Fall Meeting, San Francisco, California, USA - 12-16 December 2016
[E. Palmerio et al., oral 'Prediction of in-situ magnetic structure of flux ropes from coronal observations']

European Geosciences Union General Assembly – 24-28 April 2017
[R.A. Harrison, J. Davies, C. Perry, C. Moestl, A. Rouillard, V. Bothmer, L. Rodriguez, J. Eastwood, E. Kilpua, P. Gallagher, D. Odstrcil, oral, 'Overview of the HELCATS project (solicited)']
[E. Sanchez-Diaz, A.P. Rouillard, J.A. Davies, B. Lavraud, N.R. Sheeley, R.F. Pinto, E. Kilpua, I. Plotnikov, and V. Genot, oral, 'Observational Evidence for the Associated Formation of Blobs and Raining Inflows in the Solar Corona']
[E. Palmerio, E. Kilpua, V. Bothmer, A. Isavnin, C. Möstl, L. Green, A. James, J. Davies, R. Harrison, oral, 'Magnetic structure of Earth-directed events in the HELCATS LINKCAT catalog during 2011–2013']
[I. Plotnikov, A.P. Rouillard, J. Davies, V. Bothmer, J. Eastwood, P. Gallagher, R. Harrison, E. Kilpua, C.C. Möstl, C. Perry, L. Rodriguez, B. Lavraud, V. Genot, R. Pinto, and E. Sanchez-Diaz,oral, 'Long-Term Tracking of Corotating Density Structures Using Heliospheric Imaging (catalogue of CIRs during 2007-2014)']
[R. Pinto, A. Rouillard, D. Odstrcil, L. Mays, oral, 'Simulating and cataloguing the background solar wind conditions']

Poster presentations:

Seventh Solar Information PRocessing Workshop, La Roche-en-Ardenne, Belgium, August 18-21, 2014
[R. Harrison et al., poster 'HELCATS: Heliospheric Cataloguing, Analysis and techniques Service]

American Geosciences Union Fall Meeting, December 2014
[M. Bisi et al., poster 'The HELCATS Project: Characterising the Evolution of Coronal Mass Ejections Observed During Solar Cycle 24']

National Astronomy Meeting, Llandudno, Wales, July 2015
[R. Harrison et al., poster 'HELCATS: Heliospheric Cataloguing, Analysis and techniques Service]
[J. P. Eastwood et al., poster 'Radio signatures of coronal mass ejections in the STEREO era; initial results from the HELCATS project']

First Joint Solar Probe Plus-Solar Orbiter Workshop, September 2-4, 2015, Florence, Italy
[V. Krupar et al., poster 'The 2013 November 29 coronal mass ejection and its radio signatures']

American Geophysical Union, Fall Meeting 2015, abstract #SH53B-2498, San Francisco, USA
[V. Krupar et al., poster 'Radio Triangulation of Type II Bursts Associated with a CME - CME Interaction']

European Geosciences Union General Assembly, Vienna, Austria – 12-17 April 2016
[R. Harrison et al. - HELCATS overview poster (Session ST1.8 on Progress in Space Sciences Fostered by the European Commission)]
[Rodriguez, S. Willems, V. Pant, M. Mierla, A. Devos, S. Housteaux (solicited poster)
Automatic detection of CMEs in STEREO-HI data for the FP7 HELCATs project]

First VarSITI General Symposium, June 6-10, 2016, Bulgaria
[V. Krupar et al., poster 'Preliminary catalogue of radio burst measurements']
[R.F. Pinto et al., poster, 'Solar wind speed and flux-tube geometry']

[A. Pluta et al., 'Forecasting CME arrival times in 3D - The DDC tool']
[A.P. Rouillard et al., 'Using the HELCATS catalogue to study the connectivity of probes to coronal shocks']
[A.P. Rouillard et al., 'CDPP , GFI and HELCATS teams, Interactive tools to access the HELCATS catalogues']

AOGS, July 31-August 5, 2016, Beijing, China
[V. Krupar et al., poster 'HELCATS: Radio Burst Measurements']

13th European Space Weather Week, Ostend, Belgium – 14-18 November 2016
[R. Pinto et al., poster, 'Simulating, cataloguing and forecasting the background solar wind conditions']
[D. Barnes et al., poster, 'A Catalogue of Geometrically-Modelled Coronal Mass Ejections Observed by the STEREO Heliospheric Imagers']

European Geosciences Union General Assembly, Vienna, Austria – 24-28 April 2017
[L.Barnard, C.Scott, C. de Koning, M. Owens, J. Wilkinson, J. Davies, poster, 'Testing the current paradigm for space weather prediction with heliospheric imagers']
[I. Plotnikov, A. Rouillard, G. Share, poster, 'The magnetic connectivity of coronal shocks to the visible disk during long-duration gamma-ray flares']
[S. Murray, P. Gallagher, E. Carley, P. Zucca, poster, 'Connecting Coronal Mass Ejections to their Solar Active Region Sources']
[R. Pinto, A. Rouillard, V. Génot, T. Amari, E. Buchlin, N. Arge, C. Sasso, V. Andretta, A. Bemporad, poster, 'Validating coronal magnetic field reconstruction methods using solar wind simulations and synthetic imagery']
[V. Bothmer, N. Mrotzek, S. Murray, P. Gallagher, D. Barnes, J. Davies, R. Harrison, poster, 'CME properties and solar source region characteristics – HELCATS results']
[N. Mrotzek, V. Bothmer, J. Davies, R. Harrison, poster, 'A Multi-Model Approach to the Analysis of the Kinematics of CMEs Based on Multi-point Space Observations']
[E. Lumme, J. Pomoell, E. Kilpua, E. Palmerio, poster, 'Data-driven time-dependent magnetofrictional modelling of coronal mass ejections and sensitivity of the modelling output to the driving electric field']
[E. Sanchez-Diaz, A.P. Rouillard, J.A. Davies, B. Lavraud, E. Kilpua, I. Plotnikov, V. Genot, R. F. Pinto, poster, 'Analysis of the variability of the slow solar wind from a highly tilted neutral line: implications for the origin of the slow solar wind']
[E. Sanchez-Diaz, A.P. Rouillard, J.A. Davies, E. Kilpua, I. Plotnikov, poster, 'A catalogue of the small transients observed in STEREO HI-A and their associated in-situ measurements']
[D. Barnes, J. Davies, R. Harrison, C. Perry, C. Möstl, A. Rouillard, V. Bothmer, L. Rodriguez, J. Eastwood, E. Kilpua, P. Gallagher, poster, 'A Catalogue of Coronal Mass Ejections Observed by the STEREO Heliospheric Imagers: Results from HELCATS']
[L. Rodriguez, S. Willems, V. Pant, M. Mierla, A. Devos, S. Hosteaux, poster, 'Automatic detection of CMEs in STEREO-HI data for the FP7 HELCATs project']
[A. Isavnin, E. Kilpua, C. Möstl, E. Palmerio, J. Pomoell, R. Winslow, T. Amerstorfer, L. Mays, poster, 'Multipoint analysis of CME-CME interaction']
[C. Möstl, A. Isavnin, E. Kilpua, V. Bothmer, N. Mrotzek, P. Boakes, L. Rodriguez, V. Krupar, J. Eastwood, J. Davies, R. Harrison, D. Barnes, R. Winslow, and the HELCATS team, poster, 'Modeling of coronal mass ejections with the STEREO heliospheric imagers verified with in situ observations by the Heliophysics System Observatory']
[E. Kilpua, C. Möstl, V. Bothmer, A. Isavnin, R. Harrison, J. Davies, E. Palmerio, P. Boakes, N. Mrotzek, poster, 'Using helispheric imager observations in predicting the impact of coronal mass ejections (CMEs) at planets']
[S. Good, R. Forsyth, poster, 'Evolution of ICMEs observed by radially aligned spacecraft']
[J. Pomoell, E. Kilpua, C. Verbeke, E. Lumme, S. Poedts, E. Palmerio, A. Isavnin, poster, 'Modeling the Sun-To-Earth Evolution of the Magnetic Structure of Coronal Mass Ejections with EUHFORIA']
[A.P. Rouillard, M. Lavarra, poster, 'Testing a new flux rope model using the HELCATS CME catalogue']
[A. Rouillard, I. Plotnikov, R. Pinto, V. Génot, M. Bouchemit, J. Davies, poster, 'Interactive Tools to Access the HELCATS Catalogues']
[M. Bisi, D. Barnes, J. Eastwood, V. Krupar, J. Magdalenic, R. Harrison, J. Davies, R. Fallows, poster, 'EU HELCATS Project WP7: Combining Observations of Interplanetary Scintillation (IPS) and Heliospheric Visible-Light Imaging of CMEs and SIRs for Space-Weather Purposes']
[M. Bisi, E. Jensen, C. Sobey, R. Fallows, B. Jackson, D. Barnes, A. Giunta, P. Hick, T. Eftekhari, H.-S. Yu, D.

Odstrcil, M. Tokumaru, B. Wood, poster, 'Observations and Analyses of Heliospheric Faraday Rotation of a Coronal Mass Ejection (CME) Using the LOw Frequency ARray (LOFAR) and Space-Based Imaging Techniques']
[M. Bisi, J. Americo Gonzalez-Esparza, B. Jackson, E. Aguilar-Rodriguez, M. Tokumaru, I. Chashei, S. Tyul'bashev, P. Manoharan, R. Fallows, O. Chang, H.-S. Yu, K. Fujiki, V. Shishov, D. Barnes, poster,'The Worldwide Interplanetary Scintillation (IPS) Stations (WIPSS) Network in support of Space-Weather Science and Forecasting']
[J. Magdalenic, M. Temmer, V. Krupar, C. Marque, A. Veronig, J. Eastwood, poster,'The February 15 2011 CME-CME interaction and possibly associated radio emission']
[V. Krupar, O. Kruparova, O. Santolik, V. Bothmer, N. Mrotzek, J.P. Eastwood, poster,'Radio triangulation of solar radio emissions associated with the 2012 July 23 CME']
[J. Eastwood, V. Krupar, J. Magdalenic, M. Bisi, N. Gopalswamy, J. Davies, R. Harrison, D. Barnes, poster,'Cataloguing radio emission associated with coronal mass ejections: results from the HELCATS project'

5.3 References

We list here additional papers to which the report refers.

Antiochos S. K., DeVore, C. R., Karpen, J. T., & Mikić, Z., 2007, ApJ, 671, 936
Arge, C.N., Hildner, E., Pizzo, V.J., Harvey, J.W.: 2002, J. Geophys. Res. (Space Phys.) 107, 1319
Billings, D.E., 1996, A guide to the solar corona, Academic Press, ISBN-10: 1483254259.
Birn, J., & Hesse, M., 2009, AnG, 27, 1067
Bisi, M.M., Fallows, R.A., Breen, A.R., O'Neill, I.J., 2010, Solar Phys. 261, 149
Borovsky, J.E., Denton, M.H., 2010, J. Geophys. Res. 115, 10101
Bosman, E., Bothmer, V., Nistico, G., Vourlidas, A., Howard, R.A., Davies, J.A., 2012, Solar Phys. 281, 167.
Bothmer, V., & Schwenn, R., 1998, Annales Geophysicae 16, 1.
Brueckner, G. E., Howard, R. A. Koomen, M. J. et al., 1995, SoPh, 162, 357
Brown, D.S., Bewsher, D., Eyles, C.J., 2009, Solar Phys. 254, 185
Colaninno, R.C., Vourlidas, A., 2009, Astrophys. J. 698, 852.
Conlon, T.M., Milan, S.E., Davies, J.A., Williams, A.O., 2015, Solar Phys. 290, 2291
Cremades, H., Bothmer, V., 2004, Astron. Astrophys. 422, 307.
Davies, J.A., Harrison, R.A., Rouillard, A.P., et al., 2009, Geophys. Res. Lett. 36, 2102
Davies J. A., Harrison R. A., Perry C. H., Möstl C., Lugaz N., Rollett T., Davis C. J., Crothers S. R., Temmer M., Eyles C. J., Savani N. P., 2012, ApJ, 750, 1, 23, 12.
Davies, J.A., Perry, C.H., Trines, R.M.G.M., Harrison, R.A., Lugaz, N., Mostl, C., Liu, Y.D., Steed, K., 2013, Astrophys. J. 777, 167.
DeForest, C. E., Howard, T. A., Webb, D. F., & Davies, J. A., 2016, Space Weather 14, 32.
DeForest, C. E., & Howard, T. A., 2015, Astrophys. J. 804, 126.
Domingo, V., Fleck, B., & Poland, A. I., 1995, Solar Phys. 162, 1
Dorrian, G.D., Breen, A.R., Davies, J.A., Rouillard, A.P., Fallows, R.A., Whittaker, I.C., Brown, D.S., Davis, C.J., Harrison, R.A., Grande, M., 2010, Solar Phys. 265, 207
Einaudi, G., Chibbaro, S., Dahlburg, R.B., & Velli, M., 2001, ApJ, 547, 1167
Elliot H. A., Henney, C. J., McComas, D. J., Smith, C. W., & Vasquez, B. J., 2012, J.Geophys.Research (Space Physics), 117, A9
Eyles, C.J., Harrison, R.A., Davis, C.J., et al., 2009, Solar Phys. 254, 387
Falconer, D.A., Moore, R.L., Gary, G.A., 2008, Astrophys. J. 689, 1433.
Gibson S. E., Kucera T. A., White S. M., Dove J., Fan Y., Forland B., Rachmeler L., Downs C., Reeves, K., 2016, Frontiers in Astron. and Space Sci. 8
Good, S. W., & Forsyth, R. J., 2016, Solar Physics 291, 239.
Hardwick, S.A., Bisi, M.M., Davies, J.A., Breen, A.R., Fallows, R.A., Harrison, R.A., Davis, C.J., 2013, Solar Phys. 285, 111
Harrison, R.A., Davies, J.A., Rouillard, A.P., et al., 2009, Solar Phys. 256, 219

Harrison, R.A. Davies, J.A., Moestl, C. et al., 2012, Astrophys. J. 750, 45
Higgins, P.A., Gallagher, P.T., McAteer, R.T.J., Bloomfield, D.S., 2011, Adv. Space Res. 47, 2105.
Howard, R.A., Moses, J.D., Vourlidas, et al., 2008, Space Sci. Rev. 136, 67
Hu, Q., Qiu, J., Dasgupta, B., Khare, A., & Webb, G. M., 2014, Astrophys. J. 793, 53.
Isavnin, A., 2016, Astrophys. J. 833, 267.
Isavnin, A., Kilpua E. K. J., & Koskinen, H. E. J., 2011, Solar Physics 273, 205.
Isavnin, A., Vourlidas, A., & Kilpua, E. K. J., 2014, Solar Physics 289, 2141.
Jähne, B., 1997, Digital Image Processing (Springer-Verlag), 463.
Jian, L.K., Russell, C.T., Luhmann, J.G., 2011, Solar Phys. 274, 321
Jian, L., Russell, C.T., Luhmann, J.G., Skoug, R.M., 2006, Solar Phys. 239, 337
Jian, L.K., Russell, C.T., Luhmann, J.G., Galvin, A.B., Simunac, K.D.C., 2013, Am. Inst. Phys. Conf. Ser. CS-1539, 191
Kaiser, M.L., 2005, The STEREO mission: an overview. Adv. Space Res. 36, 1483
Kaiser, M.L., Kucera, T.A., Davila, et al., 2008, Space Sci. Rev. 136, 5
Kasper, J. C., Stevens, M. L. , Lazarus, A. J., Steinberg, J. T. , & Olgivie, K. W., 2007, ApJ, 660, 901
Kilpua, E.K.J., Luhmann, J.G., Gosling, J., et al., 2009, Solar Phys. 256, 327
King, J.H., Papitashvili, N.E., 2005, J. Geophys. Res. 110, 2104
Künzel, H., 1965, Zur Klassifikation von Sonnenfleckengruppen. Astronomische Nachrichten 288, 177.
Lapenta G., & Knoll, D., 2005, ApJ, 624, 1049
Li B., Xia L. D., Chen Y. 2011, Astron. Astrophys. 529, A148
Linton, M. G., & Moldwin, M. B., 2009, JGR, 114, A00B09
Lionello, R., Riley, P., Linker, J.A., Miki´c, Z., 2005, Astrophys. J. 625, 463
Lionello R., Velli M., Downs C., Linker J. A., Mikic Z., 2014, Astrophys. J. 796, 111
Lugaz, N., Kintner, P., Möstl, C., Jian, L. K., Davis, C. J., & Farrugia, C. J., 2012, Solar Physics 279, 497.
Magdalenic, J., Marque, C., Krupar, V., Mierla, M., Zhukov, A.N., Rodriguez, L., Maksimovic, M., Cecconi, B., et al., 2014, Astrophys. J. 791, 115
Marubashi, K., Akiyama, S., Yashiro, S., Gopalswamy, N., Cho, K.-S., & Park, Y.-D., 2015, Solar Physics 290, 1371.
McIntosh, P.S., 1990, Solar Phys. 125, 251.
Möstl, C., Rollett, T., Lugaz, N., Farrugia, C. J., Davies, J. A., Temmer, M., Veronig, A. M., Harrison, R.A., Crothers, S., Luhmann, J. G., Galvin, A. B., Zhang, T. L., Baumjohann, W., & Biernat, H. K., 2011, Astrophys. J. 741, 34.
Möstl, C. & Davies, J. A., 2013, Solar Physics 285, 411.
Möstl, C., Amla, K., Hall, J. R., Liewer, P. C., De Jong, E. M., Colaninno, R. C., Veronig, A. M., Rollett, T., Temmer, M., Peinhart, V., Davies, J. A., Lugaz, N., Liu, Y. D., Farrugia, C. J., Luhmann, J. G., Vrsnak, B., Harrison, R. A., & Galvin, A. B., 2014, Astrophys. J. 787, 119.
Möstl, C., Isavnin, A., Boakes, P. D., Kilpua, E. K. J., Davies, J. A., Harrison, R. A., Barnes, D., Krupar, V., Eastwood, J. P., Good, S. W., Forsyth, R. J., Bothmer, V., Reiss, M. A., Amerstorfer, T., Winslow, R. M., Anderson, B. J., Philpott, L. C., Rodriguez, L., Rouillard, A. P., Gallagher, P. T., & Zhang, T. L., 2017, ArXiv e-prints arXiv:1703.00705.
Palmerio, E., Kilpua, E. K. J., James, A. W., Green, L. M., Pomoell, J., Isavnin, A., and Valori, G., 2017, Solar Phys. in press.
Patsourakos, S., & Georgoulis, M. K., 2016, Astron. & Astrophys. 595, A121.
Pinto R., Grappin R., Wang,Y.-M., Léorat J., 2009, Astron. Astrophys. 497, 537
Pinto, Rouillard, Brun, 2016, Astron.omy and Astrophysics, 592, A65
Plotnikov, I., A. P. Rouillard, J. A. Davies, et al., 2016, SoPh, 291, 1853
Robbrecht, E., Berghmans, D., 2004, A&A, 425, 1097.
Robbrecht, E., Berghmans, D., Van der Linden, R. A. M., 2009, ApJ, 691, 2, 1222.
Rodriguez, L., Mierla, M., Zhukov, A.N., West, M., Kilpua, E., 2011, Sol. Phys. 270, 561.
Rollett, T., Möstl, C., Isavnin, A., Davies, J. A., Kubicka, M., Amerstorfer, U. V., & Harrison, R. A., 2016, Astrophys. J. 824, 131.
Rollett, T., Möstl, C., Temmer, M., Frahm, R. A., Davies, J. A., Veronig, A. M., Vrsnak, B., Amerstorfer, U. V., Farrugia, C. J., Zic, T., & Zhang, T. L., 2014, Astrophys. J. 790, L6.
Rouillard, A.P., Lockwood, M., Finch, I., 2007, J. Geophys. Res. 112, 5103
Rouillard, A.P., Davies, J.A., Forsyth, R.J., et al., 2008, Geophys. Res. Lett. 35, 10110

Rouillard, A.P., Davies, J.A., Lavraud, B., et al., 2010a, J. Geophys. Res. 115, 4103
Rouillard, A.P., Lavraud, B., Davies, et al., 2010b, J. Geophys. Res. 115, 4104
Rouillard, A.P., Sheeley, N.R. Jr., Cooper, et al.., 2011, Astrophys. J. 734, 7
Rouillard A. P., Sheeley N. R., Tylka A., et al., 2012, Astrophys. J. 752, 44
Sachdeva, N., P. Subramanian, R. Colaninno, A. Vourlidas, 2015, Astrophys. J. 809, 2
Sanchez-Diaz, E., Rouillard, A.P., Lavraud, et al., 2016, J. Geophys. Res. 121, 2830
Sanchez-Diaz E., Rouillard A. P., Lavraud B., et al., 2016, J. Geophys. Res. (Space Physics), 22433
Schatten, K. H., Wilcox, J. M., & Ness, N. F., 1969, SoPh, 6, 442
Scherrer, P.H., Bogart, R.S., Bush, R.I., Hoeksema, J.T., et al., 1995, Solar Phys. 162, 129
Scherrer, P. H., Schou, J., Bush, R. I., et al., 2012, SoPh., 275, 207
Schrijver, C.J., 2007, Astrophys. J. Lett. 655, L117.
Schrijver, C. J., & De Rosa, M. J., 2003, SoPh, 212, 165
Sheeley, N.R. Jr., Rouillard, A.P.: 2010, Astrophys. J. 715, 300
Sheeley, N.R. Jr., Herbst, A.D., Palatchi, et al., 2008a, Astrophys. J. 675, 853
Sheeley, N.R. Jr., Herbst, A.D., Palatchi, C.A., et al, 2008b, Astrophys. J. Lett. 674, L109
Sheeley, N.R., Walters, J.H., Wang, Y.-M., Howard, R.A., 1999, J. Geophys. Res. 104, 24739
Sheeley, N. R., & Wang, Y.-M., 2001, ApJ, 562, L107
Sheeley, N. R., & Wang, Y.-M., 2002, ApJ, 579, 874
Sheeley, N. R., & Wang, Y.-M., 2007, ApJ, 655, 1142
Sheeley, N. R., & Wang, Y.-M., 2014, ApJ, 797, 10
Sheeley, N. R., Y.-M., Wang, S. H. Hawley, et al., 1997, ApJ, 484(1), 472
Sheeley, N. R., Knudson, T. N., & Wang, Y.-M., 2001, ApJ, 546, L131
Sheeley, N. R., Lee, D. D.-H., Casto, K. P., Wang, Y.-M., & Rich, N. B., 2009, ApJ, 694, 1471
Stakhiv, M., Landi, E., Lepri, S. T., Oran, R., & Zurbuchen, T. H., 2015, ApJ, 801, 100
Stakhiv, M., Lepri, S. T., Landi, E., Tracy, P., & Zurbuchen, T. H., 2016, ApJ, 829, 117
Tappin, S.J., Howard, T.A., 2009, Astrophys. J. 702, 862
Thernisien, A.F.R., Howard, R.A., Vourlidas, A., 2006, Astrophys. J. 652, 763.
Thernisien, A., Vourlidas, A., Howard, R.A., 2009, Solar Phys. 256, 111.
Thompson, W.T., 2006, A&A, 449, 791.
Tucker-Hood, K., Scott, C., Owens, M., Jackson, D., Barnard, L., Davies, J. A., Crothers, S., Lintott, C., Simpson, R., Savani, N. P., Wilkinson, J., Harder, B., Eriksson, G. M., L Baeten, E. M., & Wan Wah, L. L., 2015, Space Weather 13, 35.
Vrsnak, B., Temmer, M., Zic, T., Taktakishvili, A., Dumbovic,, M., Möstl, C., Veronig, A. M., Mays, M. L., & Odstrcil, D., 2014, Astrophys, J. Suppl. Ser. 213, 21.
Vourlidas, A., Howard, R.A., Esfandiari, E., Patsourakos, S., Yashiro, S., Michalek, G., 2010, Astrophys. J. 722, 1522
Wang, Y.-M., Sheeley, N.R. Jr., 1990, Astrophys. J. 355, 726
Wang, Y.-M., Sheeley, N.R. Jr., 1992, Astrophys. J. 392, 310
Wang, Y.-M., Sheeley, N.R., Socker, D.G., et al, 2000, J. Geophys. Res. 105, 25133
Wang, Y.-M., N. R. Sheeley, J. H. Walters, et al., 1998, ApJ, 498, L165
Wang, Y.-M., Sheeley, N. R., Howard, R. A., St. Cyr, O. C., & Simnett, G. M., 1999, GeoRL, 26, 1203
Wang, Y.-M., Y.-K. Ko, and R. Grappin, 2009, Slow Solar Wind from Open Regions with Strong Low-Coronal Heating, Astrophys. J., 691, 760
Webb, D.F., Howard, R.A., 1994, J. Geophys. Res. 99, 4201
Winslow, R. M., Lugaz, N., Philpott, L. C., Schwadron, N. A., Farrugia, C. J., Anderson, B. J., & Smith, C. W., 2015, J. Geophys. Res. (Space Physics) 120, 6101.
Yang L. P., Feng X. S., Xiang C. Q., Liu Y., Zhao X., Wu S. T., 2012, J. Geophys. Res. (Space Physics), 117, A08110
Yurchyshyn, V., Yashiro, S., Abramenko, V., Wang, H., Gopalswamy, N., 2005, Astrophys. J. 619, 599.
Zhang, J., Richardson, I. G., Webb, D. F., Gopalswamy, N., Huttunen, E., Kasper, J. C., Nitta, N. V., Poomvises, W., Thompson, B. J., Wu, C.-C., Yashiro, S., & Zhukov, A. N., 2007, J. Geophys. Res. (Space Physics) 112, A10102.
Zheng, Y, 2013, Space Weather 11, 641.

6 ACKNOWLEDGEMENTS

The HELCATS team would like to take this opportunity to thank the EU FP7 project for supporting our project and would particularly like to thank the Project Officers, Sabri Mekaoui and Andrej Rozkov, and the Reviewer, Professor Brigitte Schmieder, for all of their support and efforts throughout the project. The STFC team would like to note and acknowledge the enthusiasm and hard work of all of the beneficiaries. The spirit of collaboration between the beneficiary groups has ensured that this project has been a pleasure to tackle, and it has surely enhanced the scientific output of the project.